

University of Alberta

***Mechanism and Kinematics of Three Translational Slides
Along the North Saskatchewan River Valley, Edmonton***

by

Soe Moe Kyaw Win



A thesis submitted to the Faculty of Graduate Studies and Research
in partial fulfillment of the

requirements for the degree of *Doctor of Philosophy*
in Geotechnical Engineering

Department of Civil & Environmental Engineering

Edmonton, Alberta
Fall 2008



Library and
Archives Canada

Published Heritage
Branch

395 Wellington Street
Ottawa ON K1A 0N4
Canada

Bibliothèque et
Archives Canada

Direction du
Patrimoine de l'édition

395, rue Wellington
Ottawa ON K1A 0N4
Canada

Your file *Votre référence*
ISBN: 978-0-494-46428-1
Our file *Notre référence*
ISBN: 978-0-494-46428-1

NOTICE:

The author has granted a non-exclusive license allowing Library and Archives Canada to reproduce, publish, archive, preserve, conserve, communicate to the public by telecommunication or on the Internet, loan, distribute and sell theses worldwide, for commercial or non-commercial purposes, in microform, paper, electronic and/or any other formats.

The author retains copyright ownership and moral rights in this thesis. Neither the thesis nor substantial extracts from it may be printed or otherwise reproduced without the author's permission.

AVIS:

L'auteur a accordé une licence non exclusive permettant à la Bibliothèque et Archives Canada de reproduire, publier, archiver, sauvegarder, conserver, transmettre au public par télécommunication ou par l'Internet, prêter, distribuer et vendre des thèses partout dans le monde, à des fins commerciales ou autres, sur support microforme, papier, électronique et/ou autres formats.

L'auteur conserve la propriété du droit d'auteur et des droits moraux qui protègent cette thèse. Ni la thèse ni des extraits substantiels de celle-ci ne doivent être imprimés ou autrement reproduits sans son autorisation.

In compliance with the Canadian Privacy Act some supporting forms may have been removed from this thesis.

Conformément à la loi canadienne sur la protection de la vie privée, quelques formulaires secondaires ont été enlevés de cette thèse.

While these forms may be included in the document page count, their removal does not represent any loss of content from the thesis.

Bien que ces formulaires aient inclus dans la pagination, il n'y aura aucun contenu manquant.


Canada

This thesis is dedicated to my mother and father,
Daw Mya Mya Win and Dr. U Kyaw Win.

ABSTRACT

River valley landslides are common in central Alberta, where several large rivers and tributaries cut the Upper Cretaceous bedrocks and overlying glacial deposits post-glacially, forming steep valleys. Failure mechanisms of river valley landslides are complex and there are uncertainties in the use of pore pressures and mobilized shear strength for stability analyses.

A series of laboratory and field investigations were conducted to improve the pore pressure measurements in weak rock. The laboratory investigation included a determination of the cement-bentonite grout properties and pore pressure response testing of grout and clay shale samples. Investigation results revealed that the grout mix with a water:cement:bentonite ratio of 2.0:1.0:0.3 could be successfully used for grout-in piezometer installation in weak rock.

To improve long term pore pressure measurements in weak rock, a flushable piezometer was developed and tested the field. The instrument, comprising a flushable adaptor, flushing tubes, a high air entry filter, and a normal vibrating wire piezometer, has ability to remove air bubbles from the piezometer cavity. Unlike a twin-tube hydraulic piezometer, the flushable piezometer installation depth is not limited by the water columns inside the flushing tubes. This ability to flush out air from the piezometer cavity significantly improves long-term pore pressure measurements in weak rock.

A detailed study of three landslides along the North Saskatchewan River Valley in Edmonton, Alberta was conducted. The study revealed that the river valley landslides

are caused by a combination of several factors, including toe erosion by the river, residential developments behind the slope crests, the rise of groundwater levels due to urban development, and softening of the bedrock at the valley wall.

Observations of the river valley landslides also revealed that these landslides can be idealized into five kinematic stages. In order to account for the formation of a graben in the stability analysis, a simple two inclined block model is introduced. This model can be used to analyse different landslide stages, starting from a single-block to a two-block movement. The results also revealed that the formation of a counter scarp, separating the active and passive blocks, triggers an acceleration of slope movement.

ACKNOWLEDGEMENT

The author would like to thanks to his supervisors Dr. C. Derek Martin, David M. Cruden and Norbert R. Morgenstern for their guidance, encouragement and support during the years of this research.

The author would like to thanks to D. Lewycky, and P. R. Lach, of The City of Edmonton, for the support for the field investigation and information required for the case studies.

The author would like to acknowledge Mr. Pete Barlow of AMEC Earth & Environmental and Mr. Tony Ruban of EBA Engineering Consultants Ltd, for information provided from geotechnical investigation in Whitemud Road and Keillor road landslide.

The unfailing help of Steve Gamble is gratefully acknowledged. Appreciation is also extended to Gerry Cyre and Christine Hereygers.

The author is very grateful to his dear parents Dr. Kyaw Win and Daw Mya Mya Win.

Finally, the author wishes to thank his wife, Thida, and lovely daughter Maple.

TABLE OF CONTENT

CHAPTER 1	Introduction	1
1.1	Background	1
1.2	Purpose of this research	4
1.3	Scope of work	5
CHAPTER 2	Literature review.....	8
2.1	Introduction.....	8
2.2	Classification of stiff clay and weak rocks	8
2.3	Instability mechanisms in weak rock slopes	10
2.3.1	Fissure softening	10
2.3.2	Pore pressure equalization and swelling	11
2.3.3	Progressive failure	14
2.3.4	Loosening	15
2.4	Shear strength behaviour of stiff clay and weak rocks	16
2.4.1	Shear strength of stiff clay and weak rock.....	16
2.4.2	Shear strength along structural discontinuities	18
2.4.3	Strength behaviour of weak rock due to softening.....	19
2.5	Failure mechanisms in weak rock	21
2.5.1	First time slide.....	21
2.5.2	Reactivated slide	23
2.5.3	Kinematics of a landslide	23
2.5.4	Rate of movement	25
2.5.5	Stability consideration	25
2.6	Summary	27
CHAPTER 3	River valley landslides in Edmonton.....	48
3.1	Introduction.....	48
3.2	Regional Geology	49
3.3	The Grierson Hill landslide.....	50
3.4	Lesueur Landslide	52
3.5	Devon Landslide	54
3.6	Pore pressure response of river valley landslides	55
3.7	Summary	56
CHAPTER 4	Pore pressure measurement in weak rocks.....	67

4.1	Introduction.....	67
4.2	Pore pressure below the ground surface	68
4.3	Response of pore pressure due to excavation	68
4.4	Pore pressure measuring instruments	69
4.4.1	Standpipe piezometers	69
4.4.2	Hydraulic piezometers	70
4.4.3	Diaphragm piezometers.....	71
4.4.4	Filters.....	72
4.4.5	Piezometric time lag.....	73
4.5	Grout-in piezometer installation	75
4.5.1	Piezometric error due to grout-in installation	76
4.6	Summary	78
CHAPTER 5 Laboratory Investigation		90
5.1	Introduction.....	90
5.2	Properties of cement-bentonite grout.....	91
5.2.1	Mechanism of cement-bentonite grout mix.....	91
5.3	Laboratory test setup	92
5.3.1	Load frame	92
5.3.2	Constant pressure system	93
5.3.3	Measurement devices	93
5.3.4	Data acquisition system	93
5.3.5	Calibration of instruments	93
5.4	Cement-bentonite grout mix.....	95
5.5	Unconfined compression tests	96
5.5.1	Testing procedure.....	96
5.6	Permeability tests	97
5.6.1	Test equipment.....	98
5.6.2	Testing Procedure	98
5.7	Laboratory test results	101
5.7.1	Unconfined compression tests.....	101
5.7.2	Permeability test	102
5.7.3	Discussion	102
5.8	Pore pressure response test of grout and clay shale samples	103
5.9	Testing Apparatus.....	104

5.9.1	Modified large triaxial cell.....	104
5.9.2	Reaction frame	104
5.9.3	Small pressure transducer	105
5.10	Sample preparation for the pressure response test.....	107
5.10.1	Grout Sample.....	107
5.10.2	Clay shale sample.....	107
5.11	Testing procedure.....	108
5.12	Results of pore pressure response tests.....	108
5.12.1	Pressure response of the grout sample.....	108
5.12.2	Pressure response of the clay shale sample	109
5.13	Summary	109
CHAPTER 6	Development of a Flushable Piezometer.....	130
6.1	Introduction.....	130
6.2	Recent development of flushable piezometer	131
6.3	The developed flushable adaptor.....	132
6.3.1	Adaptor body	133
6.3.2	Check valves	133
6.3.3	High air entry filter (HAE)	134
6.4	Flushable Piezometer	135
6.5	Laboratory testing of a flushable piezometer.....	135
6.5.1	Large triaxial cell.....	135
6.5.2	Portable calibrator.....	136
6.5.3	Readout unit	136
6.5.4	Equipment setup.....	136
6.5.5	Testing procedures	137
6.6	Field investigation program.....	138
6.6.1	Water standpipe.....	138
6.6.2	RST pneumatic piezometer (P-100-1).....	138
6.6.3	Geokon 4500-MLP vibrating piezometer	139
6.6.4	Slope Indicator's vibrating wire piezometer (Model - 52611030)	139
6.7	Field piezometer installation	139
6.7.1	Location of test area—Forest Heights Park.....	139
6.7.2	Installation plan in Forest Heights Park.....	140
6.8	Piezometer installation procedure.....	142

6.8.1	Vibrating wire piezometer assembly.....	142
6.8.2	Geokon multi-level piezometer assembly.....	142
6.8.3	Flushable piezometer assembly.....	143
6.8.4	Field installation.....	143
6.9	Monitoring procedures.....	144
6.9.1	Cluster 1.....	144
6.9.2	Cluster 2.....	145
6.10	Summary.....	146
CHAPTER 7	Keillor road landslide.....	172
7.1	Introduction.....	172
7.2	Landslide history.....	173
7.2.1	1989 Toe failure.....	173
7.2.2	1994 Keillor Road failure.....	173
7.2.3	Major failure 2002.....	173
7.2.4	Air photo review.....	174
7.3	Site investigation and instrumentation.....	175
7.3.1	Pre-2002 investigation.....	175
7.3.2	Post-failure investigation.....	175
7.3.3	Stratigraphy.....	176
7.3.4	Pore pressure regime of the slide area.....	176
7.4	Laboratory Investigation.....	178
7.4.1	Index tests.....	178
7.4.2	Direct shear tests.....	178
7.5	Post-failure landslide observations.....	182
7.5.1	Pile settlement.....	182
7.5.2	Long-term monitoring of slope movements.....	183
7.5.3	Kinematics of the slide.....	183
7.6	Slope stability analysis.....	185
7.7	Summary.....	186
CHAPTER 8	Whitemud road landslide.....	217
8.1	Introduction.....	217
8.2	Landslide history.....	217
8.2.1	1999 failure.....	217
8.2.2	Airphoto review.....	218

8.3	Site investigation and instrumentation.....	219
8.3.1	Pre-failure investigation	219
8.3.2	Post-failure investigation.....	220
8.3.3	Stratigraphy	221
8.4	Pore pressure regime of the Whitemud Road area	222
8.4.1	Pore pressure behind the valley wall.....	222
8.4.2	Pore pressure inside the displaced material.....	222
8.5	Laboratory investigation.....	223
8.5.1	Index Tests	223
8.5.2	Strength tests.....	224
8.6	Post-failure landslide observations (Whitemud Road Landslide).....	225
8.6.1	Failure plane geometry	225
8.6.2	Long-term monitoring of slope movements	226
8.7	Remedial measures.....	227
8.8	Stability analyses	228
8.9	Summary	230
CHAPTER 9	Forest heights park landslide.....	254
9.1	Introduction.....	254
9.2	Coal mine workings below Forest Heights Park	255
9.3	Slope instability at Forest Heights Park.....	255
9.4	Geotechnical investigation	256
9.4.1	Stratigraphy	257
9.4.2	Groundwater Conditions	258
9.5	Stability analyses of the river valley	259
9.6	Causes of slope instability	260
9.6.1	Toe erosion by the river	260
9.6.2	Coal mining.....	261
9.6.3	Deficient pore pressure in the bedrock.....	261
9.6.4	Post-failure slope movements and pore pressure response of the bedrock in Forest Heights Park	262
9.7	Post-failure Landslide Mechanism	263
9.8	Summary	264
CHAPTER 10	Stages in the translational sliding of 2 inclined blocks	280
10.1	Introduction.....	280

10.2	Five landslide stages	280
10.3	A simple model of the Landslide Mode	282
10.3.1	Assumptions of the analysis	282
10.3.2	Single block mechanism (Stages 1 and 2)	282
10.3.3	Two inclined blocks model (Stages 3 and 4)	283
10.3.4	Calculation of the resultant force R_2	283
10.3.5	Calculation of the safety factor of the passive block	284
10.4	Stability analysis of the Keillor Road Landslide	284
10.5	Summary	286
CHAPTER 11	Long term stability of weak rock slopes	295
11.1	Introduction	295
11.2	Delayed failure of river valley slopes	295
11.2.1	Pre-failure movements	296
11.2.2	Major failure movements	296
11.2.3	Post-failure movements	296
11.3	Characteristic of river valley landslides in Edmonton	297
11.4	Landslide investigation	298
11.4.1	Seepage water and groundwater level	299
11.4.2	Groundwater flow near the valley wall	299
11.4.3	Swelling and pore pressure equalization	299
11.4.4	Deformation monitoring	300
11.5	Proposed field instrumentation program	300
11.6	Summary	300
CHAPTER 12	Conclusions	306
12.1	Conclusions	306
12.2	Recommendations	308
References	310
APPENDIX A	The Sliding of Two Inclined Blocks	321

LIST OF TABLES

Table 2-1 Abbreviated classification of slope movements (modified from Cruden and Varnes 1996)	28
Table 4-1 Intake factor F for different piezometer types (modified from Hvorslev 1951) 79	
Table 4-2 Estimated hydrostatic time lag for various piezometer installation	79
Table 5-1 Permeability, k, of some grout mixes	111
Table 5-2 Summary of cement-bentonite grout ratios	111
Table 5-3 Permeability of cement bentonite grout samples	112
Table 5-4 Water content, unit weight, and void ratio of 28 day-old grout samples	112
Table 6-1 Piezometer installation in Forest Heights Park	148
Table 7-1 Summary of index tests	188
Table 7-2 Summary of direct shear tests performed on Keillor Road samples	188
Table 7-3 Summary of the laboratory test results for Keillor Road samples	188
Table 7-4 Average movement of the slide body	189
Table 8-1 Summary of index tests and direct shear tests	232
Table 8-2 Strength parameters used in analyses of the Whitemud Road Landslide	233
Table 8-3 Factor of safety obtained from analyses of the Whitemud Road slide area..	233
Table 9-1 Parameters used in analyses of the Forest Heights Park river valley	265
Table 9-2 Factor of safety from the analyses of slope stability in Forest Heights Park.	265
Table 10-1 Slope geometry and strength parameters at the Keillor Road Landslide....	287
Table 10-2 Critical ranges obtained from the analyses	287
Table 11-1 Summary of slope movements for major river landslides in Edmonton	301
Table 11-2 Summary of post-failure rate of movements	302

LIST OF FIGURES

Figure 2-1 A geologic classification of shales (modified from Underwood 1967)	29
Figure 2-2 Two part classification scheme (modified from Morgenstern and Eigenbrod 1974).....	30
Figure 2-3 Progressive deterioration of fissured weak rock (modified from Botts 1986).	31
Figure 2-4 Changes in pore pressure and factor of safety during an excavation of a cut slope in clay (modified from Bishop and Bjerrum 1960).....	32
Figure 2-5 Variation of \bar{r}_u with time: cutting in brown London Clay (modified from Skempton 1978).....	33
Figure 2-6 Pore pressure isochrones (modified from Koppula and Morgenstern 1984) .	34
Figure 2-7 Pore pressure measurement at Bisaccia hill (modified from Fenelli and Picarelli 1990)	35
Figure 2-8 Contours of shear strain in a slope, and its relation to corresponding stress states in an overconsolidated clay (modified from Atkinson and Bransby 1978).....	36
Figure 2-9 Shear characteristics of overconsolidated clay (modified from Skempton 1964).....	37
Figure 2-10 Summary of strength test results, triaxial and direct shear tests (modified from Sinclair and Brooker 1967).....	38
Figure 2-11 Shear strength of a model specimen having a rough surface (modified from Patton 1966)	39
Figure 2-12 Shear characteristic of clay (modified from Skempton 1970).....	40
Figure 2-13 Examples of stress-strain curve for softened and unsoftened back slope materials (modified from Eigenbrod and Morgenstern 1971)	41
Figure 2-14 Results of triaxial tests on Lake Agassiz clays in normalized p'-q space (modified from Graham and Au 1985)	42
Figure 2-15 The effect of softening on engineering behaviour of weak rock (modified from Yoshida et al. 1990)	43
Figure 2-16 Shear strength and normal pressure for cuttings in brown London Clay (modified from Skempton 1970)	44
Figure 2-17 Approximate geometry of failure surface in Cretaceous formations in western Canada (modified from Scott and Brooker 1968)	44

Figure 2-18 Diagram illustrating the ground movements which precede a landslide (modified from Terzaghi 1950)	45
Figure 2-19 Observed creep movement in a Kensal Green cutting (modified from Skempton 1964).....	46
Figure 2-20 Typical single landslides (circular and plane failure).....	46
Figure 2-21 Sliding block failure	47
Figure 3-1 Major landslide location map around the City of Edmonton	57
Figure 3-2 Landslide stages observed in Grierson Hill Landslide from 1900, 1910 to 1983 and present (modified from Martin et al. 1998)	58
Figure 3-3 Typical piezometric pressures in Grierson Hill slide (modified from Martin et al. 1984).....	59
Figure 3-4 Pore pressure distribution in Grierson Hill slide (data from Martin et al. 1984)	59
Figure 3-5 Plan view of the Lesueur Slide (modified from Thomson 1971b).....	60
Figure 3-6 Piezometric elevation vs. time (modified from Thomson 1971b).....	61
Figure 3-7 Piezometric elevation vs. time for LA9 (modified from Thomson 1971b)	62
Figure 3-8 Pore pressure profile in the Lesueur Slide (data from Thomson 1971b).....	62
Figure 3-9 Lesueur Slide slope profile along A-A, (a) Pre-failure 1963, (b) Post-failure June 1964, (c) June 1995. Stratigraphy from Thomson (1971) (modified from Cruden et al. 2002).....	63
Figure 3-10 Location of the Devon Slide (modified from Eigenbrod and Morgenstern 1971).....	64
Figure 3-11 Piezometric elevations at the Devon Slide (modified from Eigenbrod and Morgenstern 1971).....	65
Figure 3-12 Piezometric pressure vs. elevation at the Devon Slide (modified from Eigenbrod and Morgenstern 1971).....	65
Figure 3-13 Normalized pore pressure plot of Upper Cretaceous bedrock of Edmonton (data from Eigenbrod and Morgenstern 1971; Martin et al. 1984; Thomson 1971b)	66
Figure 4-1 Possible pore water pressure profiles above and below the groundwater level (modified from Ridley and Burland 1996)	80
Figure 4-2 Reduction of pore pressure after excavation of slope.....	81
Figure 4-3 Pore pressure in the London Clay cutting at Edgewarebury (modified from Vaughan and Walbancke 1973)	82
Figure 4-4 Observation well and water standpipes	82

Figure 4-5 Schematic of twin-tube hydraulic piezometer installed in fill (modified from Dunnicliff 1993)	83
Figure 4-6 Schematic of pneumatic piezometer (modified from Dunnicliff 1993)	84
Figure 4-7 Vibrating wire piezometer (modified from Dunnicliff 1993).....	85
Figure 4-8 Pore pressure response of vibrating wire piezometer and twin-tube hydraulic piezometers at Chelmarsh Dam (modified from Penman 2002)	86
Figure 4-9 Approximate response times for various types of piezometer (modified from Terzaghi and Peck 1967)	87
Figure 4-10 Model to simulate grout-in piezometer installation (grout-in hole not to scale)	88
Figure 4-11 Normalized error versus permeability ratio	89
Figure 5-1 Constant pressure system.....	113
Figure 5-2 Layout of the laboratory instrument monitoring system	113
Figure 5-3 Unconfined compression test on 14 day-old hard grout sample	114
Figure 5-4 Setup of the permeability cell	114
Figure 5-5 Unconfined compression tests on grout mix A.....	115
Figure 5-6 Unconfined compression tests of grout mix B.....	116
Figure 5-7 Unconfined compression tests of grout mix C	117
Figure 5-8 Unconfined compressive strength vs. water:cement ratio for different curing times	118
Figure 5-9 Variation in permeability with different water:cement ratio and curing time.	119
Figure 5-10 Variation of unconfined compressive strength vs. water:cement ratio by weight (modified from Mikkelsen 2002)	120
Figure 5-11 Void ratio vs. permeability for different curing times	121
Figure 5-12 Details of the modified triaxial cell base.....	122
Figure 5-13 Sketch of the set-up of the modified triaxial cell (not to scale)	123
Figure 5-14 KYOWA small pressure transducer.....	123
Figure 5-15 Photograph of the pore pressure transducer	124
Figure 5-16 Setup of small pressure transducer calibration.....	124
Figure 5-17 Pore pressure response of a small pressure transducer during the calibration test.....	125
Figure 5-18 Hard grout sample with a small pressure transducer.....	125
Figure 5-19 75 mm diameter core sample used in the pore pressure response test....	126
Figure 5-20 Small pressure transducer installation in the core sample	126

Figure 5-21 Setup of modified triaxial cell for pore pressure measurement	127
Figure 5-22 Pore pressure response of the grout sample.....	128
Figure 5-23 Pore pressure response of the clay shale sample	129
Figure 6-1 A flushable piezometer (modified from Long et al. 2004).....	149
Figure 6-2 Piezometric Elevation – Main works Ch. 1320 W (data from Long et al. 2004)	150
Figure 6-3 A new flushable piezometer (modified from Ridley et al. 2003)	151
Figure 6-4 Pore pressure measurement at a depth of 2 m in an old railway embankment constructed of compacted London Clay (modified from Ridley et al. 2003)	152
Figure 6-5 Detailed dimensions of a flushable adaptor.....	153
Figure 6-6 The Swagelok CH series check valve	154
Figure 6-7 Vibrating wire piezometer with flushable adaptor	154
Figure 6-8 Setup of a flushable piezometer.....	155
Figure 6-9 Large triaxial cell used for testing of the flushable piezometer.....	156
Figure 6-10 GE DPI 603 portable pressure calibrator.....	157
Figure 6-11 Slope Indicator vibrating wire data recorder	157
Figure 6-12 Assembly of a flushable adaptor for testing.....	158
Figure 6-13 Setup of a flushable piezometer test	159
Figure 6-14 Pressure response test of a flushable piezometer.....	160
Figure 6-15 Water standpipe used in Forest Heights Park	161
Figure 6-16 RST P-100-1 Pneumatic Piezometer	162
Figure 6-17 Geokon multi-level piezometer.....	162
Figure 6-18 Geokon 4500MLP installation details showing spring loaded mechanism in closed configuration (top), and released (bottom)	163
Figure 6-19 Slope Indicator’s vibrating wire piezometer	164
Figure 6-20 Location of field instrumentation in Forest Heights Park.....	165
Figure 6-21 Field grout-in piezometer installation in Forest Heights Park.....	166
Figure 6-22 Piezometer installation plan in Forest Heights Park (Cluster 1)	166
Figure 6-23 Piezometer installation plan in Forest Heights Park (Cluster 2)	167
Figure 6-24 Multi-level piezometers attached to grout pipe with a Ty-rap.....	167
Figure 6-25 Flushable piezometer and pneumatic piezometer attached to grout pipe .	168
Figure 6-26 Field monitoring of a flushable piezometer	168
Figure 6-27 Pore pressure monitoring results of Cluster 1.....	169
Figure 6-28 Piezometric elevation (Cluster 2).....	169

Figure 6-29 Pore pressure isochrone (07/04/2005)	170
Figure 6-30 Normalized pore pressure plot	171
Figure 7-1 Keillor Road landslide (May 2005, the City of Edmonton).....	190
Figure 7-2 Map of slide area and site investigation plan.....	191
Figure 7-3 Pre-failure and post-failure profile of Keillor Road Landslide (2003)	192
Figure 7-4 Downward movement of the upper pile wall (picture from May 2003).....	192
Figure 7-5 Forward tilting of the lower pile wall (picture from May 2003)	193
Figure 7-6 Site Investigation Plan.....	194
Figure 7-7 Stratigraphic profile behind the valley wall (Figure 7-5 Section A-A).....	195
Figure 7-8 Stratigraphic profile along Keillor Road (boreholes located at the landslide area, Figure 7-5 Section B-B).....	195
Figure 7-9 Water level observed in the slide zone	196
Figure 7-10 Long-term monitoring of piezometers	196
Figure 7-11 Changes in piezometric pressure due to slope movement	197
Figure 7-12 Pore pressure distribution in the slide area	198
Figure 7-13 Natural water content profile below the main scarp	199
Figure 7-14 Direct shear testing apparatus	200
Figure 7-15 Sample preparation for direct shear test.....	200
Figure 7-16 Volume change of intact samples during a 24-hour consolidation/swelling period.....	201
Figure 7-17 Direct shear test results of the bedrock (peak)	202
Figure 7-18 Direct shear rest of the bedrock (residual).....	203
Figure 7-19 Direct shear test results of sliding plane material	204
Figure 7-20 Failure envelope obtained from direct shear tests	205
Figure 7-21 Landslide map of Keillor Road (Spring 2003)	206
Figure 7-22 A photograph of the damaged pile wall at the Keillor Road Landslide (May 2004).....	207
Figure 7-23 Movements of the cast-in-place piles	208
Figure 7-24 Horizontal and vertical displacement of the pile wall in the Keillor Road Landslide	209
Figure 7-25 Map of Keillor Road Landslide, 2004.....	210
Figure 7-26 Slope profile survey (Pre-failure, 2003 and 2004, Figure 7-5 Section C-C)	211
Figure 7-27 Crack monitoring at the Keillor Road Landslide.....	212

Figure 7-28 Cumulative horizontal displacement of crack meters at the Keillor Road Landslide	213
Figure 7-29 Yearly rainfall (University of Alberta Weather Station)	214
Figure 7-30 Pore pressure distribution in Keillor Road	214
Figure 7-31 Slide geometry and groundwater levels used in the analysis of pore pressure distribution in Keillor Road.....	215
Figure 7-32 Parametric study of factor of safety with cohesion and main scarp distance (Keillor Road Landslide).....	215
Figure 7-33 Parametric study of factor of safety with cohesion and main scarp distance (Keillor Road Landslide).....	216
Figure 8-1 Location of Whitemud Road slide.....	234
Figure 8-2 Photograph of exposed piles on lot 5 (November 1999).....	235
Figure 8-3 Landslides along Whitemud Road (May 2002, the City of Edmonton, Line 17E, Scale 1: 5000).....	236
Figure 8-4 Locations of kettle holes and raised area before developments (based on airphotos from 1962, 1967 & 1976).....	237
Figure 8-5 Test hole location of pre-failure investigation	238
Figure 8-6 Test hole location of post-failure investigation.....	239
Figure 8-7 Cross-section behind the river valley along Whitemud Road (Figure 8-6, Section A-A, piezometer data from February 2005).....	240
Figure 8-8 Groundwater level behind the valley wall	241
Figure 8-9 Piezometric elevation of the bedrock behind the valley wall	241
Figure 8-10 Pore pressure response of displaced materials.....	242
Figure 8-11 Piezometric pressure profile of the bedrock	242
Figure 8-12 Moisture content profile at Whitemud Road Landslide.....	243
Figure 8-13 Plasticity chart of till and bedrock	244
Figure 8-14 Sieve analysis of different materials in the Whitemud Road slide area	245
Figure 8-15 Direct shear test results of Whitemud Road slide materials.....	246
Figure 8-16 Direct shear test of Bentonite in the Whitemud Road slide area	247
Figure 8-17 Pre-failure and post-failure cross-section of the Whitemud Road Landslide	247
Figure 8-18 Horizontal displacement of displaced material in the Whitemud Road Landslide	248

Figure 8-19 Total annual rainfall data together with landslide incidents on Whitemud Road	249
Figure 8-20 Comparison of slope movement and piezometric pressure in the Whitemud Road slide area	249
Figure 8-21 Plan view of drain installation in the Whitemud Road slide area	250
Figure 8-22 Drain monitoring data (September 2002)	251
Figure 8-23 Drain monitoring data (2003 & 2004)	252
Figure 8-24 Pore pressure response due to drain installation.....	253
Figure 8-25 Cross-section used in stability analyses of the Whitemud Road slide area	253
Figure 9-1 Location of Forest Heights Park	266
Figure 9-2 River valley view of Forest Heights Park (looking North, taken on 15 th July 2004).....	267
Figure 9-3 Locations of old mine adits in Forest Heights Park (mine locations from Taylor 1971).....	268
Figure 9-4 Toe slump in displaced bedrock (taken on 15 th July 2004)	269
Figure 9-5 Location of boreholes in Forest Heights Park.....	270
Figure 9-6 Stratigraphic profile behind the river valley wall.....	271
Figure 9-7 Stratigraphic profile at the toe of Forest Heights Park	272
Figure 9-8 Moisture content profile obtained from boreholes behind the valley wall and at the toe of the slope.....	273
Figure 9-9 Cross-section A-A and piezometric elevations of the bedrock and groundwater level in Forest Heights Park.....	274
Figure 9-10 Piezometric pressure of bedrock behind the valley wall and displaced material in Forest Heights Park	275
Figure 9-11 Cross-section used in the stability analyses of the Forest Heights Park river valley wall	276
Figure 9-12 Stability analysis of different main scarps in Forest Heights Park.....	276
Figure 9-13 Tension cracks in the lower trail of Forest Heights Park.....	277
Figure 9-14 Cross section of the valley wall and coal seam elevations in Forest Heights Park	277
Figure 9-15 Piezometric elevation and inclinometer displacement in the Forest Heights Park slide area	278
Figure 9-16 Long-term pore pressure response of bedrock in Forest Heights Park.....	278

Figure 9-17 Post-failure slope movement in Forest Heights Park.....	279
Figure 9-18 Cross Section B-B showing exposed till at the toe of the slope in Forest Heights Park	279
Figure 10-1 Pre-failure and post-failure cross-section (Whitemud Road Landslide)	288
Figure 10-2 Development of minor scarps (Stage-1)	288
Figure 10-3 Development of the main scarp (Stage-2)	289
Figure 10-4 Development of a counter scarp (Stage 3)	289
Figure 10-5 Major failure due to downward movement of an active block (Stage-4)....	290
Figure 10-6 Post-failure slope movements (Stage-5)	290
Figure 10-7 Slope geometry of single block analysis.....	291
Figure 10-8 Slope geometry of two inclined blocks	291
Figure 10-9 Calculation of resultant force, R_2 of the active block.....	292
Figure 10-10 Calculation of the factor of safety of the passive block	292
Figure 10-11 Variation of the factor of safety with main scarp distance R	293
Figure 10-12 Variation of the factor of safety with active block depth H_a	293
Figure 10-13 Variation of the factor of safety with main scarp dip θ	293
Figure 10-14 Variation of the factor of safety with counter scarp dip δ	294
Figure 11-1 Slope instability mechanisms in weak rocks (modified from Thomson and Tiedemann 1982).....	303
Figure 11-2 Post-failure slop movements related to groundwater table, piezometric pressure and factor of safety.....	304
Figure 11-3 Proposed instrumentation for Keillor Road Landslide.....	305
Figure A 1 Single block	324
Figure A 2 Two block analysis.....	326
Figure A 3 Calculation of resultant force R_2 , Dry case	329
Figure A 4 Calculation of the factor of safety (Dry case).....	331
Figure A 5 Calculation of resultant force R_2 ,	332
Figure A 6 Calculation of factor of safety for passive block.....	333

LIST OF SYMBOLS

CHAPTER 1

s_p	peak shear strength
s_r	residual shear strength
s_s	fully softened shear strength

CHAPTER 2

C_{u0}	undrained shear strength at natural water content
ΔC_u	strength loss after softening to equilibrium water content
Δw	changes in water content after softening
T_{50}	time of softening for loss of 50 % of C_{u0}
w_L	liquid limit
w_s	maximum water content due to slaking
I_L	liquidity index
ΔI_{L1}	change in liquidity index
Δu	change in pore pressure
A	pore pressure coefficient
B	pore pressure coefficient
$\Delta\sigma_1$	major changes in total stress
$\Delta\sigma_3$	minor changes in total stress
r_u	pore pressure ratio
k	coefficient of permeability
c_s	coefficient of swelling
OCR	overconsolidated ratio
s_p	peak shear strength
s_r	residual shear strength
c', c'_r	drained cohesion for peak and residual shear strength
σ'	effective normal stress acting on failure plane
ϕ', ϕ'_r	drained angle of internal friction for peak and residual shear strength

- i inclination of the teeth
- ϕ'_s drained angle of internal friction for fully softened strength
- σ_1, σ_3 maximum and minimum principal stress
- σ_c uniaxial compression strength
- A, B, S parameters determined from the results of triaxial test or direct shear tests using the least square method

CHAPTER 3

- ϕ', ϕ'_r drained angle of internal friction for peak and residual shear strength
- γ_t total unit weight
- c', c'_r drained cohesion for peak and residual shear strength
- u pore pressure
- GWL groundwater level

CHAPTER 4

- k coefficient of permeability
- q flow rate
- VW vibrating wire
- F intake factor which depends on the shape and dimensions of the intake
- H non-equalized pressure head, and k is the formation permeability
- T_{basic} basic time lag
- A cross-sectional area of the standpipe or an equivalent area expressing the relationship between volume and pressure changes in diaphragm piezometers.
- V total volume of flow required for equalization
- t elapsed time
- H_o total head
- H active head at time t
- T time lag
- E equalization ratio
- D cylinder diameter
- L length

LAE	low air entry
HAE	high air entry
ε	piezometric error
u_{soil}	pore water pressure at the monitoring point within the soil
u_{grout}	pore water pressure at the monitoring point within the grout
k_{grout}	permeability of grout
k_{soil}	permeability of soil

CHAPTER 5

q_u	unconfined compressive strength
k	coefficient of permeability
σ_c	isotropic confining pressure
B	the ratio of the pore pressure increase to the confining pressure increment
u_o	initial pore pressure immediately before consolidation,
u_b	back pressure, which is a constant during the consolidation, and
u	measured pore pressure on the base
A	cross sectional area of the grout sample
i	hydraulic gradient across the sample
q	flow rate

CHAPTER 6

VW	vibrating wire
HAE	high air entry filter
LAE	low air entry filter

CHAPTER 7

t_{100}	time required for 100% consolidation
t_f	time required to failure
CM	crack meter

CHAPTER 8

GWL groundwater level

CHAPTER 9

H horizontal

V vertical

PZ piezometer

V.W vibrating wire

GWL groundwater level

CHAPTER 10

DO surface of rupture

CD main scarp

ϕ_b friction angle (main Block)

ϕ_s friction angle (weak plane)

Z_w height of water level from toe of the slope

α weak plane or failure plane dip

Z_s water level at the weak plane

Z_a, Z_c water level at the active block

U_s water pressure acting on the sliding surface

U_b water pressure acting on the main scarp

OBCD displaced material

H slope height

β slope angle

θ main scarp dip

R distance from the slope crest to the main scarp

O origin of the block

H_a height of the active block

R_1, R_2 resultant force

W_a weight of the active block

W_p weight of the passive block

CHAPTER 1 Introduction

1.1 Background

Landslides are downward and outward movements of slope-forming materials composed of natural rock, soils, artificial fills, or combinations of these materials (Varnes 1958), and can occur in a wide range of environments and ground conditions. Landslides may be caused by external disturbances such as undercutting of the toe or an excavation without support. On the other hand, landslides may occur on slopes that have been stable for many years. These delayed failures include all processes that contribute to the reduction of shear strength with time. Failures of this nature are caused either by a temporary increase in pore pressure or a progressive deterioration of the strength of the soil (Terzaghi et al. 1996).

Most delayed failures occur in overconsolidated clay and weak rock deposits (Morgenstern 1977; 1990; Skempton 1970). These deposits usually include heavily overconsolidated Tertiary or older marine deposits, boulder clays, and recent lacustrine clays overconsolidated by desiccation. In this thesis the term “weak rock” refers to fine-grained, argillaceous sediments, including shale, claystone, siltstone, and mudstone, even though weak rock may be classified into (i) sedimentary, (ii) weathered, (iii) low welded-pyroclastic and (iv) fractured rock depending on origin and/or distinctive physical properties (Okamoto et al. 1981),

The term “time dependent, first time slide” indicates failure in a previously unsheared material which occurs some time after a slope has been cut or eroded (Skempton 1970). “Reactivated slide” refers to reactivation of an old landslide or movement of a previously sheared surface. Marginally stable old landslides can be reactivated by toe erosion, ground water level changes, or loading at the slope crest. Some of the contributing factors of delayed failures are;

- The initial stress condition around the slope may change due to removal of lateral support, surcharge, earthquake, volcanic activity, change in groundwater level, or freezing of pore water.
- The initial state or inherent characteristics of the material may be part of a geological setting that is favorable to landslides. These factors may exist for a long period of time without failure, and include material composition, texture, and gross structure, and slope geometry (Yang 1987).
- Changes in stability may be due to weathering and other physiochemical reactions, changes in intergranular forces due to water content and pressure in pores and fractures, and changes in structure due to stress relief (Varnes 1978).

Our knowledge of the mechanisms of landslides has significantly improved, but all landslide problems can not be solved for many reasons, including (i) difficulty in predicting fundamental features of a landslide, (ii) the random intensity of environmental factors that can trigger landslides, (iii) the large number of settlements and infrastructure to be protected, (iv) the high costs required to increase the safety of the threatened areas, and (v) the environmental impact often associated with stabilization work.

Mollard (1977) described a number of landslide types in Canada which are concentrated in physiographic regions and are associated with certain kinds of soil and rock materials, geologic structures, and topographic settings. They include: (i) mountain slopes in the Cordilleran region of western Canada, (ii) valley slides in Upper Cretaceous argillaceous bedrock, mostly bentonitic marine clay shale, silty shale, and mudstone, (iii) river bank and terrace buff in the St. Lawrence Lowland region and lower coastal regions of eastern Canada, where postglacial marine submergence and postglacial uplift formed sensitive fine-grained marine deposits, and (iv) valley walls, escarpment, and deep thaw basins in the Lower Mackenzie Valley region and adjoining plains of north western Canada, where ice-rich permafrost occurs in fine-grained soil and weathered shale materials.

As Mollard pointed out, valley slides are a common sight along the river and its tributaries in the Upper Cretaceous bedrock in the Interior Plains region of western

Canada. Several large rivers and their tributaries cut post-glacially through glacial deposits and bedrock, forming steep valleys. Slope failures along the river valley may extend for several kilometers along the side of a valley and can be many tens of square kilometers in area (Mollard 1977). Major engineering projects completed in these rocks have experienced problems with slope failure, excessive and time dependent rebound, and loosening conditions in underground excavations (Peterson 1954; Peterson 1958; Underwood et al. 1964).

Evolution of the stability of river valley slopes depends on geological factors and the geographic conditions of the environments (Esu 1966). In stiff clays and weak rocks, steep natural slopes may exist, but their stability is temporary. With time, some landslides may occur which gradually flatten the slopes until they reach a stable slope configuration (Skempton 1948; Terzaghi 1950). Several factors are possible in the delayed failure of these valley slopes. When weak rock is exposed to weathering processes on a slope face, it may degrade to a soil, particularly in areas of seepage discharge. The incision of a valley by a river over a long period of time produces a reduction in the originally high horizontal stresses in the surrounding strata that causes the natural fissures in the bedrock and soil to open up. Groundwater in the fissures can also lead to swelling and softening of the bedrock. In addition, shear can also be induced along weaker beds by the differential lateral movements associated with the relief of high lateral earth pressures. Vertical unloading also produces deflections in the beds that can induce shearing by valley rebound (Matheson and Thomson 1973). The effect of glaciation can also produce some degree of softening and shearing within the bedrock in localized areas, particularly near the bedrock contact (Cruden et al. 1989).

Skempton (1964) presented the shear characteristic of an overconsolidated clay, and defined the maximum resistance the clay can offer as the peak strength s_p . If the displacement is carried further, the shear resistance will decrease until it reaches a second limit known as the residual shear strength s_r . The in-situ strength of the overconsolidated clay will depend on various factors (e.g. weathering, swelling) and can range from values of peak strength to residual strength as described by Skempton. Skempton (1970) describes this time dependent reduction in strength as softening. The softening effect has been considered in terms of the fully softened

condition, and Skempton suggested that the peak strength of the normally consolidated clay is approximately equal to the fully softened strength s_s of an overconsolidated clay. Morgenstern (1977) stated that the special problems that arise in the consideration of slopes in heavily overconsolidated clays are associated with the selection of appropriate strength parameters, understanding the factors influencing mobilization of shear strength when failure occurs or is renewed, and diagnosing the large variety of stratigraphic situations.

Stability analyses of river valley landslides in weak rock are challenging due to the different kinematics involved in the slide. Several failure mechanisms have been proposed, (i) block slide (Hayley 1968; Scott and Brooker 1968), (ii) translational slide with graben at the head of displaced material (Cruden et al. 2002; Martin et al. 1984), (iii) steeply dipping main scarp with a horizontal sliding plane (Eigenbrod and Morgenstern 1971; Scott and Brooker 1968; Thomson 1970; 1971b). A range of mobilized strengths has also been presented by various authors, e.g., peak strength (Thomson 1970), fully softened strength (Thomson 1971b), and residual strength (Eigenbrod and Morgenstern 1971; Pennell 1969).

1.2 Purpose of this research

Based on the brief overview, the following objectives are considered for this research.

- Landslides along the North Saskatchewan River Valley in Edmonton, Alberta, usually occur in conjunction with a graben formed at the head of the displaced material. The mechanisms of these slides are complex and there has been no detailed investigation of the failure mechanisms of these slides. Therefore, a study of the landslide mechanisms and kinematics of these slides is necessary.
- Delayed failures are common occurrences along the North Saskatchewan River Valley. Assessment of these failures poses a great challenge to engineers due to the unknown factors involved. Case studies would improve the understanding of these slides.

- Triggers for river valley landslides are difficult to assess because instruments are seldom in place at the time of failure. One of the most difficult parameters to evaluate is pore pressure as the weak rock usually has very low permeability. Recently, the methodology of piezometer installations in these materials has been questioned and more research is needed to improve pore pressure measurement in weak rock.

1.3 Scope of work

The scope of work has been planned to achieve the objectives outlined above.

A review of the mechanisms of delayed failure in weak rock is presented in Chapter 2. Three main topics are discussed in this chapter. Initially, engineering properties associated with weak rock is discussed. Then the concept of a first time slide is reviewed with an overview of the softening mechanism. Finally, mechanisms and kinematics of landslides associated with weak rock are presented.

Chapter 3 reviews three well-documented landslides along the North Saskatchewan River Valley in Edmonton. Major considerations are given on the landslide mechanism and pore pressure response of the bedrock.

Chapter 4 reviews negative pore pressure development in slopes and presents the function of different piezometer types. The major focus is on negative pore pressure measurement and piezometer installation methods. A review of the grout-in installation method is also presented in this chapter.

Chapter 5 describes laboratory investigation of the cement-bentonite grout. Unconfined compression tests and permeability tests are conducted on grout samples to determine suitability for grout-in piezometer installations in weak rock. Results of pore pressure response tests on grout and clay shale samples are also presented.

Chapter 6 presents the development of a flushable piezometer system. The flushable piezometer comprises a flushable adaptor, two flushing tubes, a high air entry filter, and a vibrating wire piezometer, and is capable of removing air bubbles from the piezometer cavity from the ground surface. Unlike the twin-tube hydraulic piezometer, piezometer installation depth is not limited by the water column inside the flushing tubes. The results of field investigations are also presented together with available data from other studies.

Chapter 7 presents a case study of the Keillor Road landslide. Slope instability at Keillor Road started in the early 1980s as a toe failure. The failure gradually progressed upslope and a major failure occurred in the fall of 2002. The laboratory investigation involves index testing and direct shear testing of intact and disturbed bedrock samples. The field investigation involves monitoring of post-failure slope movements and pore pressure response of the bedrock.

Chapter 8 presents a case study of the Whitemud Road landslide. Whitemud Road landslide occurred in the fall of 1999 along the North Saskatchewan River Valley and affected seven residential lots behind the valley wall. The results of laboratory investigations, field investigations, and post-failure slope movement monitoring are presented.

Chapter 9 presents a case study of an active landslide in Forest Heights Park. Slope instability in Forest Heights Park dates back to the early 1900s when coal mining was conducted in the area. As a remedial measure, a toe berm was constructed in 1985. A field investigation was conducted at an active landslide area located in the southern portion of the park.

Chapter 10 presents five kinematic stages observed in river valley landslides. To improve the stability analysis, a simple two inclined-block model is presented. Back analyses were conducted using the two inclined-block model and the results are compared with the field observations.

Chapter 11 presents the landslide characteristics of weak rocks observed along the North Saskatchewan River Valley. This chapter also presents a new instrumentation

program for future landslide study in weak rock slopes. The proposed instrumentation program is presented with Keillor Road Landslide example.

Chapter 12 summarizes the results of this study and discusses the major contributions and finding from this study. Recommendations for future research are presented and discussed.

CHAPTER 2 Literature review

2.1 Introduction

Weak rock deposits are found throughout the world and are known for foundation and slope stability problems. Weak rocks exhibit properties that are neither characteristic of true rock nor true soil in an engineering sense, but lie in a transition zone between the two types of material (Locker 1969). The major difficulty in assessing the engineering properties of weak rock can be attributed to two unique properties of these materials (Botts 1986): (i) weak rocks are intermediate in behaviour between rock and soil, and (ii) weak rocks tend to transgress from rock-like to soil-like materials within a relatively short time period. The factors that control the magnitude and time of these changes have not been well understood. In this chapter, problems associated with overconsolidated clays and weak rocks are presented with an emphasis on landslide mechanisms.

2.2 Classification of stiff clay and weak rocks

Fine grained inorganic materials are the predominant sedimentary materials in the earth's crust (Pettijohn 1957). Terzaghi (1936) divided these materials into three categories: (i) soft, intact clays free from joints and fissures, (ii) stiff, intact clays free from joints and fissures, and (iii) stiff, fissured clays. The transition between a stiff clay and a rock is more difficult to differentiate due to the transitional nature of the material. Terzaghi and Peck (1967) state:

The materials that constitute the earth's crust are rather arbitrarily divided by the civil engineer into two categories, soil and rock. Soil is a natural aggregate of mineral grains that can be separated by such gentle mechanical means as agitation in water. Rock, on the other hand, is a natural aggregate of minerals

connected by strong and permanent cohesive forces. Since the term “strong” and “permanent” are subject to different interpretations, the boundary between soil and rock is necessarily an arbitrary one. As a matter of fact, there are many natural aggregates of mineral particles that are difficult to classify either as soil or rock.

Bjerrum (1967) proposed a classification based on bond strength and extended up to shale materials:

- overconsolidated clays (i.e., overconsolidated clays with weak or no bonds);
- clay shales (i.e., overconsolidated plastic clays with well-developed diagenetic bonds); and
- shales (overconsolidated plastic clays with strongly developed diagenetic bonds)

Underwood (1967) attempted to classify and identify shales as shown in Figure 2-1. Shales are divided into two major groups: soil-like shale which has been consolidated by the weight of overlying sediments and lacks significant amounts of intergranular cement, and rock-like shale in which the cementing material may be calcareous, siliceous, ferruginous, gypsiferous, and phosphatic. If a cementing agent is lacking, the shale may be welded or bonded by recrystallization of its clay minerals.

To quantify the classification of weak rock in a more accurate manner, Morgenstern and Eigenbrod (1974) combined earlier classification schemes based on initial properties with those schemes based on durability (Figure 2-2). This scheme first divides argillaceous material into either soil or rock based on three properties: (i) the undrained shear strength, (ii) the degree of strength loss after softening, and (iii) the degree of change in water content after softening. After this division, slaking characteristics are used to determine if any of the soil-like materials are clay shales.

In addition to the problems involved in distinguishing between soil and rock, there is no generally acceptable scheme of classification of fine grained sedimentary materials. To clarify the terminology, the following definitions are employed throughout the text.

- Shale: a highly indurated, readily fissile rock composed of predominantly silt and clay size particles;
- Clay shale: an indurated, readily fissile soft rock, which under certain circumstances can revert to a clay of medium to high plasticity, thereby assuming the physical characteristics of a highly overconsolidated clay;
- Claystone: a rock or soft rock (dependent upon the degree of induration) which is composed of predominantly clay-size particles; and
- Siltstone: a rock or soft rock (dependent upon the degree of induration) which is composed of predominantly silt size particles.

2.3 Instability mechanisms in weak rock slopes

An evaluation of the stability of weak rock slopes depends upon numerous geological factors (types, properties, and attitude of geological formations) and upon the geographic conditions of the environment (exposure and climate, quantity and kind of precipitation). The long-term stability of these slopes is assured when their average inclination is less than the friction angle ϕ' of the soil (Skempton 1964; Skempton and Delory 1957). However, in weak rock, steep natural slopes may exist, but after a shorter or longer period, some landslides may occur which gradually flatten the slope until it reaches a shape that is permanently stable (Skempton 1948; Terzaghi 1950). Some of the problems associated with delayed failures in stiff clay and weak rock slopes are discussed here.

2.3.1 Fissure softening

Since the first suggestion by Gregory (1844) that the strength of the London Clay was being reduced by a softening of the clay material adjacent to fissures, several other researchers have pointed to this mechanism to account for the deterioration of strength in many clay shales. In relation to the failure of cuttings in fissured and overconsolidated clays, Terzaghi et al. (1996) stated:

“Almost every stiff clay is weakened by a network of hair cracks or slickensides. If the surface of weakness subdivides the clay into fragments smaller than 25 mm, a slope may become unstable during construction or shortly thereafter. On the other hand, if the spacing of the joints is greater, failure may not occur until many years after the cut is made. If the spacing of the joints in a clay is greater than about 100 mm, slopes may remain stable for many years or even decades after the cut is made. The lapse of time between the excavation of the cut and the failure of the slope indicates a gradual loss of the strength of the soil. Before excavation, the clay is very rigid, and the fissures are completely closed. The reduction of stress during excavation causes deformation of the clay, and some of the fissures open. Water then enters and softens the clay adjoining these fissures. Unequal swelling produces new fissures until the larger chunks disintegrate and the mass is transformed into a soft matrix containing hard cores. A slide occurs as soon as the shearing resistance of the weakened clay becomes too small to counteract the forces of gravity”.

Botts (1986) also presented progressive deterioration of weak rock as shown in Figure 2-3. The schematic shows four cross sections of a theoretical weak rock mass, each representing different stages of deterioration. Stage 1 represents a fissured weak rock in which no alteration has occurred. At stage 2, alteration has been initiated along the fissures and progresses in stages 3 and 4 until the mass is entirely deteriorated. At stage 1, the strength and strain response is probably controlled by the frequency, strength, and orientation of the fissures, and behaves similar to a jointed rock. During the intermediate stages 2 and 3, the weak rock mass can be considered as a rock-like material with the strength controlled by the orientation and shear resistance of soft, filled joints. At stage 4 the material is in theory behaving much like a homogenous, naturally remoulded clay.

2.3.2 Pore pressure equalization and swelling

When a cut is made in a clay slope, pore pressure within the slope will respond to these changes. The pore pressure change will depend on the initial position of the groundwater level and the response of the clay to the changes in stress during

excavation. With time, the pressure in the clay adjusts until it is in equilibrium with the groundwater. A detailed discussion of this process is given by Bishop & Bjerrum (1960).

Figure 2-4 illustrates the changes in stability conditions upon excavation of a slope and a comparison is given between the behaviours of a weak, normally consolidated clay and a stiff, overconsolidated clay. During rapid excavation, the pore pressures decrease in response to the changes in total stress. After the excavation, the soil mass swells as the pore pressures increase to those governed by seepage conditions. The ultimate pore pressures are higher than those obtained after excavation and the factor of safety decreases with time during pore pressure equilibration. The change in pore pressure caused by the excavation can be determined from Skempton's (1954) equation for pore water pressure change.

$$\Delta u = B[\Delta\sigma_3 + A(\Delta\sigma_1 - \Delta\sigma_3)] \quad [2-1]$$

where

Δu = changes in pore pressure

$\Delta\sigma_1, \Delta\sigma_3$ = major and minor changes in total stress

A, B = pore pressure coefficients

In this case, both the all-round pressure $\Delta\sigma_3$ and the deviator stress $\Delta\sigma_1 - \Delta\sigma_3$ are reduced due to the excavation-induced stress relief. This means that pore pressure decreases and, depending on its initial value, could become negative. If pore pressure is reduced, the effective stress increases and improves the stability of the slope in the short term. The length of time over which this reduced pore water pressure can be sustained is a complex issue and depends on the soil type, its fabric, permeability, the sequence of construction, slope protection, and weather.

Based on piezometric measurements within the blue and brown zones of the London clay, Skempton (1977) proposed that long-term reduction in the strength of the London clay might be related to extremely slow dissipation of negative pore pressures which had been generated in response to the cutting of the slope. Field evidence of slope failures in the London Clay due to pore pressure equilibration is

presented by Chandler (1984) using pore pressure ratio \bar{r}_u (Figure 2-5). The pore pressure ratio \bar{r}_u have been obtained in two ways: (i) by direct measurement, and (ii) by back-analysis of failures. It can be seen from the figure that the pore pressure ratio of the London Clay increased with time after the slope was cut and a long term \bar{r}_u value of 0.32 was achieved.

Large areas of western Canada and the north central United States are underlain by swelling clay shales such as Bearpaw, which in its undisturbed state is homogeneous, dense, and impervious (Peterson 1954). This material has a coefficient of permeability k range of 10^{-11} to 10^{-7} m/s and a coefficient of swelling c_s range of 0.01 to 0.1 m^2/year (Koppula and Morgenstern 1984). Koppula and Morgenstern (1984) adopted a simple one-dimensional model to examine theoretically the pore pressure response of a saturated soil mass of finite thickness subject to a constant rate of erosion. Using this model, they showed the significant consequences of rapid erosion on the pore pressure field in a thick layer of low-permeability clays. Their results suggest that at the present time the valley bottom of some American and Canadian rivers could still be subject to vertical swelling deformations due to previous geological erosion.

An example of deficient pore pressure due to erosion and subsequent standstill is illustrated in Figure 2-6 (Koppula and Morgenstern 1984). In this example it is assumed that the top 50 m of soil has been removed over 5000 years by fluvial erosion. The bottom boundary is assumed to be impermeable and is 100 m below the original ground surface. The coefficient of swelling is assumed to be 0.1 m^2/year . It can be seen from the figure that substantial deficient pore pressures exist at the end of erosion, and even after 5000 years of subsequent standstill. These deficiencies have not been completely eliminated, although water is presumed to be available for satisfying the large negative hydraulic gradients.

In the view that this condition might exist for some valleys of the Italian Appennines, Fenelli and Picarelli (1990) presented results obtained from pore pressure measurements in the area surrounding the Bisaccia hill, located 120 km northeast from Naples. The hill, on top of which the small old town of Bisaccia rises, is

bounded by two deep, narrow valleys. It consists of a 50 m thick Plio-Pleistocene conglomerate slab overlying a very thick Eocene clay formation (Varicoloured Clays). Varicoloured Clays consist of stiff fissured clays and outcrop in a large area. Fenelli and Picarelli (1990) indicated that Varicoloured Clay appears very similar to the Bearpaw shale, both in the values of the index properties and in its mechanical behaviour. In particular, swelling is very significant and slow, with a swelling coefficient c_s ranging between 0.01 and 0.001 $m^2/year$. Pore pressure measurements were taken using a number of Casagrande piezometers and Mayak piezometers. At site B, seven piezometers were installed at different levels down to a depth of about 57 m. Figure 2-7 shows the pore pressure measurements at the site. A perched water table was observed at the overlying superficial deposits. In the underlying clay materials, the piezometric level is almost constant with time, not being directly influenced by the rainfall and become zero for depths greater than 15 m. Fenelli and Picarelli (1990) stressed that these pore pressure observations could help explain the morphological evolution of the area, presently characterized more by a widening of the valleys due to shallow slope movements than a deepening due to deep-seated landslides.

2.3.3 Progressive failure

Progressive failure occurs in materials that exhibit strain-weakening behaviour. The strength along a potential failure plane can be reduced progressively from peak to residual values. If the stresses at any position along the potential slip surface exceed the peak strength of the material, and if displacement is allowed, then localized failure will occur and the strength of the material at this position will decrease toward the residual value (Skempton 1964).

In the example of a slope, illustrated in the schematics of Figure 2-8, the stresses at the toe of the potential slip surface are sufficient to displace the material beyond the peak strength in the zone D-F. This will cause a redistribution of stresses in the local area such that the peak strength might likewise be exceeded in the adjacent material, as in zone F-G. This process will continue until the average shear strength along the potential slip plane is no longer sufficient to resist complete failure along

the plane, or until the redistributed stress state is such that the peak strength is no longer exceeded at any point within the slip plane.

Bjerrum (1967) presented a strain energy hypothesis which explains qualitatively the behavior of overconsolidated clays and the phenomena of long-term slope failures in these soils. Bjerrum hypothesized that during the processes of drained loading of a soil, strain energy is stored in the soil mass. Depending on the nature of the soil, the strain energy may be stored or released upon unloading. If the soil is of such a nature that diagenetic bonds are developed then energy is stored. If no bonds are developed or only weak bonds are formed then the strain energy may be released immediately or very soon after unloading. Bjerrum classified diagenetic bonds as weak, strong, or permanent.

Brooker (1967) studied the quantitative evidence gathered from a series of large scale consolidation tests which supports the strain energy hypothesis. The coefficient of earth pressure at rest was found to be a function of strain energy at a given value of over consolidated ratio, OCR. It was also shown that the degree of disintegration of overconsolidated soils during a slaking test is related to strain energy. It was inferred from the results that mineralogy and the capacity of a soil to absorb strain energy are related. The evidence suggests that certain physicochemical properties may be quantitatively related to mechanical properties through the concept of strain energy.

2.3.4 Loosening

Although there is no theory of loosening, field study confirmed that fissured soils and weak rocks lose strength with lateral strains due to loosening following excavation (Morgenstern 1990). Regardless of the explanation, when a fissured soil or mudstone mass extends laterally, there is a mechanical loosening which also leads to a reduction in strength (Morgenstern 1990).

Esu et al. (1984) presented the behaviour of a 150 m high cut slope at the Santa Barbra mine in Italy. During steepening of the cut in overconsolidated-jointed clay,

failure occurred providing a case history of a first time slide. The in situ strength was found to be less than the peak strength and was found to be time-dependent.

A similar study was carried out by Small (1989) in Highvale Coal Mine, located 80 km west of Edmonton, Alberta. The investigation involved ground response monitoring of the highwall of a mine as successive cuts were made. At the study site, the highwall was 20 to 30 m high at 40 to 50° slope, overlying 15 m of multiple seams of coal which are mined subsequently, leaving a near vertical face. The monitoring showed that the movement is essentially translational, being seated in a clay seam within the coal or beneath. An additional 100 to 200 mm of movement occurs during removal of the final 50 m. As the ground strains laterally, localization developed along the bentonite at the toe of the coal, and small slides developed along this weak layer. Excavation has induced lateral strains at the highwall of 0.6 to 0.7 %, decreasing to 0 % about 225 m from the highwall crest. Although the loosening has a stabilizing influence with respect to pore pressure, it has a destabilizing influence on mobilized strength of the slope material with progressive reduction of cohesion (Morgenstern 1990) .

Gould (1960) studied a number of cases of slides in heavily overconsolidated clays in California. On the basis of stability analysis of slopes comprised of these materials, he suggested that the strength actually mobilized in slides or mass creep is inversely proportional to the amount of displacement which has occurred previously in the shear zone. He also proposed that previous slides or even small movements have permanently damaged the shear resistance of the stiff clays.

2.4 Shear strength behaviour of stiff clay and weak rocks

2.4.1 Shear strength of stiff clay and weak rock

Skempton (1964) illustrated the shear characteristic of an overconsolidated clay as shown in Figure 2-9. This figure illustrates the results of slow drained shear tests. As the clay is strained, it builds up an increasing resistance. However, under a given effective pressure, there is a limit to the resistance that the clay can offer, and this is the peak strength s_f . If the displacement is carried further, the shear resistance will

decline (strain-softening) until a second limit, the residual shear strength s_r is reached. The residual shear strength is the minimum strength reached for a constant effective normal stress no matter how large the displacement. The plot of strength versus effective normal stress on the shear plane in Figure 2-9 indicates two very different relationships. The peak strength can be expressed by:

$$s_p = c' + \sigma' \tan \phi' \quad [2-2]$$

And the residual shear strength by:

$$s_r = c'_r + \sigma' \tan \phi'_r \quad [2-3]$$

s_p, s_r = peak and residual shear strengths

c', c'_r = drained cohesion for peak and residual shear strength

σ' = effective normal stress acting on failure plane

ϕ', ϕ'_r = drained angle of internal friction for peak and residual shear strength

Since c'_r is normally very small and in most cases zero, the residual shear strength is usually expressed by:

$$s_r = \sigma' \tan \phi'_r \quad [2-4]$$

Sinclair and Brooker (1967) presented the shear strength properties of several late Cretaceous bedrocks from Alberta determined by triaxial and direct shear test (Figure 2-10). The bedrocks are divided into three main rock types—clay shale, bentonitic shale, and bentonite, depending upon plasticity. A summary of the results of their shear tests follows:

- The effective strength from the direct shear tests is nearly the same as obtained from triaxial tests.
- For those rocks with common mineralogy and geologic history, the failure envelopes (from both triaxial and direct shear tests) are roughly parallel. The slope of the failure envelopes at pressures beyond 1700 kPa is equal to the residual effective angle of shear resistance from direct shear tests.

- The residual effective angle of shear resistance of the Edmonton shale and bentonite is approximately 8.5° . The peak effective angle of shearing resistance is also 8.5° at high pressure, but appears to be dependent upon stress level at lower pressures.

2.4.2 Shear strength along structural discontinuities

Fissured, overconsolidated clays and mudstones are known to exhibit a brittle-type stress strain curve and dilatancy at low to medium stress levels in triaxial compression tests and direct shear tests. The behaviour changes from brittle to ductile as the confining pressure increases. The failure is nonlinear at low stress levels. This observed nonlinear failure envelope can be explained from the viewpoint of the shear strength of discontinuities in a rock mass.

Patton (1966) carried out an experimental study in which direct shear tests were conducted on plaster specimens having interlocking surfaces. During shear, the specimen moves over the teeth at low normal stresses, resulting in a high angle of friction and high dilatancy. The angle of friction ϕ is due to the inclination of the teeth, i , and the angle of friction of the material. As the normal stress increases the dilatancy decreases. At higher normal stress, no dilatancy will occur and the shear plane will pass entirely through intact material. A bimodal failure envelope results as shown in Figure 2-11. For real soil, even at low normal stress, some asperities on discontinuities are sheared off and only at very high stress can shear take place entirely through the intact rock. A nonlinear failure envelope is obtained instead of the bimodal failure envelope.

Skempton and Petley (1967) established a tentative classification of discontinuities based on occurrence and relative shear movement, and described it as follows:

- Principal displacement shears, such as those found in landslides, faults, and bedding plane slips, were reported as subplanar and polished; the strength was at or very near the residual strength. Relative shear displacements on the shear surface were described as more than 10 cm.

- For minor shears, with somewhat irregular surfaces on which the relative movements have been small (less than 1 cm), the strength may be appreciably higher than residual.
- Joint surfaces, including systematic joints, displayed a “brittle-fracture” texture with little or no relative shear movement. Available tests indicated that the fracture which produced the joint virtually destroyed the cohesion but reduced the friction angle ϕ' by only a very slight amount. Movements of not more than 5 mm, however, were sufficient to bring the strength along the joint to the residual and to polish the joint.

The typical characteristics of fissured, overconsolidated clay can be summarized according to a comprehensive experimental study by Bishop et al. (1965) on undisturbed blue London Clay:

- The stress-strain curve is of a brittle type for low to medium stress levels and changes gradually from the brittle to ductile type as the effective confining pressure increases.
- The transition of the volume change from contraction to dilation occurs just before or when the peak stress is reached.
- The failure envelope is markedly nonlinear at low stress levels.

2.4.3 Strength behaviour of weak rock due to softening

Historically, the softening effect has been considered in terms of the fully softened condition, such as complete reduction of the cohesion intercept in the Mohr-Coulomb failure criterion. Roscoe et al. (1958) defined the critical state of an ideal clay in drained shear tests and the critical state corresponds to the strength of a normally consolidated clay and the water content in this state is equal to that attained ultimately by the overconsolidated clay due to expansion during shear. For real soil exhibiting sensitivity, bonding, and preferred particle orientation, the behaviour pattern is more complex. Skempton (1970) showed that peak strength of the normally consolidated clay can be used to approximate the critical state and hence to estimate the fully softened strength of an overconsolidated clay (Figure 2-12).

During a landslide investigation in Devon, Eigenbrod and Morgenstern (1971) conducted drained triaxial compression tests on unsoftened and softened Upper Cretaceous bedrock. Their results indicated that the softened material was more ductile than the unsoftened siltstone, exhibiting a greater strain at failure (Figure 2-13). The strength envelope for the unsoftened material was substantially higher than that for the softened material with an effective shear strength of $\phi' = 32^\circ$ and $c' = 80$ kPa. The strength envelope for the softened material curved at higher pressure with an effective shear strength of $\phi' = 33^\circ$ and $c' = 9$ kPa.

To understand the mechanism of strength reduction due to softening in stiff clay and weak rock Graham and Au (1985) carried out a series of triaxial tests under undrained and drained conditions on samples of fissured, overconsolidated Lake Agassiz clays over a wide range of effective stress levels, including very low stress levels. Sample conditions were: undisturbed, swollen under low effective stresses, or subjected to five cycles of freezing and thawing.

Undisturbed samples exhibited strain-softening characteristics with high dilatancy under drained conditions. The freeze-thaw-cycled samples showed a less pronounced peak in their stress-strain curves, with less dilatancy. The swollen samples exhibited intermediate characteristics. The strength envelopes obtained from these tests are presented in Figure 2-14. As shown, swelling and freeze-thaw cycles reduce the shear strength. The strength envelopes for these samples tend to become parallel to those for undisturbed samples at higher stress levels. Further, they appear to approach the critical-state line. Graham and Au (1985) also stated that during undrained tests, effective stress paths of swollen and freeze-thaw-cycled samples exhibited stress paths similar to those of undisturbed samples rather than for the remolded samples.

Yoshida et al. (1990) suggested that the effect of softening is to decrease the shear strength of a material with time and to reduce its tendency to dilate. Furthermore, it was suggested that the reduction of shear strength due to softening can be represented as a lowering of the failure envelope and reduction in the high nonlinearity at low stress levels, as presented in Figure 2-15.

A simple nonlinear failure criterion is proposed by Yoshida et al. (1990) for time-dependent softening. The failure criterion is used to describe the effect of softening observed in materials such as overconsolidated clays and soft rocks. It is expressed in terms of maximum and minimum principal stresses, uniaxial compression strength, and three strength parameters. The effect of softening can be represented in this failure criterion through a time-dependent reduction in the strength parameters. The variation in shear strength during softening is embraced from the initial strength to the fully softened condition. The proposed failure criterion consists of maximum and minimum principal stress σ_1 and σ_3 , uniaxial compression strength σ_c , and three parameters A, B, S, and is expressed as follows:

$$\sigma_1 = \sigma_3 + A\sigma_c \left(\frac{\sigma_3}{\sigma_c} - S \right)^{\frac{1}{B}} \quad [2-5]$$

The parameters A, B, and S can be determined from results of triaxial compression tests or direct shear tests using the least square method (Yoshida et al. 1990).

2.5 Failure mechanisms in weak rock

2.5.1 First time slide

It has been recognized that natural slopes and man-made slopes in weak rocks may fail by landslide some considerable time after the slope was formed. The mechanism of time reduction in shear strength has been discussed in Section 2.3. Usually mobilized shear strengths in first-time slides are between peak and residual shear strengths depending on the softening condition of the slide material (Mesri and Shahein 2003). Skempton (1970) described that the displacement required to reduce an overconsolidated clay to the fully softened condition is several times greater than the displacement at peak strength but is considerably less than that corresponding to residual strength. He stated that the post-peak changes of a slope may be considered to be composed of two successive stages:

- Dilatancy and the opening of fissures leading to an increase in water content and culminating in a drop in strength to the fully softened value, at which stage there is a softened shear zone with numerous discontinuous shears;
- Development of principal shears of appreciable length, some of which eventually link together and form a continuous shear when the residual strength is reached along the entire slip surface.

Skempton (1964; 1970) made the following points relating to long-term slope stability in overconsolidated clays:

- After a slide has taken place, the strength of the slip surface is equal to the residual value. The residual strength is associated with strong reorientation of the clay particles.
- First-time slides in slopes in nonfissured clays correspond to strengths only slightly less than the peak.
- A first-time slide in fissured clay tends towards, and does not fall significantly below, the fully softened strength (Figure 2-16).

Mesri and Shahien (2003) reanalyzed 99 case histories of slope failures in 36 soft clays to clay shales. They analyzed 107 sections using observed actual slip surface. Most stiff clays and clay shales contain stratigraphic discontinuities such as bedding planes and laminations. Their findings are summarized below:

- The fully softened shear strength is shown to be the lower bound for mobilized shear strength in first-time slope failures in homogeneous soft to stiff clays and on the slip surfaces cutting across bedding planes and laminations.
- For many first-time slope failures it appears that part of the slip surface is at the residual condition.
- For excavated slopes, the residual condition could be present before the final slope is formed or it may develop in response to excavation by progressive deformation along nearly horizontal surfaces including bedding planes or laminations.

- Delayed first-time failure of slopes in stiff clays and clay shale is caused by propagation of the residual condition into the slope on horizontal or sub-horizontal surfaces including stratigraphic discontinuities.
- The residual condition is present on the entire surface of reactivated landslides.

2.5.2 Reactivated slide

The reactivated slide refers to reactivation of old landslides or movement of previously sheared surfaces. Marginally stable old landslides are located in river valley or other slopes. These can be reactivated by toe erosion, groundwater level changes, or loading at the slope crest. Since these slopes are marginally stable, slight changes in slope geometry can cause movement. For the reactivated slide, residual strength mobilizes along the failure plane.

2.5.3 Kinematics of a landslide

Landslides are relatively rapid downslope movements of soil and rock that take place characteristically on one or more discrete bounding slip surfaces that define the moving mass (Hutchinson 1988). According to Cruden and Varnes (1996), any landslide can be classified and described by two nouns: the first describes the material and the second describes the type of movements, falling, toppling, sliding, spreading, or flowing, as shown in Table 2-1. The complete identification of the movement can be described by adding descriptors such as activity and description in front of the two-noun classification system (Cruden and Varnes 1996).

In a rotational slide, the surface of rupture is curved concavely upward and the slide movement is roughly rotational about an axis that is parallel to the ground surface and transverse across the slide. In a translational slide, the mass displaces along a planar or undulating surface of rupture, sliding out over the original ground surface. Often, slope movements involve a combination of one or more of the principal types of movement described in Table 2-1, either within various parts of the moving mass or at different stages in development of the movements and these are termed

complex slope movements (Varnes 1978) . These slides, however cannot move until sufficient internal deformations of the slide mass have taken place to produce a kinematically admissible mechanism. These deformations commonly take the form principally of high-angled internal shears in the rearward part of the slide, which give rise to counterscarps and graben formation between these and the rear scarp (Hutchinson 1988).

In general, slope instabilities which develop in weak rocks involve complex landslides of the rotational and translational types. Typical characteristics of such slides include rupture surfaces with steep main scarps, formation of minor scarps due to initial deformation and shear along the surfaces within the displaced mass as the primary rupture surface is formed, and graben structures (Cruden 1997; Cruden and Varnes 1996).

The movement of a translational slide is commonly controlled structurally by surfaces of weakness, such as faults, joints, bedding planes, and variation in shear strength between layers of bedded deposits, or by contact between firm bedrock and overlying detritus (Varnes 1978). Scott and Brooker (1968) stress that landslides in the Cretaceous formation of western Canada are retrogressive in nature and the surface of rupture is composed of two portions (Figure 2-17). The portion AB is a flat concave-up arc, connecting with the portion BC. The surface BC is nearly horizontal and is often seated in a relatively weaker material such as bentonite or montmorillonitic clay. The slide may commence on the surface A1B1 and retrogress to some other surface AB. Retrogression ceases when the overall slope angle becomes sufficiently small.

Another complex landslide mechanism commonly found in bedded weak rock is the formation of a graben at the head of displaced material. Varnes (1978) presented an example of landslide development in horizontal sequences of claystone and coal caused by relaxation of horizontal stresses resulting from reduction in thickness of overlying strata. Cruden et al. (1991) collected geometric data from translational slides in central Alberta, in which a graben was formed. These slides occurred in poorly indurated, flat-lying sedimentary rocks of Upper Cretaceous age. Measurements of graben width and site exploration of the depth to the rupture

surface suggest that the graben width is about 90 % of the depth to the rupture surface (Cruden et al. 1991).

2.5.4 Rate of movement

A qualitative description of movements associated with a landslide has been given by Terzaghi (1950). He distinguishes first a general condition of creep which continues fairly steadily until the slide-producing agent begins to reduce the factor of safety of the slope. From then until failure constitutes the phase of pre-failure movement in which the rate of downslope movements accelerates until the landslide occurs. The considerably rapid movements during failure are succeeded by a phase of stability or of post-failure movements as shown in Figure 2-18.

A field example of the slope movements before and during the failure is presented by Skempton (1964). The displacement-time curve in brown London Clay at Kensal Green covering 13 years before collapse is shown in Figure 2-19. From the figure, it can be seen that pre-failure movements are characterized by accelerating and finally relatively high rates of movement. In the Kensal Green failure, slope movements were several cm/day during the week preceding the failure and reached a few decimeters/day on the last day.

2.5.5 Stability consideration

2.5.5.1 Kinematics of the slide

In soil mechanics, limit equilibrium techniques are routinely used in the analysis of landslides where translational or rotational movements occur on distinct failure surfaces (Bishop 1955; Morgenstern and Price 1965; Sarma 1979). Analyses are undertaken to provide either a factor of safety or, through back-analysis, a range of shear strength parameters at failure. All limit equilibrium techniques share a common approach based on a comparison of resisting forces/moments mobilized and the disturbing forces/moments. Methods may vary, however, with respect to the slope

failure mechanism in question (e.g., translational or rotational sliding), and the assumptions adopted in order to achieve a determinate solution.

In general, soil slope stability analysis can be divided into two major classes (Das 1993):

- Mass procedure. In this case, the mass of the soil above the surface of sliding is taken as a unit. This procedure is useful when the soil that forms the slope is assumed to be homogeneous, although this is hardly the case in most natural slopes.
- Method of slices: In this procedure, the soil above the surface of sliding is divided into a number of vertical parallel slices. The stability of each of the slices is calculated separately. This is a versatile technique in which the nonhomogeneity of the soils and pore water pressure can be taken into consideration. It also accounts for the variation of the normal stress along the potential failure surface.

Limit equilibrium solutions used for rock slope instabilities are largely based on solutions introduced by Hoek & Bray (1977) and assume translational sliding of a rigid body along a plane or, in the case of a wedge, along the intersection of two planes. Since the sliding block does not undergo any rigid body rotations, all forces pass through the centroid of the block. Furthermore, as in all limit equilibrium solutions, it is assumed that all points along the sliding planes are on the verge of failure. These assumptions make the problem statically determinate, permitting the simple calculation of the ratio of resisting forces and driving forces. Resisting forces are provided by the shear strength of the sliding surface (e.g., cohesion and friction), and driving forces generally consist of the down-slope weight component of the sliding block and water pressures along the boundaries of the block. Typical landslides that can be analyzed with limit equilibrium analyses are presented in Figure 2-20.

In large landslides, failure planes are seldom single and usually involve several failure planes and different types of movement; they may occur in different areas of the displaced mass, sometimes simultaneously. The example of composite

landslides is presented in Figure 2-21 and these kinds of movements may not be suitable for limit equilibrium analysis.

2.5.5.2 Seepage and groundwater in weak rocks

Groundwater acting on weak rock slopes is a significant stability factor. Some massive-appearing weak rocks are composed of layers of different permeabilities. Joints and fissures also exist in these bedrocks. Intact weak rock may have a coefficient of permeability on the order of 10^{-12} m/sec. The intact layers may be adjacent to other more pervious layers. Water seeping through the more permeable layers may develop large artesian or uplift pressures on the less permeable layers. Perched water tables are common in areas where weak rocks are overlain by glacial and postglacial deposits. The rapid seepage of water from such sources may initiate unfavorable conditions on slopes. In the upper weathered zone, the permeability along cracks, fissures, and joints may be several orders of magnitude greater than the permeability of intact shale.

2.6 Summary

Instability mechanisms observed in stiff clays and weak rocks are reviewed in this chapter. The main softening mechanisms are fissure softening, pore pressure equalization, and progressive failure and loosening. The presence of discontinuities in the slope body accelerates the rate of softening and increases the chance of sliding along the discontinuities. In stiff clay and weak rock, movements can occur along horizontal bedding planes, presheared surfaces and weak planes. External and internal agents contribute to time dependent reduction in shear strength. The mechanisms of landslides in stiff clay and weak rock have been presented and discussed.

Table 2-1 Abbreviated classification of slope movements (modified from Cruden and Varnes 1996)

TYPE OF MOVEMENT	TYPE OF MATERIAL		
	BEDROCK	ENGINEERING SOILS	
		PREDOMINANTLY COARSE	PREDOMINANTLY FINE
Fall	Rock fall	Debris fall	Earth fall
Topple	Rock topple	Debris topple	Earth topple
Slide	Rock slide	Debris slide	Earth slide
Spread	Rock spread	Debris spread	Earth spread
Flow	Rock flow	Debris flow	Earth flow

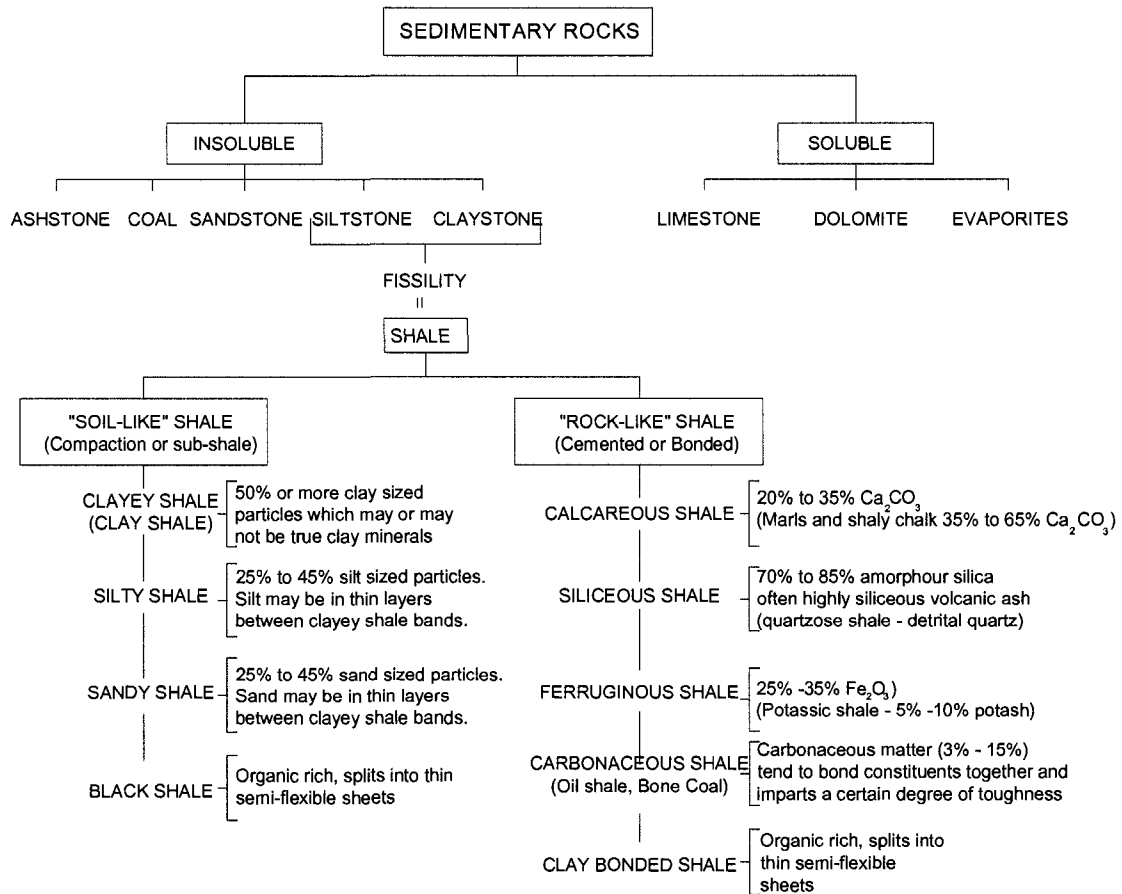
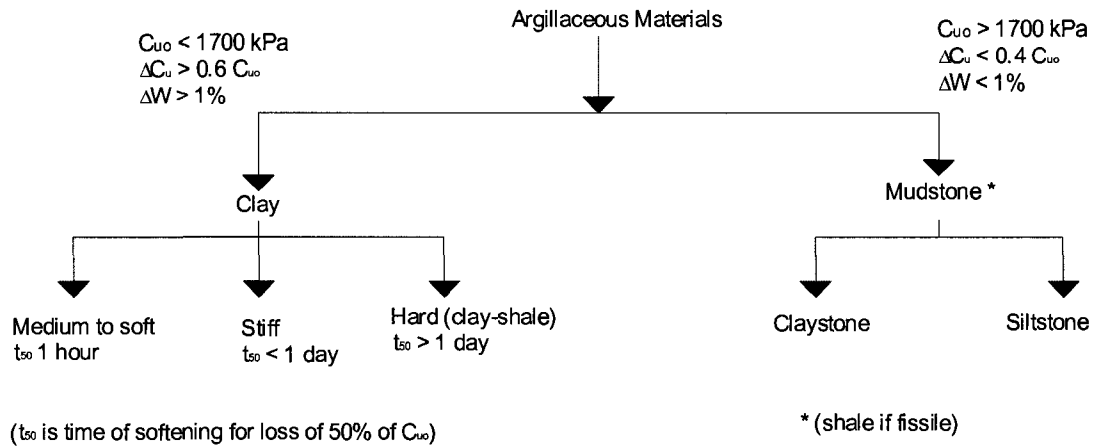


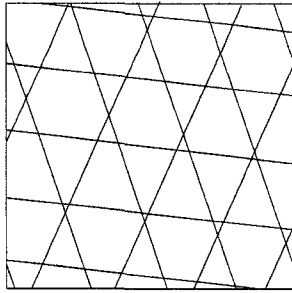
Figure 2-1 A geologic classification of shales (modified from Underwood 1967)



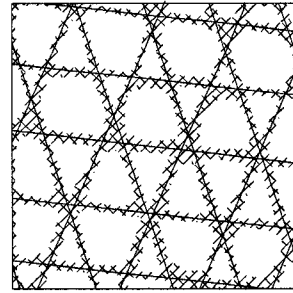
C_{u0} = Undrained shear strength at natural water content
 ΔC_u = Strength loss after softening to equilibrium water content
 ΔW = Change in water content after softening
 t_{50} = Time of softening for loss of 50% of C_{u0}

		Amount of Saking $w_s = w_l$				
		very low VL $w_l < 20$	Low L $20 < w_l < 50$	Medium M $50 < w_l < 90$	High H $90 < w_l < 140$	Very high VH $w_l > 140$
Rate of Saking $\Delta L_{L1} = L_1 - L_0$ 2h water immersion	Slow S $\Delta L_L < 0.75$	VL S	L S	M S	H S	VH S
	Fast F $0.75 < \Delta L_L < 1.25$	VL F	L F	M F	H F	VH F
	Very fast VF $\Delta L_L > 1.25$	VL VF	L VF	M VF	H VF	VH VF
		VL	L	M	H	VH
		S	S	S	S	S
		F	F	F	F	F

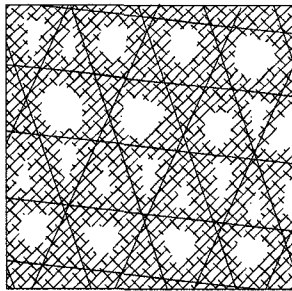
Figure 2-2 Two part classification scheme (modified from Morgenstern and Eigenbrod 1974)



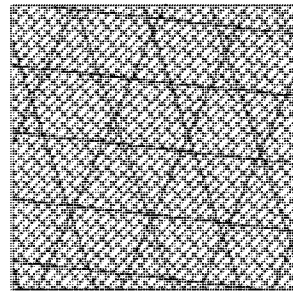
Stage 1 (before alteration)



Stage 2 (initial alteration along fissures)



Stage 3 (intermediate stage of fissure alteration)



Stage 4 (final stage of fissure alteration)

Figure 2-3 Progressive deterioration of fissured weak rock (modified from Botts 1986)

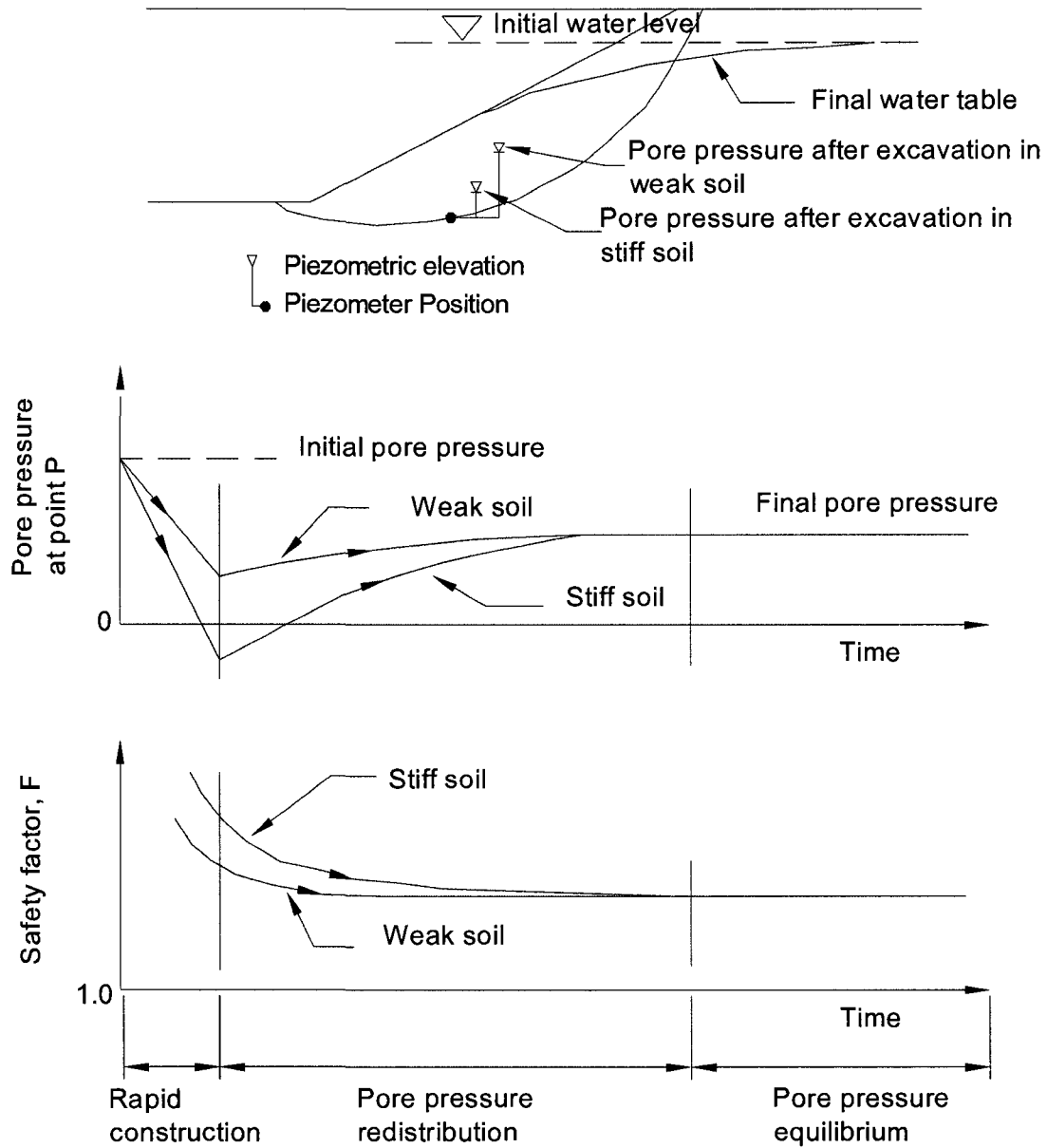
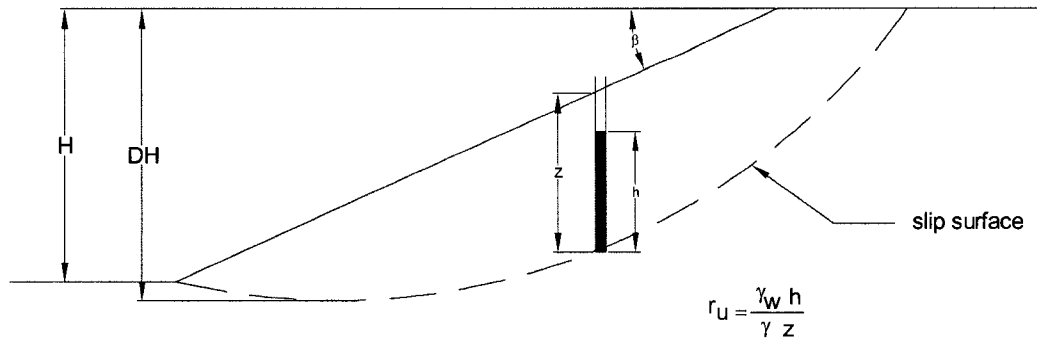


Figure 2-4 Changes in pore pressure and factor of safety during an excavation of a cut slope in clay (modified from Bishop and Bjerrum 1960)



- h = piezometric height
- γ_w = piezometric weight
- γ = unit weight of clay
- r_u = average value of r around slip surface
- D = depth factor

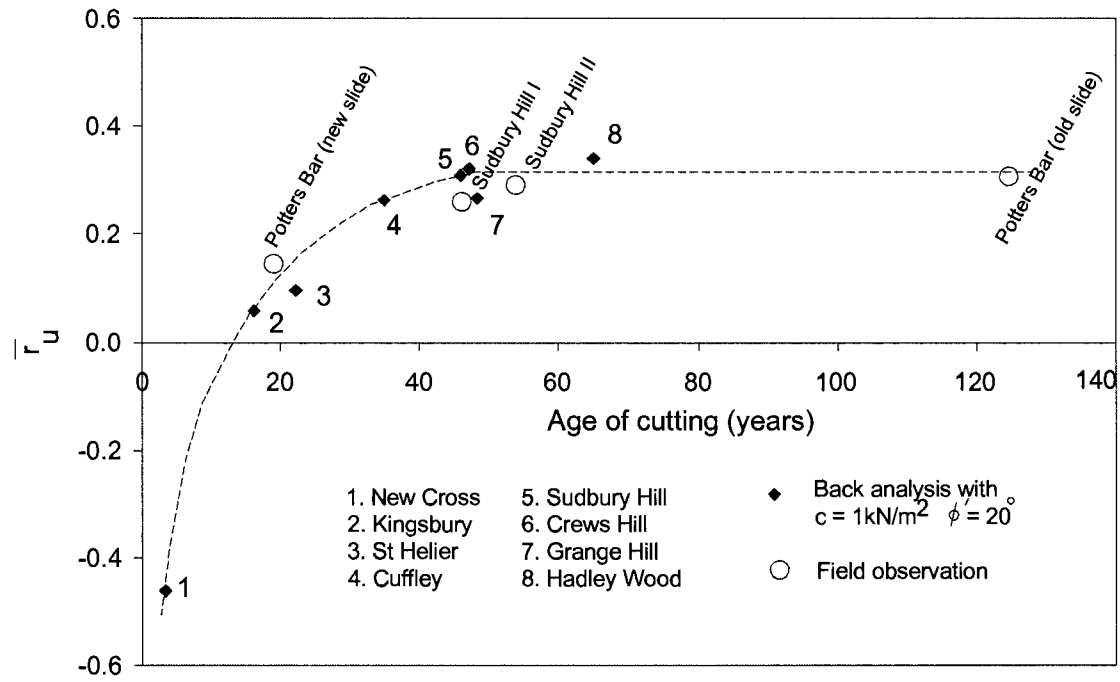


Figure 2-5 Variation of \bar{r}_u with time: cutting in brown London Clay (modified from Skempton 1978)

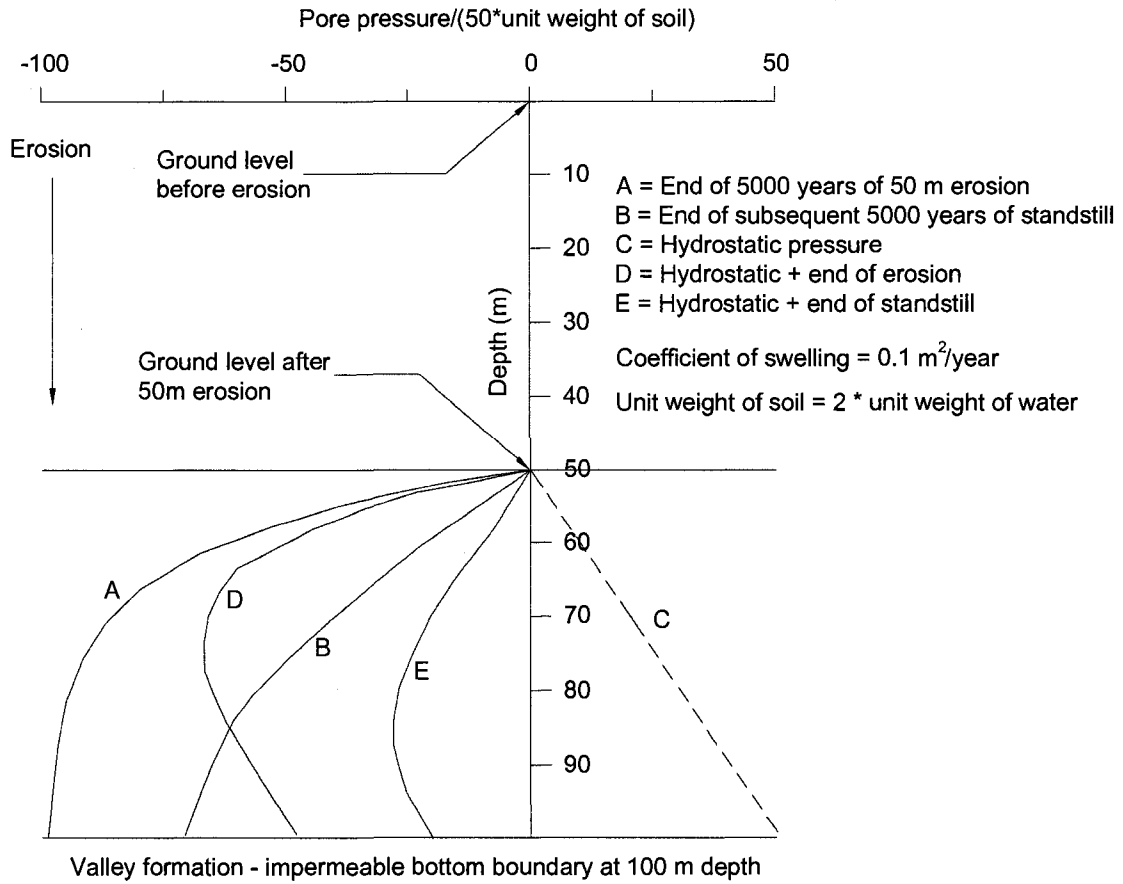


Figure 2-6 Pore pressure isochrones (modified from Koppula and Morgenstern 1984)

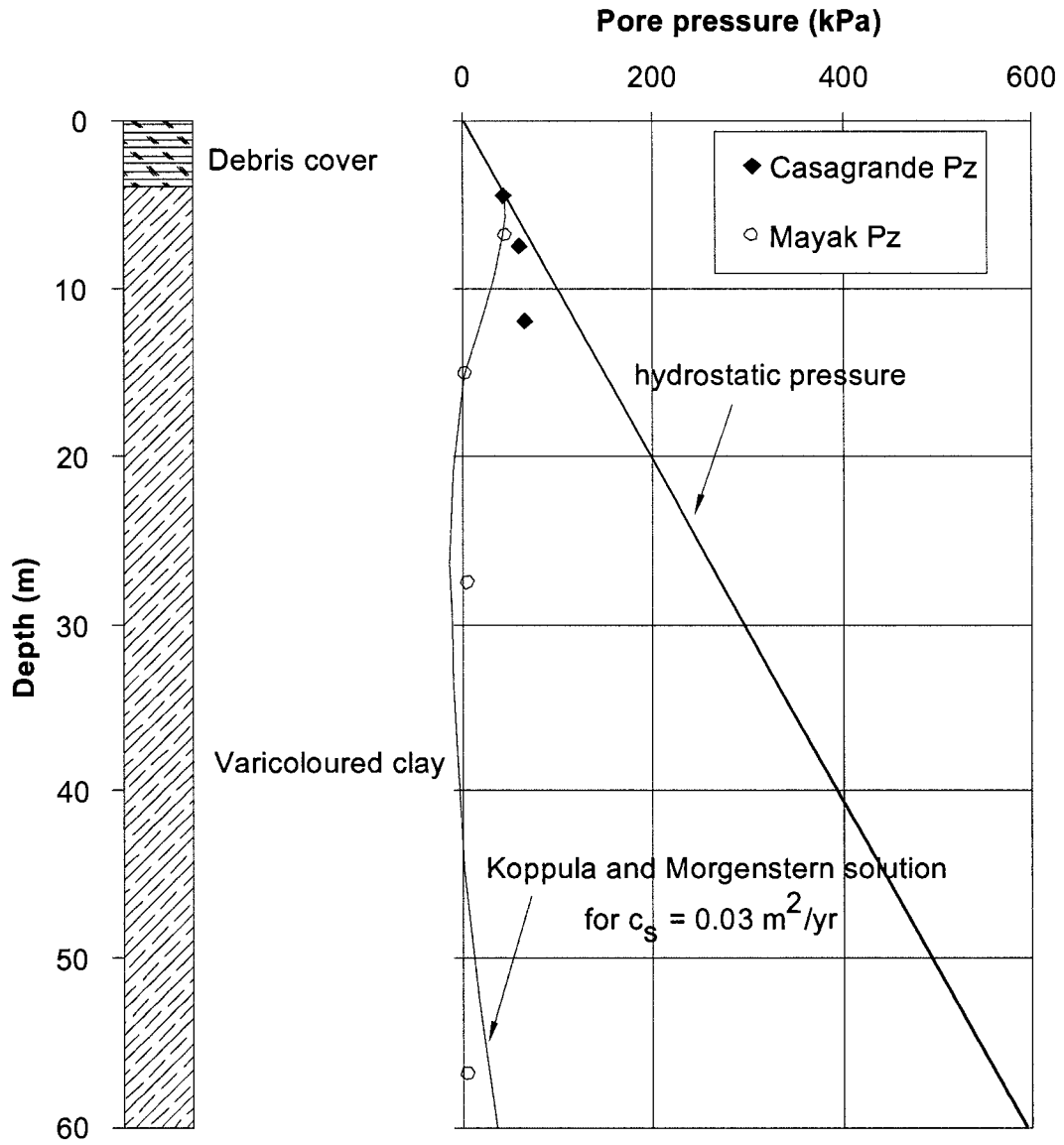


Figure 2-7 Pore pressure measurement at Bisaccia hill (modified from Fenelli and Picarelli 1990)

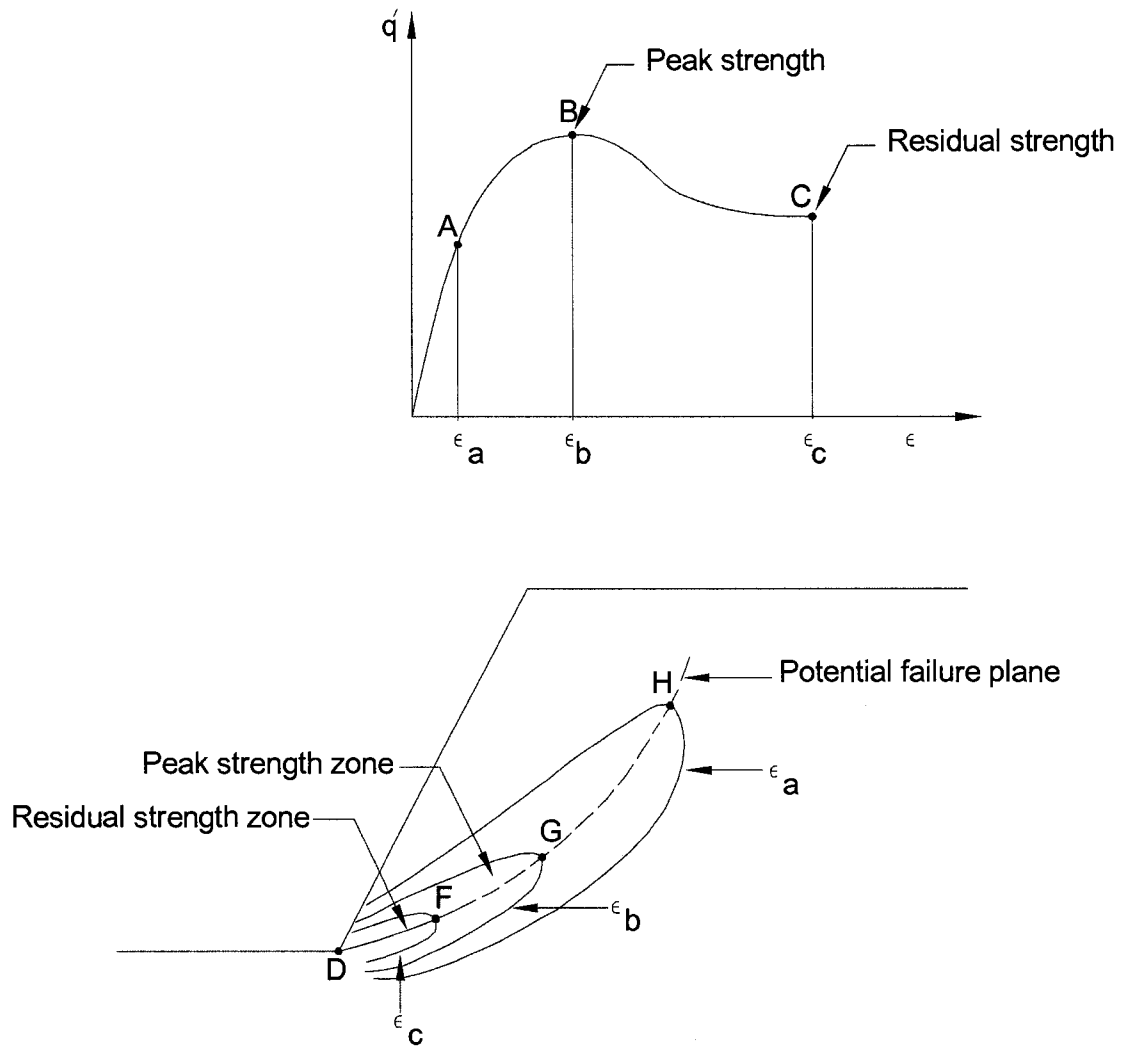


Figure 2-8 Contours of shear strain in a slope, and its relation to corresponding stress states in an overconsolidated clay (modified from Atkinson and Bransby 1978)

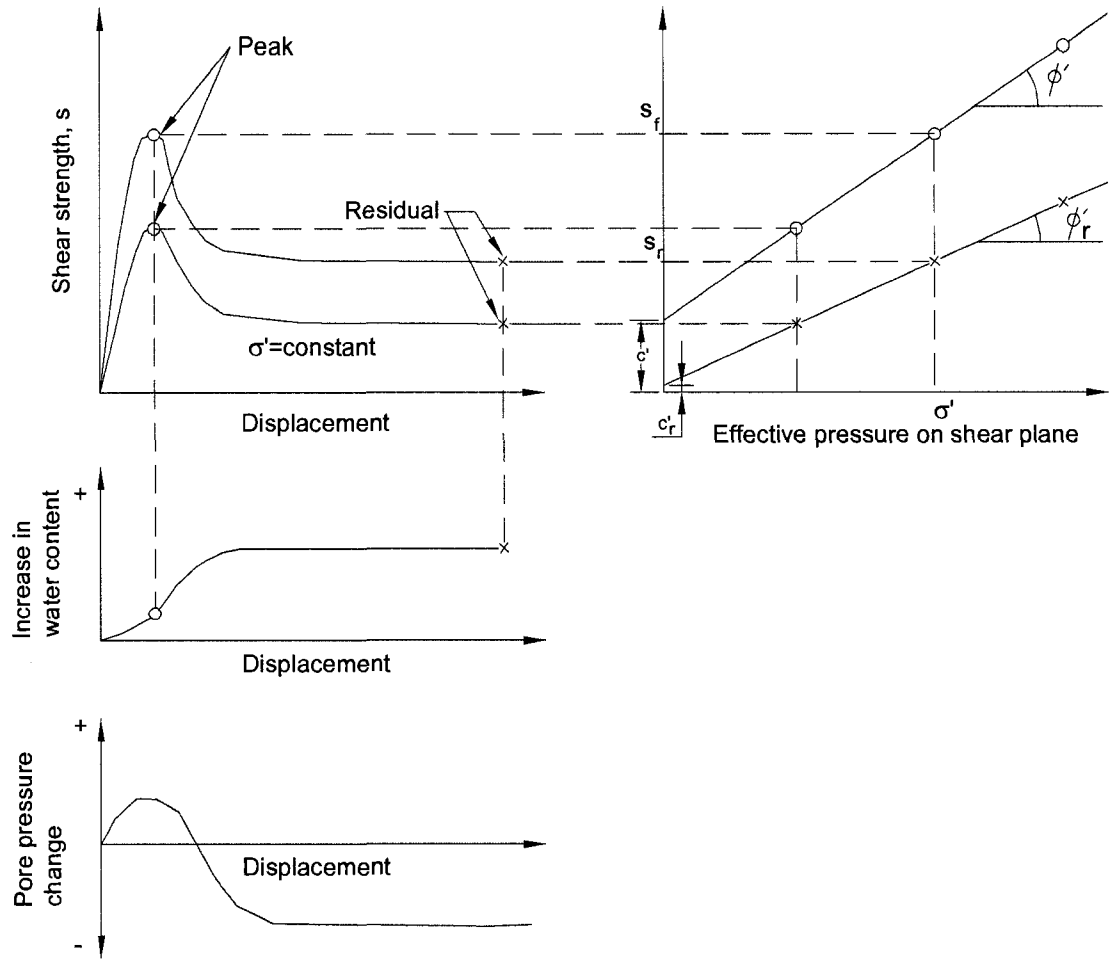


Figure 2-9 Shear characteristics of overconsolidated clay (modified from Skempton 1964)

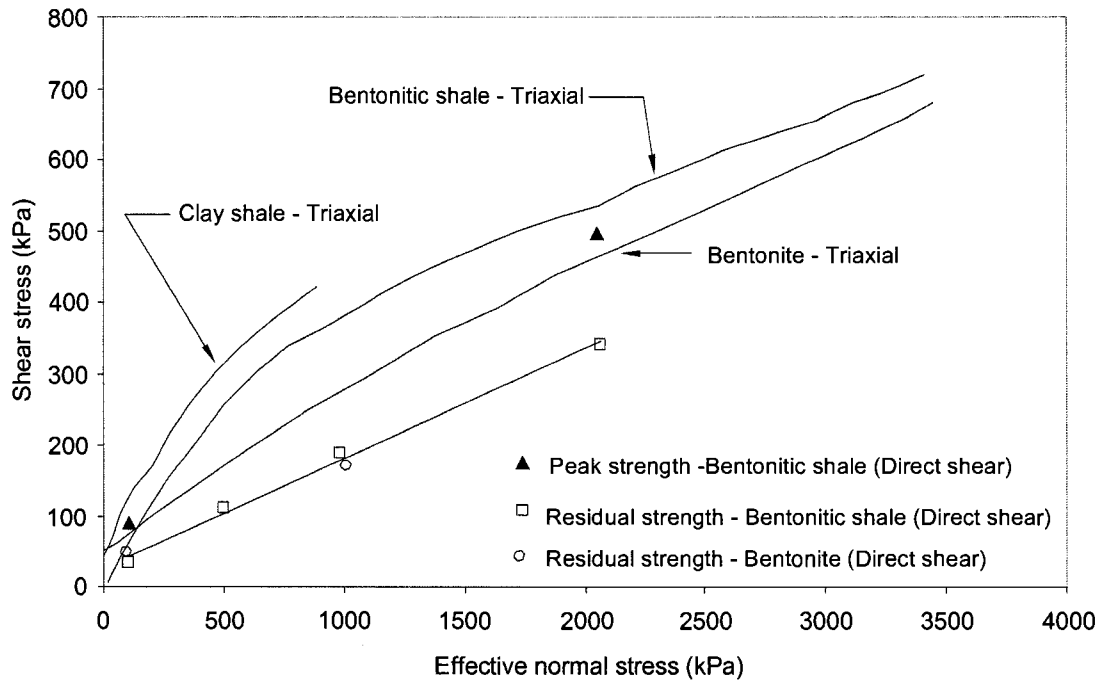


Figure 2-10 Summary of strength test results, triaxial and direct shear tests (modified from Sinclair and Brooker 1967)

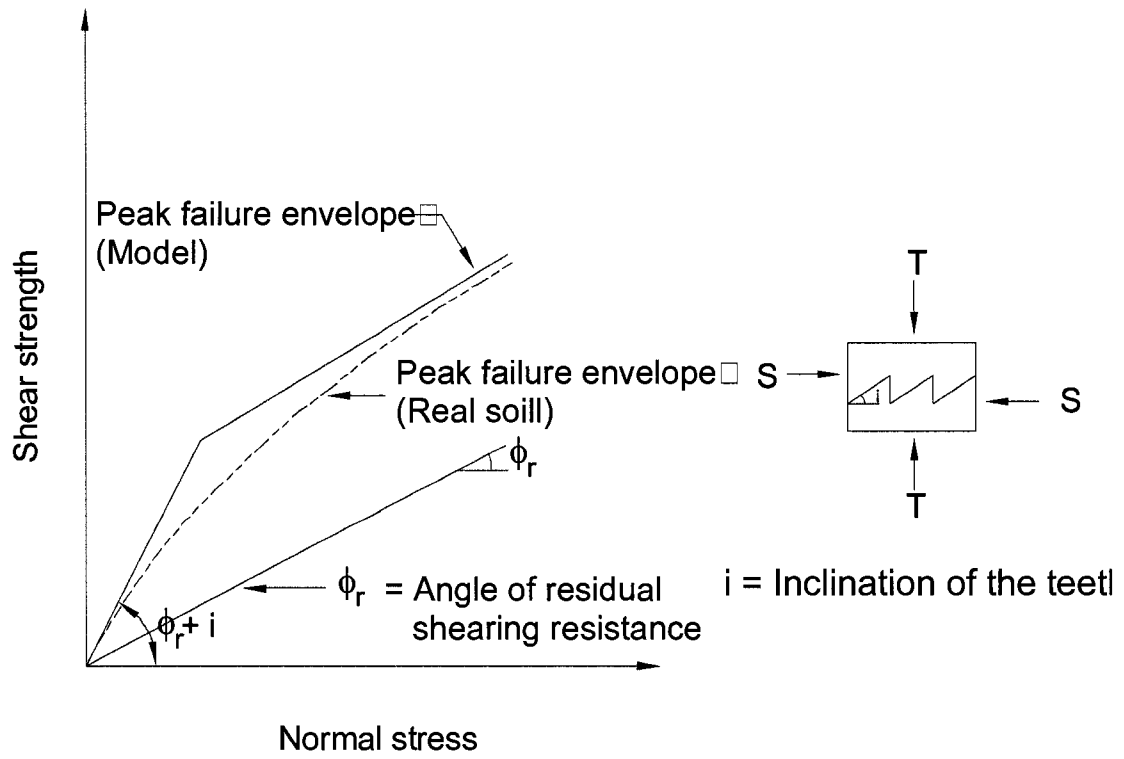
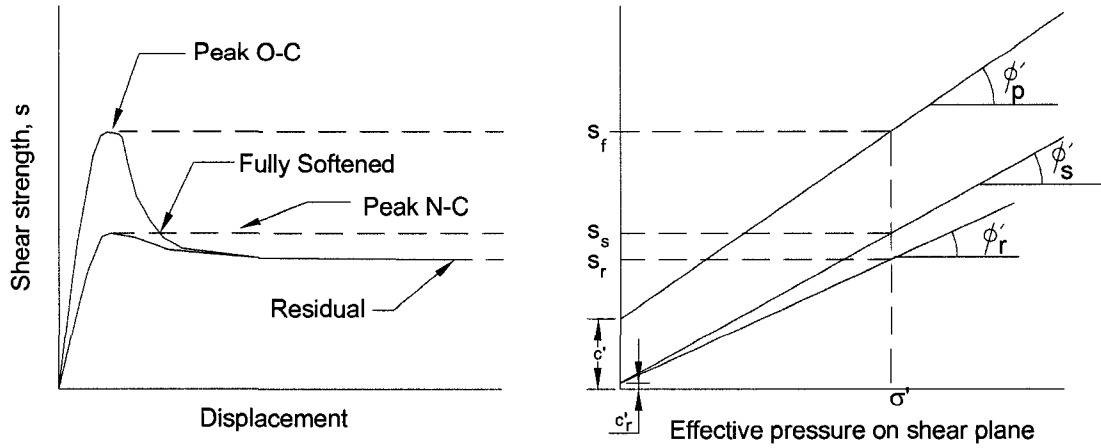


Figure 2-11 Shear strength of a model specimen having a rough surface (modified from Patton 1966)



s_f = peak strength

s_s = fully softened strength

s_r = residual strength

ϕ'_p = peak friction angle strength

ϕ'_s = fully softened friction angle

ϕ'_r = residual friction angle

c' = peak cohesion

c'_r = residual cohesion

Figure 2-12 Shear characteristic of clay (modified from Skempton 1970)

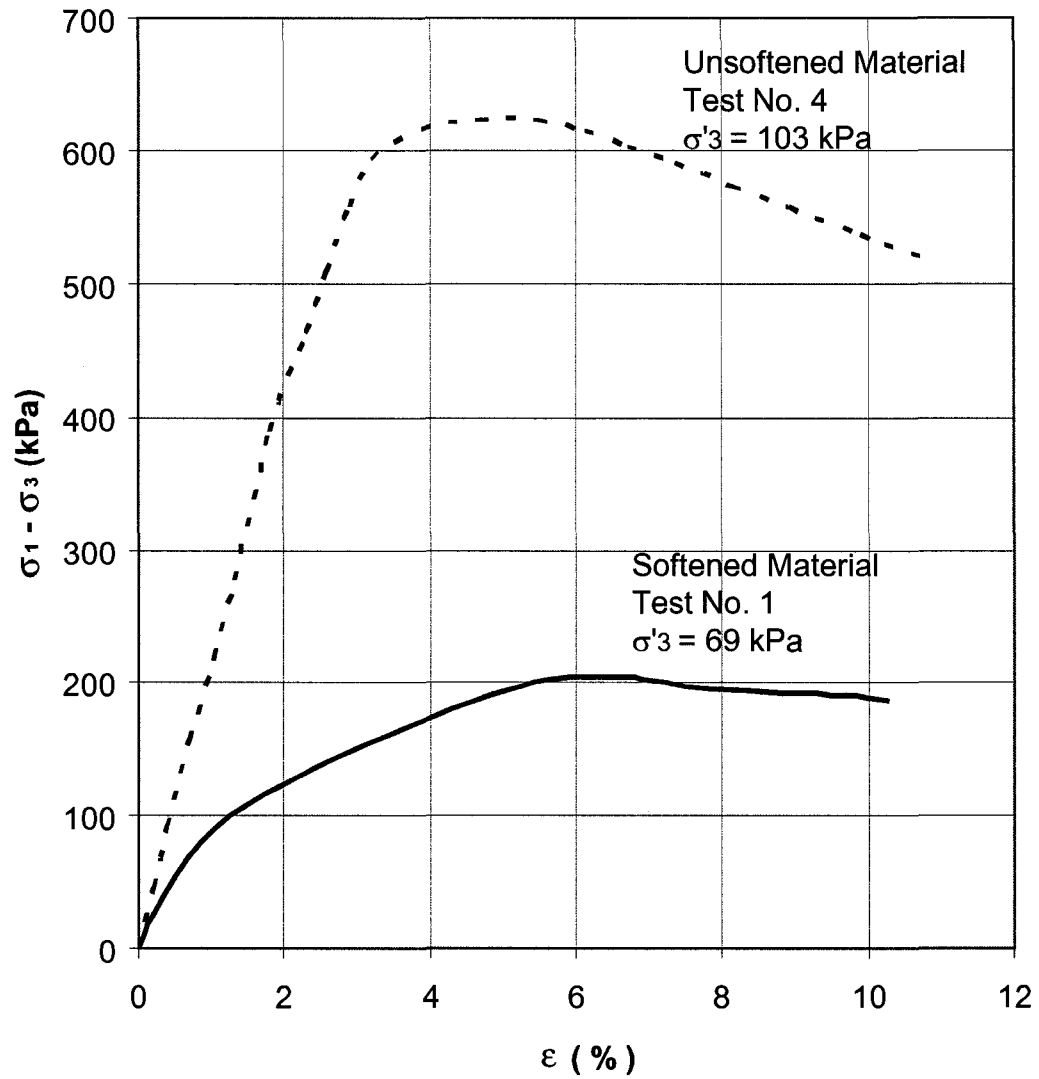


Figure 2-13 Examples of stress-strain curve for softened and unsoftened back slope materials (modified from Eigenbrod and Morgenstern 1971)

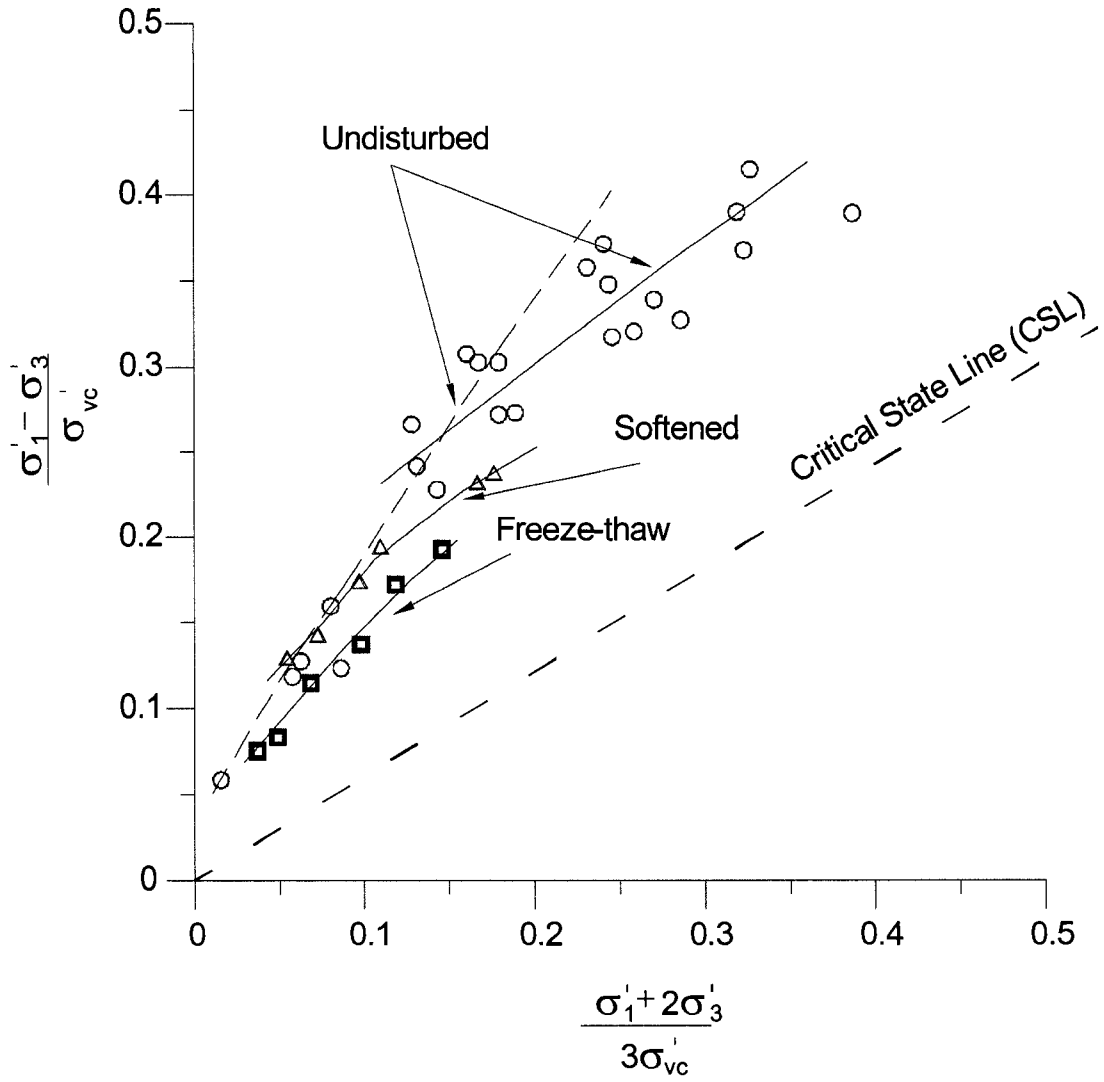


Figure 2-14 Results of triaxial tests on Lake Agassiz clays in normalized p'-q space (modified from Graham and Au 1985)

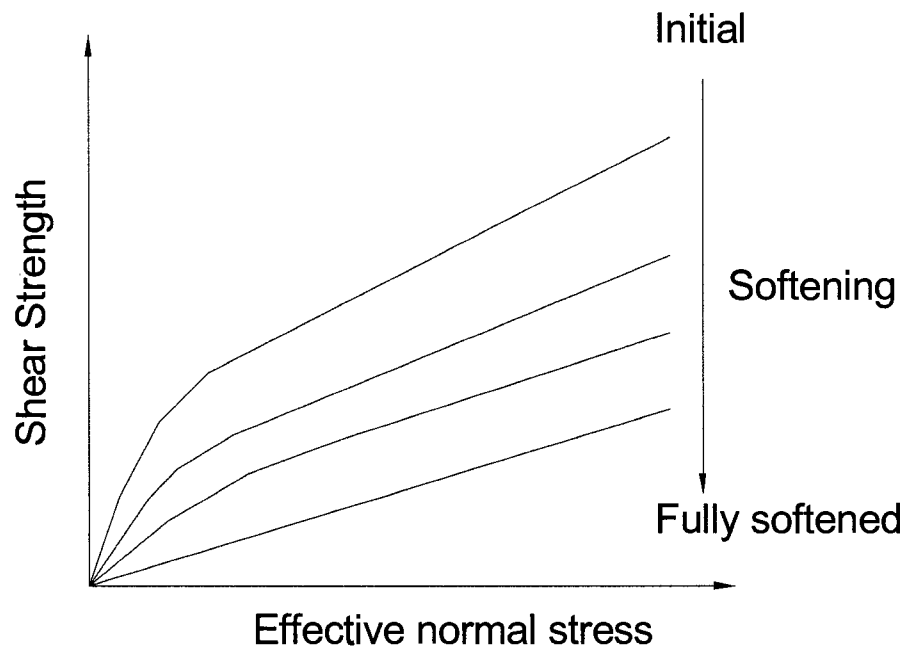
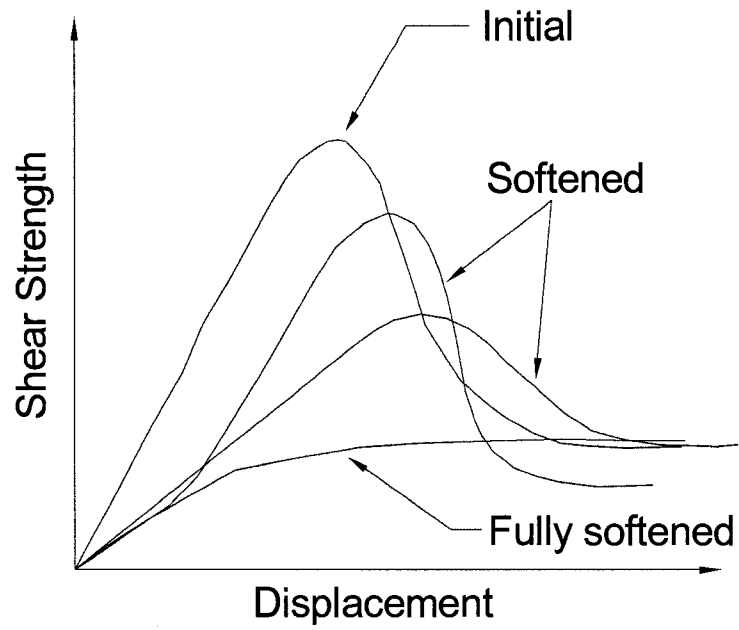


Figure 2-15 The effect of softening on engineering behaviour of weak rock (modified from Yoshida et al. 1990)

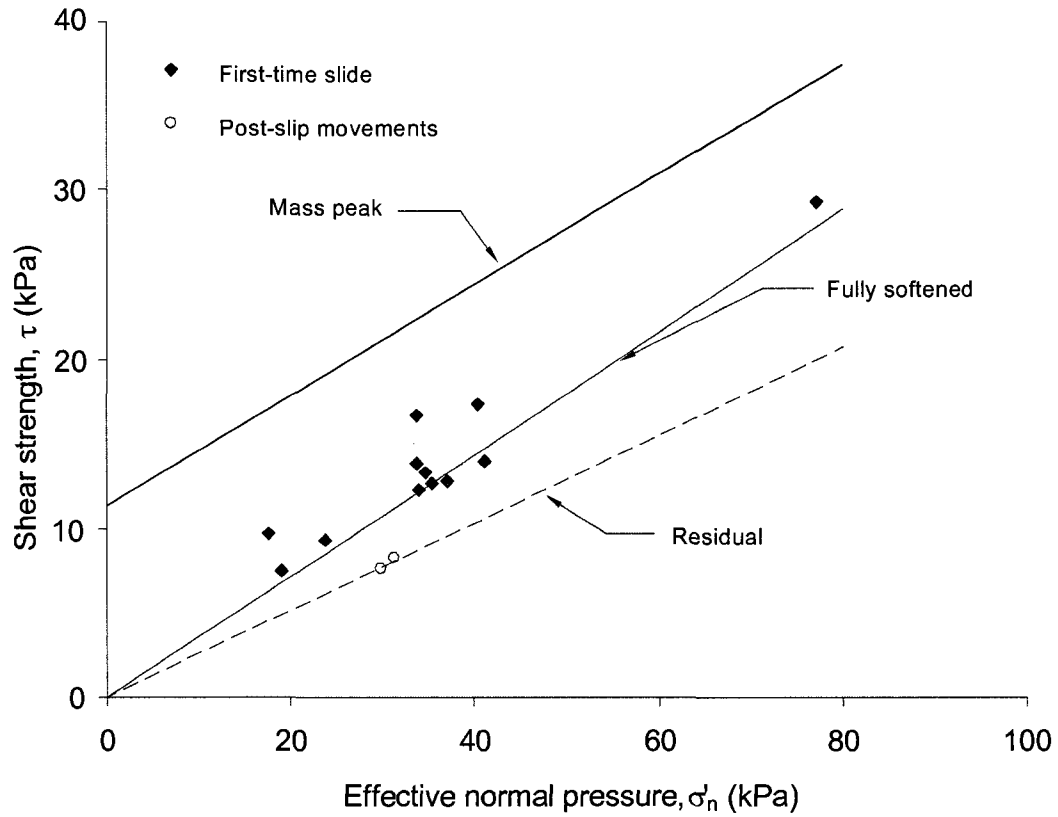


Figure 2-16 Shear strength and normal pressure for cuttings in brown London Clay (modified from Skempton 1970)

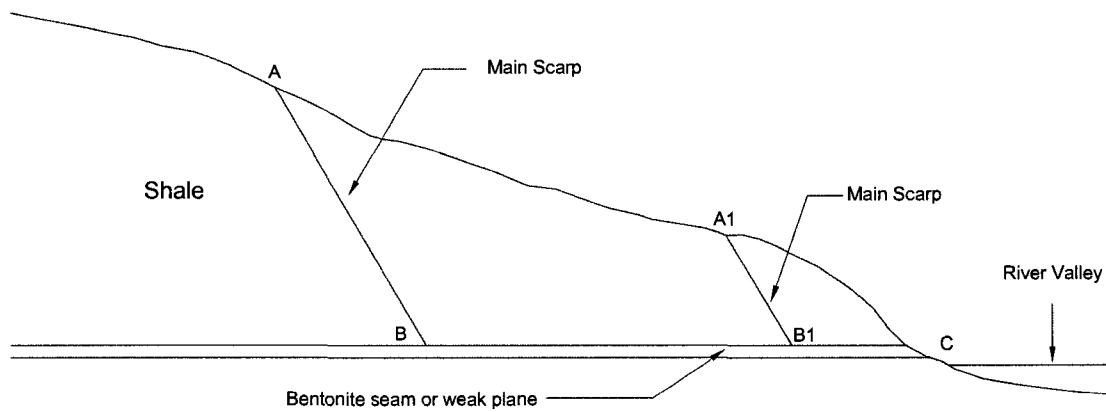


Figure 2-17 Approximate geometry of failure surface in Cretaceous formations in western Canada (modified from Scott and Brooker 1968)

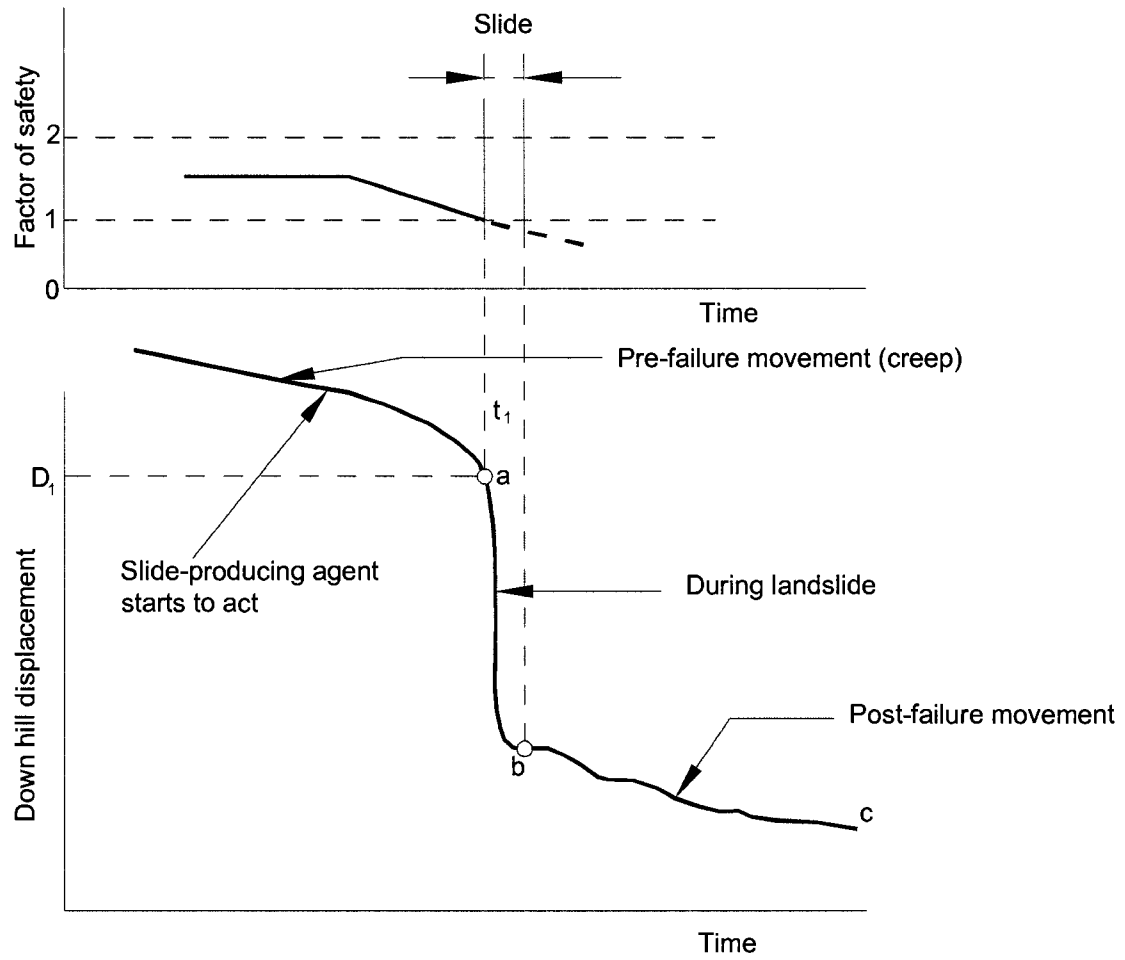


Figure 2-18 Diagram illustrating the ground movements which precede a landslide (modified from Terzaghi 1950)

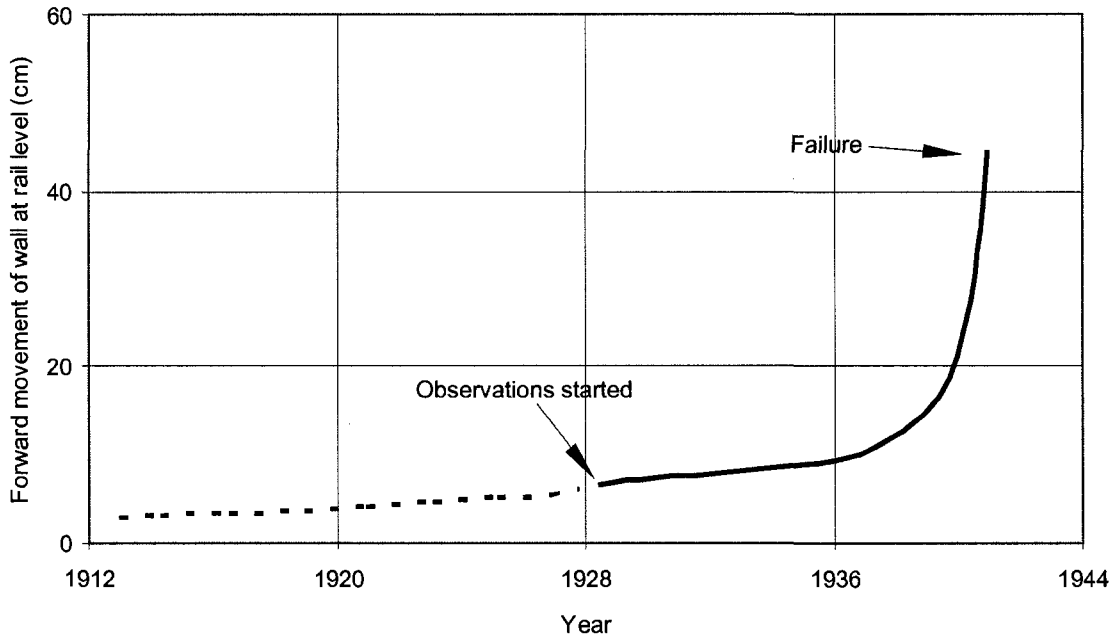


Figure 2-19 Observed creep movement in a Kensal Green cutting (modified from Skempton 1964)

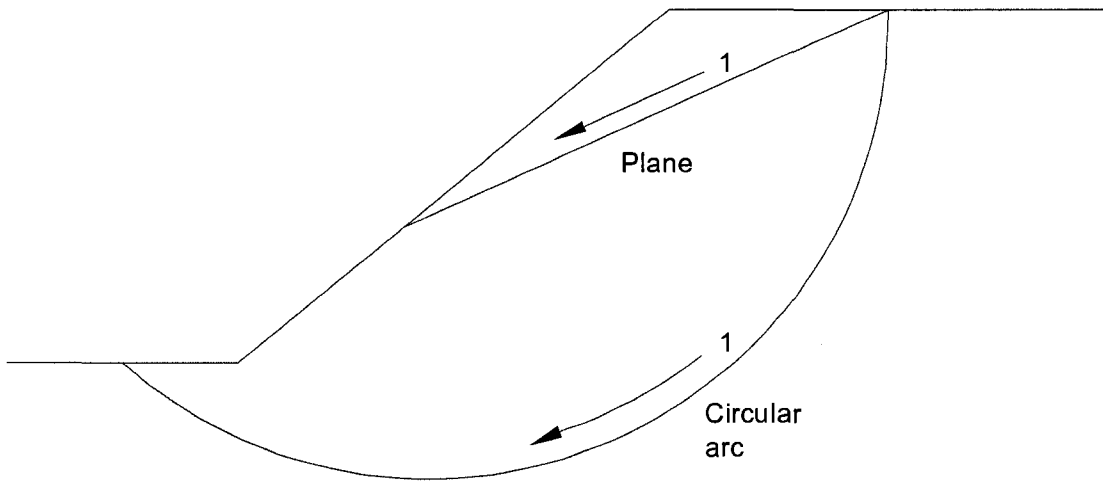


Figure 2-20 Typical single landslides (circular and plane failure)

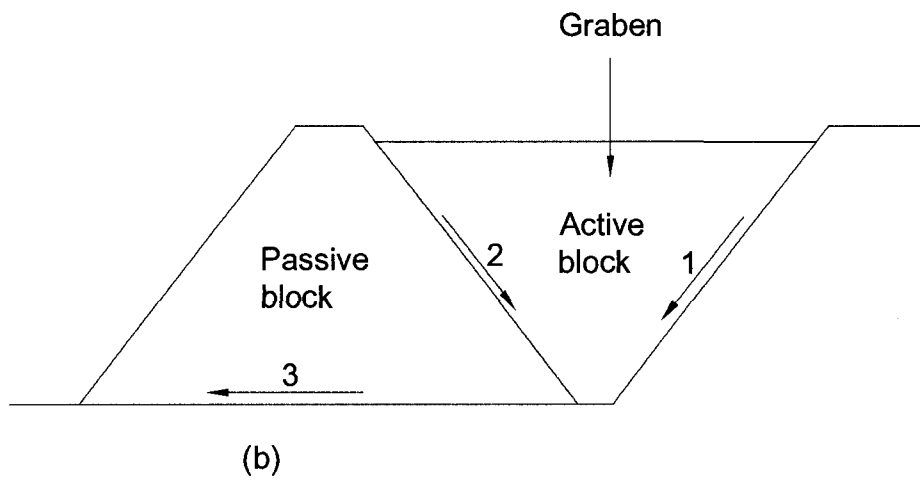
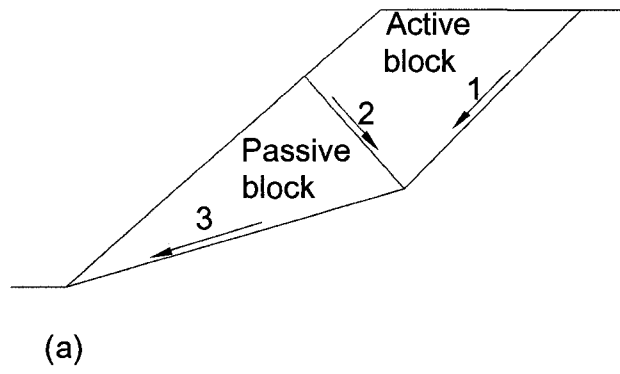


Figure 2-21 Sliding block failure

CHAPTER 3 River valley landslides in Edmonton

3.1 Introduction

The instability of natural slopes in central Alberta is well known and a number of case studies have been reported (Cruden et al. 1998; Morgenstern 1979; Painter 1965; Pennell 1969; Thomson 1971b; Thomson and Hayley 1975). In Edmonton, the North Saskatchewan River cut its present valley postglacially. The valley slopes are often steep with changes in profile due to variations in geological formation. The river banks are marginally stable (Thomson 1970) and slope failures along the river valley often affect city infrastructure. Case histories of landslides (Cruden et al. 2003; Cruden et al. 2002; Thomson and Tiedemann 1982) showed a common mode of failure: translational movement along a weak layer in the bedrock. Usually, a graben is formed the head of the displaced material after the slope failure. Some of the major landslides along the North Saskatchewan River Valley in the Edmonton area are presented in Figure 3-1 (Eigenbrod and Morgenstern 1971; Martin et al. 1984; SoeMoe et al. 2003; SoeMoe et al. 2005; SoeMoe et al. 2006; SoeMoe et al. 2007; Thomson 1971b).

Stability analyses of the river valley landslides in Edmonton are a challenge due to different kinematics involved in the slides. Furthermore, accurate observations of pore pressure at the time of failure were sparse and it was difficult to determine actual pore pressure during the time of failure. Morgenstern (1977) stated that the special problems that arise in the consideration of slopes in heavily overconsolidated clays are associated with the selection of appropriate strength parameters, understanding the factors influencing mobilization of shear strength when failure first occurs or is renewed, and diagnosing the large variety of stratigraphical situations.

In this chapter, three well-documented case studies of landslides along the North Saskatchewan River Valley are discussed. Major consideration is given to landslide mechanism, pore pressure response of weak rocks, and slope stability.

3.2 Regional Geology

Edmonton is located on the Alberta Plains. The regional geology consists of Upper Cretaceous bedrock of the Edmonton Group, comprising the Horseshoe Canyon, the Whitemud and the Battle Formations (Elliot 1958; Irish 1970; Ower 1958). The Edmonton Group is underlain by the marine shales of the Bearpaw Formation, and the Belly River Formation (Kathol and McPherson 1975).

The Horseshoe Canyon Formation consists of interlayered, fine-grained calcareous and bentonitic sandstones, bentonitic and carbonaceous claystones, siltstones, and mudstones, with interbedded bentonites and coal seams (Kathol and McPherson 1975). It is a brackish to fresh-water deposit that has been poorly consolidated. The clay fraction in these materials exceeds 40 percent and the dominant clay mineral is montmorillonite (Locker 1969). The bedding planes are not laterally continuous over long distances and display rapid changes over short intervals. The sandstones are fine grained bentonitic and often grade to poorly cemented and weak siltstone. The coal seams are of variable quality and generally 0.4 to 0.6 m in thickness.

Prior to glaciation, rivers had developed a mature drainage system in the bedrock having a northeastly flow toward Hudson Bay. The buried Beverly Valley in north Edmonton is a dominant preglacial feature of the areas. During the Pleistocene, the broad preglacial valleys partially infilled with sands and gravels known as Saskatchewan sands and gravels (Carlson 1967). In the Edmonton area, the only advance of ice was during the Wisconsin period (Bayrock and Hughes 1962). It is estimated that an ice sheet up to 1.5 km thick flowed from the north and northeast (Godfrey 1993). During glaciation, till was laid down directly on the bedrock or on the Saskatchewan sands and gravels. Till, typically 8 to 15 m thick, consists of a clay matrix with numerous local bedrock fragments and a few carbonate fragments in the sand fraction. The bedrock surface was thrust and folded by the thick ice, and in

some areas large blocks of bedrock were transported by the glacial ice. This displaced bedrock is commonly encountered in the local glacial till. During the glacial retreat, glacial Lake Edmonton deposited sediments comprising up to 15 m of highly plastic clays, which graded into fine silty sands near their base (Bayrock and Hughes 1962).

The surficial deposits comprise fluvial sands and gravels, which date back to the late Wisconsin (Andriashek 1988). The surficial deposits in the Edmonton area have been extensively investigated and mapped in detail by Kathol and McPherson (1975) and Andriashek (1988). The thickest deposits are found in buried valleys. Tedder (1986) states that the thickness of the surficial sediments varied from 30 m within the preglacial valleys to 5 m over the bedrock uplands. Painter (1965) indicated that the sands are fine to coarse textured, light to grayish brown in color, and gravel particles are composed of quartzite and cherts with some arcose pebbles.

The groundwater flow through the low permeable till and Upper Cretaceous bedrock is predominantly downward. The Edmonton Group is the major aquifer in the Edmonton area and wells are commonly shallower than 90 m (Kathol and McPherson 1975). Wells in thick, fractured coal seams provide the highest yields, although wells are also completed in the poorly indurated sandstone layers (Kathol and McPherson 1975). The Saskatchewan sands and gravels are highly permeable and usually saturated, thus providing the best aquifer among the surficial deposits. Interconnected sand lenses within the glacial till, as well as the alluvium in the low level terraces along the North Saskatchewan River also provide potential sources of water. Within these deposits, aquifers consisting of sand and gravel, sandstone, and fractured coal are capable of yielding groundwater at a rates of up to 8 L/sec (Stein 1982).

3.3 The Grierson Hill landslide

The first documented landslide in Edmonton, the Grierson Hill landslide, took place in the fall of 1901. Prior to the failure, the valley wall was steep, with a slope angle of about 24 ° overall (Martin et al. 1998). Overburden, 14 to 20 m thick, consists of

lacustrine clay, clay till, and sand. The local bedrock, Upper Cretaceous Horseshoe Canyon Formation, consists of clay shale interbedded with sandstone and siltstone. Several coal seams exist in the sequence and in some cases these are associated with thin bentonite layers.

The 1901 landslide damaged seven buildings and the Humberstone coal mine. A graben developed at the head of the displaced material (Godfrey 1993). Survey records showed significant slide activity until approximately 1910 (Martin et al. 1984). The landslide took the form of a translational slide along a horizontal bentonite shear surface located below the mine working as shown in Figure 3-2. Survey records showed that significant slide activity continued until approximately 1910 (Martin et al. 1984). During this time, the crest of the slope had retrogressed some 35 m and the toe had moved out 40 to 50 m into the river (Martin et al. 1998).

Different stages in the development of the Grierson Hill landslide are shown in Figure 3-2 A to D. Martin et al. (1998) indicated that the 1901 slide was a first-time slide occurred along a horizontal bentonite layer located below the mine workings. The slide was believed to have been caused by a combination of prolonged precipitation, the loss of backscarp strength due to subsidence into the mine workings, and the presence of bentonite layers in the bedrock. The present slope configuration is shown in Figure 3-2 D. As shown in the figure, the riverbank has moved out some 120 m from its original preslide position.

In 1980, the City of Edmonton installed 21 pneumatic piezometers around the Grierson Hill landslide area and regular monitoring was conducted during the period of September 1980 to November 1981. The results of pore pressure measurements together with the cross section of the slide are presented in Figure 3-3. As shown, a perched water level is located in the overlying till and the displaced material. Downward seepage patterns are found in the displaced material. Piezometers installed below the sliding plane registered only 1 or 2 m of head. Piezometers installed in the displaced materials registered 4 to 5 m of piezometric head. Long term monitoring results showed only small changes in piezometric pressure and little response to seasonal precipitation patterns.

The piezometric pressure of the bedrock and the displaced material, measured 80 years after the failure, together with the hydrostatic pressure of the perched water level, is presented in Figure 3-4. As shown, measured piezometric pressures are significantly lower than the hydrostatic pressure of the perched water level, indicating that the pore pressure regime of the slope is not yet equalized 80 years after the major failure.

3.4 Lesueur Landslide

The Lesueur Slide is located on the outside of a bend of the North Saskatchewan River at eastern part of the City of Edmonton (Painter 1965; Pennell 1969; Thomson 1971a; Thomson 1971b). On September 3, 1963 a major slide occurred leaving a scarp 7 m high and a part of a house cantilevered over the scarp (Figure 3-5). Detailed site investigations were carried out after the failure in 1963 and 1964 (Thomson 1971b). The stratigraphic profile consists of fine glacial lake sands, till, terrace sands, and gravel overlying clay shales and bentonitic clay shales of Upper Cretaceous age. The preslide slope angle was 26° and the valley wall height was about 33 m. The drill holes behind the valley indicated that a perched water level is located in the overlying till deposit.

Five Bishop Type, twin tube hydraulic piezometers were installed after the 1963 failure. Two were located in BH-4 and one each in BH-5, 7, and 8 (Figure 3-5). The former two piezometers were located in the outside of the displaced material and the latter two piezometers were located in the displaced material. Mercury manometers, deairing apparatus, and ancillary controls were housed in a small building located outside the slide zone. Polyethylene coated 4.75 mm O.D. nylon tubing connected the tips and the gauge house. Groundwater was used in all the lines and a small propane heater kept the system warm during the winter. Pore pressure readings were taken over the period November 1, 1964 to April 15, 1965 at approximately 2-week intervals. The piezometers in BH-4 and BH-7 showed a piezometric elevation of 2 to 4 m below tip elevation in December 1964 to January 1965 (Figure 3-6).

In late July 1967, another hole, LA-9 (Figure 3-5), was drilled behind the slope crest and a water standpipe was installed in this location. Monitoring data of LA-9 revealed that the groundwater level was located in the overlying till deposit. In November 1967, a University of Alberta transducer piezometer (Brooker and Lindberg 1965) was installed inside the standpipe and readings were recorded until August 1968 (Figure 3-7). As shown in Figure 1-8, the piezometer measured the piezometric pressure of the bedrock, which was about 8 m head.

The piezometric pressure of the bedrock and the displaced material, measured 3 years after the failure, together with the hydrostatic pressure of the perched water table, is presented in Figure 3-8. As shown, measured piezometric pressures are significantly lower than the hydrostatic pressure of the perched water level. Some of the piezometers registered negative pore pressure probably due to dilation of the bedrock.

Thomson (1971b) conducted stability analyses in terms of effective stress and used a noncircular failure surface comprised of a steeply dipping section and an essentially horizontal section. Thomson indicated that the Lesueur Slide was a first-time failure, but the overall strength that was mobilized was less than the full peak strength. He also indicated that the peak angles of shearing resistance were mobilized but the cohesion developed had a value between peak and residual.

Cruden et al. (2002) compared the surveyed results in 1964, 1971, 1992, 1995, 1997, and 1998, and indicated that the slope is still active 34 years after the failure. The main scarp grew in height from 7.5 m on 4 September 1963 to 13.9 m in 1995, but retrogressed only 3 m. The displaced material extended up to 24 m into the North Saskatchewan River. From the observation of the Lesueur Slide, Cruden et al. (2002) identified at least three stages in the post-failure evolution of this complex translational slide. Observed landslide stages are as follows:

- The first stage lasted only a few hours on September 3 and 4, 1963, when rapid movement formed the graben at the head of the main body and pushed the foot of the landslide into the North Saskatchewan River (Figure 3-9b).
- In the next stage, the slow to very slow sinking of the active block accompanied the very slow advance of the foot into the river. This stage

ended about 1995 when the downward driving motion of the active block halted, possibly because the block now rested on the horizontal part of the rupture surface.

- In the third stage of movement, the passive block was no longer driven forward into the river by the sinking active block. Therefore, erosion by the river steepened the slope of the accumulation of the displaced material at the toe of the slide and triggered small rotational slides on the surface of separation (Figure 3-9c).

3.5 Devon Landslide

The Devon Landslide (Eigenbrod and Morgenstern 1971) is located adjacent to Highway No. 60 where it crosses the valley of the North Saskatchewan River near Devon, about 12 miles upstream of Edmonton (Figure 3-10). During the summer of 1965, highway improvements were undertaken and the road leading down the valley wall was reconstructed to reduce grades and ease horizontal curves. Parts of the preexisting slopes on the North wall of the valley were cut back to 2.75:1, about 20° to the horizontal. The height of the slope was about 35 m and the vertical difference in elevation between the top of the cut and ditch invert was about 20 m. Before the construction in March 1965, tension cracks had been observed in the slope and the actual landslide occurred in the fall of 1965.

Field investigation revealed a sheared bentonite layer behind the slide. Eigenbrod and Morgenstern (1971) indicated that the Devon Slide was actually located in a larger older slide which had presumably developed during valley formation. Piezometers were installed to determine the water pressure distribution in the area adjacent to the slip. Since the bedrock consists of impermeable bentonite mudstone and sandstone, University of Alberta piezometers (Brooker et al. 1968) were used to minimize the piezometric time lag. A perched water table was found to be located in the overlying till deposit. Piezometer PZ-1, 2, and 4 were installed in the coal beneath the bentonite layer at the base of the slide and these piezometers registered 0.5 to 1 m piezometric head. PZ-3, located 4 m above the failure plane, registered 4

m piezometric head. Continuous readings were taken for periods of two years for PZ-1, 2, and 4 and one year for PZ-3. A water well near the slide area had been drilled to a depth just above the bedrock and the water level was reported to be about 2 to 4 m below the ground surface. Long term pore pressure measurements, together with the groundwater level observed from the water well, is presented in Figure 3-11.

Eigenbrod and Morgenstern (1971) conducted back analysis using the general noncircular limit equilibrium method as described by Morgenstern and Price (1965). The failure plane geometry was determined from the steeping dipping main scarp and horizontal sliding plane, as shown in Figure 3-12. Zero water pressure was taken as acting on the shear plane in the bentonitic clay while water pressure in the back scarp was computed from the observed piezometric level. A parametric analysis was conducted by varying the values of shear strength along the horizontal sliding plane. It was found that a mobilized friction angle of 8° with zero cohesion gave a factor of safety of 1.01. They concluded that although the slide was a first-time slide, it was part of a much larger slide block moved presumably when the valley was being formed.

3.6 Pore pressure response of river valley landslides

A review of pore pressure on weak rock slopes along the North Saskatchewan River Valley revealed two pore pressure systems on the bedrock and the overlying deposits. A perched water level is located in the overlying glacial deposit. The piezometric pressure of the bedrock is significantly below the hydrostatic pressure and in some cases, pore pressure readings are negative. Among three different types of piezometers used in the Upper Cretaceous bedrock, only twin-tube hydraulic piezometers registered negative pore pressure. To compare the pore pressure measurement results from different landslide investigations, measured pore pressures are normalized with hydrostatic pressure and the results are presented in Figure 3-13. A normalized pore pressure of 1 is the same as the hydrostatic pressure and 0 indicates there is no pore pressure in the bedrock. The results show that the measured pore pressures in the bedrock are below the hydrostatic pressure. Normalized pore pressure values of different landslides ranged from 0.8 to 0

depending on locations and depths. It is noted that the piezometric pressures measured in the displaced material show higher normalized pore pressures, about 0.4 to 0.8. Most of the piezometers installed below the sliding plane registered normalized pore pressures of 0 to 0.4.

3.7 Summary

A review of three well documented landslides along the river valley in Edmonton is presented together with the pore pressure response of the bedrock during the slide. These landslides are complex rock slides-earth slides and retrogressive in nature. Continued slope movements have been observed long after the failure. During failure, the head of the displaced material moved downward as the main body translated along a surface of rupture located in the bedrock.



1. Whitemud Road Landslide – fall 1999 (SoeMoe et al. 2006)
2. Keillor Road Landslide – fall 2002 (SoeMoe et al. 2005)
3. Grierson Hill Landslide – fall 1901 (Martin et al. 1984)
4. Forest Height Park Landslide – early 1900s (SoeMoe et al. 2007)
5. Lesueur Landslide – 1963 (Thomson 1971b)
6. Devon Landslide – fall 1965 (Eigenbrod and Morgenstern 1971)

Figure 3-1 Major landslide location map around the City of Edmonton

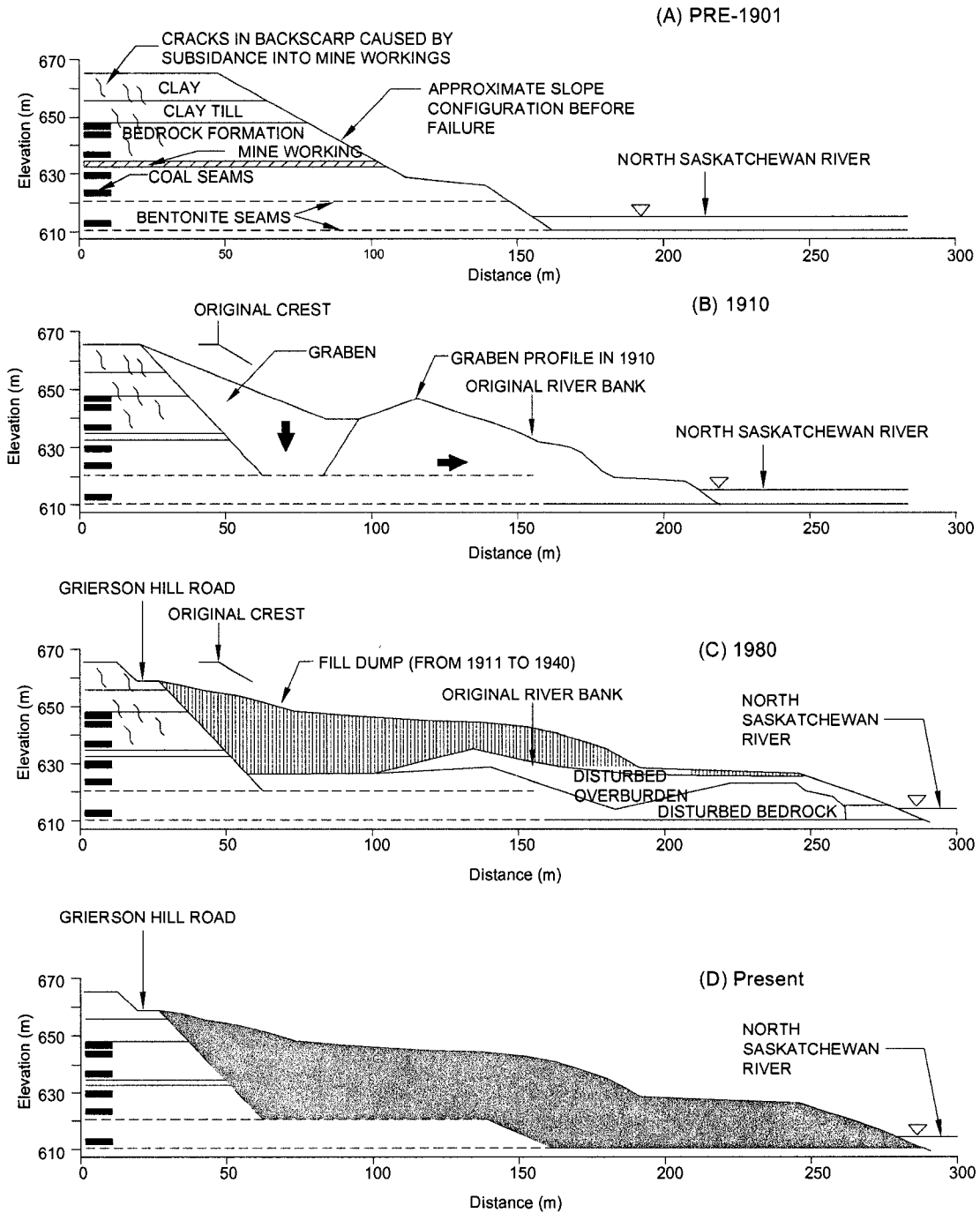


Figure 3-2 Landslide stages observed in Grierson Hill Landslide from 1900, 1910 to 1983 and present (modified from Martin et al. 1998)

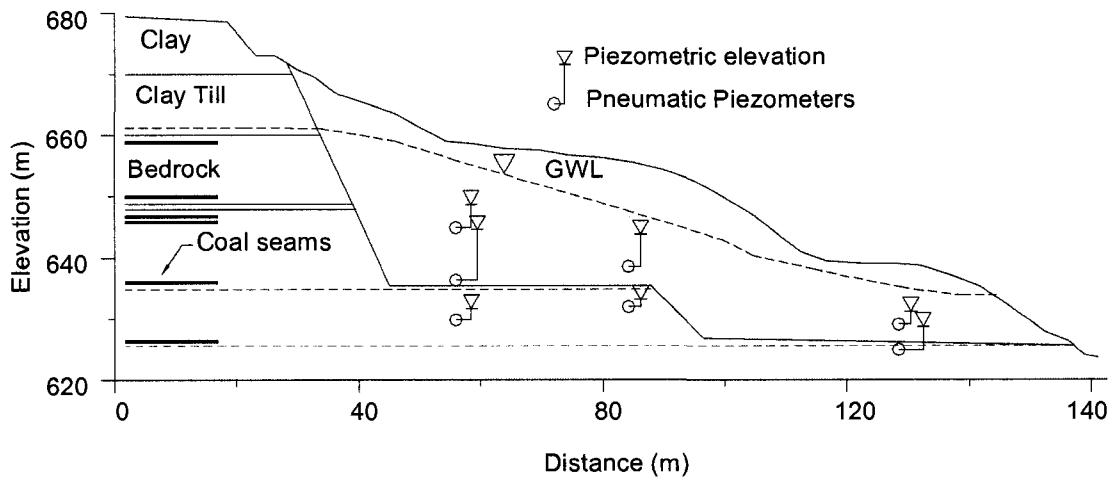


Figure 3-3 Typical piezometric pressures in Grierson Hill slide (modified from Martin et al. 1984)

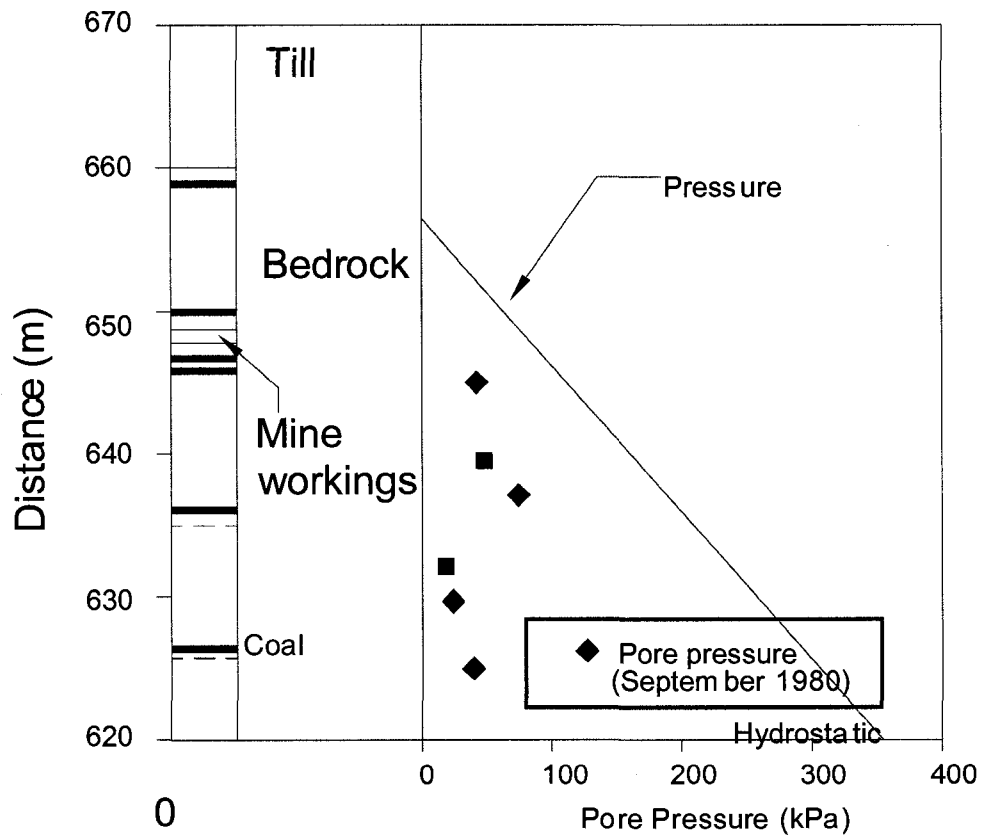


Figure 3-4 Pore pressure distribution in Grierson Hill slide (data from Martin et al. 1984)

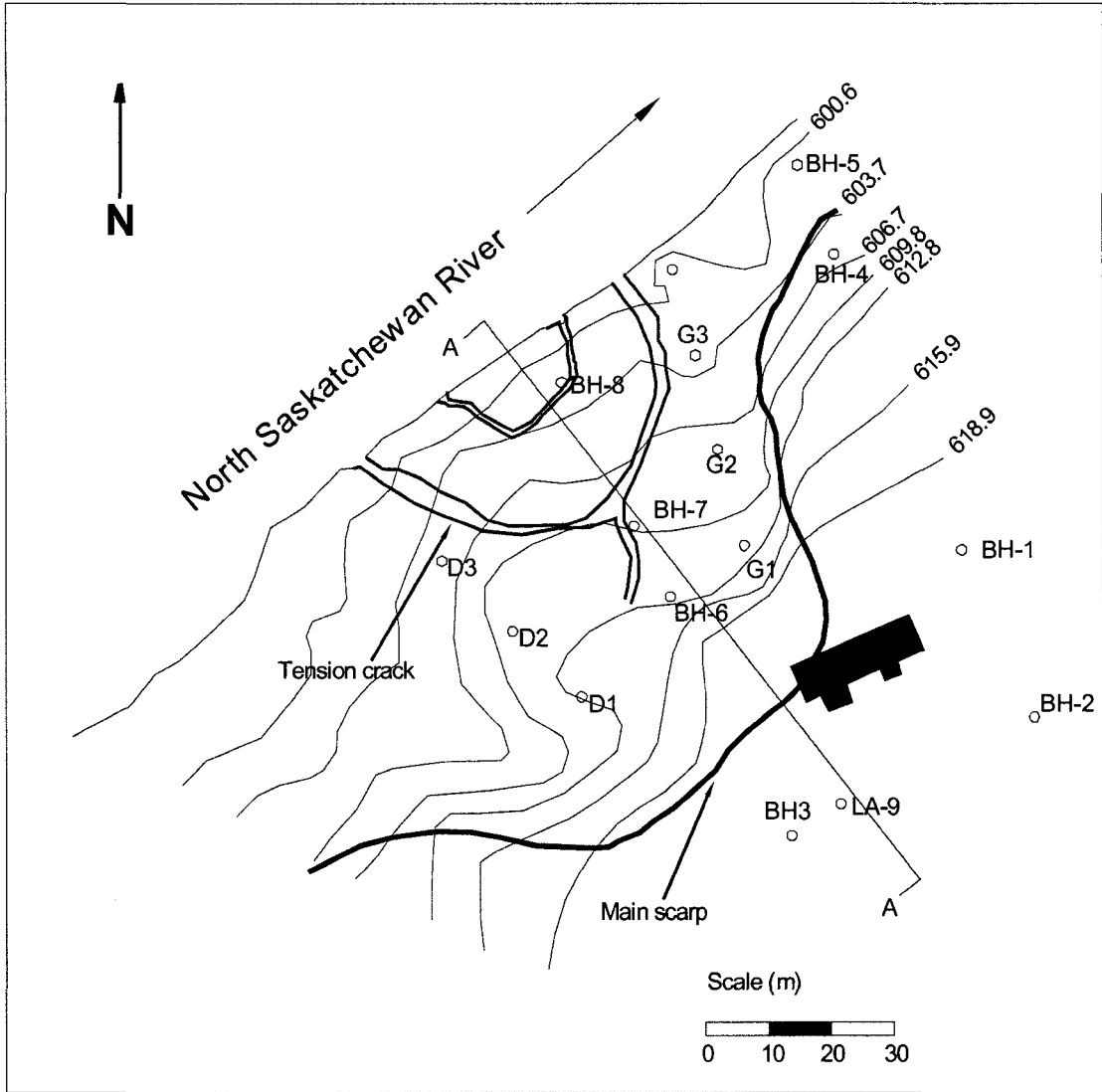


Figure 3-5 Plan view of the Lesueur Slide (modified from Thomson 1971b)

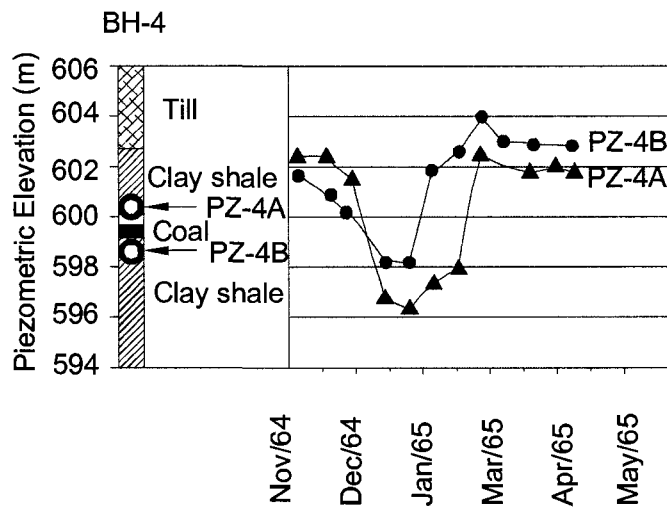
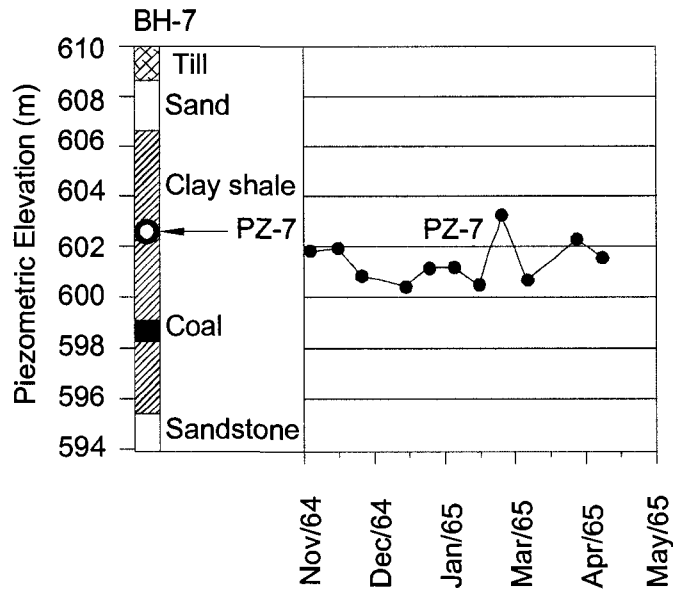


Figure 3-6 Piezometric elevation vs. time (modified from Thomson 1971b)

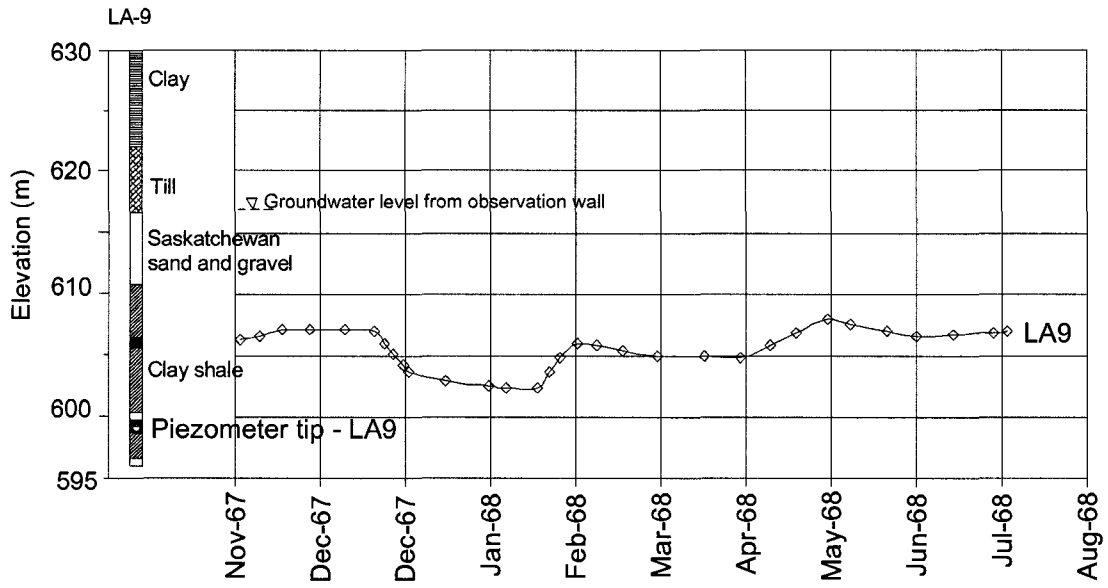


Figure 3-7 Piezometric elevation vs. time for LA9 (modified from Thomson 1971b)

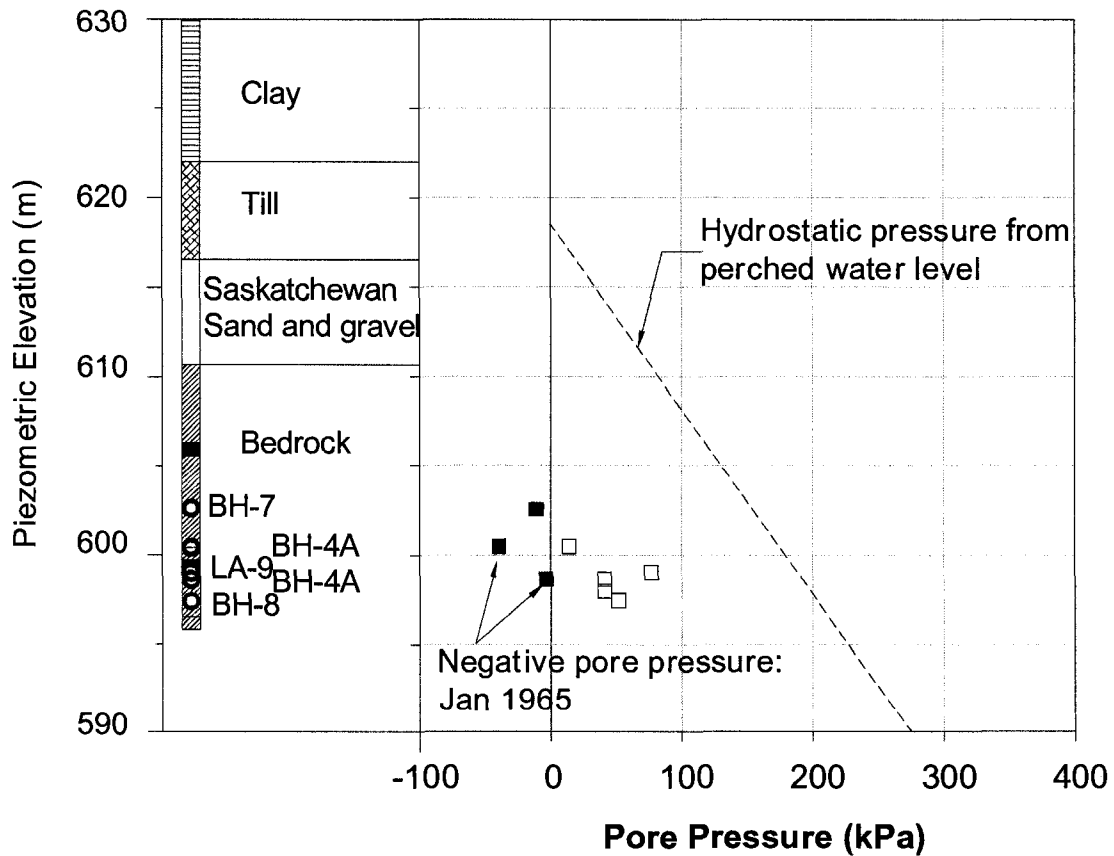


Figure 3-8 Pore pressure profile in the Lesueur Slide (data from Thomson 1971b)

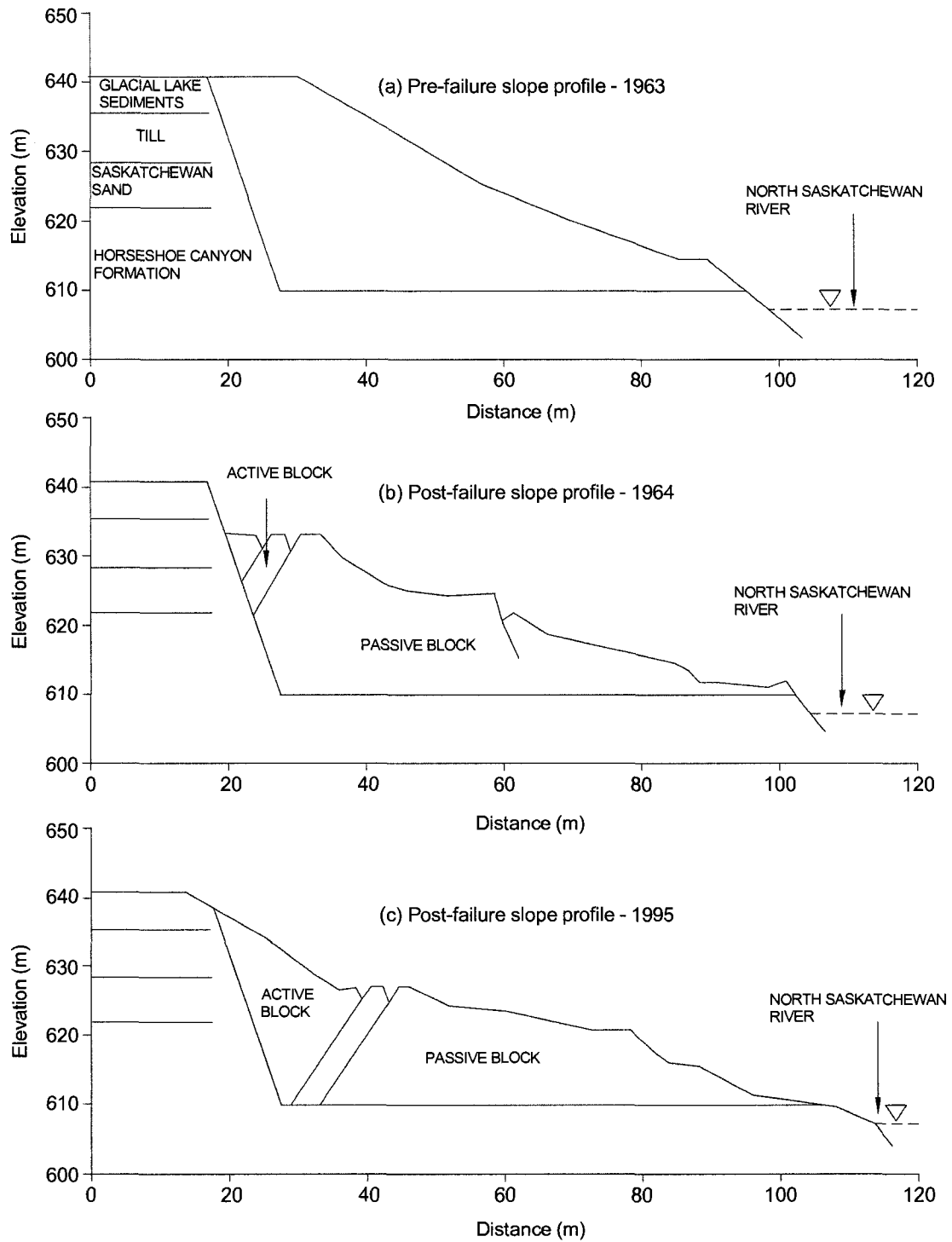


Figure 3-9 Lesueur Slide slope profile along A-A, (a) Pre-failure 1963, (b) Post-failure June 1964, (c) June 1995. Stratigraphy from Thomson (1971) (modified from Cruden et al. 2002)

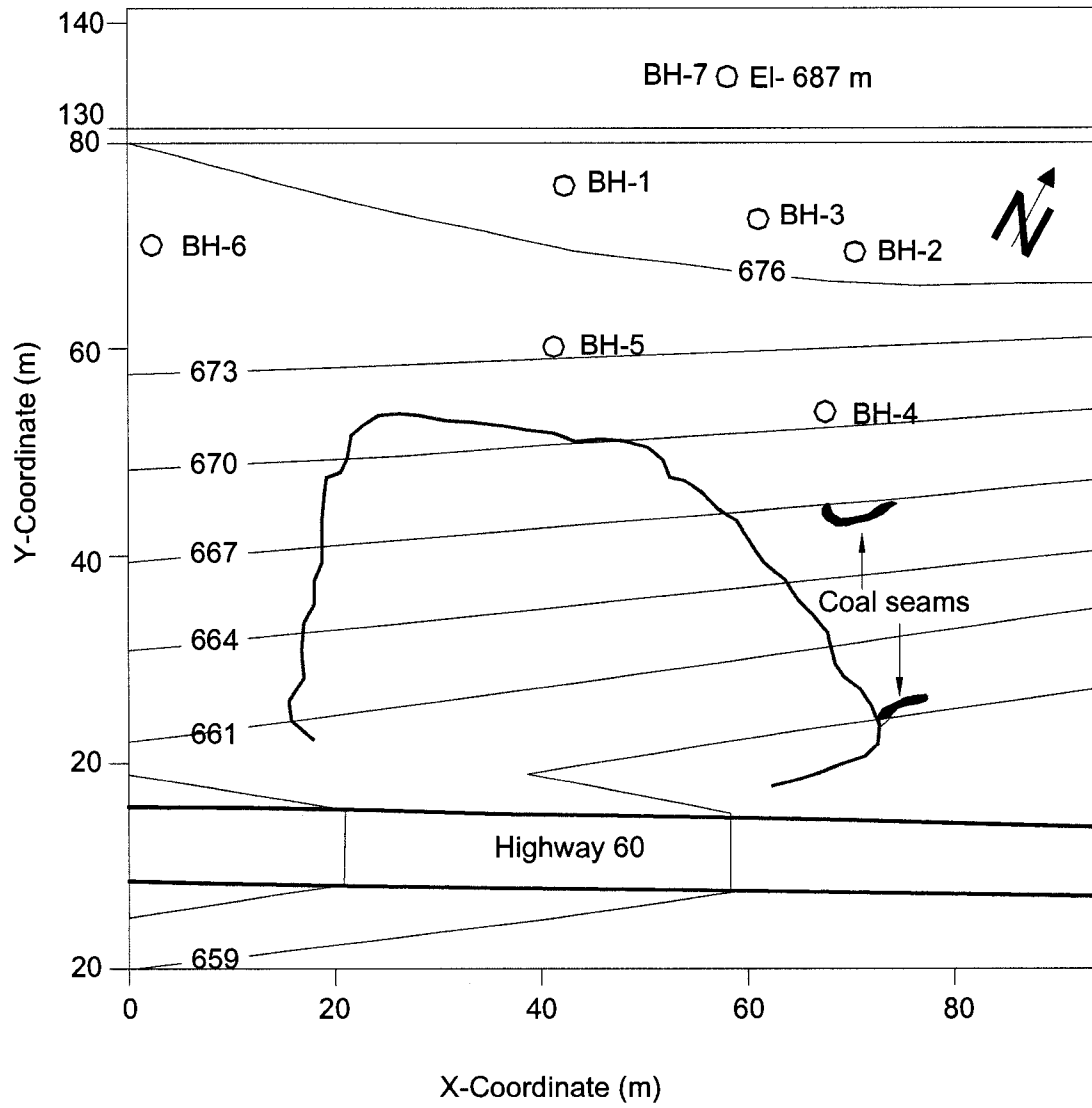


Figure 3-10 Location of the Devon Slide (modified from Eigenbrod and Morgenstern 1971)

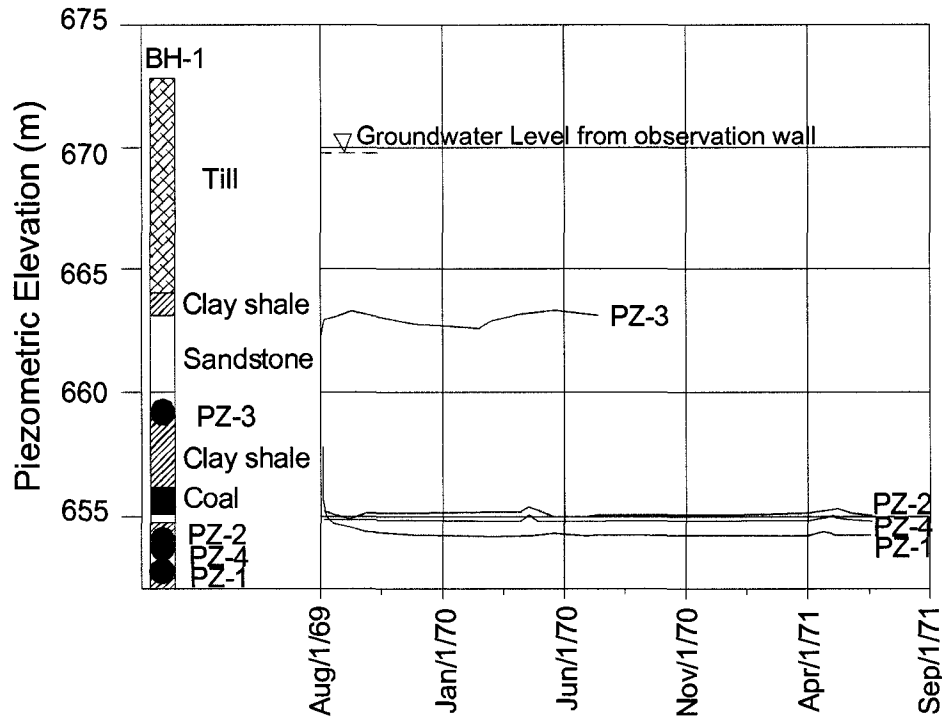


Figure 3-11 Piezometric elevations at the Devon Slide (modified from Eigenbrod and Morgenstern 1971)

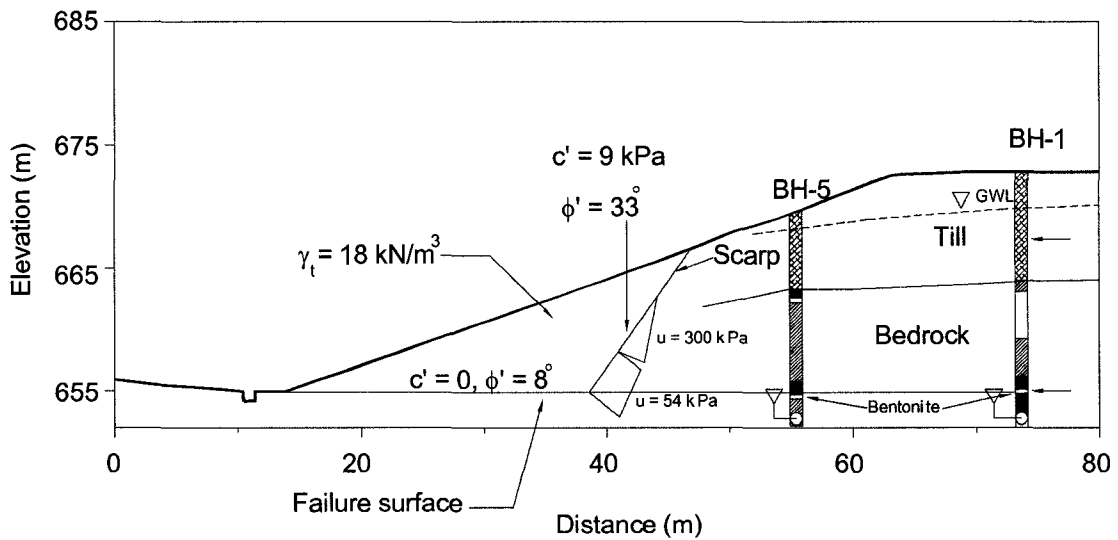


Figure 3-12 Piezometric pressure vs. elevation at the Devon Slide (modified from Eigenbrod and Morgenstern 1971)

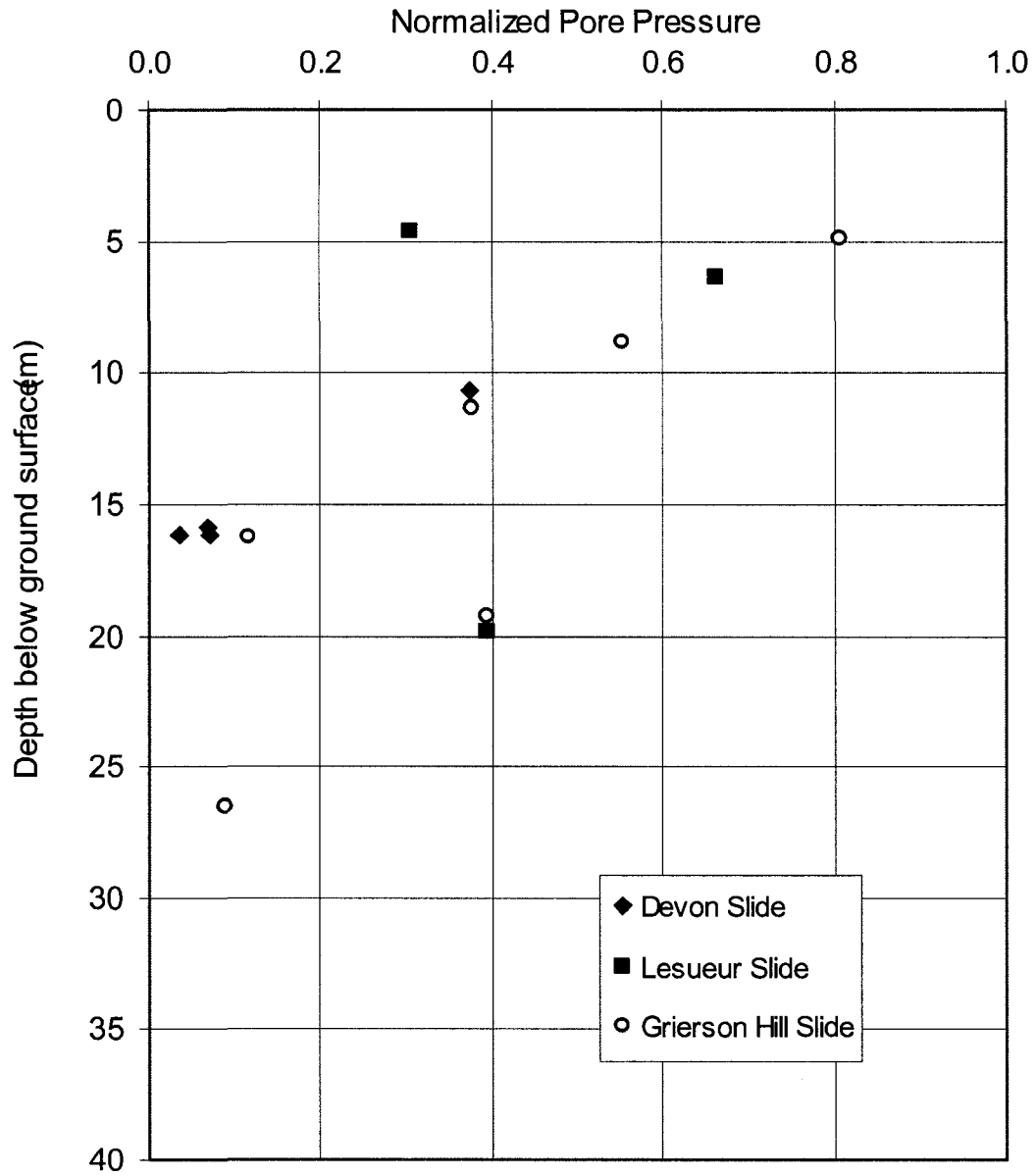


Figure 3-13 Normalized pore pressure plot of Upper Cretaceous bedrock of Edmonton (data from Eigenbrod and Morgenstern 1971; Martin et al. 1984; Thomson 1971b)

CHAPTER 4 Pore pressure measurement in weak rocks

4.1 Introduction

Geotechnical engineering projects usually deals with subsurface materials and geotechnical engineers have to design surface structures with very little information about subsurface data. To supplement the uncertainties, geotechnical engineers usually install different type of instruments in the ground to better understand the subsurface condition. Among the different types of instruments, piezometers are designed to monitor the groundwater and pore pressure condition of the subsurface

In dam and embankment construction, piezometers are usually installed in the fill material to monitor pore pressure response during construction. In landslide studies, piezometers are installed to determine the pore pressure regime around the slide area. Piezometers are also useful in monitoring seepage control measures, drainage systems, and the effects of construction and operation of the project on the groundwater system in the vicinity of the project.

Among the several types of piezometers available for geotechnical engineering projects, most piezometers are designed to measure piezometric head (the positive pore pressure), even though both positive and negative pressures can be found in natural materials. Traditionally, piezometers are installed with the sand filter and bentonite seal. This installation method originated from standpipe piezometers, which require a large intake area to monitor pore pressure changes (Mikkelsen and Green 2003).

The instability near surface bedrock formation in central Alberta is well known and a number of case studies have been reported (Cruden et al. 1998; Morgenstern 1979;

Painter 1965; Pennell 1969; Thomson 1971b; Thomson and Hayley 1975) and the most deficiency in accessing slope stability weak rock is lack of dependable pore pressure measurements. In order to improve the understanding of pore pressure regime in low permeable weak rocks, several pertinent factors involving pore pressure measurements in weak rocks are presented in this chapter. The main focus is given on negative pore pressure measurement and the suitability of grout-in installation in weak rock.

4.2 Pore pressure below the ground surface

Voids in natural soil may be saturated and full of water, or there may be discontinuous and air bubbles present in the water or, the water may be isolated. The water in soil voids below the groundwater level is usually continuous and pore pressure below the groundwater level is usually positive. Soil that lies above the water table is not subject to a positive hydrostatic pressure. But molecular and physico-chemical forces acting at the boundary between soil particles cause water to be drawn up into the empty void spaces. This attraction is known as soil suction. Evaporation from the surface may eventually lower the pore pressure enough for the water in the soil near the surface to partially drain out of the voids. The voids will subsequently be filled by a combination of air and water. The process creates a zone of soil, part of which is saturated and part is unsaturated, and the pore water pressures in this zone will be predominantly negative (Figure 4-1).

4.3 Response of pore pressure due to excavation

When the ground is excavated to form a cut slope, the reduction in effective stress induces negative pore water pressures if the ground remains undrained (Figure 4-2a, b). This change can give the slope a temporary stability in the short term, but this stability can be lost if pore water pressures increase. The time between initial slope formation and failure can range from a few days to many decades. The potential for instability can be assessed by measuring in situ pore water pressures (which could still be negative) and comparing them with expected long-term pore water pressures (Figure 4-2c). The change in pore pressure u caused by the excavation can be

determined from Skempton's (1954) classical equation for pore water pressure change as presented in Section 2.3.2.

Vaughan and Walbancke (1973) presented the field evidence of pore pressure reduction due to excavation from a London Clay cutting located in the Hendon Motorway (M1) at Edgwarbury (Figure 4-3). Negative pore pressure was observed at each of five piezometers installed below the cut slope although the cutting had been completed nine years earlier in 1964 and piezometers were installed in 1973. The piezometers were of the twin-tube hydraulic type developed by A. W. Bishop, with high air-entry ceramic filters (Bishop et al. 1960).

4.4 Pore pressure measuring instruments

For a piezometer to measure correct pore pressure below the ground, it must satisfy two basic criteria (McKenna 1995): (i) The measured pressure must be sufficiently close to the pore-water pressure of the target formation, and (ii) the piezometer must equilibrate to changes in the pore-water pressure of the target formation. Piezometers available in today's market usually satisfy these basic criteria, but, depending on the piezometer types and installation methods, pore pressure response time can vary significantly. Different piezometer types used in current geotechnical practice are discussed here.

4.4.1 Standpipe piezometers

The simplest form of pore pressure measuring device is the observation well which consists of an open ended tube perforated near its base (Figure 4-4 a). The space between tube perforations and the wall of the borehole is normally packed with sand or fine gravel, and the top of the borehole is sealed to prevent the flow of surface water. The depth to the water level is measured by lowering an electronic probe down the open standpipe. The observation well is simple to install, but it cannot measure water pressure at a certain level. Instead it is assumed that a simple groundwater regime exists and there is no upward or downward flow between strata of differing permeability.

To overcome the disadvantage of the observation well, the most common practice is to determine the water pressure over a limited depth by sealing off a section of borehole. This system, known as a standpipe piezometer, consists of a porous tip embedded in sand or gravel at the level of pressure measurement and connected to a plastic tube extended to the ground surface (Figure 4-4 b). The sand filter is sealed above and below with grout, usually with bentonite pellets.

4.4.2 Hydraulic piezometers

The twin-tube hydraulic piezometer was developed for installation in foundations and fills during construction of embankment dams (Dunnicliff 1993). It consists of a porous filter element connected to two plastic tubes, with a Bourdon tube pressure gauge on the end of each tube (Figure 4-5). U-tube manometer or electrical pressure transducers can be used instead of Bourdon tube pressure gauges. The piezometric elevation is determined by combining the average pressure gauge reading with the elevation of the pressure gauges. When both plastic tubes are completely filled with liquid, both pressure gauges will indicate the same pressure. If gas has entered the system through the filter, tubing, or fittings, the gas can be removed by flushing. Dunnicliff (1993) stated that the application for twin-tube hydraulic piezometers is limited to long-term monitoring of pore water pressures in embankment dams and the flushing tubes can not rise significantly above the minimum piezometric elevation since water inside the flushing tubes can not sustain high subatmospheric pressure. If high-quality de-aired water is used, the tubing can only be installed up to 6 m above the minimum piezometric elevation (Dunnicliff 1993). Periodic flushing with de-aired water is needed to remove any gas bubbles that have accumulated.

The trend in recent years has been to move away from hydraulic piezometers, because of the need for a relatively elaborate terminal measuring house, difficulties in measurements caused by air bubbles in the tubes, and the need for considerable skill and care to keep the system operating (Sherard 1981). The major advantages of hydraulic piezometers are the absence of inaccessible moving parts or electrical components and the ability to flush the piezometer cavity. Disadvantages include the need for a terminal enclosure to contain the readout and flushing arrangements; in

addition, the enclosure must be protected from freezing either by heating it or by constructing it below the frost line. Also, the routing of tubing must be planned so that it does not rise significantly above the minimum piezometric elevation; otherwise the liquid will be required to sustain a subatmospheric pressure, and liquid is likely to become discontinuous. Periodic flushing with de-aired water is needed to remove any gas bubbles that have accumulated in the flushing system.

4.4.3 Diaphragm piezometers

4.4.3.1 Pneumatic piezometer

Since 1960, development of diaphragm piezometers has eliminated the need for hydraulic piezometers. In a pneumatic piezometer, a flexible membrane functions as a separator between the water and the gas (nitrogen) used to back-pressure the membrane to counter balance the water pressure acting on it (Figure 4-6). The back pressure is regulated and measured by a read-out unit at the surface. The main advantages of pneumatic piezometers are that they have no long-term drift and they are very reliable. On the other hand, taking measurements is time consuming and automation is difficult, expensive, and unreliable (Dunnicliff 1993). Typically, the amount of water displaced by the diaphragm is very small (<0.002 cc) and the total fluid volume of the tip is low; therefore, the time required for equalization between the groundwater pressure and the air line pressure is very small.

4.4.3.2 Vibrating wire piezometer

In a vibrating wire (VW) piezometer, the diaphragm is attached with a vibrating wire element (Figure 4-7). Fluid pressures acting upon the outer face of the diaphragm cause deflections of the diaphragm and changes in tension and frequency of the vibrating wire. The changing frequency is sensed and transmitted to the readout device by an electrical coil acting through the wall of the capsule. The vibrating wire piezometer is easy to read and very accurate. The amount of water displaced by the diaphragm is very small (<0.001 cc) and response time is good in all soils. Vibrating wire piezometers are also easy to automate and can be used reliably for remote measurements.

4.4.4 Filters

All piezometers include an intake filter which separates the pore fluid from the structure of the soil. The fluid in this cavity connects with the soil pore fluid through the filter and the pressure of the fluid in the cavity is measured. In order to obtain correct pore pressure, the piezometer needs to fulfill the following two requirements:

- The pressure of the fluid in the piezometer cavity is presumed to be equal to the pressure in the soil pore fluid. In partly saturated soils containing two pore fluids at different pressures, equalization with either pore pressure may be possible.
- The pressure in the piezometer cavity must be measured and generally transmitted to some point remote from the point of measurement.

The air entry value of the filter is defined as the pressure differential at which a blow-through of gas or air occurs when the filter is fully saturated. Thus, a filter with a high air entry (HAE) value is a fine filter that will allow a high pressure differential before blow-through occurs. Low air entry (LAE) filters are coarse filters that readily allow passage of both gas and water. A typical LAE filter has a pore diameter of 0.02 to 0.08 mm, and an air entry value range of 3 to 30 kPa. A filter with a pore diameter of 0.05 mm has a permeability to water of about 3×10^{-2} cm/sec.

HAE filters have very fine pores and the surface tension of the water in the pores prevents the entry of air. HAE filters were originally used with hydraulic piezometers to monitor negative pore-water pressures in clay-core dams (Penman 2003). Filters used for this purpose typically have pore diameters of 0.001mm, air entry values of at least 200 kPa, and permeability to water of about 3×10^{-6} cm/sec (Penman 2002). Diaphragm piezometers such as the VW piezometer can be installed with high-air entry filters, but there is no mechanism for saturating the filter insitu after the piezometer installation. The VW piezometer will become ineffective for measuring negative pore pressures if air bubbles accumulate in the piezometer cavity.

Penman (2002) presents comparison of pore pressure response using LAE and HAE filters at Chelmarsh dam where the hydraulic piezometers using two filter types were placed side by side in the fill during construction. The results revealed that the pore

water pressure measured by the piezometer using HAE filter was initially a negative pore pressure of nearly -7 m water head, whereas the piezometer with LAE filter, measuring the pore gas pressure, gave an initial pressure of only about -0.3 m head of water. As the height of the fill above the piezometer increased, both pressures increased. Penman (2002) indicated that if the both piezometers had been installed at a lower level, the two measurements would have become the same when all the gas had been driven into solution.

4.4.5 Piezometric time lag

Hvorslev (1951) reported a method of calculating the response time of a piezometer. His theory assumes that the soil surrounding the piezometer is isotropic, fully saturated and infinite in extent, that no swelling or consolidation occurs, and that there are no hydraulic losses in the piezometer system. The relationship between volume change and pressure change in the piezometer system is assumed to be linear and for unit pressure increase the volume of water entering the system is called the volume factor (V).

Hvorslev (1951) described a hydrostatic time lag as the time required for water to flow to or from the measuring device until a desired degree of pressure equalization is attained. Derivation of the basic equation for determination of the hydrostatic time lag is similar to the equations for a falling-head permeameter and is based on the assumption that Darcy's Law is valid and that water and soil are incompressible. The flow rate, q , is given by Hvorslev (1951):

$$q = FkH \quad [4-1]$$

where,

F = intake factor which depends on the shape and dimensions of the intake

H = nonequalized pressure head

k = formation permeability

K = permeability of the soil

The basic time lag, T_{basic} , is defined as the time required for equalization of the pressure difference when the original rate of flow, $q = FkH$, is maintained.

$$T_{basic} = \frac{V}{q} = \frac{AH}{FkH} = \frac{A}{Fk} \quad [4-2]$$

where,

A = Cross-sectional area of the standpipe or an equivalent area expressing the relationship between volume and pressure changes in diaphragm piezometers

V = Total volume of flow required for equalization

When the groundwater level is constant, the head ratio, H/H_o , is determined by the equation

$$\frac{H}{H_o} = e^{-\frac{t}{T}} \quad [4-3]$$

Where,

t = elapsed time

H_o = total head

H = active head at time t

T = time lag

And the equalization ratio, E , by

$$E = 1 - \frac{H}{H_o} = 1 - e^{-\frac{t}{T}} \quad [4-4]$$

An equalization ratio of 90 % corresponds to 2.3 times the basic time lag and an equalization ratio of 99 % means the time lag is twice as long as it would be for 90 % equalization. The response time of a piezometer is dependent upon the intake factor, F , which is a constant reflecting the size and shape of the piezometer filter intake and the volume factor, V , which is equal to the volume of water which must enter a piezometer system to cause a unit increase in pressure. In general, the response

time of a piezometer is directly proportional to the volume factor and inversely proportional to the intake factor. Hvorslev (1951) presented values of F for a number of forms of intakes as shown in Table 4-1.

Approximate response times for various types of piezometers are shown in Figure 4-9 (Terzaghi and Peck 1967). As shown in the figure, diaphragm piezometers have fast pore pressure response and 90 % pore pressure equalization can be achieved within minutes.

4.5 Grout-in piezometer installation

In situ pore pressure measurements in soil and rock are standard geotechnical engineering practice. Current piezometric installation practice originates from standpipe piezometers which require large intake area to register the pore pressure changes in the surrounding materials (Dunncliff 1988; 1993). Installing a piezometer with a sand pocket and a bentonite seal above it is a laborious process and can be difficult.

Modern diaphragm piezometers require a very small volume of water to activate the sensor diaphragm. Piezometer installation step of sand and bentonite seal placement can be eliminated and diaphragm piezometers can be fully grouted into the borehole (Contreras et al. 2007; McKenna 1995; Mikkelsen and Green 2003). Vaughan (1969) demonstrated that in certain conditions the sand intake zone around the piezometer tip can be omitted and the entire borehole can be grouted, including the piezometer. To be successful in a grout-in installation, the grout must have a permeability value lower than the surrounding material so that it prevents the flow of water through the borehole, similar to the traditional bentonite seal.

Assuming a grout permeability of 10^{-8} cm/sec, times required to achieve 99 % pore pressure equalization for water standpipe and for vibrating wire piezometers for conventional and grout-in installations are presented in Table 4-2. As shown, a 2.5 cm diameter water standpipe with a conventional installation requires 20 months to obtain 99% pore pressure equalization, but only 0.11 and 8.8 seconds are required

for a vibrating wire piezometer with a conventional and grout-in installation, respectively.

4.5.1 Piezometric error due to grout-in installation

With the aid of Darcy's Law, Vaughan (1969; 1973) introduced the applicability of a grout-in piezometer installation. He developed closed-form solutions which showed that the error in the measured pore pressure is significant only when the permeability of the borehole grout is more than two orders of magnitude greater than the permeability of the surrounding ground. These closed-form solution equations were developed for hydrostatic pore water pressure distribution and were a function of the sand pack intake factor. As a result, in order for the fully-grouted method to work, there must be permeability requirements placed on the grout mix used to backfill the borehole.

If the grout is less permeable than the surrounding ground, the fluid flow will be mostly radial between the target formation and the piezometer cavity. If the grout is more permeable than the formation, the formation will largely control the equalization time (Vaughan 1969), but this condition will lead to piezometric errors due to vertical fluid flow along the borehole. This is particularly significant with low permeability materials like stiff clays and weak rocks, where the permeability can be as low as 10^{-10} cm/sec. The piezometric error due to grout-in installation can be defined as the difference in pore pressure between the soil and grout.

$$\varepsilon = u_{\text{soil}} - u_{\text{ground}} \quad [4-5]$$

where,

ε = piezometric error

u_{soil} = pore water pressure at the monitoring point within the soil

u_{grout} = pore water pressure at the monitoring point within the grout

This piezometric error will depend on the grout permeability relative to the surrounding soil permeability. To understand the piezometric error generated in a grout-in installation, a seepage analysis has been conducted to simulate the

seepage around a grout-in piezometer installation. This analysis is used to evaluate the impact of grout permeability on low permeability soil. The seepage model is conducted using SEEP/W software, a computer modeling program developed by Geo-slope International, Calgary, Alberta (Krahn 2004b). SEEP/W uses a finite element technique to simulate flow and pore pressure distribution within porous media.

Figure 4-10 shows a conceptual model developed to simulate the seepage around a piezometer installed using the fully-grouted method. The axisymmetric flow model includes a 7-cm radius cement-bentonite grout column surrounded by soil of constant permeability. The cement-bentonite column is 27.5 m long and the soil layer is 40 m thick with a radius of 40 m. The piezometric error of two points within the soil and the grout located at a distance of 20 m below the ground were selected for comparison. The seepage analyses were performed simulating upward and downward flow using two sets of imposed total head, 10 and 20 m that induce flow under steady-state seepage conditions. This set of boundary conditions corresponds to a one dimensional flow condition in the vertical direction. In all cases, fully saturated conditions are used for all the materials in the model.

Several model runs are made with the permeability ratio $k_{\text{grout}}/k_{\text{soil}}$ varying from 1 to 10^6 . Figure 4-11 shows the results of the seepage simulation in terms of the piezometric error ϵ . It can be seen from Figure 4-11 that the piezometric error is less than 1 m head for a permeability ratio of 100 for downward and upward flows condition with 10 and 20 m total head. The piezometric error increases up to 2 and 3 m head for the permeability ratio of 1000 for 10 and 20 m total head. As the permeability ratio increases to 10^6 , the piezometric error increases up to 3.5 to 5 m head for 10 and 20 m imposed total head, respectively. From the results shown in Figure 4-11 it is apparent that the permeability of the grout can be up to 2 orders of magnitude greater than the surrounding soils without causing significant error. This finding is in good agreement with Vaughan (1969).

4.6 Summary

This chapter reviewed the several factors which control the insitu pore pressure measurement. The current method of piezometer installation originated from standpipe piezometers which require large intake areas to pore pressure changes in the surrounding material. Modern diaphragm piezometers require an infinitely small volume of water to activate the sensor diaphragm and diaphragm piezometers can be fully grouted into the borehole. To understand the piezometric error generated in a grout-in installation, a seepage analysis was conducted to simulate the seepage around a grout-in piezometer installation. The analysis results are in good agreement with previous findings; it was found that the permeability of the grout can be up to 2 orders of magnitude greater than the surrounding soils without causing significant error.

Table 4-1 Intake factor F for different piezometer types (modified from Hvorslev 1951)

Shape of Filter Tip	Intake Factor, F
Cylinder: dia D, length L	$\frac{2\pi L}{2.3 \log_{10} \left[\frac{L}{D} + \sqrt{1 + \left(\frac{L}{D} \right)^2} \right]}$
Sphere: diameter D	$2\pi D$
Flat disc: diameter D	$2.75D$

Table 4-2 Estimated hydrostatic time lag for various piezometer installation

Piezometer Type	Installation Method	Intake Length cm	Intake Diameter cm	Equalization Volume for 100cm head of water	Flow rate for 100 cm head cm ³ /sec	99 % Pressure Equalization Time
2.5 cm Water Standpipe	Conventional	45	15	17671.5	2.E-03	20 months
Vibrating Wire Piezometer	Conventional	30	15	0.0001	4.E-03	0.11 seconds
Vibrating Wire Piezometer	Grout-in	-	0.19	0.0001	5.E-05	8.8 seconds

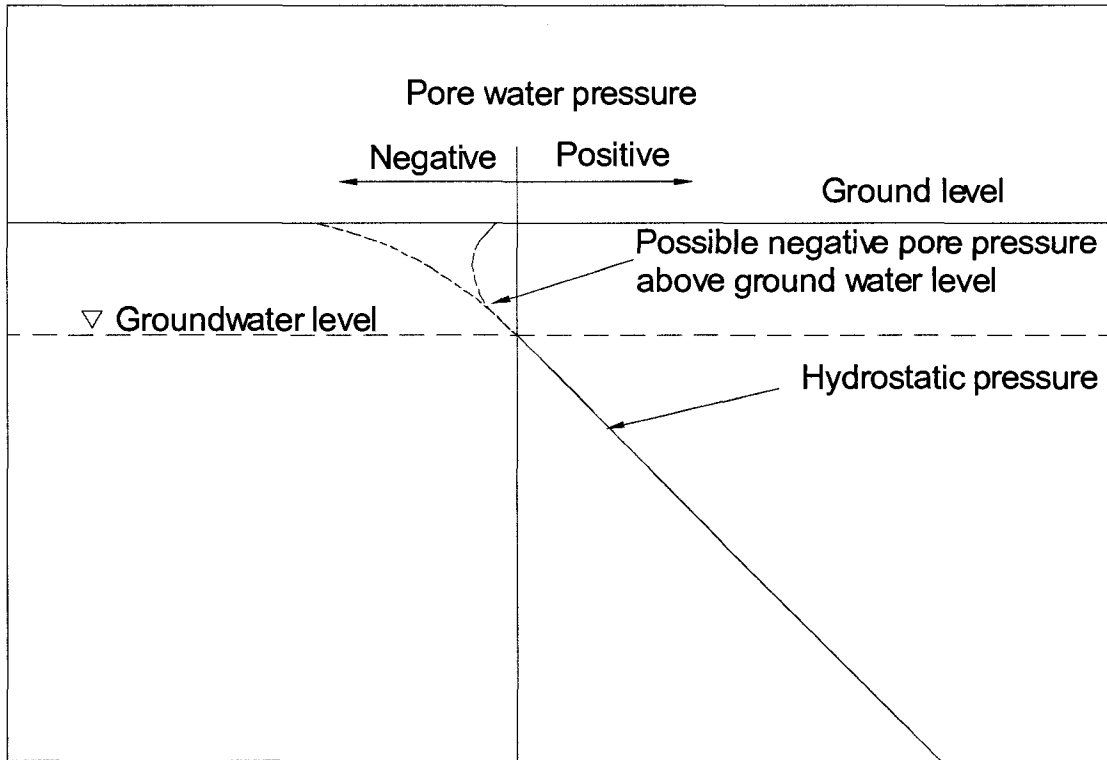
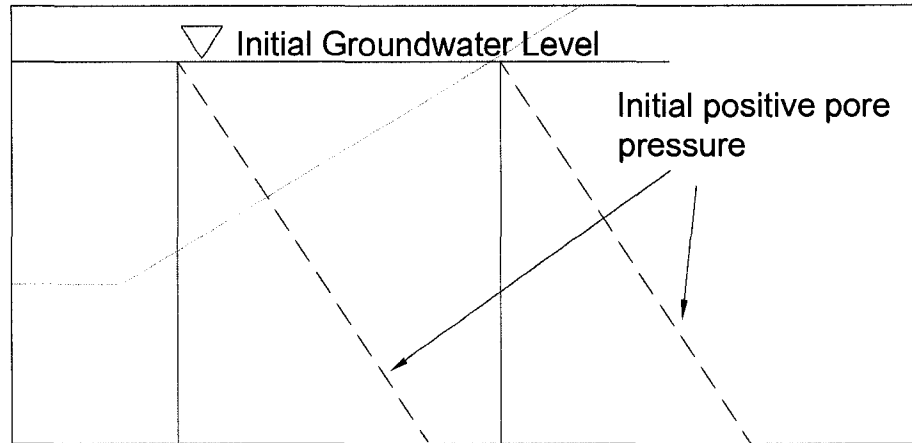
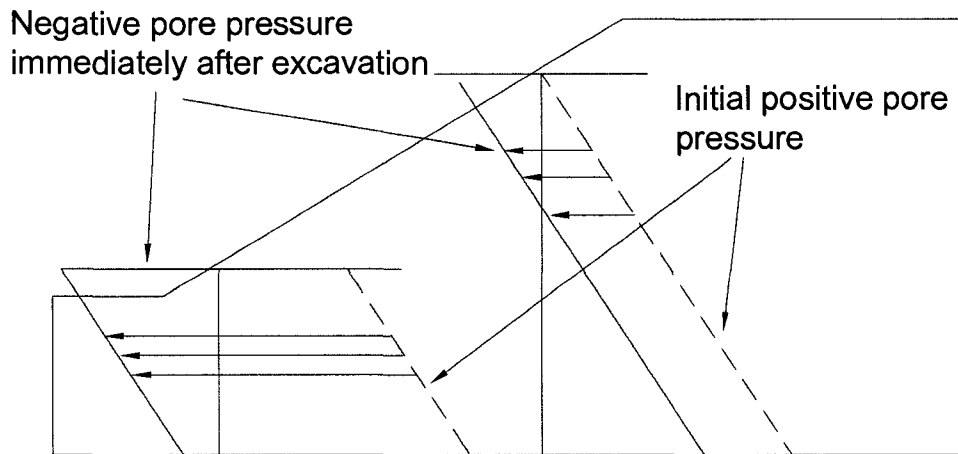


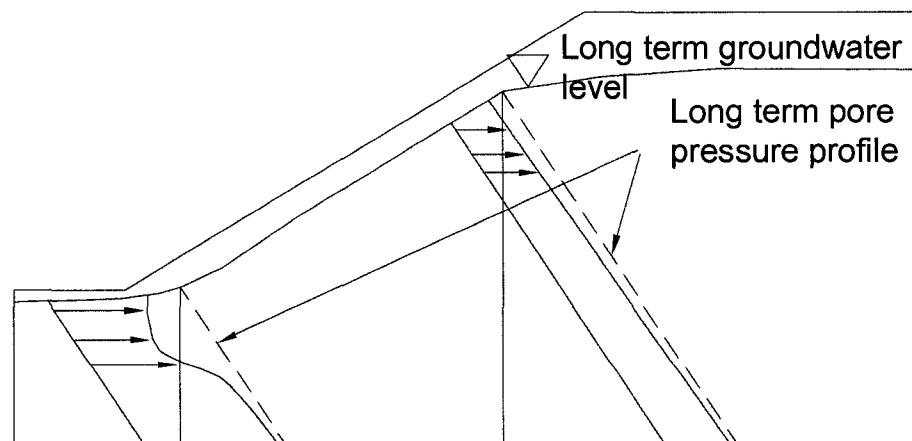
Figure 4-1 Possible pore water pressure profiles above and below the groundwater level (modified from Ridley and Burland 1996)



(a) Pore pressure profile before excavation



(b) Pore pressure profile immediately after excavation



(c) Long term pore pressure profile after excavation

Figure 4-2 Reduction of pore pressure after excavation of slope

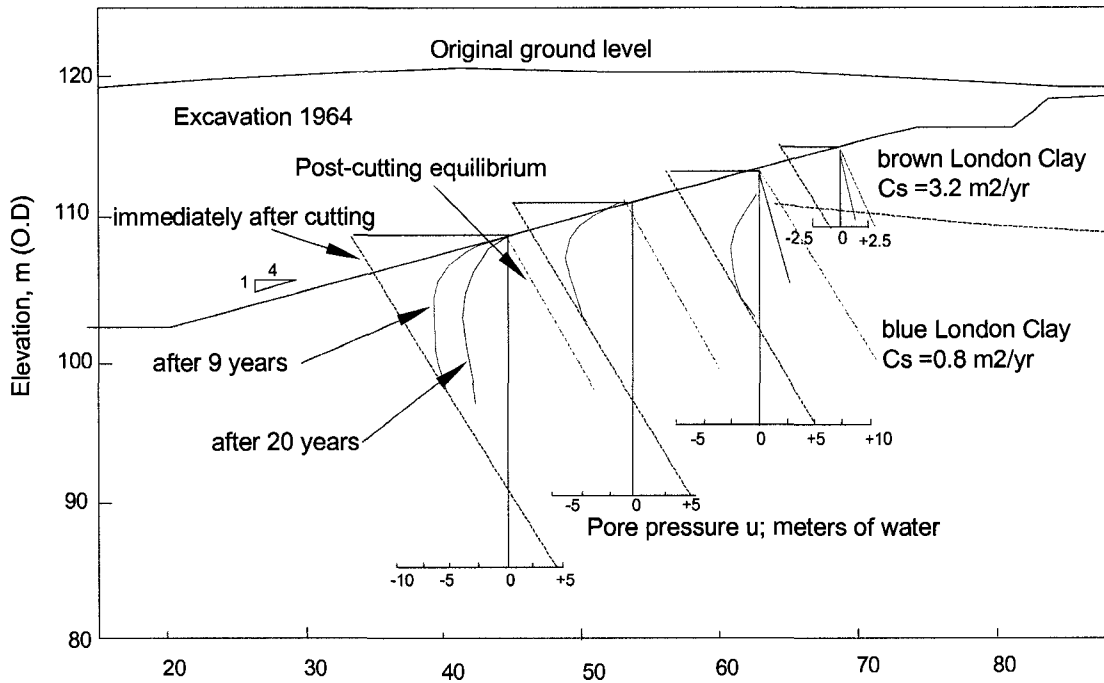


Figure 4-3 Pore pressure in the London Clay cutting at Edgwarebury (modified from Vaughan and Walbancke 1973)

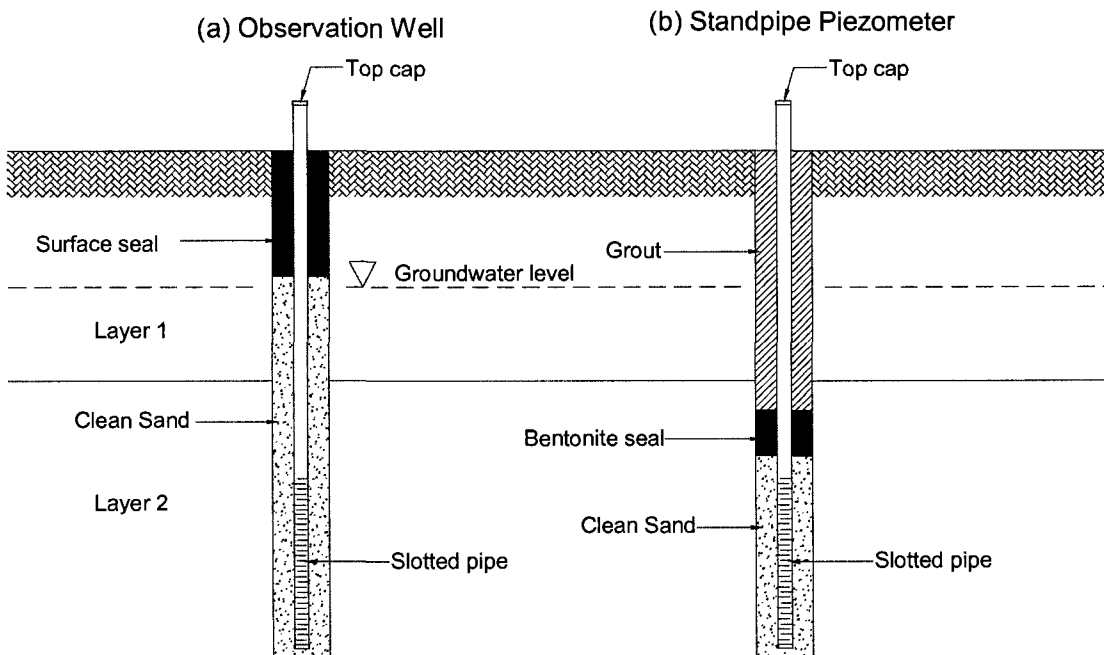


Figure 4-4 Observation well and water standpipes

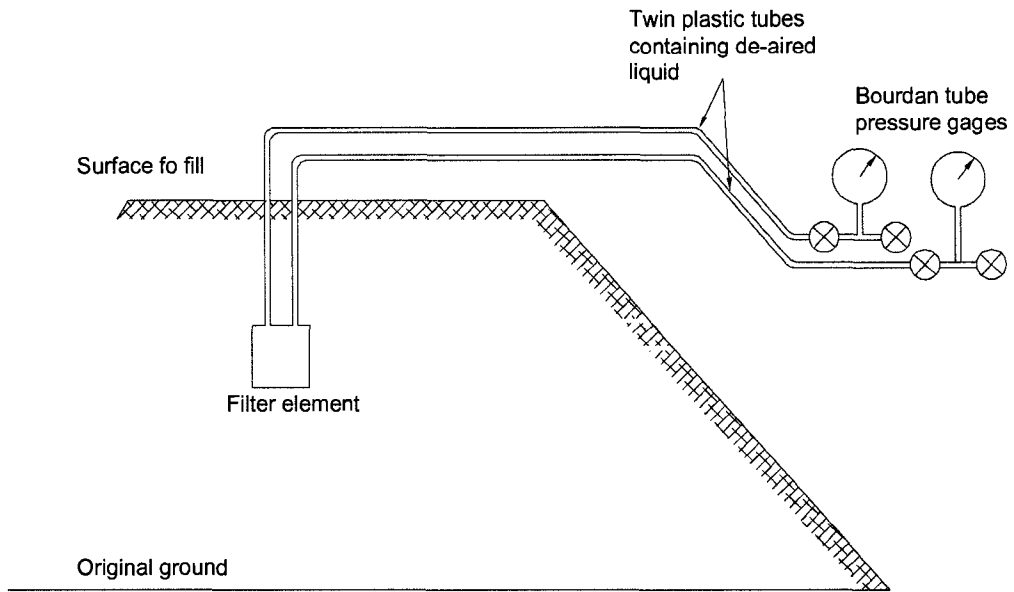


Figure 4-5 Schematic of twin-tube hydraulic piezometer installed in fill (modified from Dunicliff 1993)

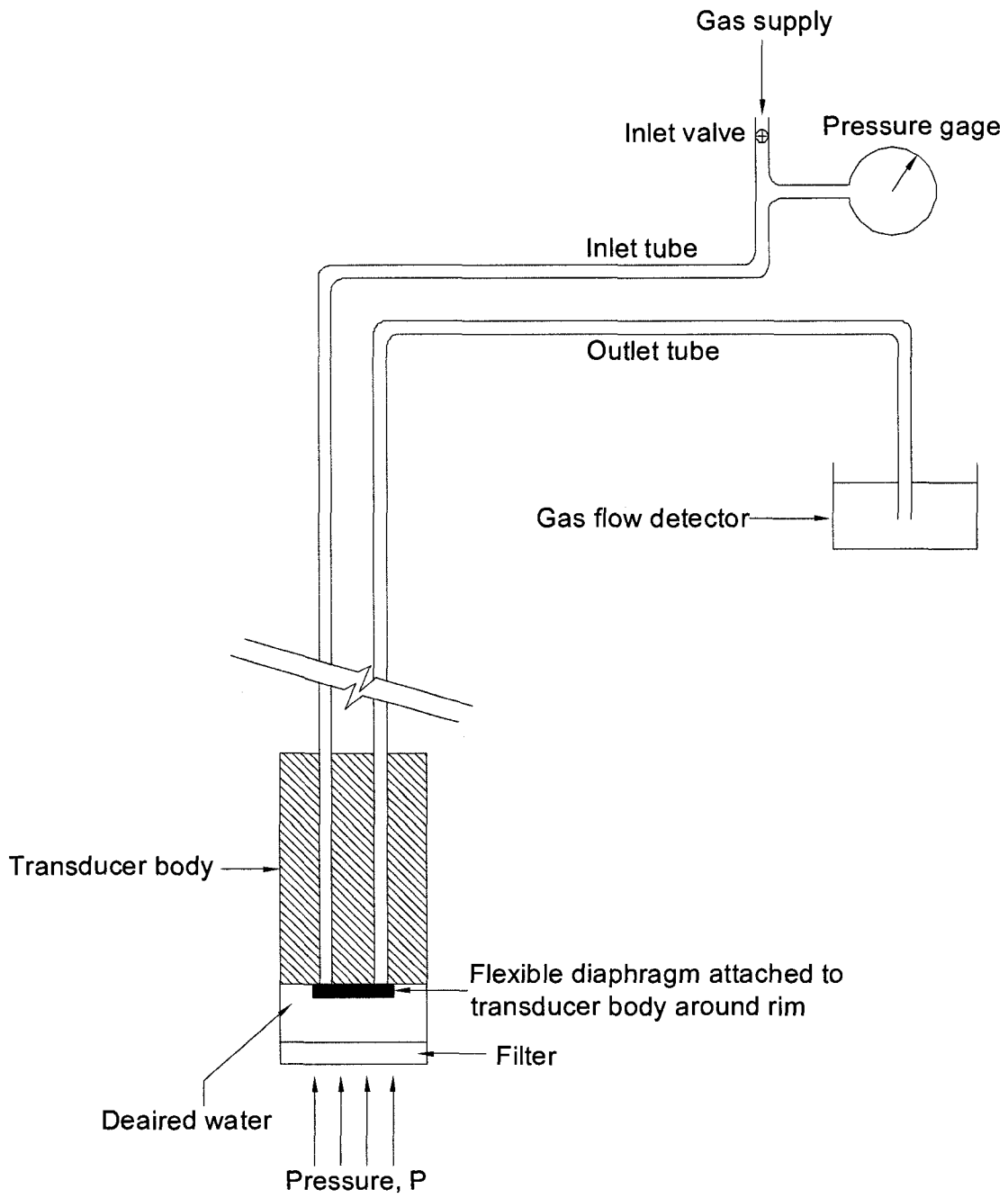


Figure 4-6 Schematic of pneumatic piezometer (modified from Dunnycliff 1993)

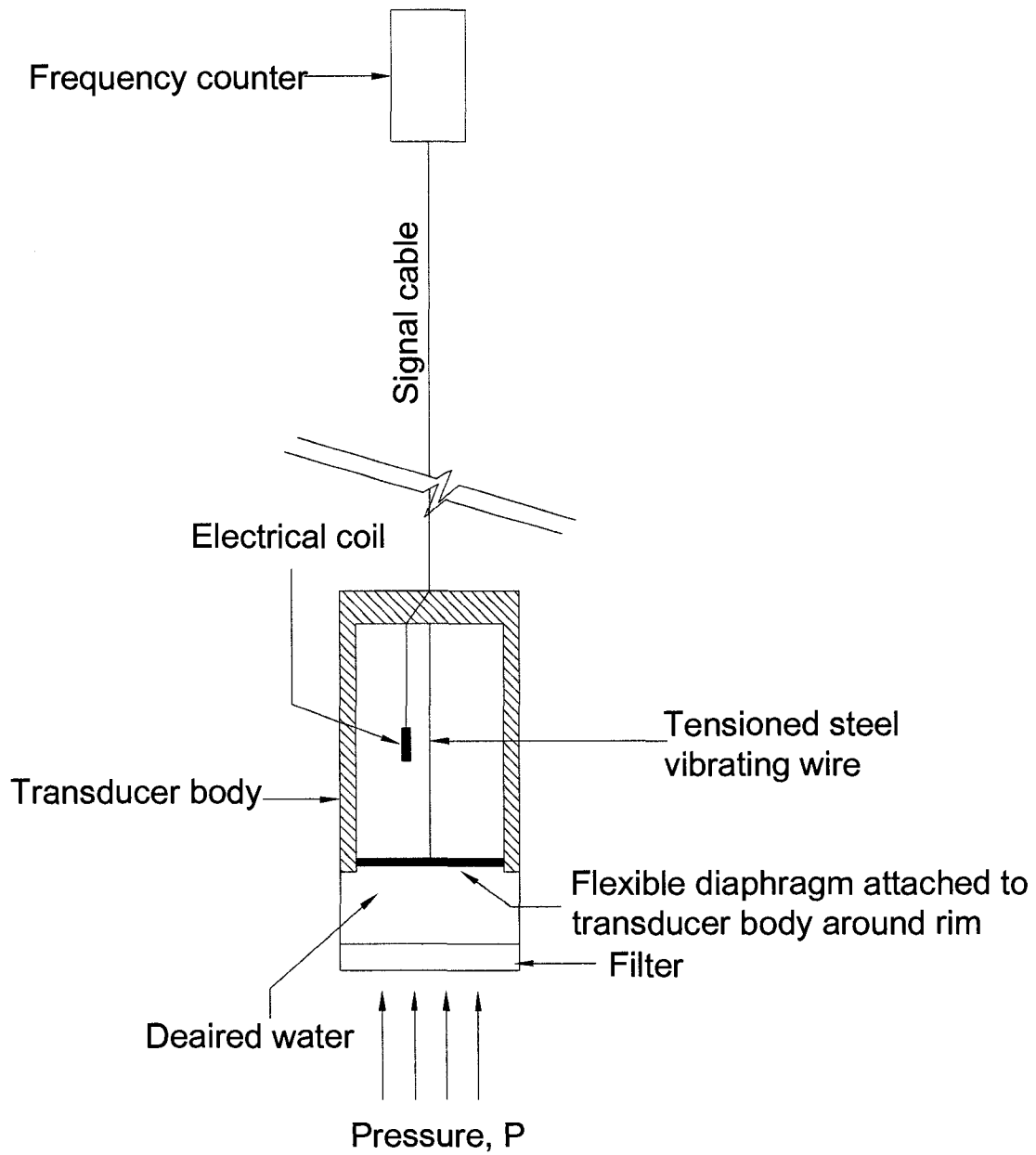


Figure 4-7 Vibrating wire piezometer (modified from Dunnycliff 1993)

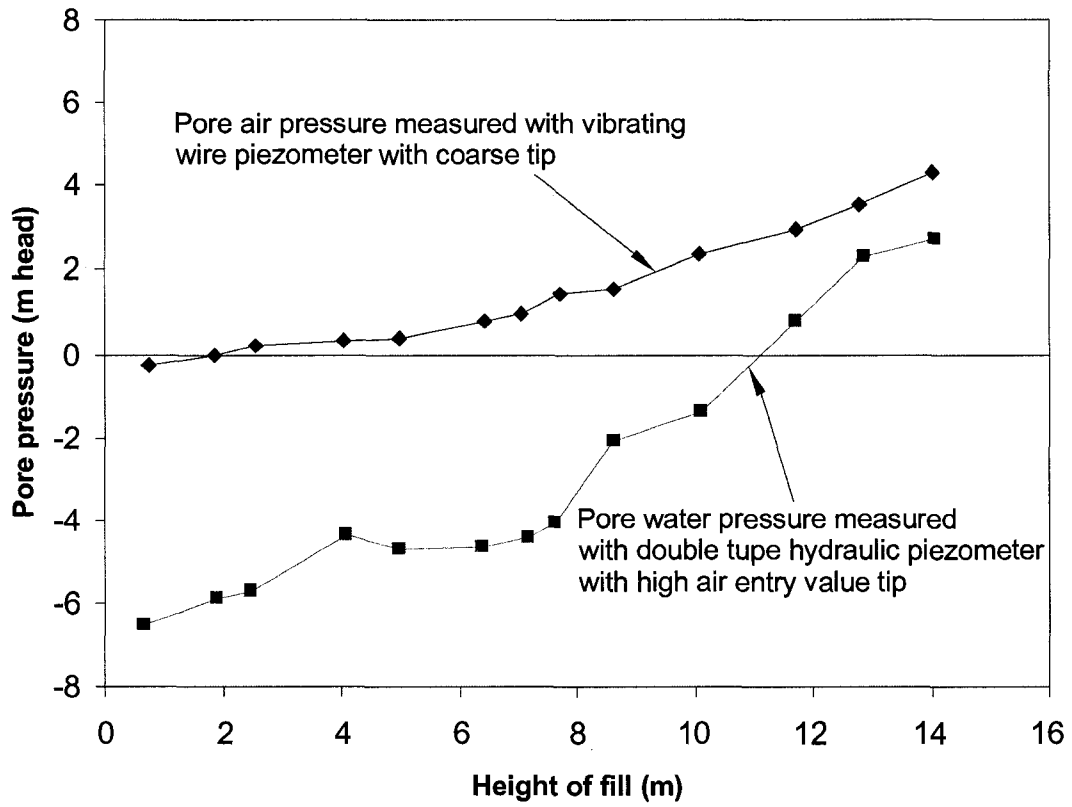


Figure 4-8 Pore pressure response of vibrating wire piezometer and twin-tube hydraulic piezometers at Chelmarsh Dam (modified from Penman 2002)

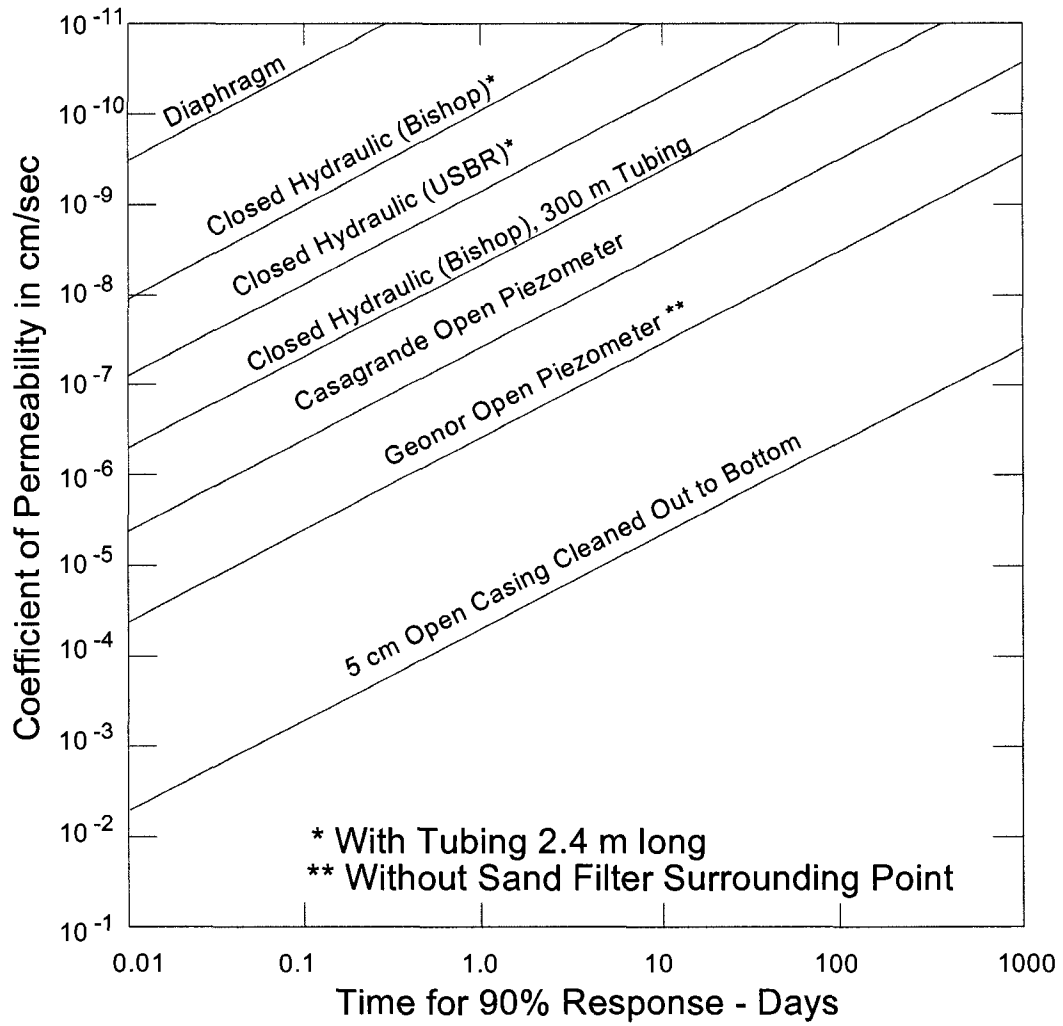
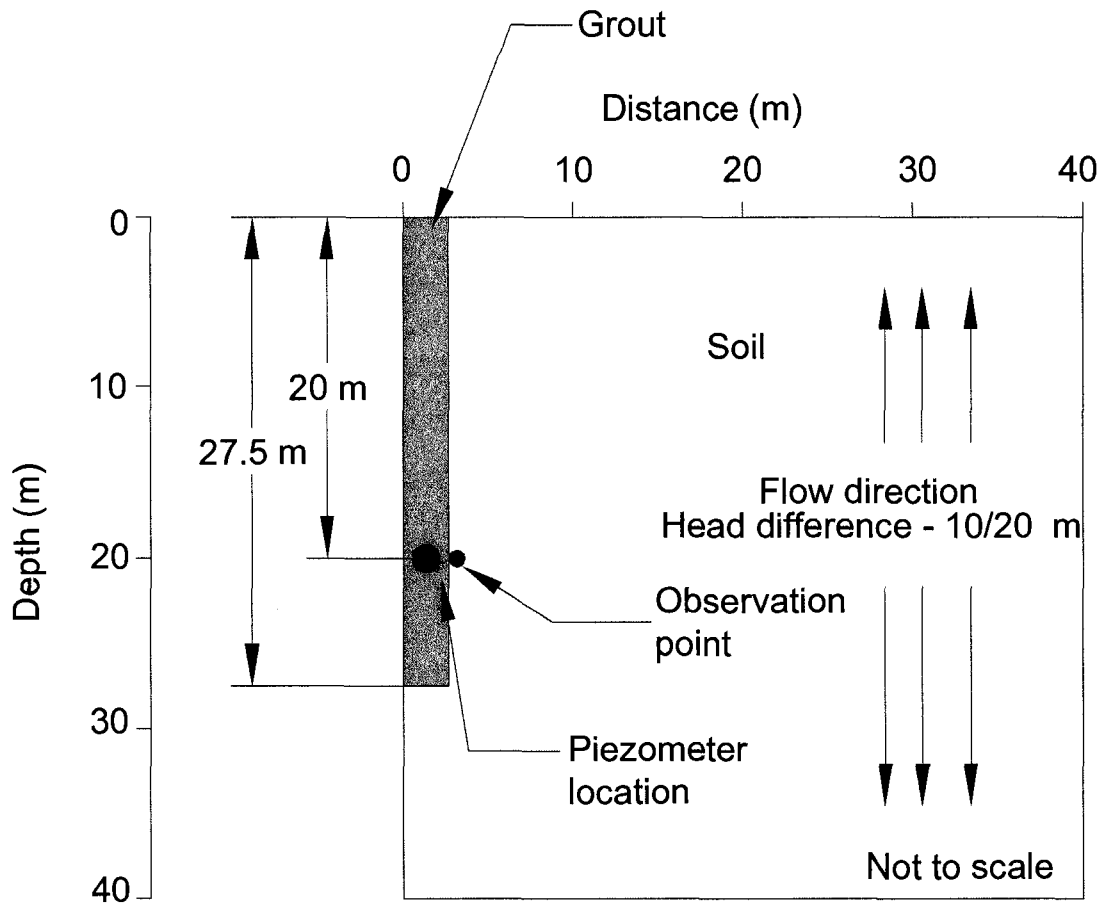


Figure 4-9 Approximate response times for various types of piezometer (modified from Terzaghi and Peck 1967)



Boundary condition

Axisymmetric flow model

Grout radius - 7 cm

Soil layer - 40 m thick, 40 m radius

Flow direction - upward and downward flow

Imposed head - 10 and 20 m

Figure 4-10 Model to simulate grout-in piezometer installation (grout-in hole not to scale)

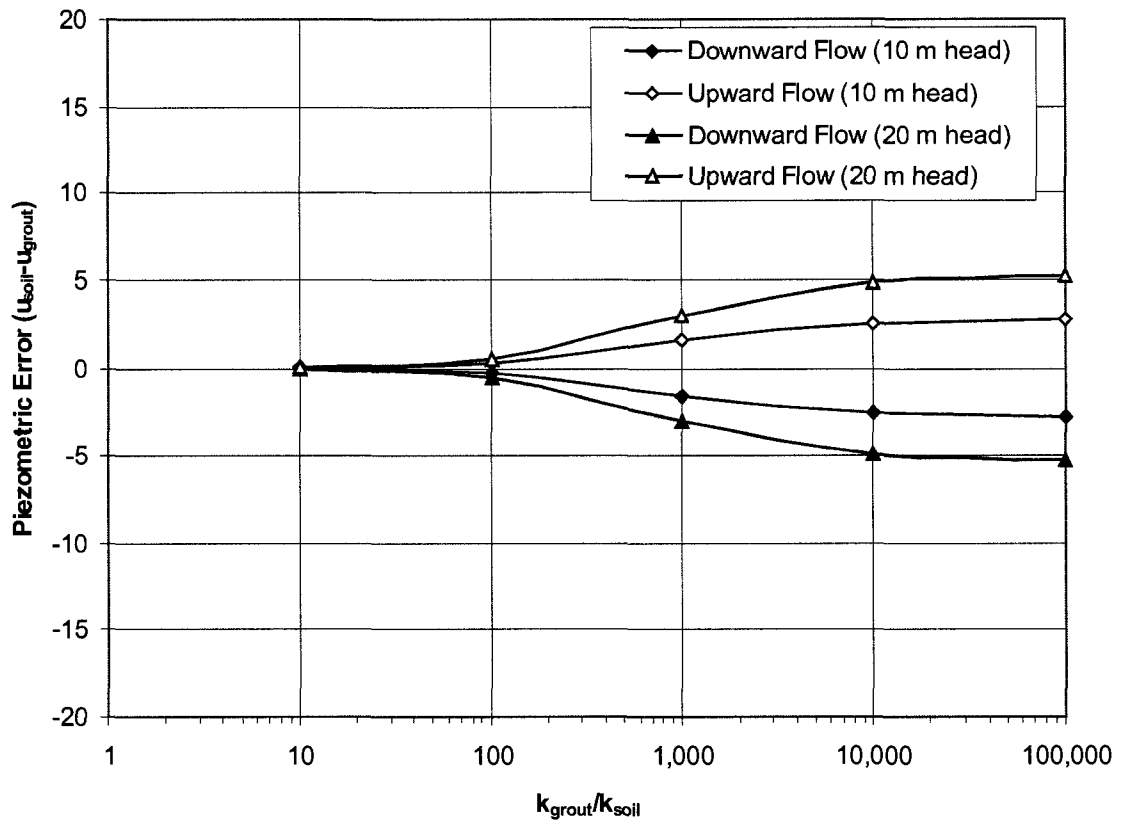


Figure 4-11 Normalized error versus permeability ratio

CHAPTER 5 Laboratory Investigation

5.1 Introduction

In grout-in piezometer installation, the set grout should have a permeability similar to the surrounding material to prevent preferential water flow through the grout (Chapter 4; McKenna 1995; Mikkelsen 2002; Mikkelsen and Green 2003; Vaughan 1969). When set, the cement-bentonite grout is a highly porous solid with a low permeability (10^{-5} to 10^{-7} cm/sec) (Mikkelsen 2002), while bentonite-chip seals used in conventional installations have a laboratory permeability value of about 10^{-9} cm/sec (Filho 1976). Even though the permeability of the set grout is low enough for sandy or silty materials, careful consideration is required for low permeability soil and rock. In weak rock like the Upper Cretaceous bedrock of western Canada the permeability of this rock can be as low as 10^{-9} cm/sec (Koppula and Morgenstern 1984).

To determine the applicability of grout-in installation in weak rock, it is required to determine the engineering properties of the cement-bentonite grout mix. In this study, laboratory tests were conducted to determine the engineering properties of three grout mix ratios. Index tests, unconfined compression tests, and permeability tests were conducted on 7, 14, and 28 day-old grout samples. In-sample pore pressure response tests were also carried out using a small pressure transducer. A large triaxial cell was modified to facilitate the in-sample pore pressure measurement.

5.2 Properties of cement-bentonite grout

5.2.1 Mechanism of cement-bentonite grout mix

Ordinary Portland cement is a heterogeneous substance containing minute tricalcium silicate (C_3S), dicalcium silicate (C_2S), tricalcium aluminate (C_3A), and a solid solution described as tetracalcium aluminoferrite (C_4A) (Lea 1956) as the major strength-producing compounds. In the presence of water, hydration of the cement occurs rapidly. The major hydration (primary cementation) products are hydrated calcium silicates (C_2SH_x , $C_3S_2H_x$), hydrated calcium aluminates (C_3AH_x , C_4AH_x) and hydrated lime ($Ca(OH)_2$). The first two hydration products listed above are the main cementitious products formed. The hydrated lime is deposited as a separate crystalline solid phase. These cement particles bind the adjacent cement grains together during hardening and form a hardened skeleton matrix which encloses unaltered soil particles.

Bentonite is an absorbent aluminium phyllosilicate and is generally an impure clay consisting mostly of montmorillonite, $(Na,Ca)_{0.33}(Al,Mg)_2Si_4O_{10}(OH)_2 \cdot (H_2O)_n$. Two types of bentonite exist: swelling bentonite, also called sodium bentonite, and nonswelling bentonite or calcium bentonite. Bentonite is formed from the weathering of volcanic ash, most often in the presence of water. Sodium bentonites are characterized by high swelling, high liquid limit, and high thermal durability. The vast majority of the montmorillonites are calcium bentonites and are characterized by much lower swelling and liquid limit values compared to natural sodium bentonite. When bentonite powder is immersed in water, the water molecules, aided by the hydration and ionization of the exchangeable cations, enter between the clay plates. While the plates are dispersed in linear-like fashion the bentonite slurry will be fluid. Left to stand, the particles become orientated with negative plates to positive edges, producing thickening and a gel-like structure. When restirred, the slurry becomes fluid. This effect is known as thixotropy and is reversible.

A mix of bentonite and water may not be volumetrically stable, and introducing cement reduces the expansive properties of the bentonite once the cement-bentonite grout initially sets (Mikkelsen 2002). When cement, bentonite, and water are mixed,

the strong bases dissolve the silica and alumina from both the clay minerals and the amorphous materials on the clay particle surfaces in a manner similar to the reaction between a weak acid and a strong base. The hydrous silica and alumina will then gradually react with the calcium ions liberated from the hydrolysis of the cement to form insoluble compounds (secondary cementitious products) which harden when cured. The cementation strength of the primary cementitious products is much larger than that of the secondary products.

The shear strength of bentonite mixed with cement will be higher than that of undisturbed bentonite within one to two hours after the mixing. The rate of the strength increase will depend on the ratio of water and cement. The formation of the primary and secondary cementitious materials inside the grout mix proceeds slowly and continuously for months. It can be expected that the strength of the grout mix will generally increase with time until the completion of the reactions. DJM Research Group (1984) reported that an average value of $2/3$ of the 28 day strength of the grout mix can be achieved at the age of 7 days for all cement contents. As the cement content increases, the permeability of the grout mix decreases (Suzuki 1982). The permeability of the grout mix also decreases with an increasing curing period. This is most probably due to impervious hardened cement hydrates, which hinder the movement of the pore water in the enclosed matrix.

5.3 Laboratory test setup

Laboratory tests were conducted in the Soil Mechanics Laboratory at the University of Alberta, Edmonton. To obtain accurate and reliable data from the laboratory investigation, it is important to use the proper equipment and measuring devices. The laboratory equipment used in the present study is described below.

5.3.1 Load frame

Unconfined compression tests were conducted with a motorized load frame manufactured from Wykeham Farrance Ltd. The load frame is fitted with a multi-speed gearbox, with speed ranging from 0.0001 to 5 mm/min.

5.3.2 Constant pressure system

The required cell pressure and back pressure for permeability tests are obtained from a constant pressure system utilizing an air compressor to generate pressure. With the help of a pressure regulator, constant air pressure is supplied to distribution lines. Using a pressure regulator and a pressure reservoir, the required pressure can be obtained for the tests. This system can supply a maximum pressure of 1000 kPa. The setup of a constant pressure system is presented in Figure 5-1.

5.3.3 Measurement devices

The measuring devices used in the present study consist of load cell, displacement transducers (LVDT), pressure transducers, and volume change meters. These devices are checked and calibrated prior to testing.

5.3.4 Data acquisition system

Advances in electronics have helped in testing and data collection. For the present study, data were collected using Data Dolphin data logger and software. During the test, data are stored on an erasable memory chip inside the data logger. Data collecting, programming, and viewing can be conducted with the Data Dolphin software which allows one to view the current status, set up the logger, and generate graphs. One can also export data to other programs for more detailed analysis and presentation. Figure 5-2 shows the data logging and measurement system used in the present laboratory investigation.

5.3.5 Calibration of instruments

Instruments are calibrated by determining the relationship between an observed reading and the physical quantity being measured. The correct and accurate

calibration of instruments is essential for obtaining reliable data during the laboratory investigation.

5.3.5.1 Strain gauge pressure transducers

The strain gauge pressure transducer (1034 kPa) was calibrated with a hydraulic loader and a Data Dolphin data logger. The following procedure was utilized in pressure transducer calibration.

- Power up the transducer by connection to the data logger,
- Record the zero output and input voltages,
- Assemble the transducer in the hydraulic loader,
- Cycle the transducer to its capacity and back several times,
- Incrementally load and unload the transducer to capacity, taking readings of pressure and output voltage.

5.3.5.2 Displacement transducer - Linear variable differential transformer (LVDT)

Displacement transducers (LVDT) were calibrated against a micrometer. The calibration procedure was as follows.

- Power up the displacement transducer by connecting to the data logger,
- Manually move the shaft and observe the output cycles,
- Starting at one extreme, incrementally move the shaft toward the opposite limit,
- Record the micrometer readings and output voltages at each increment.

5.3.5.3 Volume change meter (LVDT DC type)

The volume change measuring device, 100 cc capacity and 0.01 cc resolution, is comprised of a piston connected to a linear transducer and sealed against a precision-machined calibration chamber so that the linear movement of the piston is exactly proportional to the volume of water in the calibration chamber. The device includes a panel with a reversing valve system to measure the water flow in both directions. The calibration procedure was as follows.

- Power up the volume change device by connecting the linear transducer to the data logger,
- Connect the water pressure line to one of the cell pressure lines,
- Starting at one extreme, allow the water to flow the volume change device and record the output voltages and water volume (from graduated burette).

5.3.5.4 Load cell for unconfined compression tests

The load cell for unconfined compression test was calibrated against a hydraulic loading system gauge. The calibration procedure was as follows.

- Power up the load cell by connecting to the data logger,
- Assemble the load cell in the load frame and balance the arm,
- Record the input and output voltage readings (correspond to zero applied force),
- Incrementally load the transducer to capacity. Record load and output voltage at each increment,
- Continue reading during the unloading process.

5.4 Cement-bentonite grout mix

The main purpose of this study was to determine the optimum grout ratios for grout-in piezometer installation in low-permeability, weak rocks. For that, it is required to conduct strength and permeability tests on several grout mix ratios. At present there are not a well defined grout mix ratios for grout-in piezometer installations in different soil and rock types. McKenna (1995) utilized water:cement:bentonite in a ratio by weight of 1.25:1:0.03 for grout-in piezometer installation at the Syncrude Canada Ltd. oil sands mine site in Fort McMurray, Alberta. Mikkelsen (2002) recommended two grout mix weight ratios of water:cement:bentonite for geotechnical instrument installation: (i) 6.6:1:0.4 for soft soils and (ii) 2.5:1:0.3 for hard soils. The permeability of set grout varied depending on the grout mix ratio and can be ranged from 10^{-5} to 10^{-8} cm/sec (Contreras et al. 2007; Mikkelsen 2002). The range of permeability values for the cement bentonite grout mix is presented in Table 5-1.

Three grout mix ratios were selected for the present investigation. General-purpose Portland cement Type GU and sodium base bentonite powder were used for the grout mix. Each batch of the mix was prepared as follows:

- The required amount of water, cement, and bentonite were determined and weighted with a scale.
- Mixing was done by a standard mixer.
- Water and bentonite were mixed until the bentonite was completely dissolved without lumps.
- The required amount of cement was then added to the mixer and mixed until the cement and bentonite were completely dissolved without any lumps.
- After mixing, the grout mix was poured into a PVC cylindrical mould (75 mm diameter x 180 mm height) and stored in a moisture and temperature controlled room.

The summary of 3 grout mix ratios (water:cement:bentonite by weight) together with laboratory tests conducted are presented in Table 5-2.

5.5 Unconfined compression tests

In an unconfined compression test, a cylindrical specimen is subjected to a steadily increasing axial load until failure occurs. No drainage of pore water from the specimen is permitted during the axial loading. The unconfined compressive strength q_u is defined as the maximum unit axial compressive stress at failure or at 15 % strain. This test is applicable only to coherent materials such as saturated clays or cemented soils that retain intrinsic strength when removed from confining pressure. The current investigation is carried out in accordance with ASTM D2166 (2004), a standard test method for unconfined compressive strength of cohesive soils.

5.5.1 Testing procedure

Unconfined compression tests were carried out on 7, 14, and 28 day-old grout samples. The following procedure was utilized for the unconfined compression testing of the grout mix samples.

- On the day of the test, the grout sample was removed from the curing room and the sample was extruded from the PVC mould by cutting side of the mould.
- The extruded sample was checked for any defects that might have developed during the extrusion process.
- Using a sharp knife, the sample was trimmed to obtain approximately 75 mm in diameter and 150 mm in height. Care was taken to achieve smooth and flat surfaces for top and bottom ends of the sample.
- The initial sample diameter, height, and weight were measured before the test.
- The grout sample was then placed on a loading frame together with top and bottom loading caps.
- The load cell and the displacement transducers were adjusted for proper position and their cables were connected to the data logger.
- Tests were conducted using a constant displacement rate of 0.4 mm/min.
- After the test, the mode of failure was sketched and recorded.
- A portion of the sample was used for water content determination.

A photograph of the unconfined compression test conducted on a grout sample is presented in Figure 5-3.

5.6 Permeability tests

Constant head permeability tests were conducted on 14 and 28 day-old grout samples in accordance with ASTM Standard D5084 (2004), a standard test for measurement of hydraulic conductivity of saturated porous materials using a flexible wall permeameter. A large triaxial cell apparatus was utilized for the permeability test on grout samples. The specimen proportions in terms of height to diameter ratio could range from 1:1 to 2:1 (Head 1992). During the test, the specimen is subjected to known conditions of effective stress under the application of an applied back pressure, and a constant hydraulic gradient is applied across it. The coefficient of permeability k is determined by measuring the volume of water passing through the specimen over a given time.

5.6.1 Test equipment

The permeability test apparatus included a triaxial cell, a pore pressure system, and a volume change measuring device. Instead of two pressure systems in a normal triaxial test, an additional constant pressure system is required to supply a second back pressure. One constant pressure system is connected to the base of the specimen, one to the top, and a third to apply cell confining pressure. The arrangement of the triaxial cell and the layout of the system are shown in Figure 5-4.

5.6.2 Testing Procedure

On the day of the test, the grout sample was removed from the curing room and the sample was extruded from the PVC mould. Care was taken not to damage the grout sample. The top and bottom of the sample were trimmed to obtain a sample size of 75 mm in diameter and 75 mm in height. Then the initial dimension of the grout sample was measured and weighed before the sample was set up in the permeability cell. The following procedures were utilized for permeability testing:

- The grout sample was trimmed to the desired dimension and weighed.
- The pressure lines at the cell base were flushed with deaired water to remove entrapped air bubbles.
- A saturated porous stone was placed on the pedestal with a filter paper at the top.
- The grout sample was then placed on top of the porous stone.
- The filter paper, top porous stone, and top loading cap were placed on top of the grout sample.
- The grout sample was covered with a rubber membrane and sealed with O-rings on the top cap and the pedestal.
- After connecting the back pressure lines on the top cap and the cell base, the triaxial cell was placed on the cell base and filled with deaired water.

5.6.2.1 Saturation

During the triaxial testing, the commonly used procedure for assessing the degree of saturation in the sample and apparatus is summarized by Bishop and Henkel (1962) and Head (1992). The procedure involves shutting off the drainage line to the sample, then applying increments of isotropic confining pressure σ_c and measuring the undrained pore pressure increase with each increment of the confining pressure. The ratio of the pore pressure increase to the confining pressure increment is known as B value. The following steps were followed to compute the B parameter.

1. Before applying the increments of confining pressure, initial readings of confining pressure, back pressure, and pore pressure were recorded.
2. With the pore pressure fluid drainage closed, a 50 kPa increment of isotropic confining pressure was applied.
3. The pore pressure response of the sample was measured, and B value was calculated as a ratio of the resulting increase in the pore pressure to the cell pressure increment.
4. The pressure in the back-pressure system was increased. A pressure difference of 10 kPa between the confining pressure and the back pressure was maintained during the saturation process. This process was repeated until the samples achieved B values of 0.95 to 0.97.
5. With the new back pressure level, Steps 2, 3, and 4 were repeated. These incremental B values were conducted for at least three pressure levels to ensure that the pore pressure response had stabilized.
6. For the soft grout sample (grout mix A), the required saturation was achieved around 400 kPa cell pressure. A higher cell pressure, around 450 to 500 kPa, was required for the hard grout samples (grout mixes B and C) to achieve the required degree of saturation.

5.6.2.2 Consolidation

After the saturation, the specimen was consolidated under an equal all-round pressure. During consolidation, drainage of the excess pore pressure took place from the upper and bottom ends of the sample. The drainage of pore water resulted in a decrease in volume and increase in the effective stress, which after

consolidation was equal to the difference between the confining pressure and the pore pressure remaining in the sample. The consolidation of a sample can be judged at any time from the pore pressure dissipation U , expressed as follows:

$$U = \frac{u_o - u}{u_o - u_b} \times 100\% \quad [5-1]$$

where

u_o = initial pore pressure immediately before consolidation,

u_b = back pressure, which is a constant during the consolidation, and

u = measured pore pressure at the base.

5.6.2.3 Permeability testing

After the sample obtained the required consolidation, permeability tests were conducted on the grout sample. The following steps were taken during the permeability test.

- Once the required degree of saturation was achieved, the back pressure was reduced 10 to 15 kPa below the cell pressure to allow the sample to consolidate before the permeability test.
- A pressure difference of 10 to 15 kPa was maintained for the cell pressure and the maximum back pressure.
- To initiate flow through the sample, back pressure at the top was reduced while back pressure at the bottom was kept constant, thus creating a hydraulic gradient.
- When steady flow was observed from the in-flow and out-flow volume change meters, the readings were recorded for the permeability calculation.
- The permeability tests were conducted at several hydraulic gradients, ranging from 15 to 20.

The permeability of grout samples can be calculated from the plot of cumulative flow against time. From the linear portion of the graph, the flow rate can be obtained and the permeability k of the grout sample is calculated using following equation:

$$k = \frac{q}{Ai} \quad [5-2]$$

where

A = cross sectional area of the grout sample (cm²),

i = the hydraulic gradient across the sample,

q = flow rate (cc/sec), and

k = the permeability (cm/sec).

5.7 Laboratory test results

5.7.1 Unconfined compression tests

Nine unconfined compression tests were conducted on 7, 14, and 28 day-old grout samples. The results showed that the strength of the set grout mixes increase with curing time and cement content.

The unconfined compression test results of grout mix A are presented in Figure 5-5. The unconfined compressive strengths of 15, 30, and 70 kPa are achieved from 7, 14, and 28 day-old grout samples, respectively. All samples achieved peak strength around 1 % strain. After achieving peak strength, no significant decrease in strength was observed from 7 and 14 day-old samples, but some decrease in strength was observed in 28 day-old grout samples.

The unconfined compressive test results of grout mix B are presented in Figure 5-6. Unconfined compressive strengths of 260, 370, and 510 kPa were achieved for 7, 14, and 28 day-old grout samples, respectively. All samples achieved peak strength around 0.8 % strain and the strength decreased significantly after reaching peak strength, indicating the brittle nature of the grout samples.

The unconfined compressive test results of grout mix C are presented in Figure 5-7. The unconfined compressive strengths of 390, 510, and 1120 kPa were achieved for 7, 14, and 28 day-old grout samples, respectively. The 7 day-old grout sample achieved peak strength at around 1.0 % strain. The 14 and 28 day-old grout samples

achieved peak strengths at around 0.7 to 0.8 % strains. Grout mix C also showed significant strength reduction after peak strength, indicating brittle behaviour.

Figure 5-8 summarizes the results of the unconfined compressive strength of 7, 14, and 28 day-old grout samples for different water:cement ratios. The figure shows that the unconfined compressive strength decreases with an increase in water:cement ratio. The unconfined compressive strength of 28 day-old grout is approximately 1170 kPa at a water:cement ratio of 2:1, then decreases to approximately 80 kPa with a water:cement ratio of 6.6:1. The strength increase is more pronounced in grout mix samples with lower water:cement ratios. The unconfined compressive strength of grout mix C increased from 380 kPa in 7 days to 1170 kPa after 28 days curing time.

5.7.2 Permeability test

Six permeability tests were performed on grout samples. For grout mix A, a hydraulic gradient of 15 was required to get steady flow through the sample. For grout mixes B and C, a hydraulic gradient of 20 was required to obtain steady flow through the sample. The permeability test results of 14 and 28 day-old grout samples are presented in Figure 5-9. As shown, the permeability of the grout mix decreases with a decreasing water:cement ratio and with increasing curing time. The range of permeability values obtained from the three grout mix samples are presented in Table 5-3.

5.7.3 Discussion

Both unconfined compression tests and permeability tests on grout samples revealed important engineering properties for different grout mix ratios. The water content, unit weight, and void ratio of the different grout mix ratios are presented in Table 5-4. Void ratio is calculated from the average specific gravities of cement and bentonite, 3.15 and 2.4, respectively.

Grout mix C, with a water:cement;bentonite ratio of 2:1:0.3, achieved the highest strength and lowest permeability. An unconfined compressive strength of 1170 kPa was achieved from 28 day-old grout mix C. To compare the current study with previous studies, the unconfined compressive strength of 28 day-old grout samples is plotted with data obtained from other studies (Mikkelsen 2002), as shown in Figure 5-10. The results obtained from the current study are in good agreement with previous studies.

Figure 5-11 shows the variation in permeability with void ratio. The data indicate that a lower void ratio typically exhibits lower permeability while a higher void ratio exhibits higher permeability; this is common for most soil types. Within the grout mixes, the cement has a greater influence on the void ratio than the bentonite and can be considered as the controlling factor in the permeability of the grout. The difference between 14 and 28 day-old grout permeabilities is relatively small, as shown in Figure 5-11. The permeability value of grout mix C is within a range that could be used for grout-in installation in weak rock (within two orders of magnitude difference). Thus, grout mix C was selected for use in field grout-in piezometer installations.

5.8 Pore pressure response test of grout and clay shale samples

In order for grout-in installation to be successful, the piezometer inside the grout must be able to measure the pore pressure changes in the surrounding weak rock. To determine the pore pressure response of grout mix and the weak rock, it was decided to conduct pore pressure response tests on grout and bedrock samples. In conventional triaxial tests, pore pressure is measured at the base of the specimen, through the cell base. For tests on low permeability material like clay shale, pore pressure inside the specimen may not be uniform and the pore pressure at the center of the specimen may not be same as that at the base where the measurement is usually taken. To get a true pore pressure response, pore pressure measurement should be conducted inside the specimen.

In-sample pore pressure response tests were carried out using a small pressure transducer. A large triaxial cell was modified to facilitate the in-sample pore pressure measurement. For the grout sample, grout mix C with a water:cement: bentonite weight ratio of 2:1:0.3 was used. For the bedrock samples, clay shale samples obtained during the Keillor Road landslide investigation (Chapter 7) were utilized.

5.9 Testing Apparatus

To facilitate in-sample pore pressure measurement, a suitable testing apparatus is needed. A large triaxial apparatus was modified to facilitate the placement of a small pressure transducer inside the sample. This apparatus has the capability to continuously measure the in-sample pore pressure with response to the cell pressure changes. The pore pressure measuring system includes following components:

- A modified large triaxial cell,
- A reaction frame, and
- A small pressure transducer.

5.9.1 Modified large triaxial cell

The modified large triaxial cell comprises a cell body, cell base, pedestal, and loading caps; it has a maximum working pressure of 2000 kPa. No modification was necessary for the cell body. The cell base, 264 mm in diameter and 27 mm thick, was made from a light metal alloy and has four inflow and outflow ports. To facilitate the installation of an internal pore pressure transducer, a 3.2 mm (1/8") hole was bored through the center of the pedestal and the cell base. The internal pressure transducer's wire tubing could be passed through the center hole. The detail of the modified triaxial cell base is shown in Figure 5-12.

5.9.2 Reaction frame

Steel reaction frame includes a square base plate, two steel columns with screw threads, and an upper reaction steel bar. The steel columns are 800 mm long and one end was welded to the square base. The height of the top reaction bar can be

adjusted with screws and nuts on each column. The detail of the reaction frame with the modified triaxial cell is presented in Figure 5-13.

5.9.3 Small pressure transducer

The pore pressure measurement includes the base pore pressure measurement and the in-sample pore pressure measurement. The pore pressure measurement at the base of the specimen is relatively straight forward and conventional (Bishop and Henkel 1962), but the pore pressure measurement inside a sample is challenging due to small sample size and disturbance which may be caused when inserting a pressure transducer.

In order to measure pore pressure inside the sample, an ultra-small pressure sensor (Kyowa Model PS-10KB) was used. This small transducer comes with a foil strain gauge and Wheatstone bridge in a very small and thin mainframe. When combined with a general strain amplifier, the transducers uniquely detect a distribution of spot pressures.

The Kyowa Model PS-10KB pressure sensor is 6 mm in diameter, 6.7 mm in length, and has a pressure range of 0 to 1000 kPa (Figure 5-14). To protect the sensor during testing, it is encased with a hollow brass cylinder, 9 mm in diameter and 20 mm in length. The brass cylinder is 1.5 mm thick, and has a depression at the top to facilitate placement of a 2 mm thick porous filter. The pressure sensor is located 4 mm below the top of the brass cylinder, forming a cavity between the filter and the sensor, which can be filled with water before installing the transducer.

To protect the transducer wire during testing, the wire was threaded inside 3.2 mm diameter tubing. The bottom portion of the brass cylinder, together with wire tubing, was filled with flexane-80 to form a watertight seal. The small size of the pressure sensor permitted a minimum disturbance to the sample during transducer installation. A photograph of the small pore pressure transducer, together with the brass cylinder and tubing, is presented in Figure 5-15.

After the small pressure transducer was assembled, the transducer was calibrated under controlled pressure and the results were compared with a normal pressure transducer. The calibration procedure for the small pressure transducer was as follows:

- The top cavity of the transducer was filled with water and covered with a saturated porous stone.
- The wire tubing of the small transducer was pushed through the 3.2 mm hole at the center of the pedestal and cell base, and was sealed from the base.
- The pressure lines at the cell base were flushed with deaired water to remove entrapped air.
- The cell body was locked on the cell base and filled with deaired water.
- A normal pressure the transducer was connected to one of the pressure ports at the cell base.
- Wire from the small pressure transducer and the normal pressure transducer were connected to the data logger.
- A portable pressure calibrator, GE DPI 603, was connected to the cell pressure line at the cell base.
- Pressure was applied incrementally through the pressure calibrator and the output voltage of the small pressure transducer was recorded.
- Changes for both the loading and unloading cycles were recorded.
- Once the calibration factors were established, the loading and unloading cycles were repeated and the changes from both transducers were recorded.

The setup of pressure calibration is presented in Figure 5-16. Results of the small pressure transducer calibration are presented in Figure 5-17. During the test, cell pressure was applied in 50 kPa increments from 0 to 1000 kPa. Both transducers produced similar pressure as shown in Figure 1-17. This calibration test confirmed that the developed small pressure transducer could be utilized successfully in laboratory tests.

5.10 Sample preparation for the pressure response test

5.10.1 Grout Sample

Pore pressure response tests were conducted on 28 day-old grout mix C sample. The sample preparation was the same as described in Section 5.4. Immediately after the grout was prepared, the small transducer was placed in the middle of the PVC mould and the grout mix was poured into the mould. Then the PVC mould, together with grout and the small transducer, were cured for 28 days.

5.10.2 Clay shale sample

Pore pressure response tests are conducted on clay shale samples obtained from the Keillor Road landslide investigation. Core samples 75 mm in diameter were collected with a triple tube, PQ type core barrel. Immediately after the core was retrieved from the coal barrel, the core samples were wrapped in plastic, coated with paraffin wax, and stored in a humid room until the time of testing. For the pore pressure response test, a uniform section of clay shale coal sample was selected for testing (Figure 5-19).

Introducing the small pressure transducer in the clay shale sample involved the following steps.

- The core sample was cut at both ends using an electric saw to obtain 150 mm length.
- A hole with a diameter slightly larger than the small transducer (9 mm) was drilled at the center of the core sample to a depth of 80 mm.
- The transducer was pushed inside the core sample to the bottom of the hole. Care was taken to make sure that the filter was firmly in contact with the bottom of the hole.
- The remaining gap behind the transducer was filled with the cement bentonite grout.

Figure 5-20 is a diagram of the clay shale core sample with the small transducer installed.

5.11 Testing procedure

The testing procedure for the pore pressure response test is as follows.

- A large triaxial cell was modified for the pressure response test (Figure 5-21).
- Before testing, all pressure lines of the base plate were flushed with distilled water to remove entrapped air bubbles.
- The sample, together with the small transducer, was placed on the pedestal and the wire tubing is pulled out from the hole through the pedestal and the base plate. The hole and the wire tubing were sealed using a precision cap.
- The sample was covered with a rubber membrane and O-rings are placed on the top cap and the pedestal.
- After placing the cell body on the base plate, cell pressure and back pressure lines were connected with the pressure system and the transducer wires were connected with the data logger.
- Sample saturation is carried out as described in Section 5.6.2.1.
- After saturation, the back pressure line is closed and the pore pressure response of the sample is measured using different cell pressures.

5.12 Results of pore pressure response tests

5.12.1 Pressure response of the grout sample

The results of the pore pressure response test on the grout sample are presented in Figure 5-22. It was observed that the response of the transducer was rapid and always greater than a 94 % equalization ratio after 10 seconds. The remaining 6 % response took a much greater time. Pore pressure equalization of 99 % was achieved within 5 minutes of pressure increase, indicating a fast response of the grout sample. No significant difference in pore pressure response was observed between the bottom and center of the specimen.

5.12.2 Pressure response of the clay shale sample

The results of the pore pressure response tests on the clay shale sample are presented in Figure 5-23. Equalization ratios of 62 % and 50 % were achieved within 1 minute from the bottom and center of the sample, respectively. An equalization ratio of 90 % was achieved within 4 minutes. Then the increase in pore pressure of the sample slowed and a pore pressure equalization of 99 % was achieved within 30 minutes at the bottom of the sample and within 70 minutes at the center of the sample. This suggests that the rate is controlled by a redistribution of pore pressure within the sample.

These results show that grout-in installation could be successfully used in clay shale bedrock in Edmonton. The pore pressure response of the grout sample was fast, achieving 99 % pressure equalization in 5 minutes. Due to low permeability and overconsolidation, the bedrock sample shows a slower equalization time, achieving 99 % pressure equalization in 70 minutes.

5.13 Summary

A series of laboratory tests were conducted to improve the pore pressure measurement in weak rock. The laboratory tests included the unconfined compression test, the permeability test, and the pore pressure response test. The strength of grout mix A was similar to soft clay with the high water content. Only 20 kPa of unconfined compressive strength was achieved for the 28 day-old soft grout sample. Grout mix B achieved unconfined compressive strength of 510 kPa and a permeability range of 2.3 to 7.9×10^{-6} cm/sec after a curing period of 28 days. The unconfined compressive strength of grout mix C was 1170 kPa and the permeability ranged from 4.3 to 6.1×10^{-7} cm/sec after a 28 day curing period. From the strength and permeability properties of the grout, grout mix C was selected for the field grout-in piezometer installation. Pore pressure response testing of grout and clay shale samples revealed that they achieved 99% pore pressure equalization within 5 and 70 minutes, respectively.

The following summarizes the findings from the laboratory investigation.

- The strength and permeability of cement-bentonite grout is a function of the water:cement ratio and the curing time.
- Permeability decreases with a decreasing water:cement ratio.
- Both strength and permeability of grout can be adjusted for grout-in piezometer installations in weak rock.

Table 5-1 Permeability, k, of some grout mixes

Grout Type	Characteristic	Permeability (cm/sec)	Source
Cement- Bentonite	w:c:b 4:1:1	5×10^{-8}	Vaughan 1973
Cement- Bentonite	w:c:b 2.0:1:0.36	10^{-7}	Contreras et al. 2007
Cement- Bentonite	w:c:b 6.55:1:0.40	10^{-5}	Contreras et al. 2007

(w:c:b) – water:cement:bentonite ratio by weight

Table 5-2 Summary of cement-bentonite grout ratios

Mix No.	Water:Cement:Bentonite Ratio by weight	Unconfined Compression Test	Permeability Test
A	6.6:1.0:0.4	7, 14, 28 days	14, 28 days
B	2.5:1.0:0.3	7, 14, 28 days	14, 28 days
C	2.0:1.0:0.3	7, 14, 28 days	14, 28 days

Table 5-3 Permeability of cement bentonite grout samples

Sample	Curing Time (days)	B value	i	Cell pressure	k (cm/sec)	Water Content (%)
Grout Mix A	14	0.97	15	400	4.0 to 6.5 x 10 ⁻⁵	273
Grout Mix A	28	0.96	15	400	1.7 to 3.1 x 10 ⁻⁵	273
Grout Mix B	14	0.95	20	500	5.8 to 7.1 x 10 ⁻⁶	151
Grout Mix B	28	0.95	20	500	2.3 to 7.9 x 10 ⁻⁶	151
Grout Mix C	14	0.95	20	500	7.9 to 8.4 x 10 ⁻⁷	138
Grout Mix C	28	0.95	20	500	4.3 to 6.1 x 10 ⁻⁷	138

Table 5-4 Water content, unit weight, and void ratio of 28 day-old grout samples

Grout Mix	Water:Cement:Bentonite Ratio	Water Content (%)	Unit Weight (g/cm ³)	Void Ratio
A	6.6	273	1.24	7.6
B	2.5	151	1.32	4.2
C	2	138	1.34	3.9

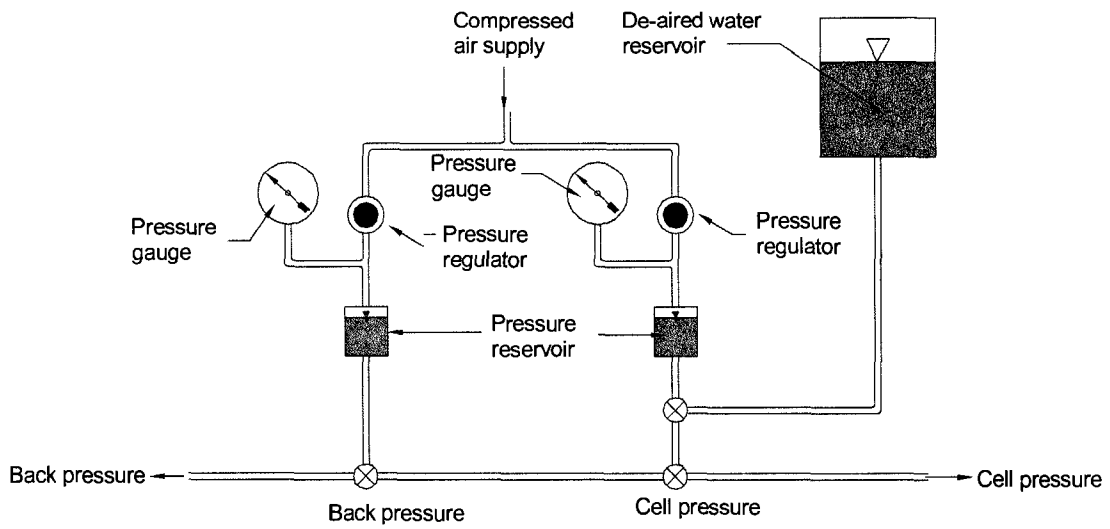


Figure 5-1 Constant pressure system

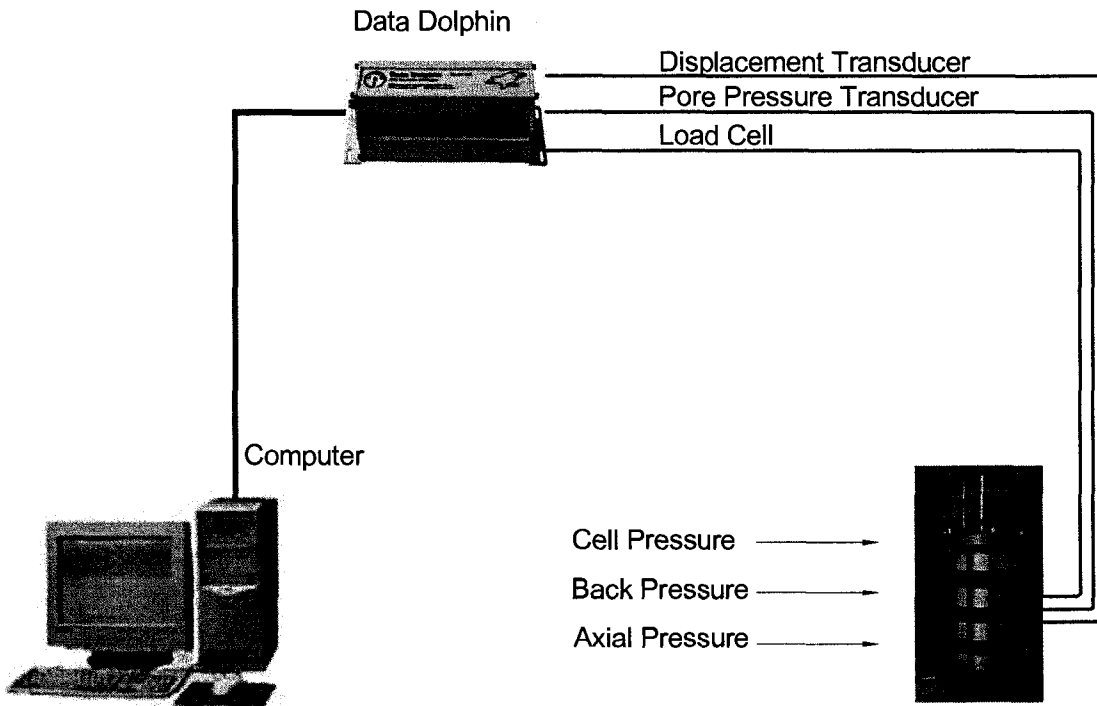


Figure 5-2 Layout of the laboratory instrument monitoring system

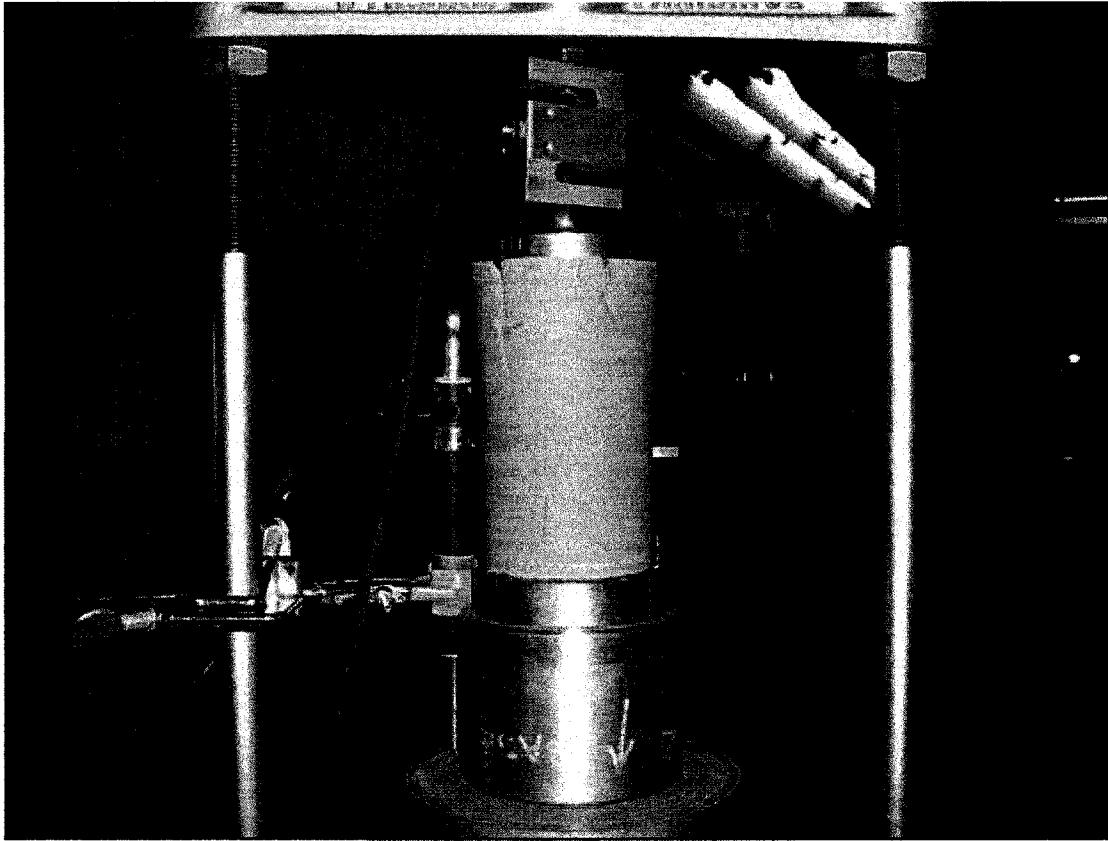


Figure 5-3 Unconfined compression test on 14 day-old hard grout sample

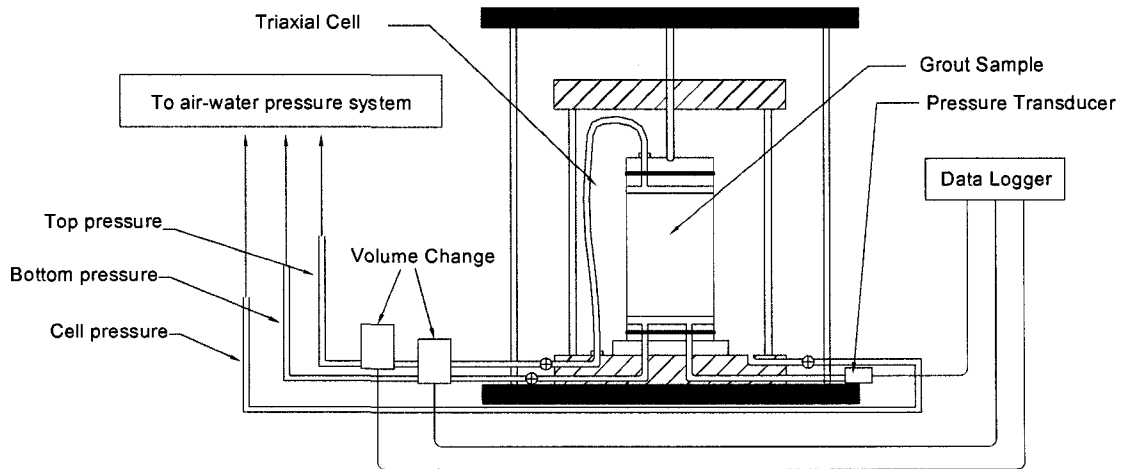


Figure 5-4 Setup of the permeability cell

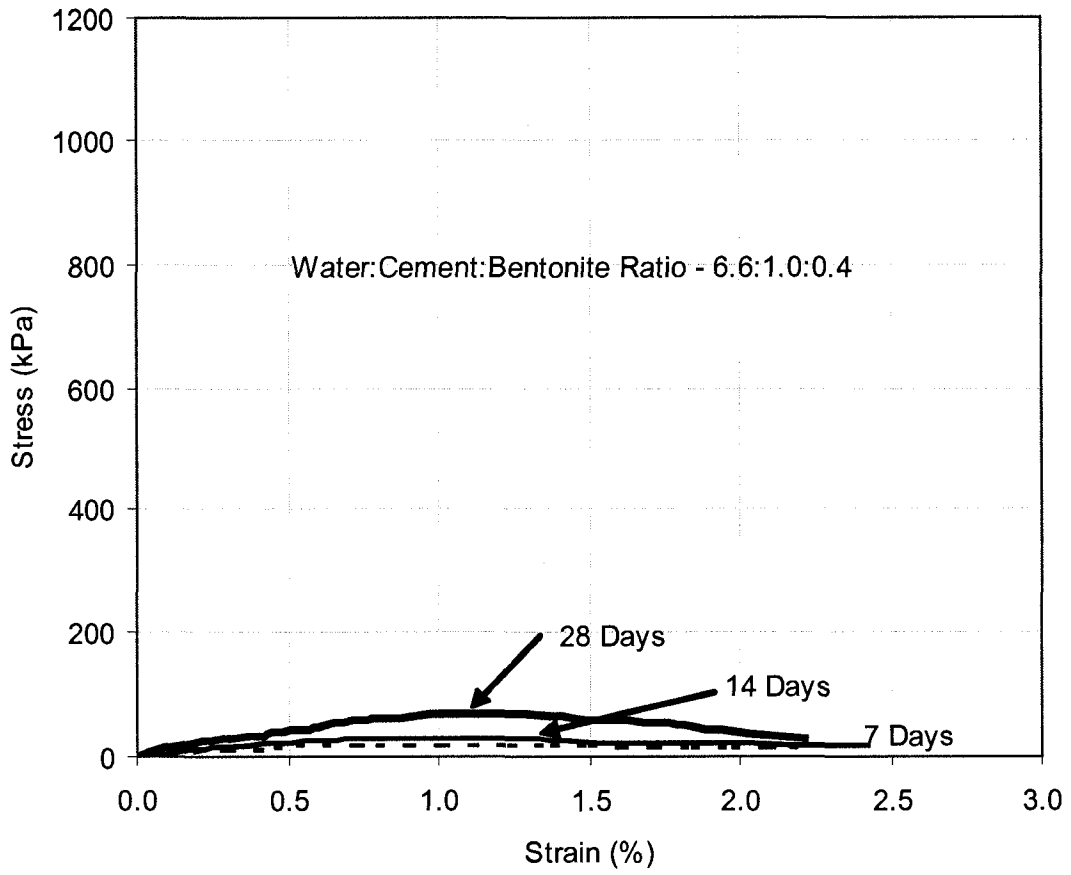


Figure 5-5 Unconfined compression tests on grout mix A

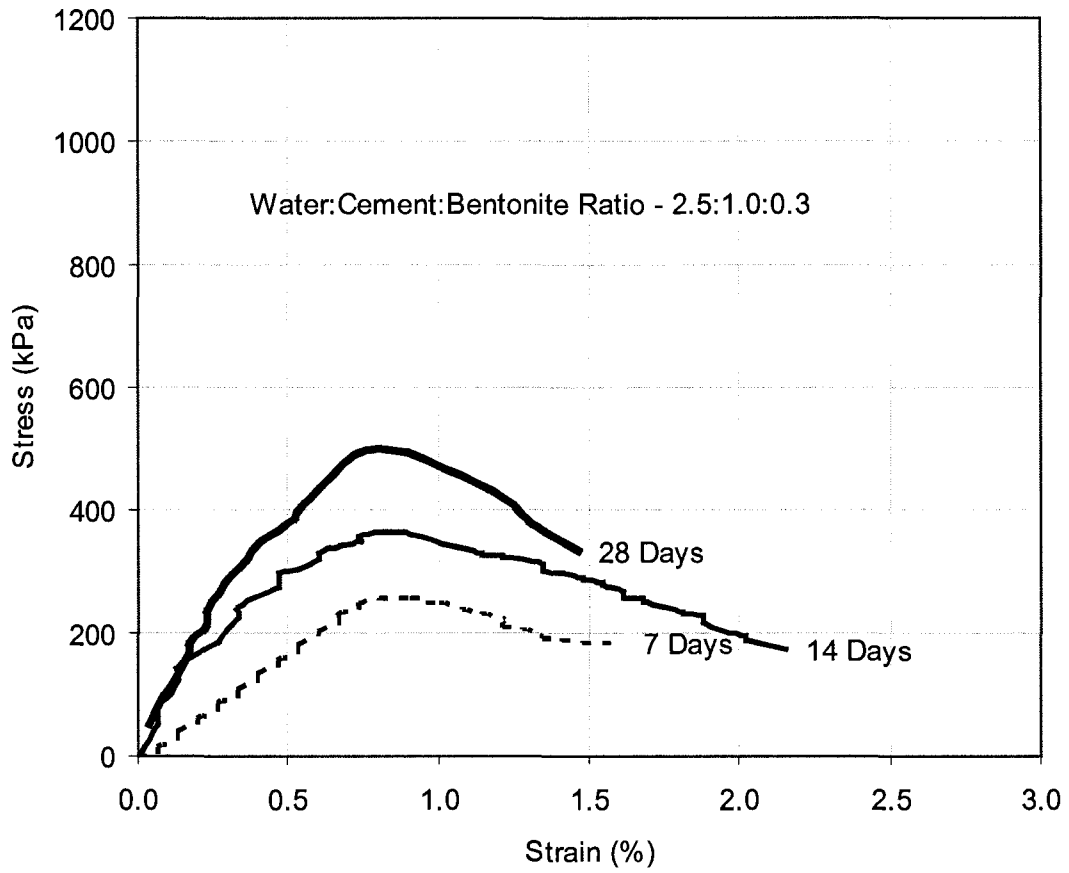


Figure 5-6 Unconfined compression tests of grout mix B

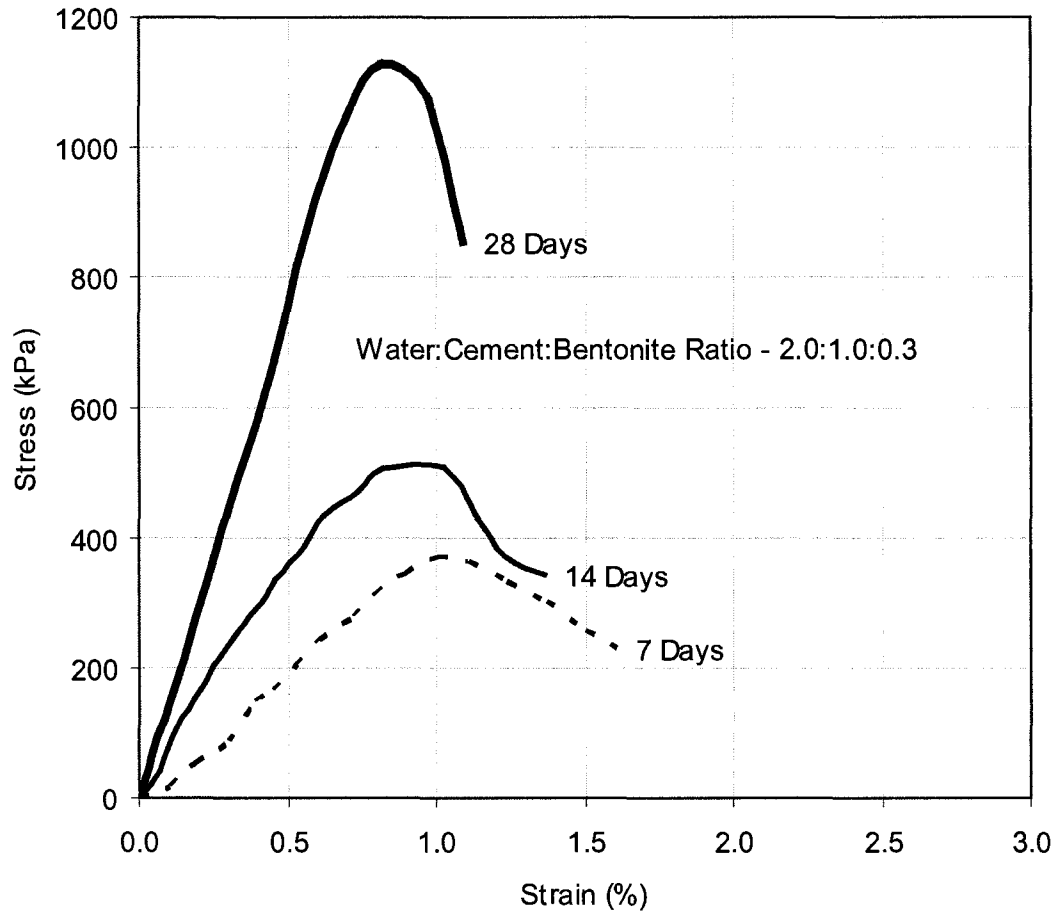


Figure 5-7 Unconfined compression tests of grout mix C

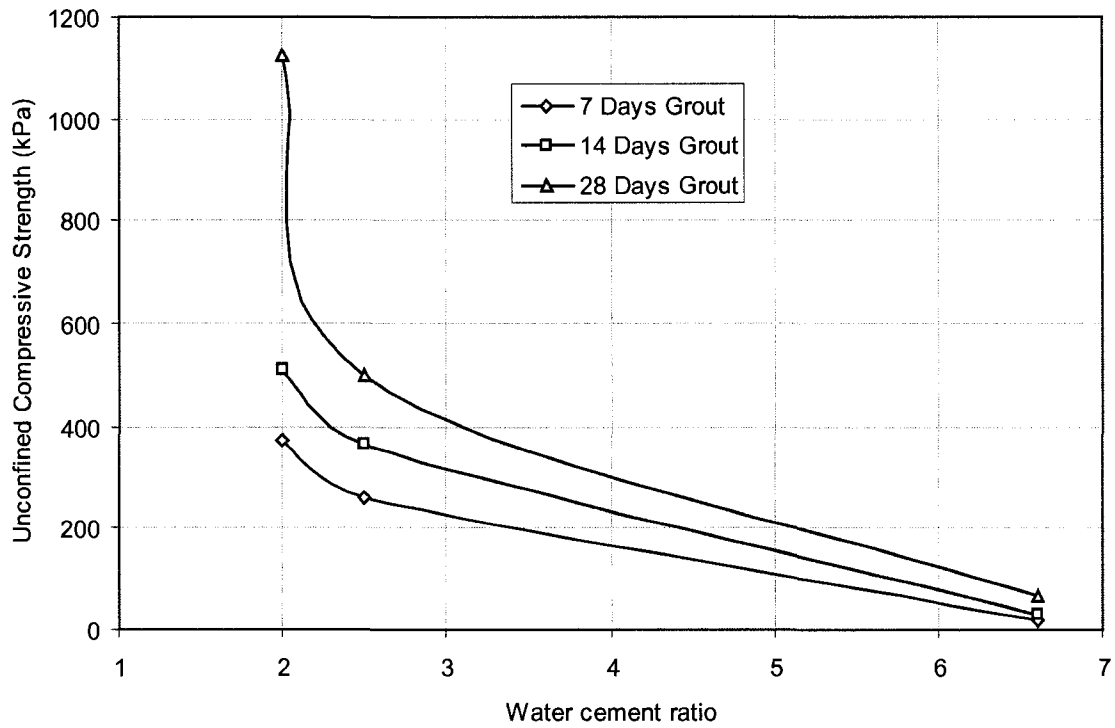


Figure 5-8 Unconfined compressive strength vs. water:cement ratio for different curing times

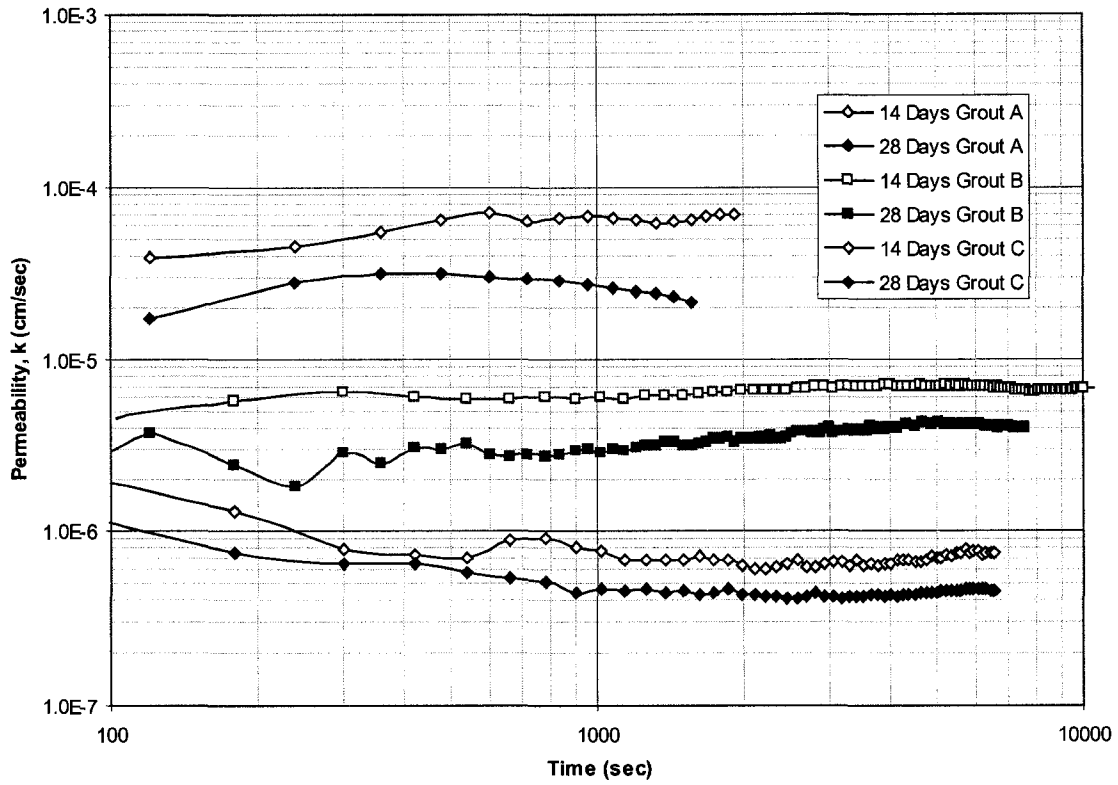


Figure 5-9 Variation in permeability with different water:cement ratio and curing time

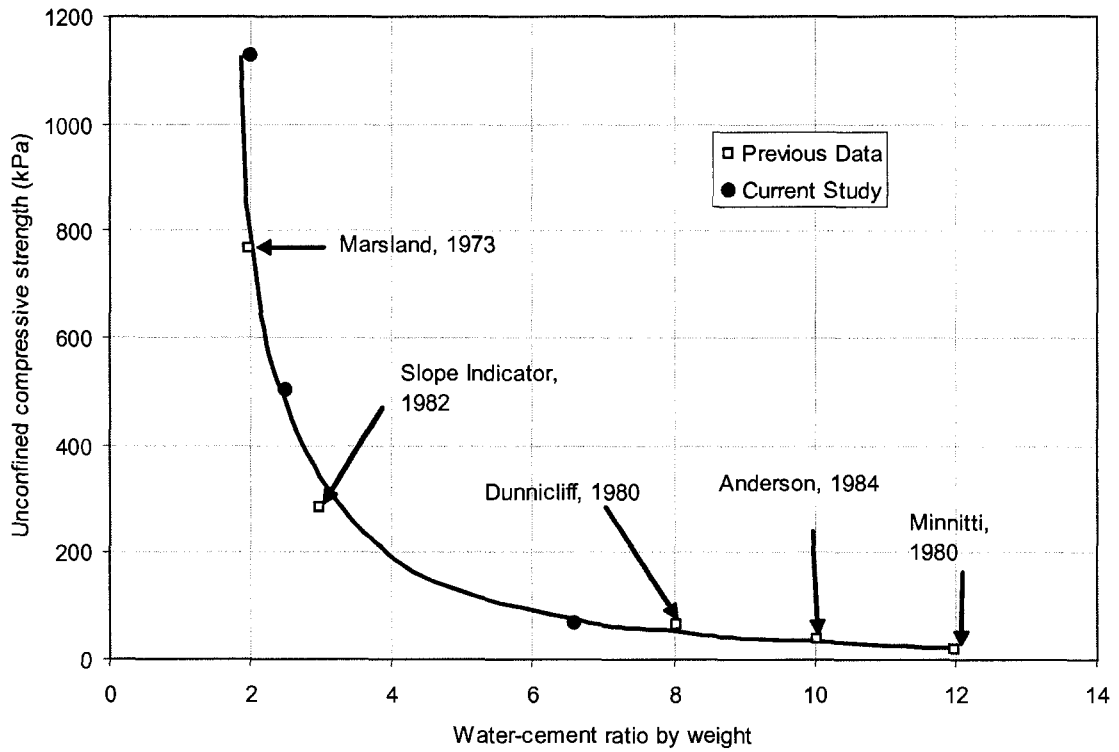


Figure 5-10 Variation of unconfined compressive strength vs. water:cement ratio by weight (modified from Mikkelsen 2002)

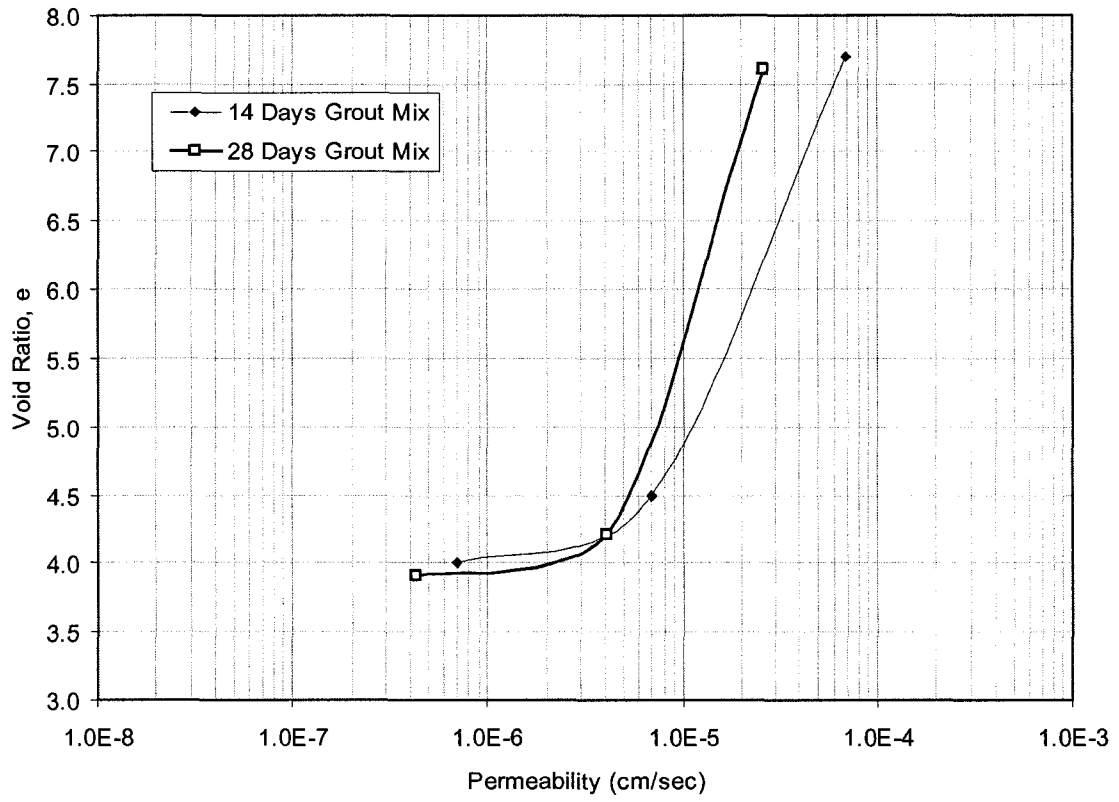


Figure 5-11 Void ratio vs. permeability for different curing times

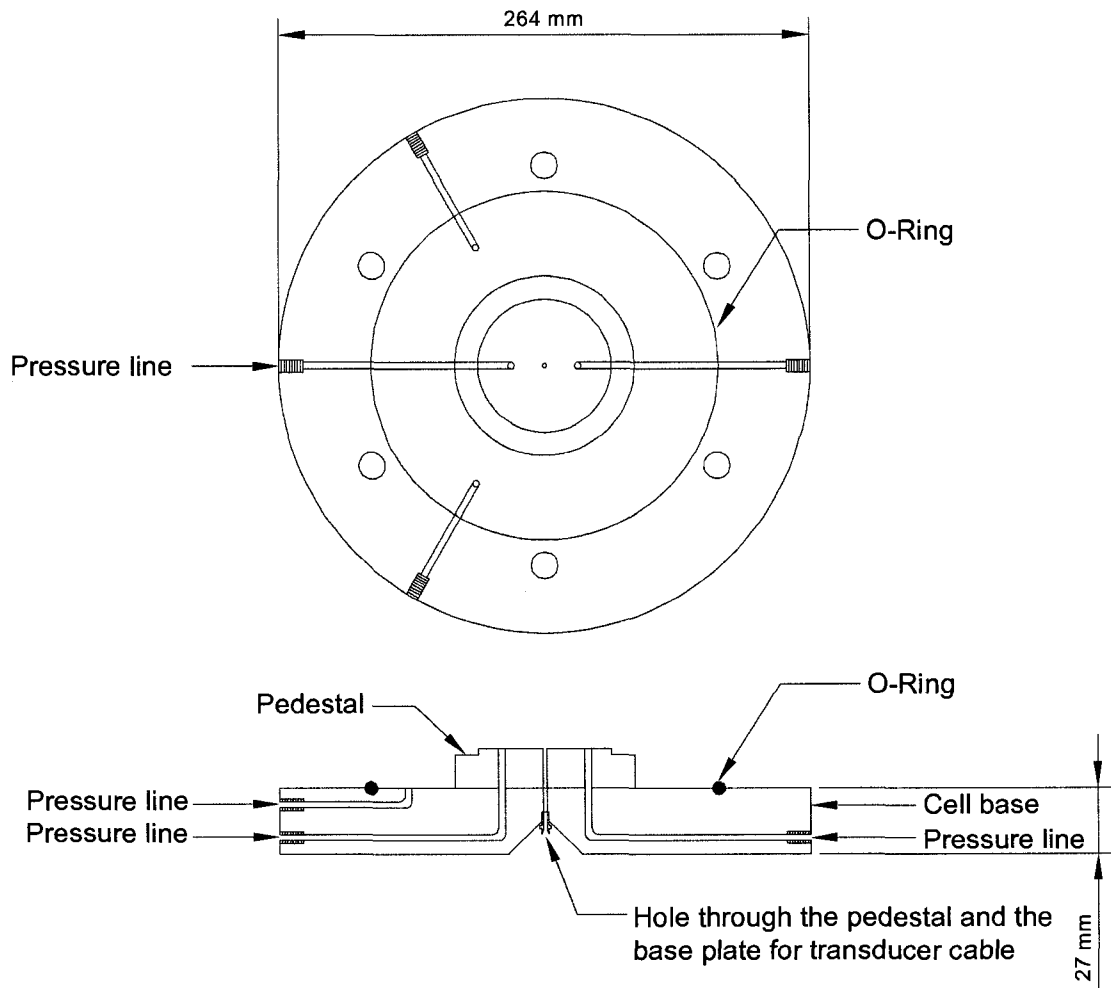


Figure 5-12 Details of the modified triaxial cell base

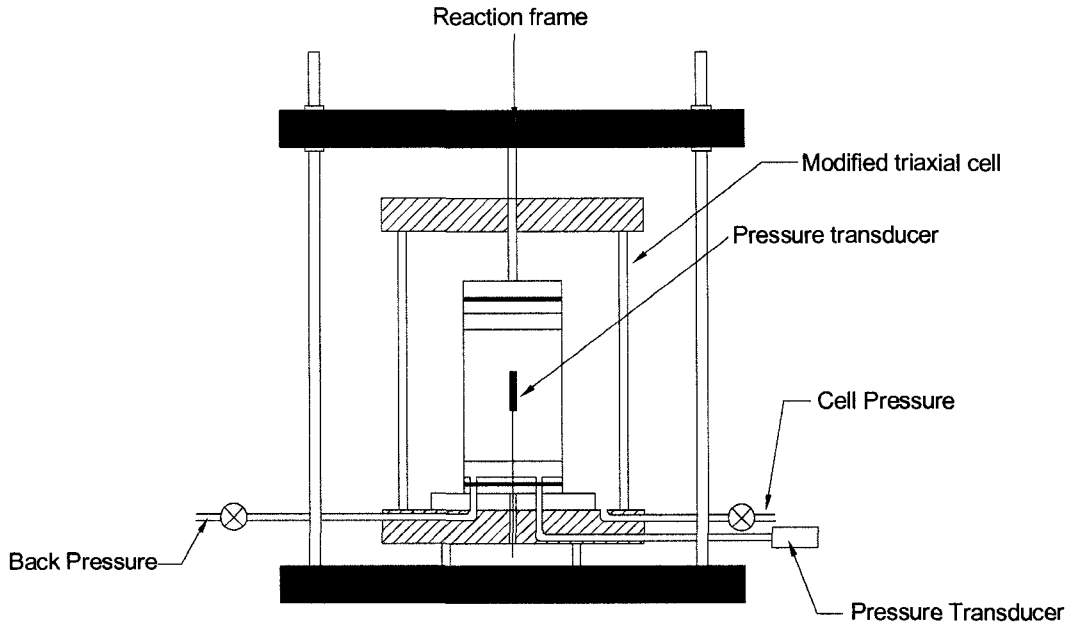


Figure 5-13 Sketch of the set-up of the modified triaxial cell (not to scale)

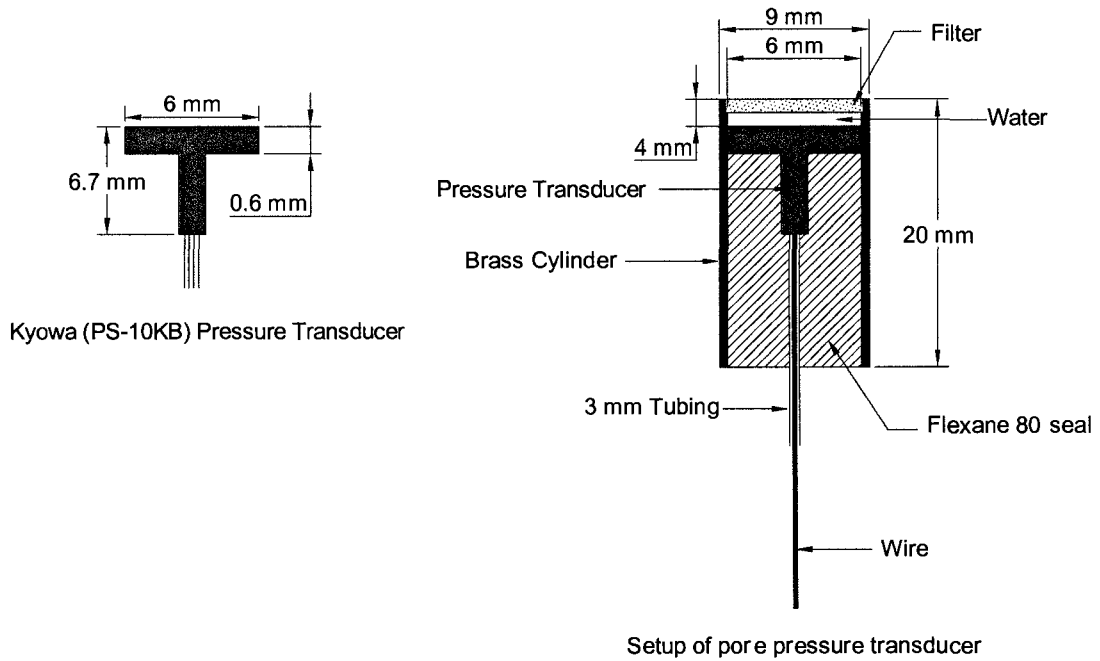


Figure 5-14 KYOWA small pressure transducer

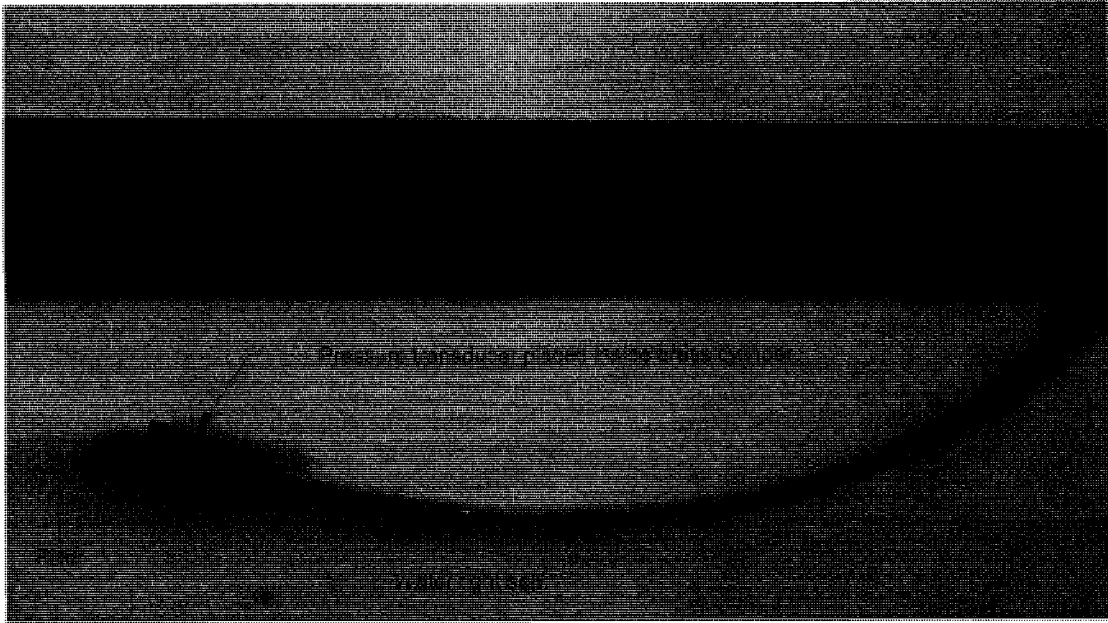


Figure 5-15 Photograph of the pore pressure transducer

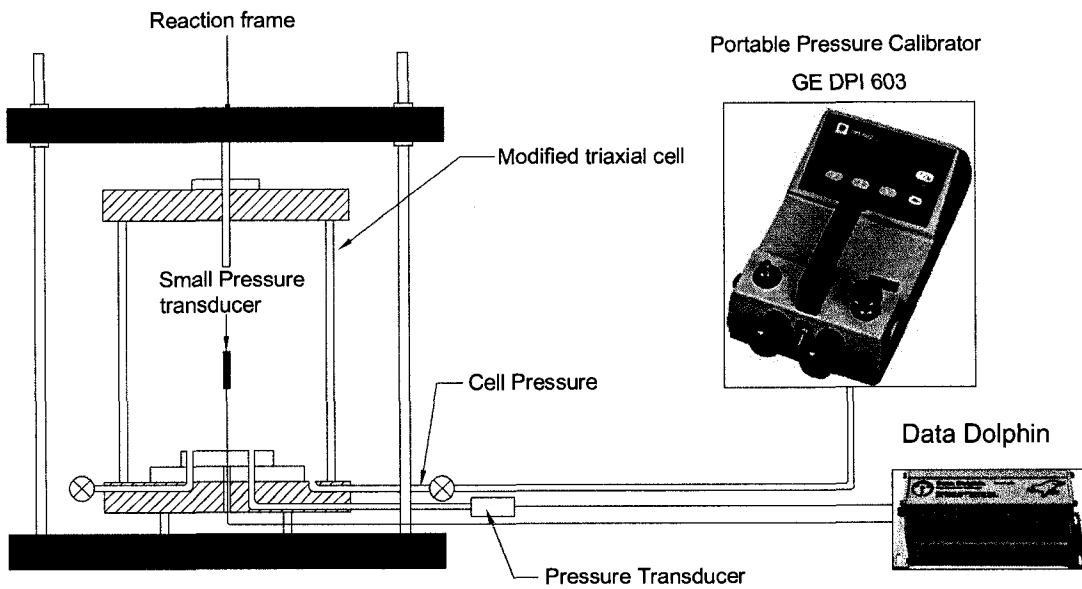


Figure 5-16 Setup of small pressure transducer calibration

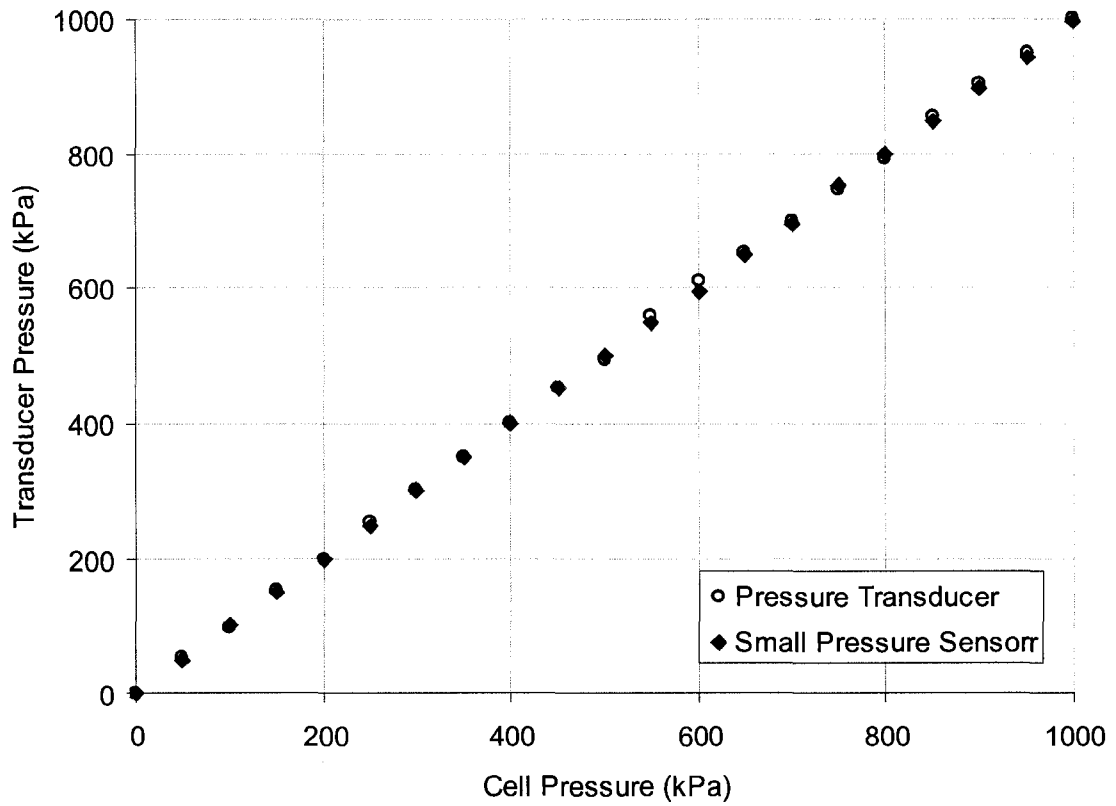


Figure 5-17 Pore pressure response of a small pressure transducer during the calibration test

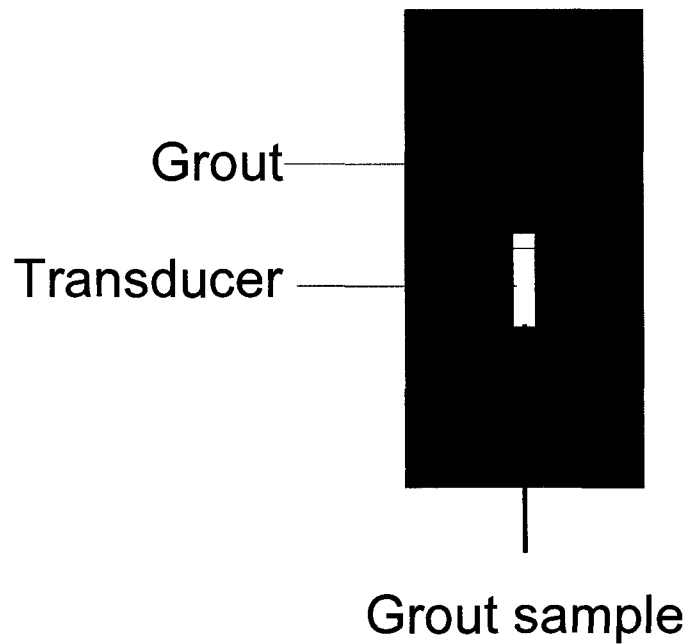


Figure 5-18 Hard grout sample with a small pressure transducer

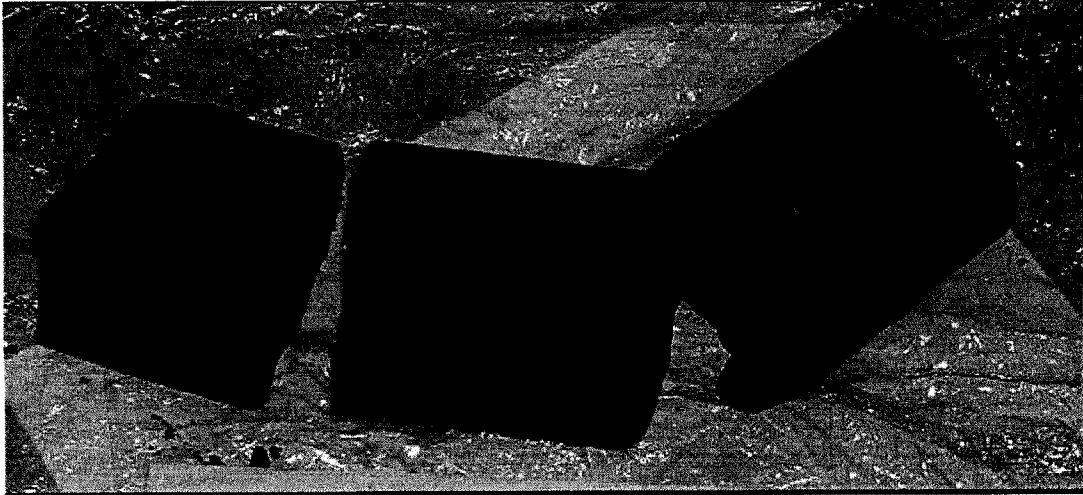


Figure 5-19 75 mm diameter core sample used in the pore pressure response test

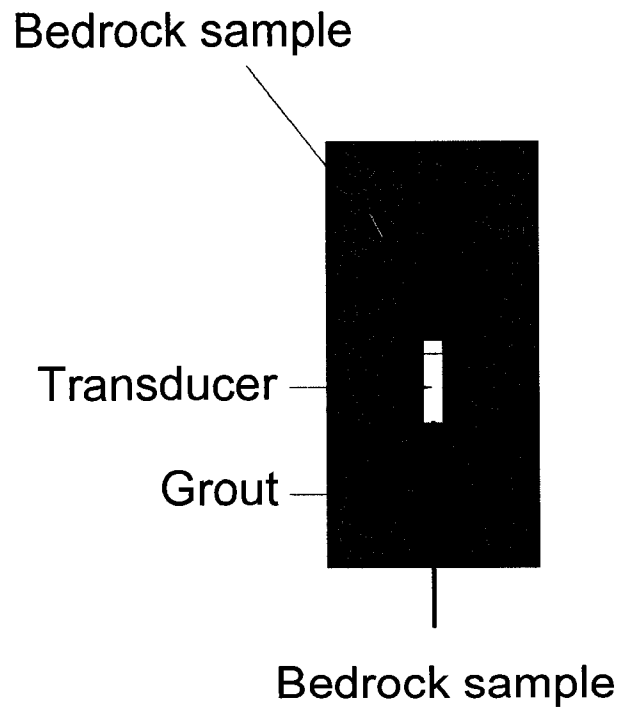


Figure 5-20 Small pressure transducer installation in the core sample

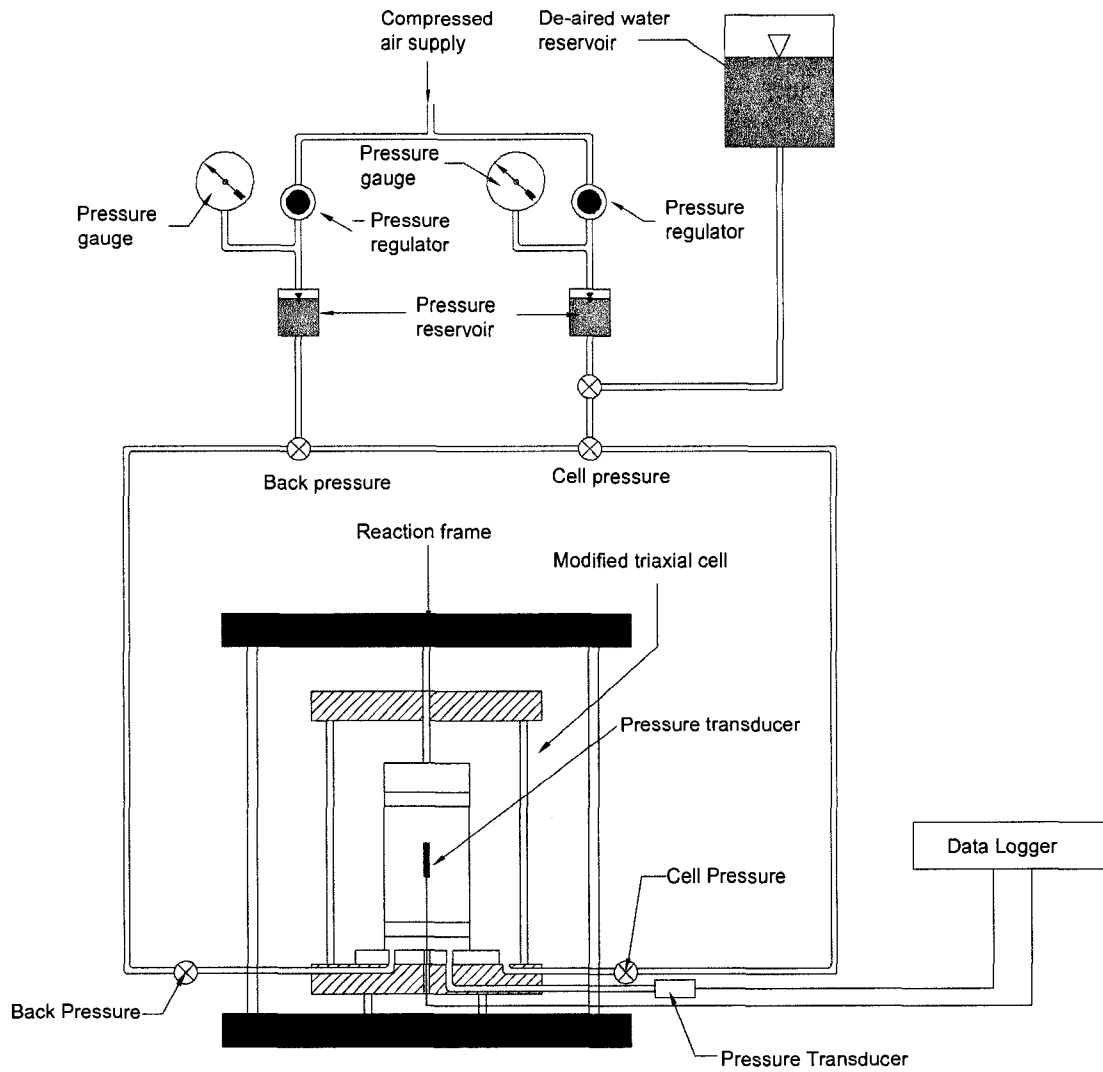


Figure 5-21 Setup of modified triaxial cell for pore pressure measurement

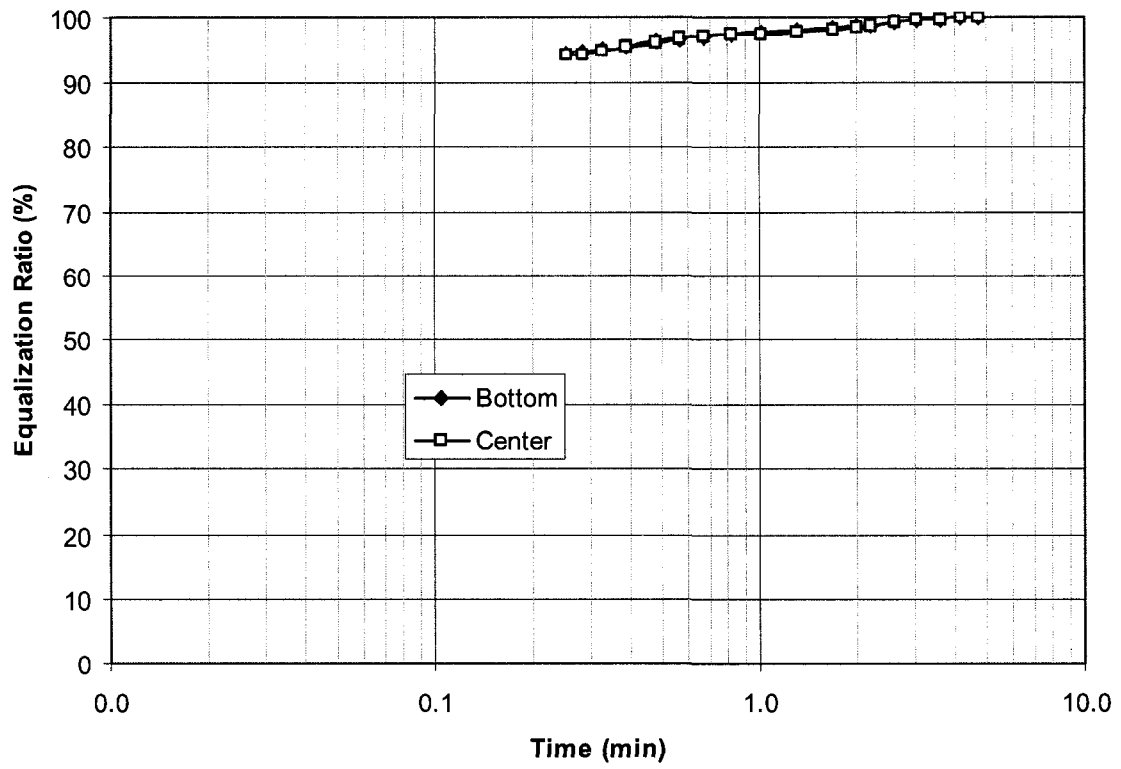


Figure 5-22 Pore pressure response of the grout sample

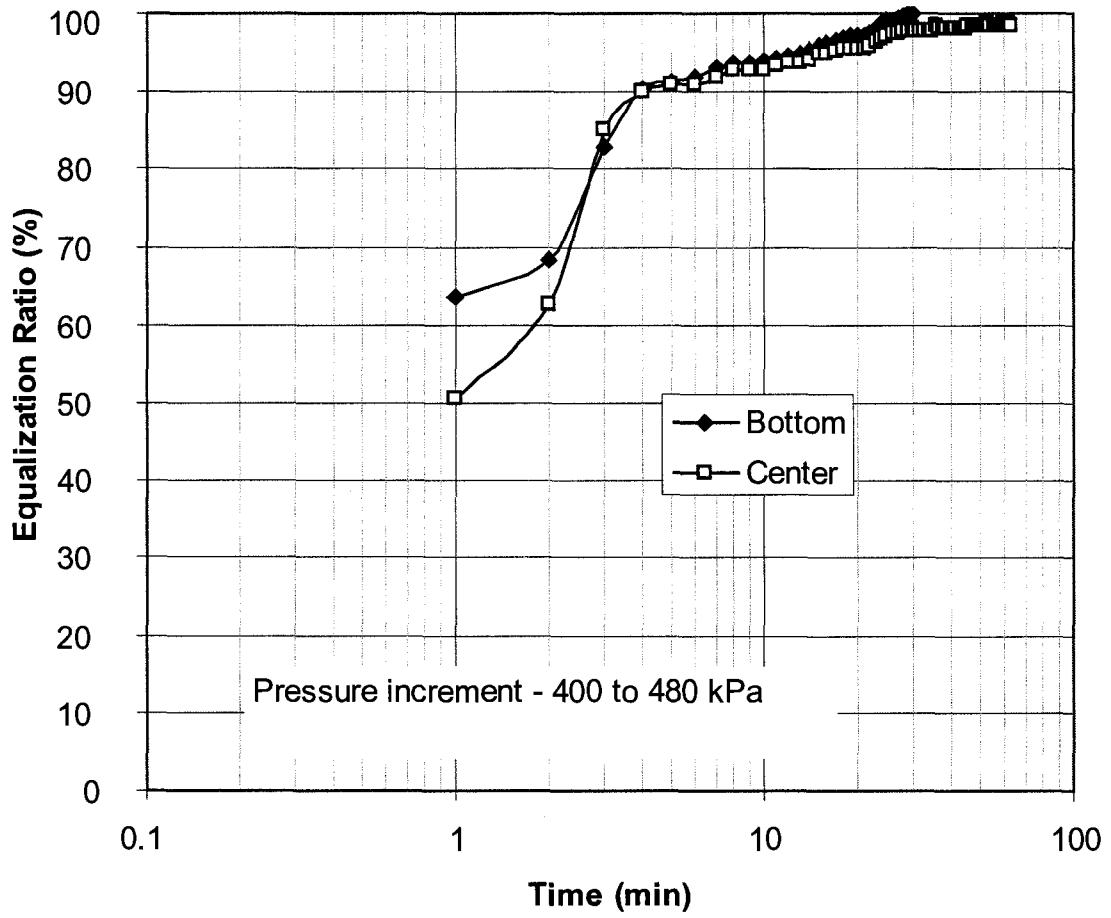


Figure 5-23 Pore pressure response of the clay shale sample

CHAPTER 6 Development of a Flushable Piezometer

6.1 Introduction

In current geotechnical practice, diaphragm piezometers are usually installed with low air entry filters. When used with low air entry filters, diaphragm piezometers may measure the pressure in the pore air when it is significantly different than the pore water pressure (Sherard 1981). Sherard (1981) indicated that vibrating wire (VW) piezometers can measure negative pore water pressure when used with a high air entry filter. But air may enter inside the piezometer cavity through the filter, or at a higher negative pore pressure, air bubbles may form within the piezometer cavity due to cavitation, and this can disrupt pore pressure measurements.

The long term performance of most piezometers is poor in the presence of a negative pore water pressure and it is essential that there is a means of removing air from the piezometer cavity. Among available piezometers discussed in Chapter 4, only twin-tube hydraulic piezometers have the facility to remove air bubbles from the piezometer cavity. However, the twin-tube hydraulic piezometer has a limited installation depth (e.g. tubing can not rise 6 m above the piezometer tip). In order to improve the pore pressure measurement in weak rock slopes that may have negative pore pressure, (i) the piezometer should be fitted with a high air entry filter with deairing facility, and (ii) the piezometer installation depth should not be limited due to flushable tubing

A new piezometer system, comprised of a flushable adaptor and a normal vibrating wire piezometer has been developed for pore pressure measurements in weak rock. The adapter is equipped with a high air-entry filter and is able to circulate water from the ground surface. By using two check valves, the flushable piezometer can be installed to a great depth not affected by the water column inside the flushing tubes.

The major advantage of this system is that the normal vibrating wire piezometer can be easily converted into a flushable piezometer with the use of the adaptor system.

6.2 RECENT DEVELOPMENT OF FLUSHABLE PIEZOMETER

Long et al. (2004) described a flushable piezometer used during construction of the Dublin Port Tunnel project in Ireland. This flushable piezometer was developed by ITM Ltd. using a vibrating wire piezometer fitted with water lines to circulate water from the ground. However, this system does not have the facility to seal off the piezometer cavity from the flushing tubes. Thus, this flushable piezometer is similar to a twin tube hydraulic piezometer fitted to a vibrating wire sensor. A section of this piezometer is presented in Figure 6-1 and some of the notable features of this piezometer are as follows:

- The piezometer is approximately 50 mm in diameter, 300 mm long, and has a 50 mm long filter.
- The filter unit is constructed with a 1 bar high air entry filter, supplied by Fiarey Industrial Ceramics Ltd. It has a maximum pore size of 1 micron and an apparent porosity of 40 to 45 %.
- The volume of water in the chamber between the filter unit and pressure measuring diaphragm is approximately 12.5 cm³.
- The flushing lines consist of two 3.7 mm inside diameter tubes.

The performance of this flushable piezometer was tested during a 12 m deep trial excavation (Figure 6-2). Flushable piezometers were installed in relatively homogeneous low permeability till at 4 m, 8 m, and 12 m below the ground surface before the excavation. The initial groundwater level was 2 m below the ground surface and before the excavation, the piezometers responded to the initial groundwater level. As the excavation progressed, the piezometric pressure of the till decreased due to stress relief. The lowest values of pore water pressure were recorded by the 12 m piezometer, with a minimum value of about -8 kPa.

Ridley et al. (2003) developed a flushable piezometer system comprising of pressure sensor, hydraulic valve and inlet and outlet ports connected to the surface with color-

coded flexible tubing (Figure 6-3). These facilities allow air that forms in the sealed reservoir to be flushed out. A hydraulic valve located in the piezometer head and operated from the surface was used to open and close the flushing parts. A miniature pressure sensor was located in the head of the piezometer and connected to the surface via a waterproof electric cable. It had a porous filter with a nominal blow-through pressure of 1 kPa. The placement of the pressure sensor and hydraulically operated valve in the head of the piezometer (and therefore at the same depth as the measurement) removes the requirement to correct for the head of water in the flushing tubes and increases the suction range that can be measured. The pressure sensor was calibrated for the range of +65 kPa to -100 kPa.

An example of pore pressure measurement using the flushable piezometer is presented in Figure 6-4 (Ridley et al. 2003). The flushable piezometer was installed at a depth of 2 m in an old railway embankment constructed of compacted London Clay. As shown in the figure, cycles of negative pore pressure are observed due to infiltration from the ground surface. The figure also shows the pore pressure response during the flushing process, where negative pore pressure is reduced to zero and then gradually falls back to the surrounding pore pressure (Figure 6-4).

6.3 The developed flushable adaptor

The developed flushable adaptor is a simple device which replaces the filter location in a normal vibrating wire piezometer. The main function of this adaptor is to flush out air bubbles from the ground surface when necessary and seal off the piezometer cavity when flushing is completed. This ability to seal off the piezometer cavity from the water column in the flushing tubes enables the piezometer to be installed to great depths. The developed flushable adaptor system consists of three components:

- an adaptor body,
- two one-way check valves, and
- a high air entry filter.

6.3.1 Adaptor body

The adaptor body, 52.2 mm in length, 19.28 mm outer diameter, and 7.13 mm inner diameter, was precision-machined from cylindrical solid steel. The top end of the adaptor was designed to fit with a high air entry filter and the bottom end of the adaptor was designed to fit into the filter location of the vibrating wire piezometer.

The side of the adaptor body has two 3.2 mm holes with elbow connectors. These holes were designed to connect with two one-way check valves. The total volume of the water inside the adaptor cavity is about 1.6 cm³. To promote water circulation during the flushing process, the adaptor cavity was divided into two compartments using a separator bar. This allows the water to flow through the top and bottom of the cavity from one side to the other side, removing entrapped air bubbles. The detailed dimensions of the developed adaptor body are presented in Figure 6-5.

6.3.2 Check valves

A check valve is a mechanical device that allows fluid to flow in one direction only. A check valve is normally in the closed position but it can be opened by pressure; “cracking” pressure is the minimum pressure required to open the valve. Two check valves, one for input and one for output, were utilized with the flushable adaptor. The principals of check valve systems are as follows:

- Input and output check valve flow directions are positioned to control pressurize water flow through the input check valve into the piezometer cavity and through the output check valve out of the piezometer cavity, respectively.
- Under normal conditions both check valves are closed and the piezometer cavity is tightly sealed.
- As water pressure in the de-airing tube is increased, the input check valve will open when the water pressure is greater than the cracking pressure of the valve.
- The pressurized water flows into the piezometer cavity together with entrapped air bubbles. When the water pressure inside the cavity is greater than the cracking pressure of output check valve, the valve opens and the pressurized water flows through the output check valve.

- This flushing process removes air bubbles inside the piezometer cavity.
- Once the water pressure in the flushing tube is below the cracking pressure, both check valves will close to seal off the piezometer cavity.

The cracking pressure of the check valves can be adjusted to facilitate the piezometer installation depth and expected pore pressure. In general, the cracking pressure of the input check valve must be greater than the water column pressure inside the flushing tube and the expected negative pore pressure at the location of the piezometer. The cracking pressure of the output check valve must be greater than the possible maximum positive pore water pressure at the installation depth. For instance, if 150 kPa cracking pressure check valves are used for both input and output valves, and the piezometer is to be installed 10 m below the surface, the flushable piezometer will be able to monitor at least 50 kPa negative pore pressure and 150 kPa positive pore pressure.

Several types of check valves with different cracking pressures were considered for the adaptor. The Poppet type CH series check valve, manufactured by Swagelok, was selected for the flushable adaptor. This type of check valve has a ¼" (6.4 mm) end connection and is available with different cracking pressures. The Swagelok CH series check valve is presented in Figure 6-6.

6.3.3 High air entry filter (HAE)

The main purpose of a filter is to separate the pore fluid from the structure of the soil to the water inside the piezometer cavity. The air entry value of the filter is defined as the pressure differential at which blow-through of fluid occurs. A filter with a high air entry value is a fine filter that allows a high pressure differential before blow-through occurs.

High air entry filters are usually used in unsaturated soils to measure pore water pressure as opposed to pore gas pressure, in an attempt to keep gas out of the measuring system (Penman 2002). Filters used for this purpose have a 1 micron pore diameter and an air entry value of 100 kPa. This keeps air out of the measuring

system and allows measurement of negative pore-water pressure. The high air entry effect is operative only when the filter is saturated with water. When water drains out of the filter, the high air entry effect disappears.

6.4 Flushable Piezometer

The flushable piezometer system combines the developed flushable adaptor and the normal vibrating wire piezometer. The bottom end of the adaptor body was designed to fit into the filter location of the vibrating wire piezometer (Figure 6-7). This allows a water tight seal between the adaptor body and the piezometer. The high air entry filter (HAE) with a 100 kPa blow-through pressure was fitted on the top part of the adaptor body. Input and output check valves were connected to the adaptor body through elbow fittings and flushing tubes were connected to the check valves. The complete setup of the flushable piezometer is presented in Figure 6-8.

6.5 Laboratory testing of a flushable piezometer

To determine the performance of the developed flushable piezometer, both flushing mechanisms and pore pressure response tests were conducted in the laboratory. The main concern for the flushable piezometer was the sealing mechanism of the piezometer cavity under normal conditions and the applicability of the flushing mechanism. Pore pressure response tests were conducted using a large triaxial cell, a portable pressure calibrator, and a vibrating wire piezometer readout unit. These instruments are described in the following sections.

6.5.1 Large triaxial cell

A large triaxial cell was used to test the flushable piezometer in the laboratory (Figure 6-9). The triaxial cell is 26.5 cm in diameter and 32 cm in height and has a cell base with 26.5 cm in diameter with 4 pressure ports.

6.5.2 Portable calibrator

The GE DPI 603 portable pressure calibrator has a standard pressure range of -90 kPa to 1000 kPa (Figure 6-10). The required pressure can be generated using an integral hand pump. A volume adjuster provides fine control of the pressure and a venting valve enables pressure release without disconnecting the device under test. The pressure/vacuum switching facility enabled the hand pump to decrease the pressure to -90 kPa.

6.5.3 Readout unit

The Slope Indicator VW data recorder is a recording readout for pluck-type vibrating wire sensors, resistance temperature detectors (RTDs), and thermistors. It is simple to operate and can store up to 2000 readings. Data can be transferred to a personal computer for processing with a spreadsheet. Readings can be obtained by connecting a sensor signal cable to the recorder's panel-mounted binding posts (Figure 6-11).

6.5.4 Equipment setup

Testing procedures for the flushable piezometer were as follows.

- The flushable adaptor was connected to the vibrating wire piezometer together with a high air entry filter.
- Input and output check valves with flushing lines were connected to the adaptor body. The flushing lines were connected to two pressure ports at the cell base (Figure 6-12).
- Deaired water was flushed through the pressure port and check valves to remove entrapped air inside the flushing line and piezometer cavity.
- The piezometer cable was threaded through a hole at the cell top and the hole was tightly sealed with an o-ring and cap.
- Once the flushable piezometer was positioned inside the cell, the triaxial cell was locked on the cell base and filled with deaired water.

- The cell pressure line was connected with a GE pressure calibrator and the piezometer cable was connected to the readout unit.

The complete setup including the flushable piezometer, vibrating wire readout unit, and GE portable pressure calibrator is shown in Figure 6-13.

6.5.5 Testing procedures

Pressure response tests were conducted using two check valves each with 100 kPa cracking pressure. Tests were conducted by changing the cell pressure from -60 kPa to 100 kPa and monitoring the pressure response of the flushable piezometer. During the test, water was flushed through the piezometer cavity to check the flushable piezometer mechanisms. The detailed testing procedures were as follows:

- Cell pressure was increased in 10 kPa increments from 0 kPa.
- The pore pressure response of the piezometer was recorded with the readout unit.
- At 30 kPa cell pressure, water pressure was increased slowly through the input flushing tube until water came out from the output flushing tube. During this process, the piezometer recorded a maximum pressure of 100 kPa, a pressure equal to the cracking pressures of the check valves. Once the water circulation stopped, the piezometer recorded the normal cell pressure.
- This process was repeated at a cell pressure of -40 kPa. During this process, the water pressure inside the piezometer increased up to 100 kPa (equal to the cracking pressures of the check valves).

This pressure response test confirmed that the flushable piezometer mechanisms work properly and that check valves can be successfully used to seal off the piezometer cavity after the flushing process. The pore pressure response of the flushable piezometer during the pressure response test is presented in Figure 6-14.

6.6 Field investigation program

The field investigation program was designed to improve pore pressure measurements in weak rock. Several different piezometer types including the water standpipe, pneumatic piezometers, and vibrating wire piezometers were used in the field investigation. The main focus was on piezometer type, the air entry value of the filter, and applicability of the developed flushable piezometer to the field. The following were considered in piezometer selection:

- Long term monitoring of pore pressure measurements in weak rock using pneumatic and vibrating wire piezometers,
- Use of low air entry (LAE) and high air entry (HAE) filters in the vibrating wire piezometer,
- Advantages of installing the filter directly in contact with the borehole wall as indicated by Penman (2002), and
- Use of the flushable piezometer in weak rock slopes to monitor negative pore pressures.

Different types of piezometers utilized in the field investigation are presented below.

6.6.1 Water standpipe

The main purpose of a water standpipe is to measure the groundwater level in the overlying glacial deposit and displaced materials of a valley wall. PVC pipes with 25 mm diameter and 6 m slotted section were used. The slotted section of the pipe was surrounded by clean sand and the remaining section was sealed with cement grout to prevent the flow of water from the ground surface. A typical water standpipe installation plan is shown in Figure 6-15.

6.6.2 RST pneumatic piezometer (P-100-1)

RST pneumatic piezometers utilize a direct reading of the pneumatically operated diaphragm from the readout unit. The P-100-1 model consists of a pneumatic piezometer encapsulated in a sand-filled, slotted PVC as shown in Figure 6-16. This

body has a 70 micron porous plastic filter in addition to the 50 micron stainless steel filter at the piezometer tip. With 0.002 cc displacement, measurements can be made under essentially zero volume change conditions.

6.6.3 Geokon 4500-MLP vibrating piezometer

The Geokon 4500MLP piezometer is a pluck-type vibrating wire piezometer with a built-in thermistor (Figure 6-17). In this model, the normal filter tip is replaced by a tube leading to a much larger, curved filter plate designed to be spring loaded so that it can be pressed against the walls of the borehole as shown in Figure 6-18. This model is designed for a maximum pore pressure of 700 kPa and can measure negative pore pressures up to 100 kPa. To use this type of piezometer, boreholes should be at least 100 mm in diameter and not more than 30 mm larger than the nominal size for which the spring loading mechanism is designed.

6.6.4 Slope Indicator's vibrating wire piezometer (Model - 52611030)

Slope Indicator Model 52611030 vibrating wire piezometer is a pluck-type vibrating wire piezometer with built-in thermistor (Figure 6-19). This model is designed for a maximum pore pressure of 700 kPa. It is supplied with a 50-micron sintered stainless steel filter for general use. Slope Indicator can also supply 1-micron stainless steel filter for special use.

6.7 Field piezometer installation

6.7.1 Location of test area—Forest Heights Park

The field installation was carried out in Forest Heights Park, located on the eastern bank of the North Saskatchewan River between Dawson Bridge and 98 Avenue, Edmonton, Alberta. This installation work was done during a landslide investigation in the area (Chapter 9). The bedrock in the study area comprises of fine grained, bentonitic sandstone and siltstone interbedded with bentonitic claystone. Coal seams and bentonite beds of variable thickness are common throughout the formation. The

valley slope has an average height of 50 m, with an elevation of 660 m at the flat upland area. A low level terrace is located at the toe of the slope and a toe berm was constructed in the 1980s to protect the river bank. The slope angle of the upper slope ranges from 30° to 35° and the lower slope angle ranges from 25° to 40°. Figure 6-20 shows the location of field instrumentation in Forest Heights Park.

6.7.2 Installation plan in Forest Heights Park

Instruments were installed in two locations in Forest Heights Park as shown in Figure 6-20. Cluster 1 was located in the lower trail, 35 m below the slope crest, and Cluster 2 was located just behind the slope crest, in the flat upland area (Figure 6-21).

In Cluster 1, instruments were installed using a hollow stem auger drill. The stratigraphy below Cluster 1 is as follows:

- Immediately below the trail level is a 1 m thick colluvial deposit which overlies the bedrock. The colluvial deposit comprises silty clay with low to intermediate plasticity, coal fragments, and organic matter.
- The bedrock comprises clay shale, coal, and bentonite seams. A 0.7 m thick coal seam is located 3 m below the trail level. Pure bentonite seams about 0.2 to 0.3 m thick are located about 6.5 and 8.5 m below the trail level.

Instruments in Cluster 1 included one water standpipe, one inclinometer, one vibrating wire piezometer, two Geokon vibrating wire piezometers, two RST pneumatic piezometers, and one flushable piezometer. The water standpipe was installed 9 m below the trail level with a 6 m slotted section surrounded by clean sand. In order to compare the results of the different types of piezometer, piezometers were installed in two holes, 04-04A and 04-04B. In borehole 04-04A, one vibrating wire piezometer, one pneumatic piezometer, and one flushable piezometer were installed at 8.4, 8.7, and 9 m below the trail level, respectively. In borehole 04-04B, one pneumatic piezometer and two multi-level piezometers were installed at 8.4, 8.7, and 9 m below the trail level, respectively. The detailed installation plan is presented in Figure 6-22.

Cluster 2 was located 2 m behind the slope crest, about 60 m above the river level (Figure 6-21). Due to deeper installation depths, a rotary drilling rig was utilized for sampling and instrument installation. The following stratigraphic profile is obtained from the drill holes.

- Below the flat upland area is a 5 to 6 m thick lacustrine clay deposit interbedded with silt layers.
- Lacustrine clay is underlain by a 9 to 10 m thick sand and till deposit. The sand deposit is generally in a dense to very dense state with a moisture content of less than 10 %. The till is low plastic and has a moisture content range of 15 to 25 %.
- The till deposit is underlain by Upper Cretaceous bedrock, comprising clay shale and sandstone interbedded with coal and bentonite seams. The clay shale is low to intermediate in plasticity with a moisture content range of 18 to 22 %. Bentonite seams vary in thickness from 20 to 250 mm, but these layers are not continuous throughout the valley wall. Bentonite is very high to extremely high in plasticity with a moisture content range of 40 to 45 %.

Instruments in Cluster 2 include one water standpipe, one inclinometer, two RST pneumatic piezometers, one Geokon multi-level vibrating wire piezometer, and one flushable piezometer. The inclinometer (IN-01) was installed from the slope crest, about 60 m deep. The water standpipe (WS-01) was installed up to the contact of till and bedrock, about 16 m deep. The water standpipe had a 6 m slotted section at the bottom, surrounded by clean sand. The remaining part of the hole was filled with cement grout.

In Cluster 2, piezometers (PZ-01) were installed at two elevations. The first group, comprising a pneumatic and a flushable piezometer, was installed at 18.7 m and 19 m below the slope crest, respectively, just below the till and bedrock contact. The second group, comprising a pneumatic and a multi-level vibrating wire piezometer, was installed at 35.7 m and 36 m below the slope crest, respectively. The detailed installation plan and stratigraphic profile are presented in Figure 6-23.

The instrument installation in Forest Heights Park, including piezometers and filter types used in each cluster are presented in Table 6-1.

6.8 Piezometer installation procedure

With the success of the laboratory investigation of the cement-bentonite grout mix, it was decided to utilize the grout-in installation method in this investigation. Grout mix C, with a water:cement:bentonite ratio by weight of 2.0:1:0.3 was used. This grout-in installation method was simple, fast, and less prone to error compared to the traditional installation method (Mikkelsen and Green 2003). By using a grout-in installation method, multiple piezometers can be installed in a single borehole at different depths. The installation procedure is discussed below.

6.8.1 Vibrating wire piezometer assembly

The vibrating wire piezometer assembly was as follows:

- 2.5 cm diameter grout pipes were laid on the ground and attached to the required length.
- The installation depths of the instruments were determined from the stratigraphic profile of the borehole.
- The filters were saturated using a vacuum at the laboratory and transported to the site submerged under water.
- The piezometer cavity was filled with deaired water and the filter was attached to the piezometer under water.

6.8.2 Geokon multi-level piezometer assembly

The Geokon multi-level piezometer was assembled as follows:

- The large filter tube and piezometer cavity were filled with water using a syringe.
- Special care was taken to prevent the entry of air into the piezometer system.
- The piezometer was held to the grout pipe with a single nylon Ty-rap that passes through two holes on opposite sides of the grout pipe.

Figure 6-24 shows the setup of Geokon multi-level piezometer attached to the grout pipe.

6.8.3 Flushable piezometer assembly

The flushable piezometer was assembled as follows.

- The flushable adaptor was connected to the Slope Indicator vibrating wire piezometer and a high air entry filter.
- Flushing lines were connected to the input and output check valves and the integrity of the seal was checked by flushing water through the piezometer cavity.
- The flushable piezometer unit was attached to the grout pipe with duct tape as shown in Figure 6-25.

6.8.4 Field installation

The field installation procedure was as follows.

- Grout pipe was assembled on the ground with piezometers attached at predetermined positions.
- After assembly of the piezometers and grout pipe, the grout pipe was pushed into the borehole together with the piezometer cables.
- When the grout pipe was at the desired depth, a steel rod was dropped inside the grout pipe to cut the nylon Ty-rap placed around the Geokon multi-level piezometer, leaving the spring loaded filters in firm contact with the borehole wall.
- Grout mix was prepared using a water:cement:bentonite ratio of 2.0:1:0.3. A rig pump fitted with a jet nozzle in a 50-gallon barrel was used to prepare the grout mix. First, a measured quantity of clean water was poured into the mixing barrel and pumping and circulation was started. Second, the required amount of cement was added to the water and mixed thoroughly. Third, the bentonite powder was slowly added into the jetting area of the barrel. Extra care was taken to avoid forming clumps of bentonite. As the required amount of bentonite was added, the watery mix changed to an oily consistency.

When the instruments were in place, the mix was pumped through the grout-pipe.

6.9 Monitoring procedures

Pore pressure readings were taken immediately after grouting the borehole. The readings were collected daily until the pore pressure stabilized with that of the surrounding ground. After pressure stabilization, readings were collected at two week and one month intervals. Pneumatic piezometers were measured with a monitoring unit equipped with nitrogen gas. Vibrating wire piezometers were measured using a data recorder supplied by Slope Indicator. After installation, the flushable piezometers were tested for the performance of the flushable mechanism using a portable hand pump. This process included taking initial readings of the flushable piezometer and flushing out the piezometer cavity from the ground. Once the flushing process was completed, the flushable piezometer readings usually returned to the initial value indicating that the seals were working properly after the installation. Figure 6-26 is a photograph of the installed flushable piezometer together with a hand pump used in the field and readout unit.

6.9.1 Cluster 1

Pore pressure monitoring results of Cluster1 are presented in Figure 6-27 together with the stratigraphic profile of the area. The water standpipe data revealed a groundwater level located at 1.2 m (elevation 629.6 m) below the trail level. Immediately after installation, all piezometers registered the pressure head of the grout mix. Within a week, the piezometers started to register the pore pressure of the surrounding material.

Vibrating wire piezometers installed below the trail level registered a piezometric head range of 2.2 m to 3 m. Pneumatic piezometers initially registered 4 m piezometric head. Among the vibrating wire piezometer, the lowest piezometric head was 2.2 m, observed from the flushable piezometer with the high air entry filter. The Geokon multi-level piezometer with spring loaded filters registered a slightly higher

piezometric head, about 2.5 m, and the Slope Indicator vibrating wire piezometer with a low air entry filter registered a head of about 3 m. During the monitoring period of November 2004 to early April 2005, all vibrating wire piezometers showed constant piezometric head readings. During the middle of April 2005, significant slope movements occurred at this location and a decrease in piezometric head was observed until the piezometers were damaged by the movements. Inclinator displacements revealed that the piezometers were located 1 m below the surface of rupture. During March and April of 2005, some variations in the groundwater level were observed due to snow melt and rainfall. The vibrating wire piezometers installed in the bedrock did not respond to these changes.

Even though the vibrating wire piezometers showed constant pore pressure one week after installation, a steady decrease in pore pressure was observed from the pneumatic piezometer until it was damaged by slope movements. The reason for this decrease was not clear. Over the long term, the piezometric pressure measured from the pneumatic piezometer tended to converge with the piezometric pressure from the vibrating wire piezometers.

6.9.2 Cluster 2

In Cluster 2, piezometers were installed at two elevations. A flushable piezometer and a pneumatic piezometer were installed 19 m below the ground surface and a pneumatic piezometer and a multi-level piezometer were installed 36 m below ground surface. The measured piezometric elevations, together with the groundwater level and stratigraphic profile, are shown in Figure 6-28. As shown, a perched water level was located in the overlying till, 12 m below the upland area. Seasonal variations in the groundwater level were observed in the spring and summer.

The flushable piezometer and the pneumatic piezometer, installed 18.7 and 19 m below the slope crest, registered 2.3 and 2.8 m piezometric head, respectively. The multi-level piezometer and pneumatic piezometer, installed 35.7 and 36 m below the slope crest, registered 4 m and 4.2 m piezometric head, respectively. Similar to Cluster 1, the vibrating wire piezometers equalized with the surrounding material in

one to two weeks after installation and showed constant piezometric pressure after that. A steady decrease in piezometric head was observed from the pneumatic piezometers installed at this location.

Figure 6-29 shows the pore pressure isochrone of the study area. The hydrostatic pressures were calculated from the observed perched water levels. As shown in the figure, piezometric readings of the bedrock are significantly lower than the hydrostatic pressure. The maximum pore pressure measured in the bedrock was 35 kPa at a depth of 36 m below the crest. This finding is in good agreement with Koppula and Morgenstern (1984), suggesting that the valley bottom of some American and Canadian rivers could still be subject to vertical swelling deformations due to previous geological erosion.

Figure 6-30 shows a plot of pore pressure readings normalized with hydrostatic pressure. As shown in the figure, the normalized pore pressures of Cluster 1 ranged from 0.22 to 0.38 and the normalized pore pressures of Cluster 2 ranged from 0.16 to 0.17. The higher normalized pore pressure in Cluster 1 was related to the pore pressure response of the displaced material where the piezometers were installed.

6.10 Summary

A flushable piezometer was developed to improve pore pressure measurements in weak rock. The flushable piezometer is capable of flushing out air bubbles from the piezometer cavity and sealing off the cavity when the flushing is completed. This ability to seal off the piezometer cavity enables the piezometer to be installed at great depths.

The field investigation involved installation of different piezometer types in Upper Cretaceous bedrock. The monitoring results revealed that significant deficient pore pressure exists in the bedrock. Only a slight difference in piezometric pressure was observed with the use of high air entry and low air entry filters. The pore pressure response confirmed the findings from earlier studies. It also confirmed that there was no connection between the perched water level and the piezometric pressure of the bedrock. Although there were some variations in perched water levels during spring

and summer, piezometric pressures in the bedrock did not respond to these changes. Piezometers installed immediately below the sliding plane responded to slope movements by showing a decrease in piezometric pressure.

In weak rock, a faster pore pressure equalization time was observed from the vibrating wire piezometer compared to the pneumatic piezometer. The pore pressure response of the pneumatic piezometer appears to decrease with time, and the reason for this behaviour is unknown. The results of this field investigation indicate that vibrating wire piezometers are more suitable than pneumatic piezometers for monitoring pore pressure changes in river valley slopes with weak rock formation.

Table 6-1 Piezometer installation in Forest Heights Park

Instruments	Cluster 1			Cluster 2		
	No.	Filter	Depth	No.	Filter	Depth
Pneumatic Piezometer	2	LAE	8.7 m	2	LAE	18.7 m/35.7 m
Vibrating Wire Piezometer	1	LAE	8.4 m			-
Flushable Piezometer	1	HAE	9 m	1	HAE	19 m
Multi-level Piezometer	2	LAE	8.4 m/8.9 m	1	LAE	36 m
Water standpipe	1	-	9 m	1		20 m
Inclinometer	1	-	20 m	1		50 m

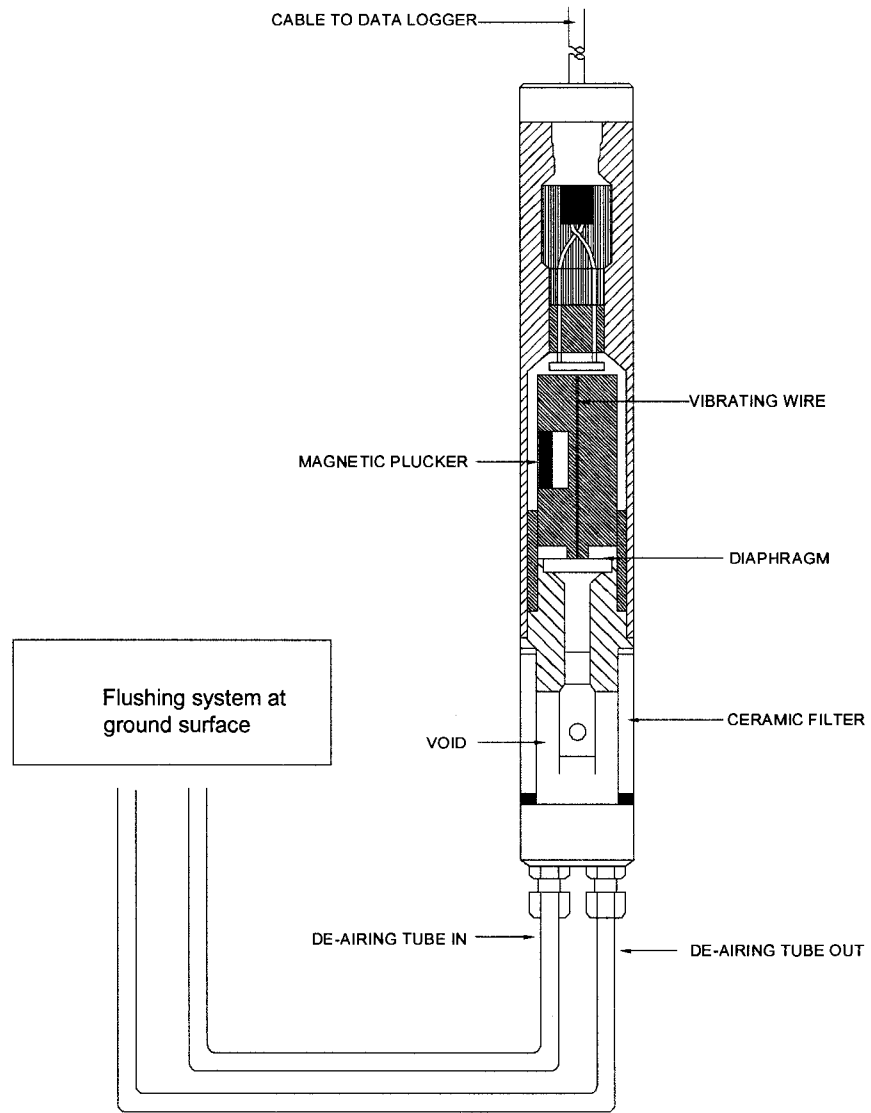


Figure 6-1 A flushable piezometer (modified from Long et al. 2004)

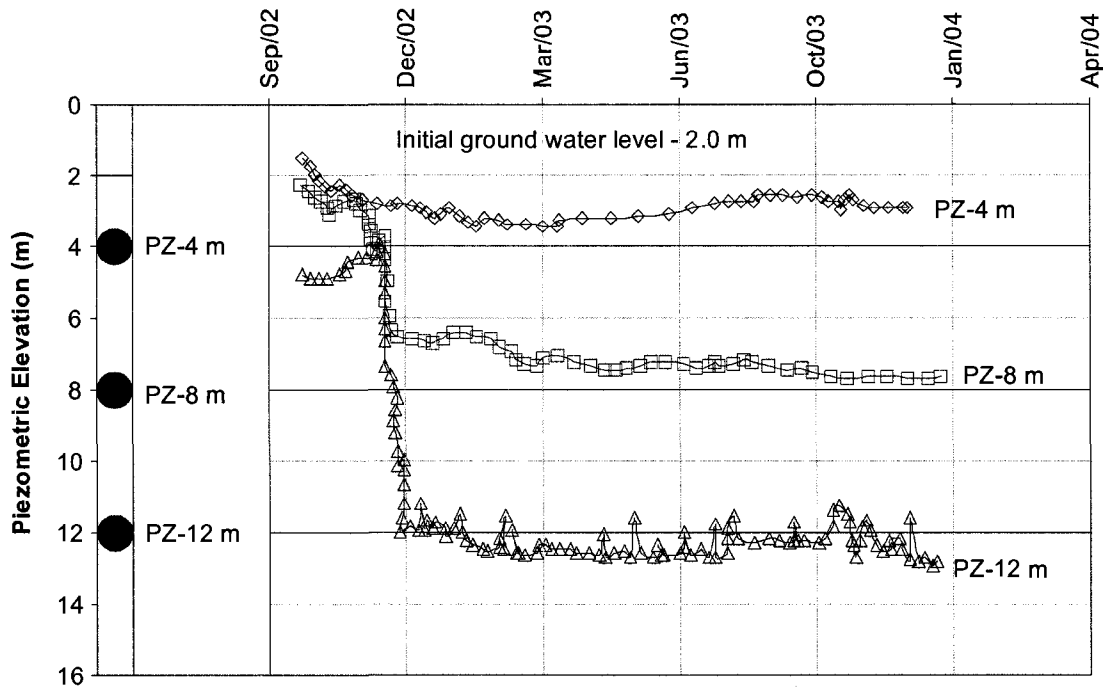


Figure 6-2 Piezometric Elevation – Main works Ch. 1320 W (data from Long et al. 2004)

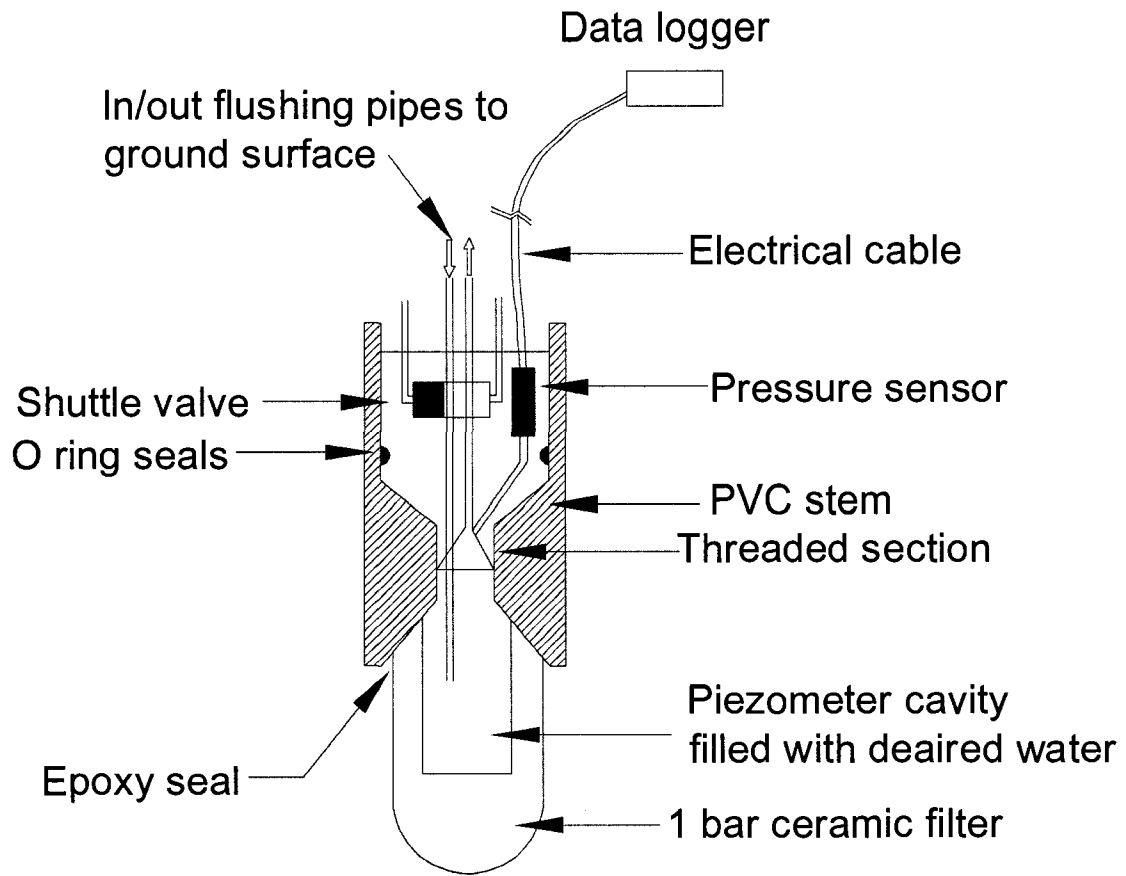


Figure 6-3 A new flushable piezometer (modified from Ridley et al. 2003)

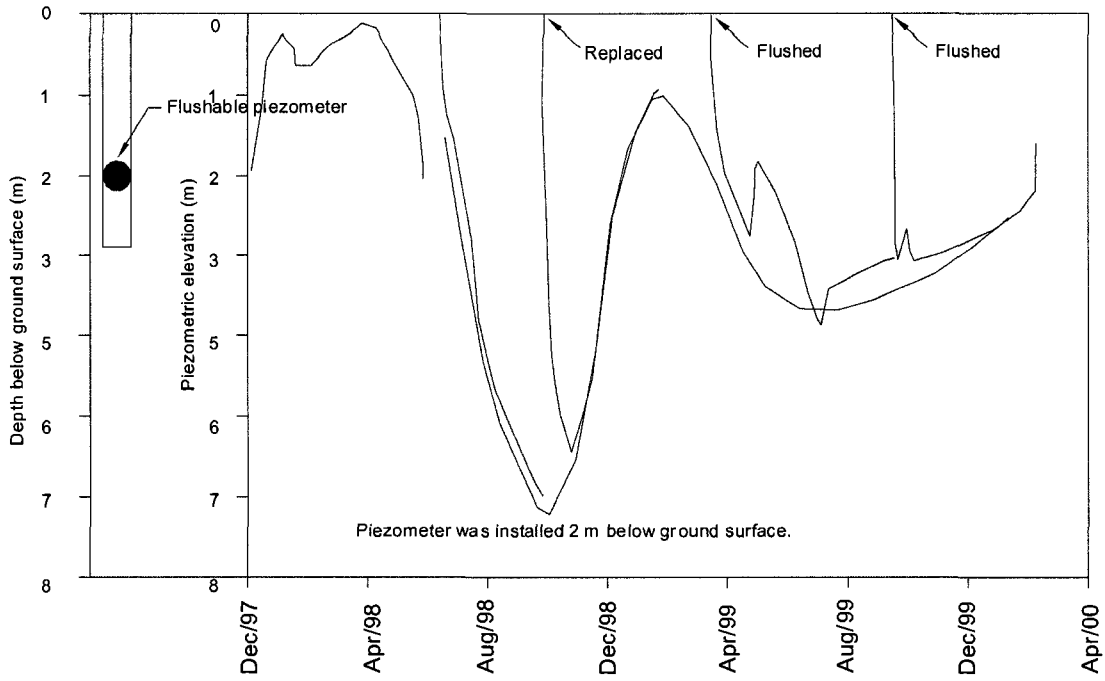


Figure 6-4 Pore pressure measurement at a depth of 2 m in an old railway embankment constructed of compacted London Clay (modified from Ridley et al. 2003)

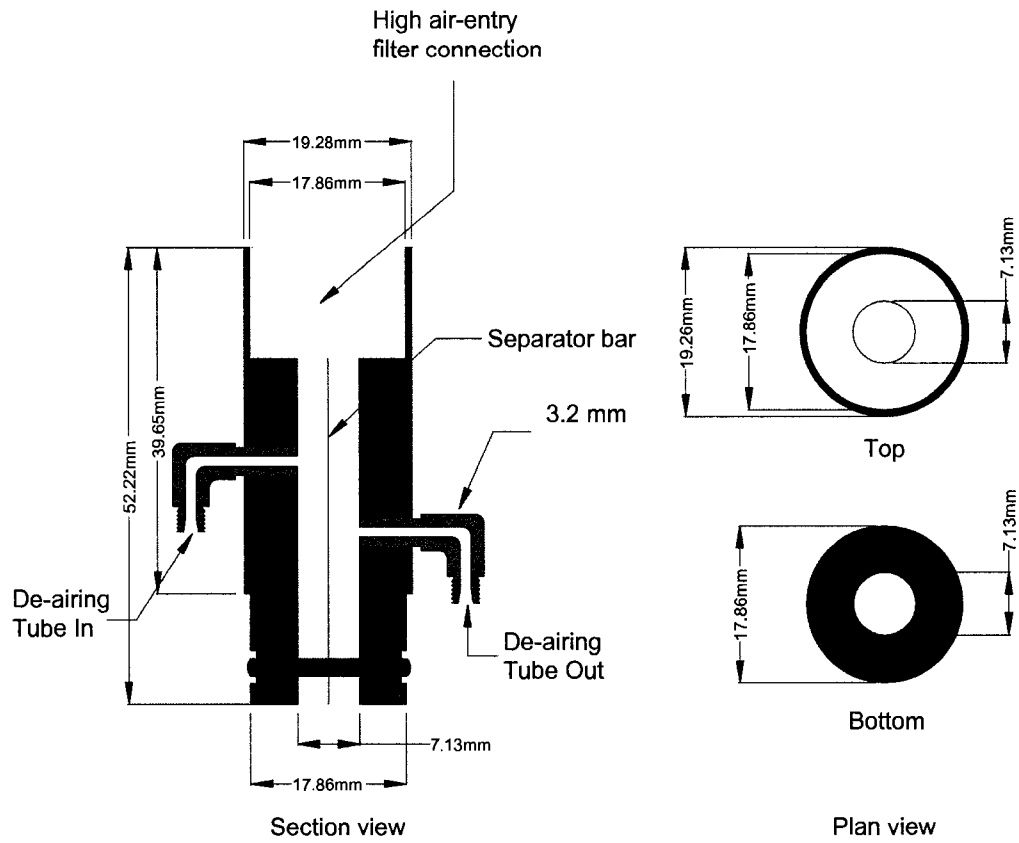
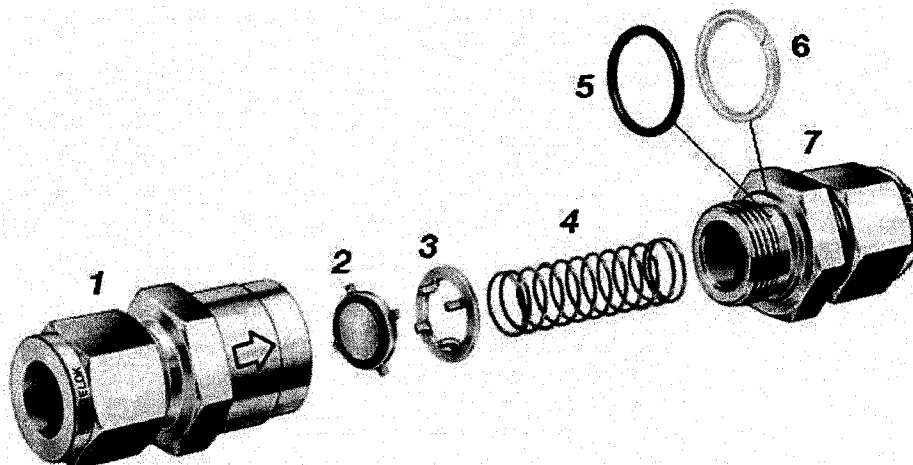


Figure 6-5 Detailed dimensions of a flushable adaptor



- | | |
|----------------|----------------|
| 1. Inlet body | 4. Spring |
| 2. Poppet | 5. O-ring |
| 3. Poppet stop | 6. Backup ring |
| | 7. Outlet body |

Figure 6-6 The Swagelok CH series check valve

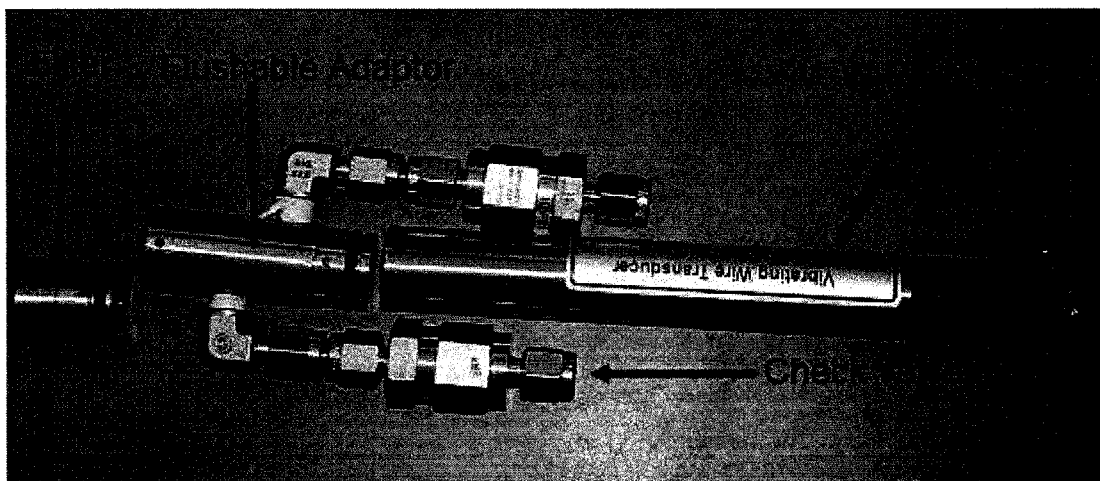


Figure 6-7 Vibrating wire piezometer with flushable adaptor

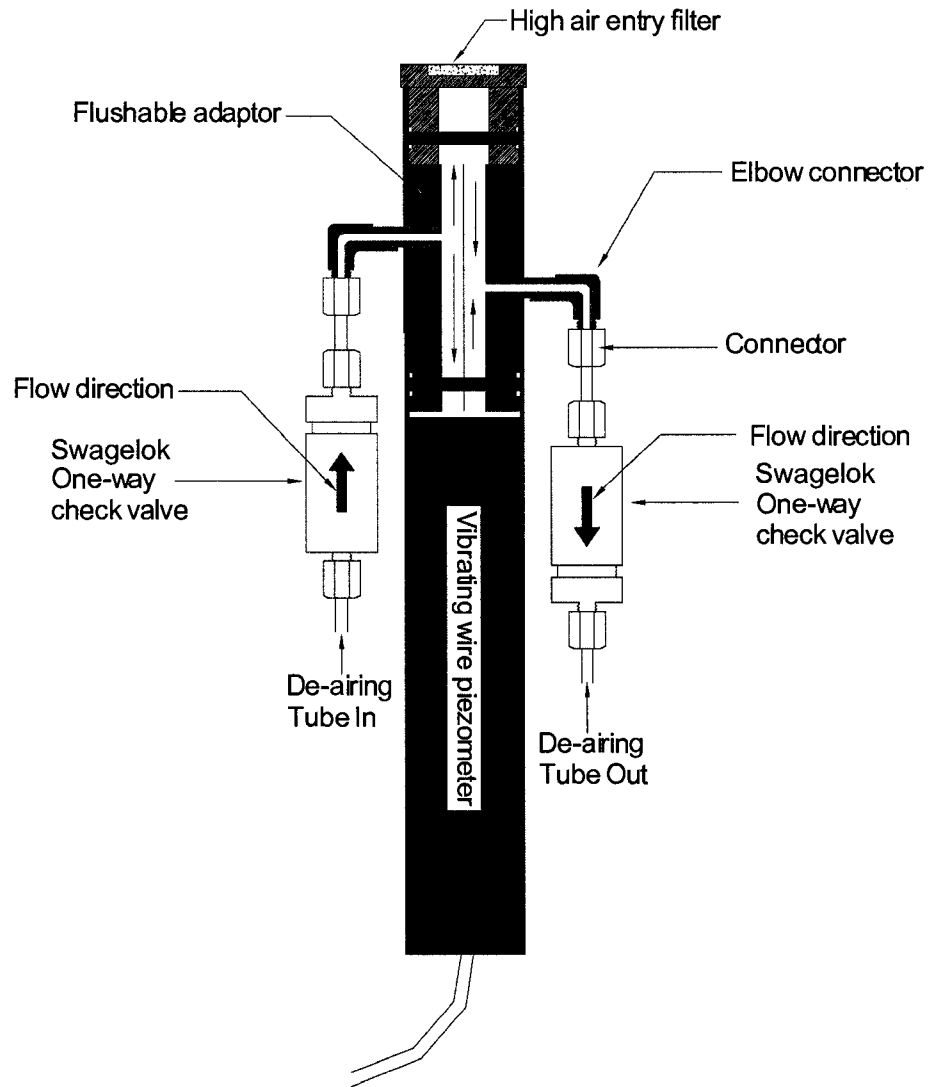


Figure 6-8 Setup of a flushable piezometer

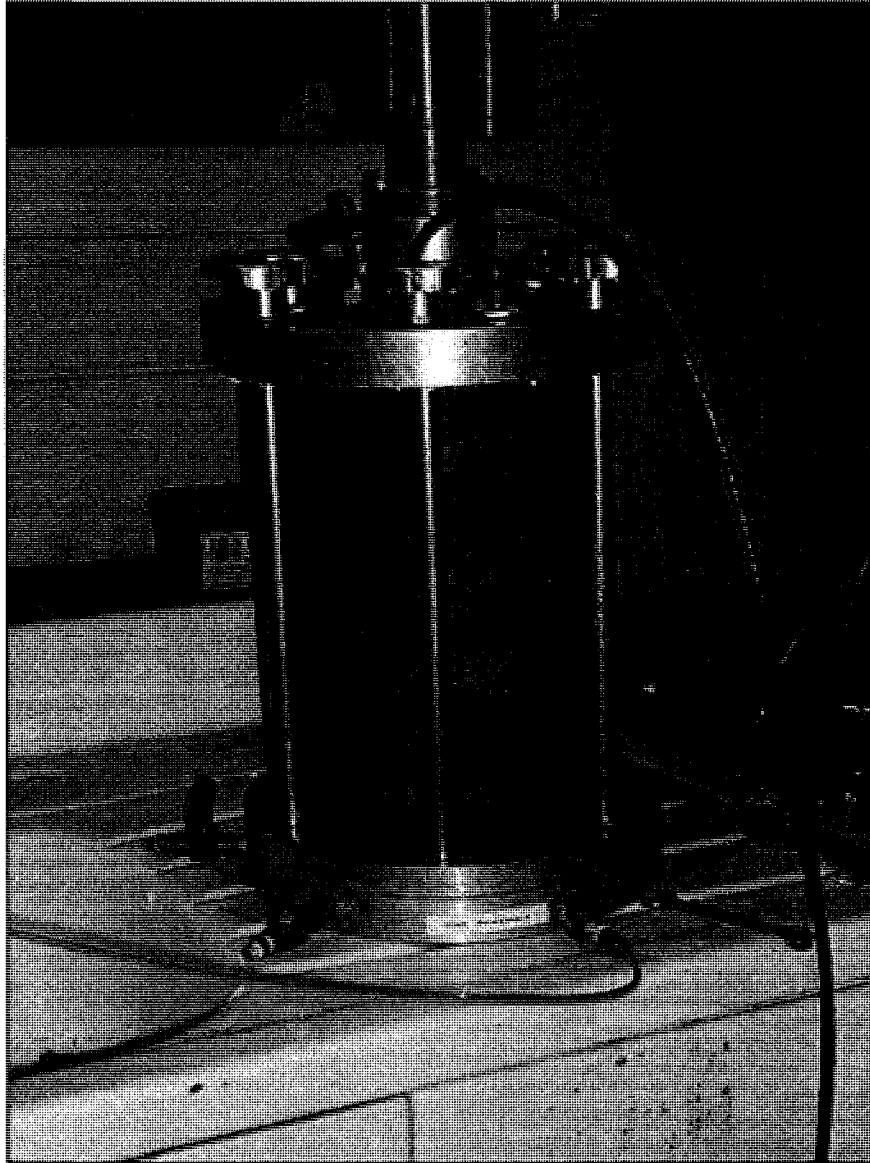


Figure 6-9 Large triaxial cell used for testing of the flushable piezometer



Figure 6-10 GE DPI 603 portable pressure calibrator



Figure 6-11 Slope Indicator vibrating wire data recorder



Figure 6-12 Assembly of a flushable adaptor for testing



Figure 6-13 Setup of a flushable piezometer test

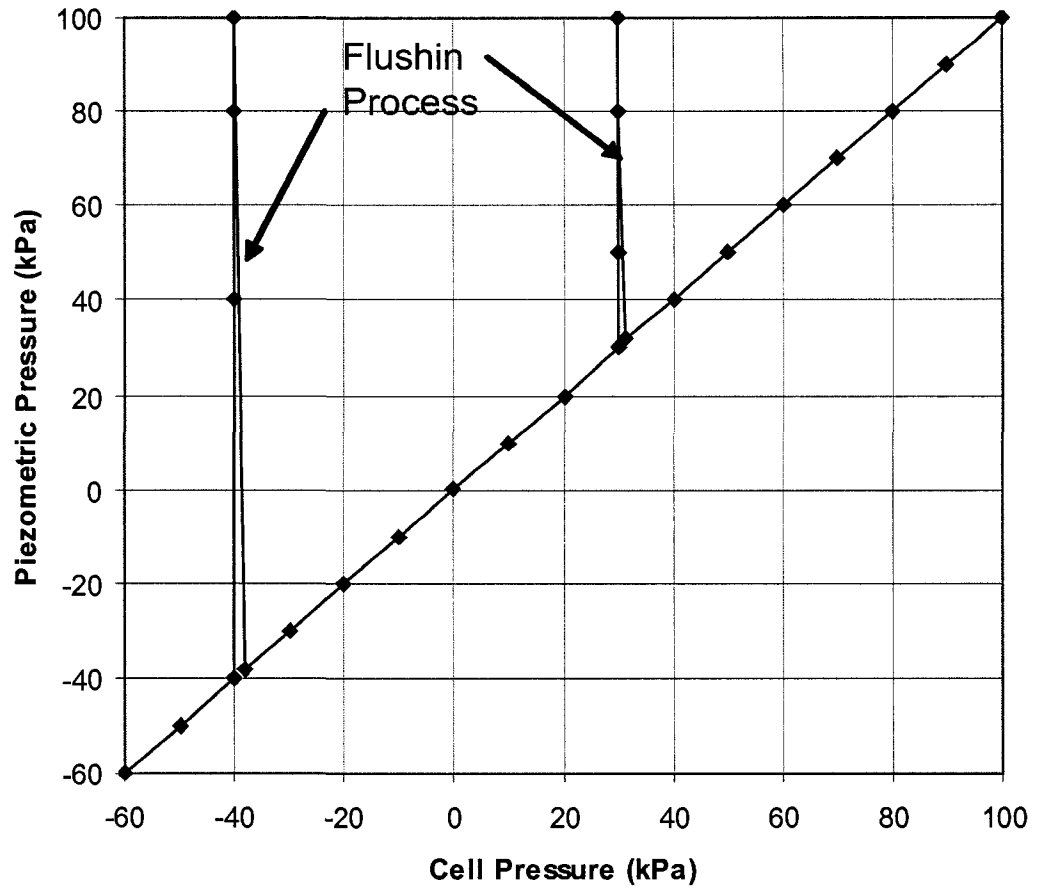


Figure 6-14 Pressure response test of a flushable piezometer

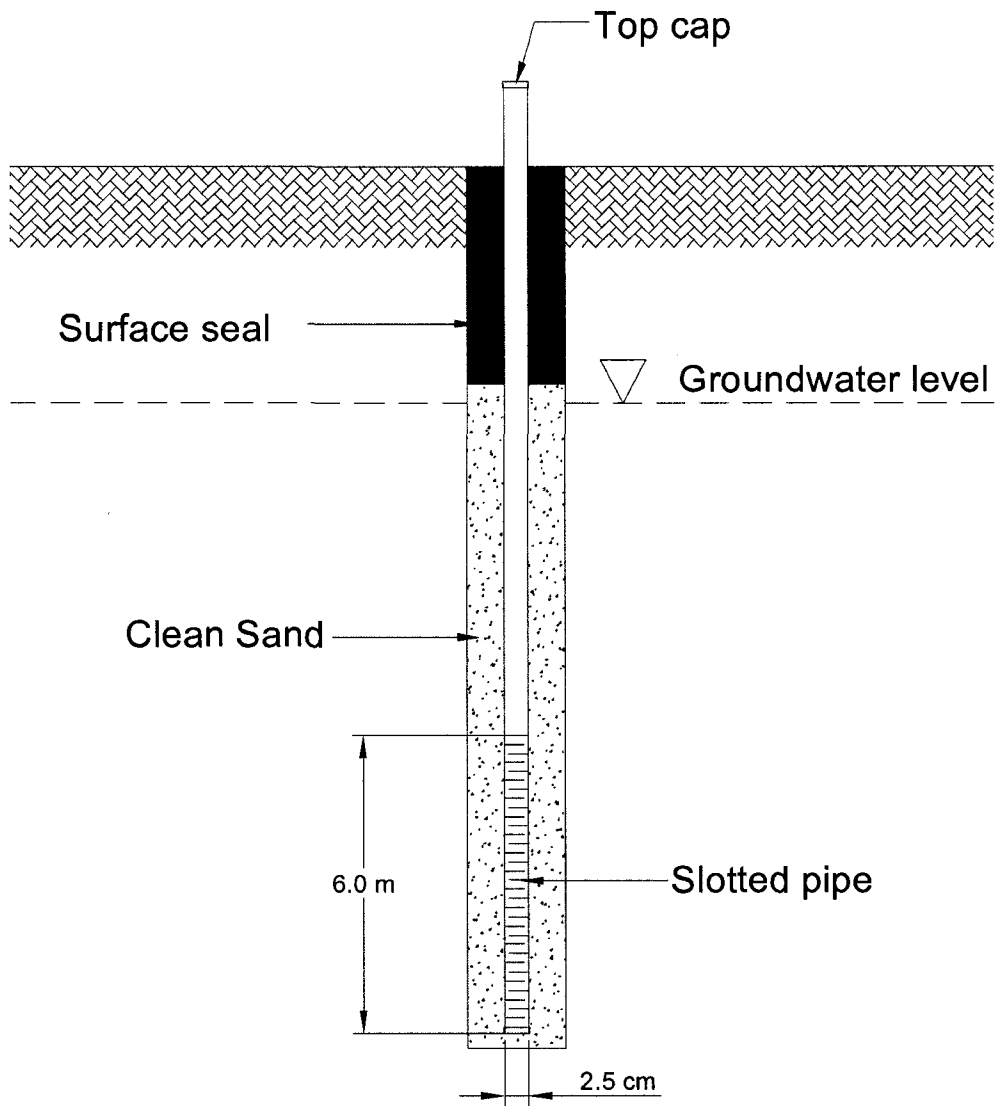


Figure 6-15 Water standpipe used in Forest Heights Park

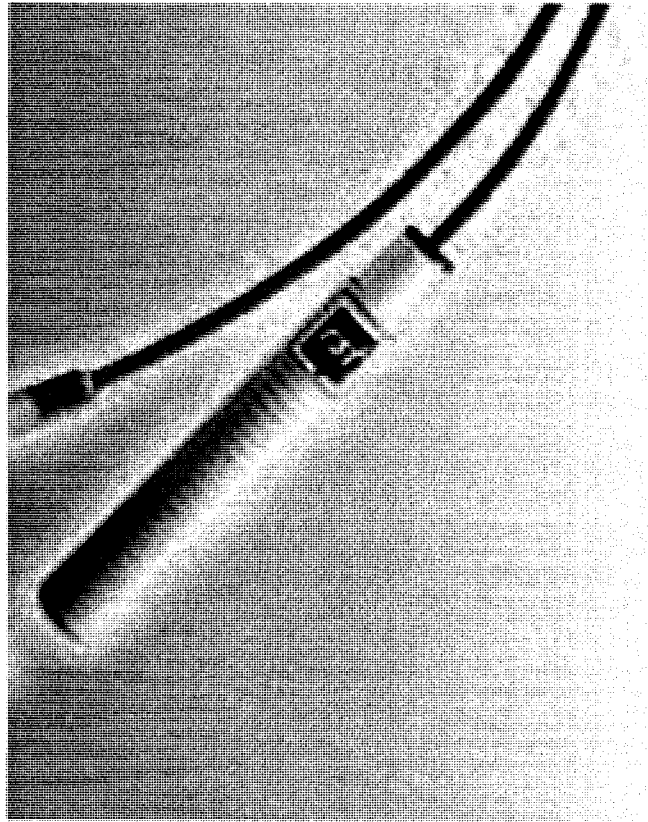


Figure 6-16 RST P-100-1 Pneumatic Piezometer

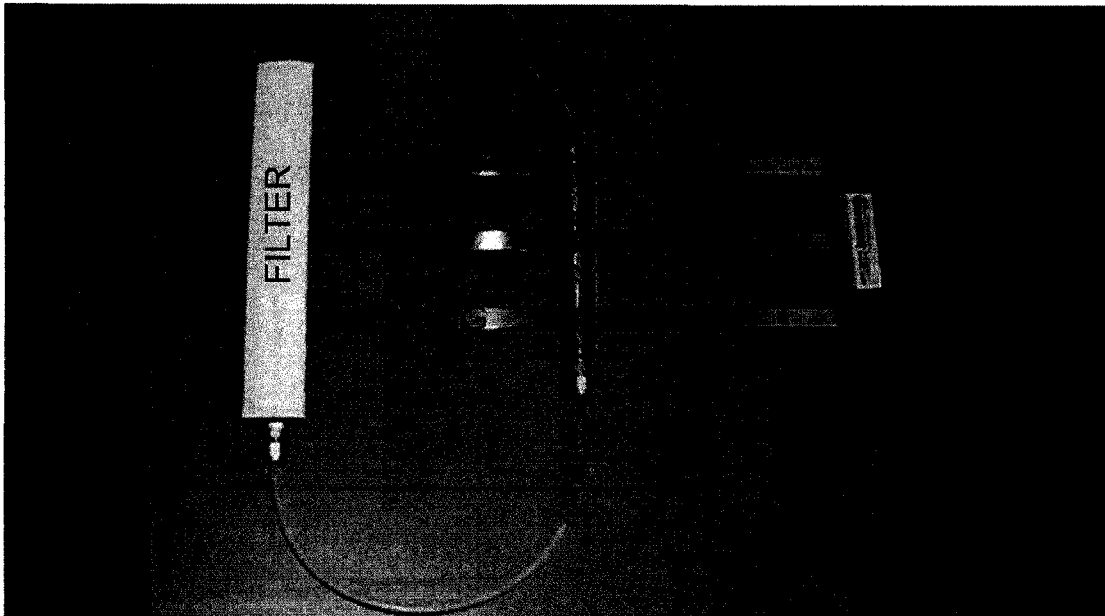


Figure 6-17 Geokon multi-level piezometer

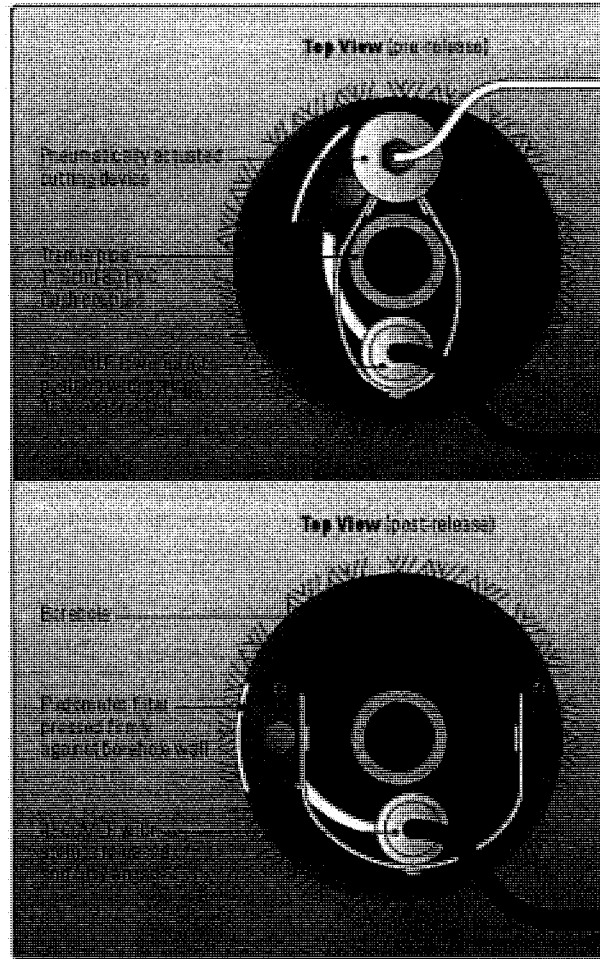


Figure 6-18 Geokon 4500MLP installation details showing spring loaded mechanism in closed configuration (top), and released (bottom)



Figure 6-19 Slope Indicator's vibrating wire piezometer

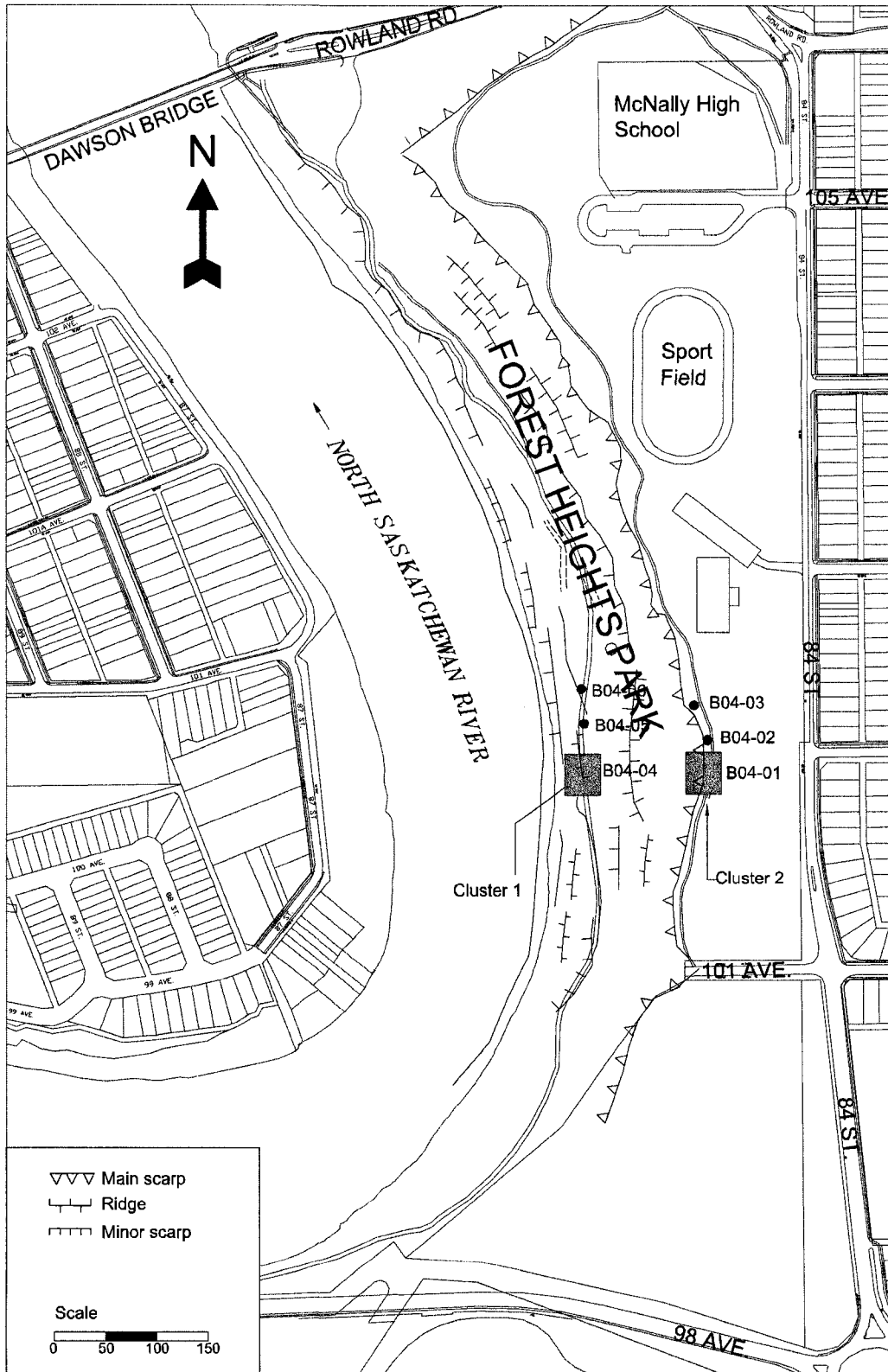


Figure 6-20 Location of field instrumentation in Forest Heights Park

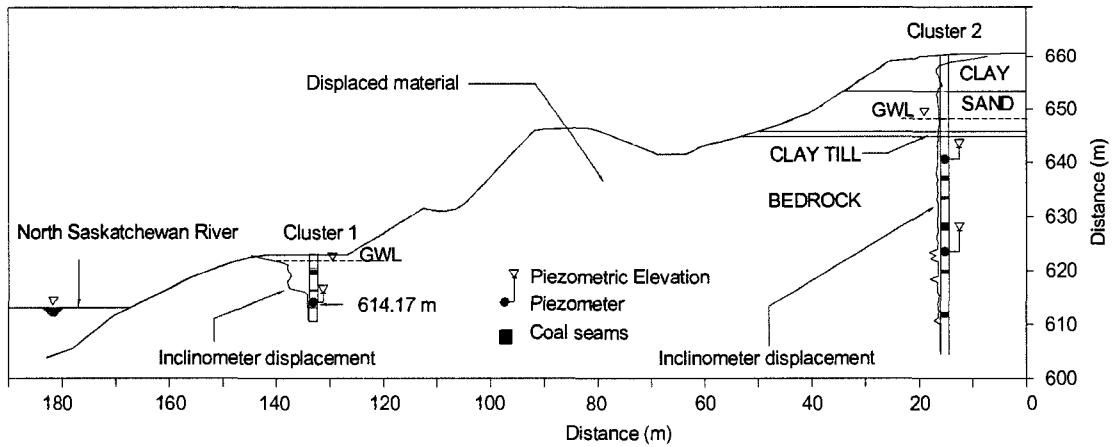


Figure 6-21 Field grout-in piezometer installation in Forest Heights Park

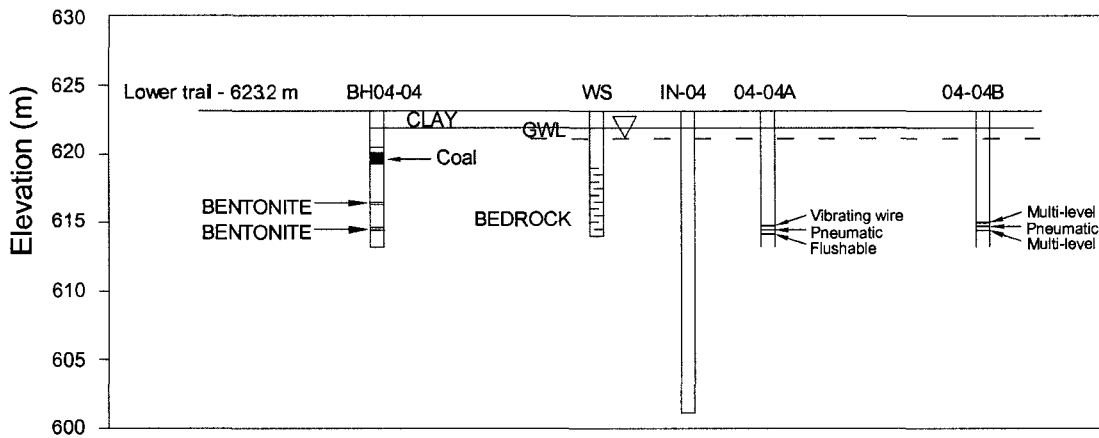


Figure 6-22 Piezometer installation plan in Forest Heights Park (Cluster 1)

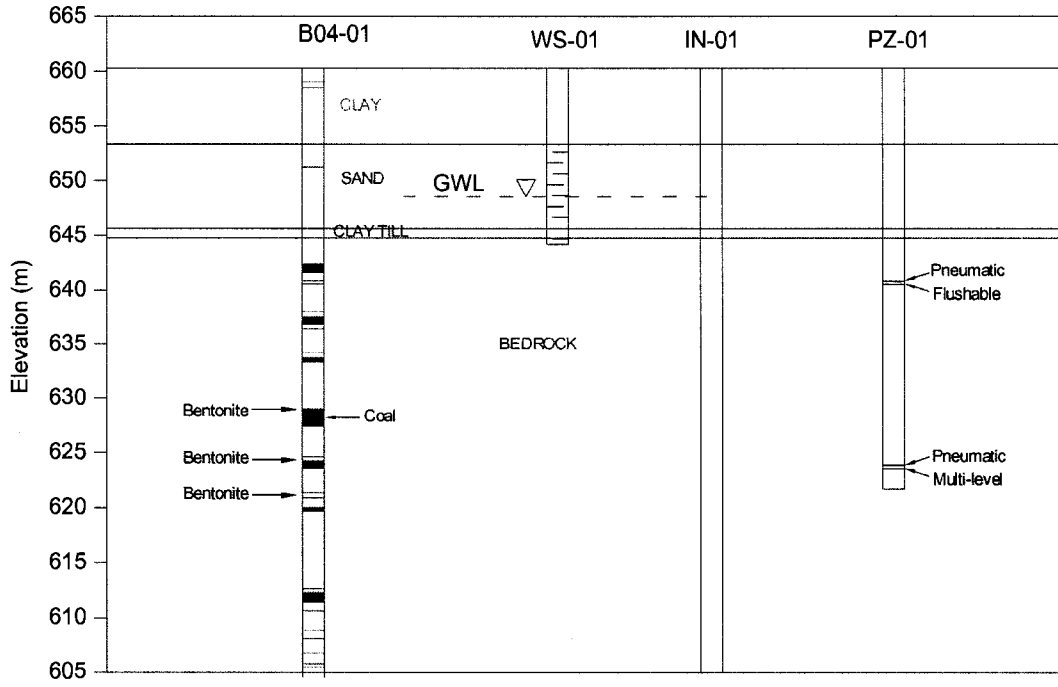


Figure 6-23 Piezometer installation plan in Forest Heights Park (Cluster 2)

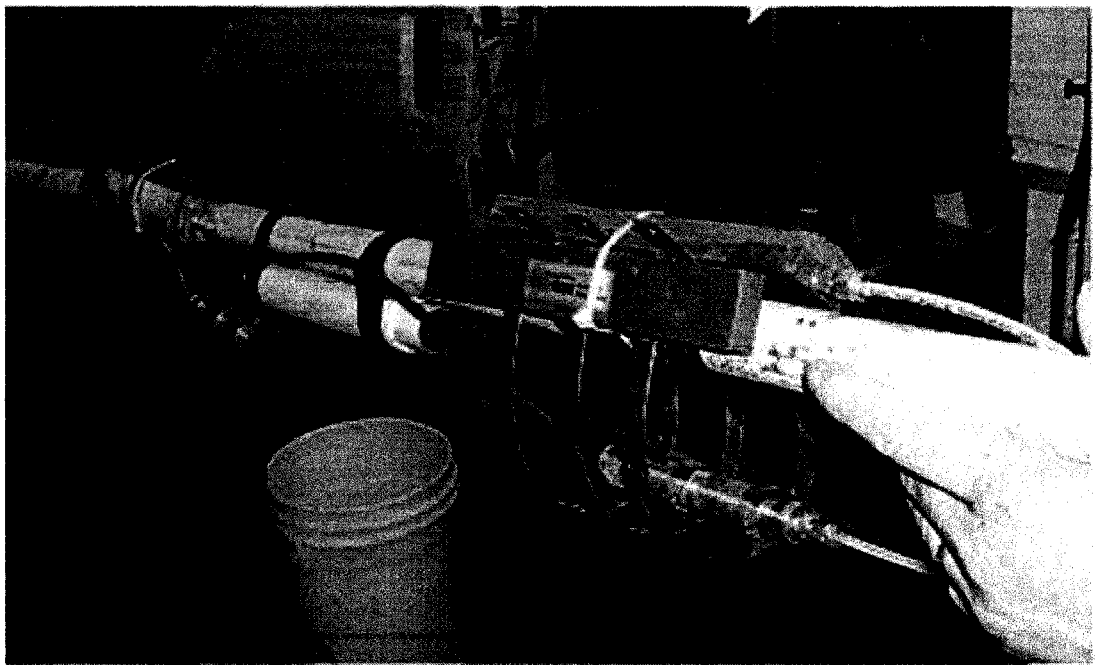


Figure 6-24 Multi-level piezometers attached to grout pipe with a Ty-rap

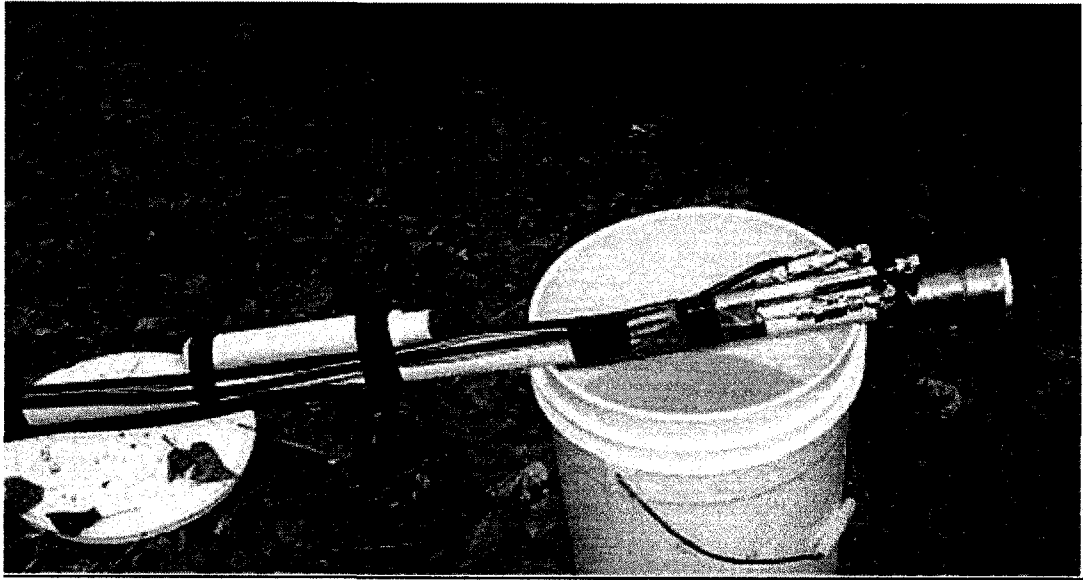


Figure 6-25 Flushable piezometer and pneumatic piezometer attached to grout pipe

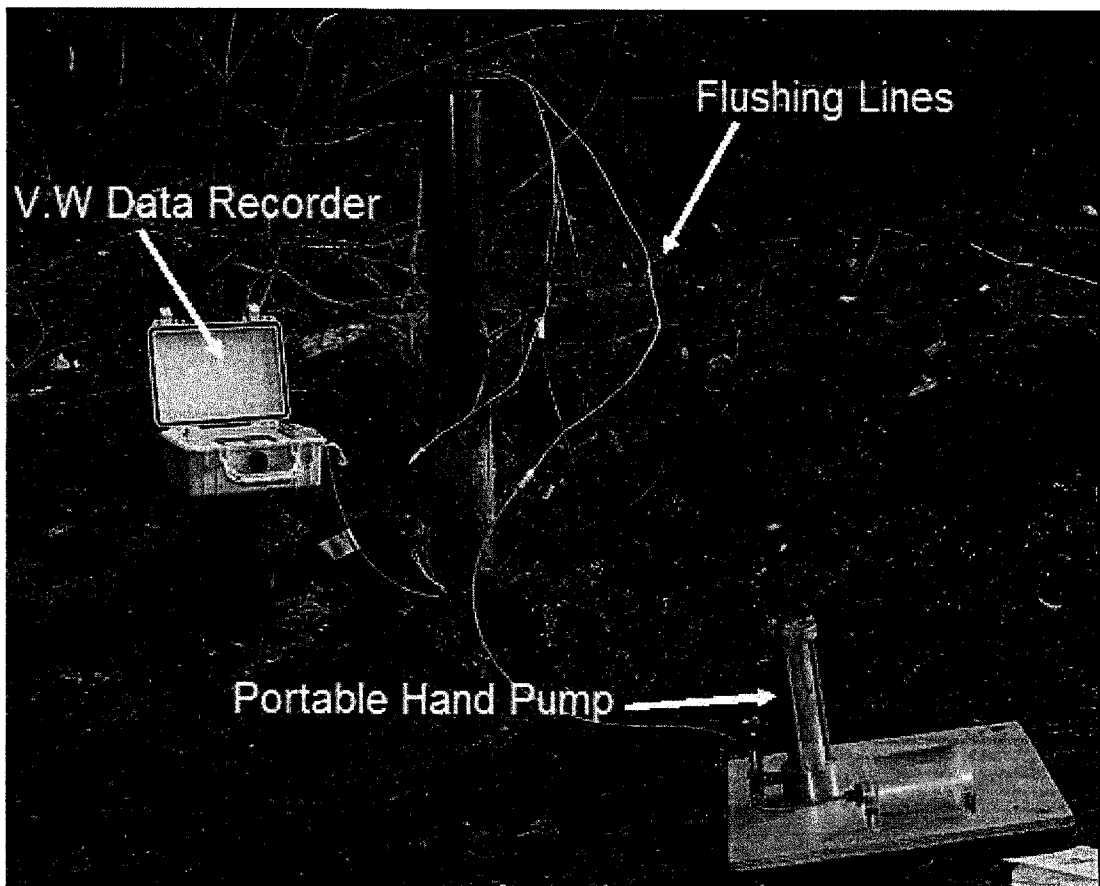


Figure 6-26 Field monitoring of a flushable piezometer

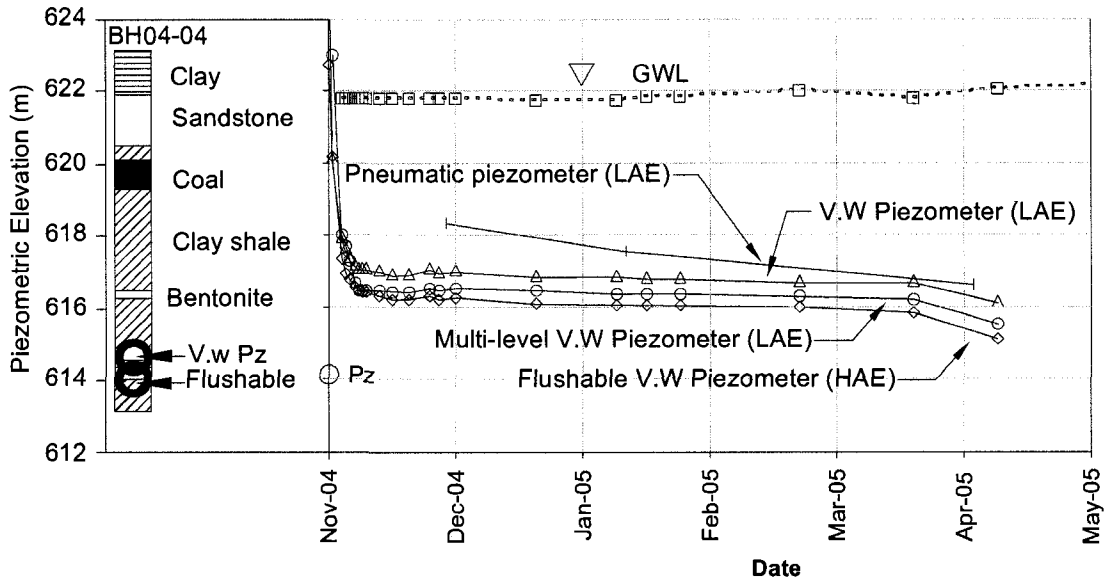


Figure 6-27 Pore pressure monitoring results of Cluster 1

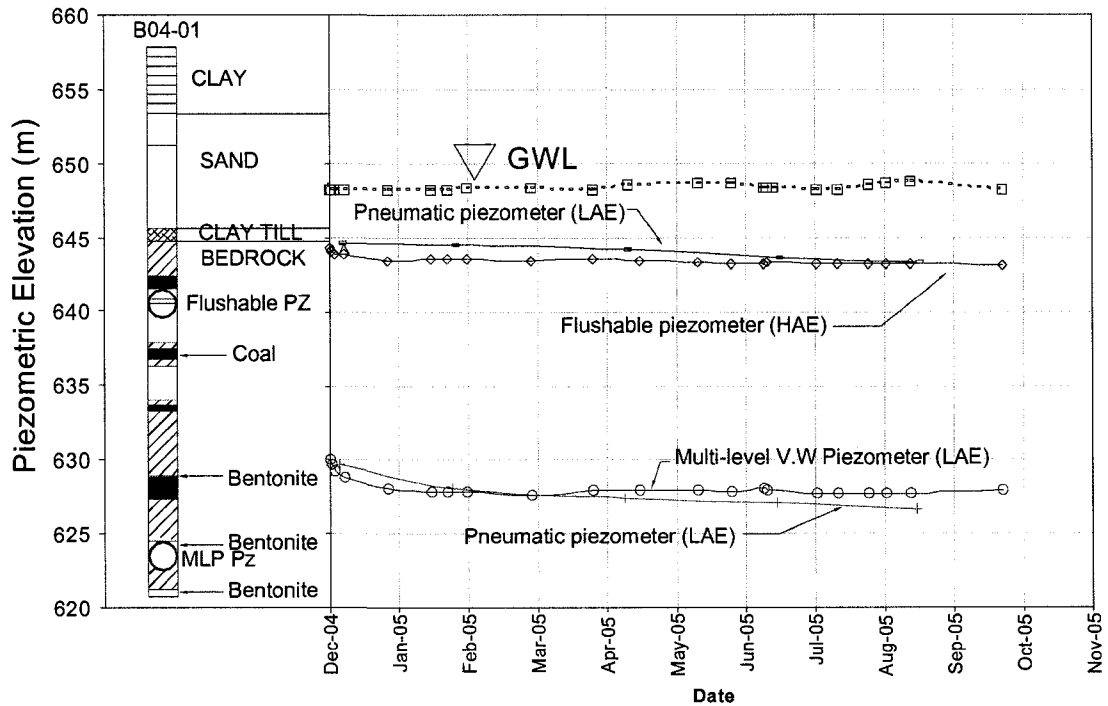


Figure 6-28 Piezometric elevation (Cluster 2)

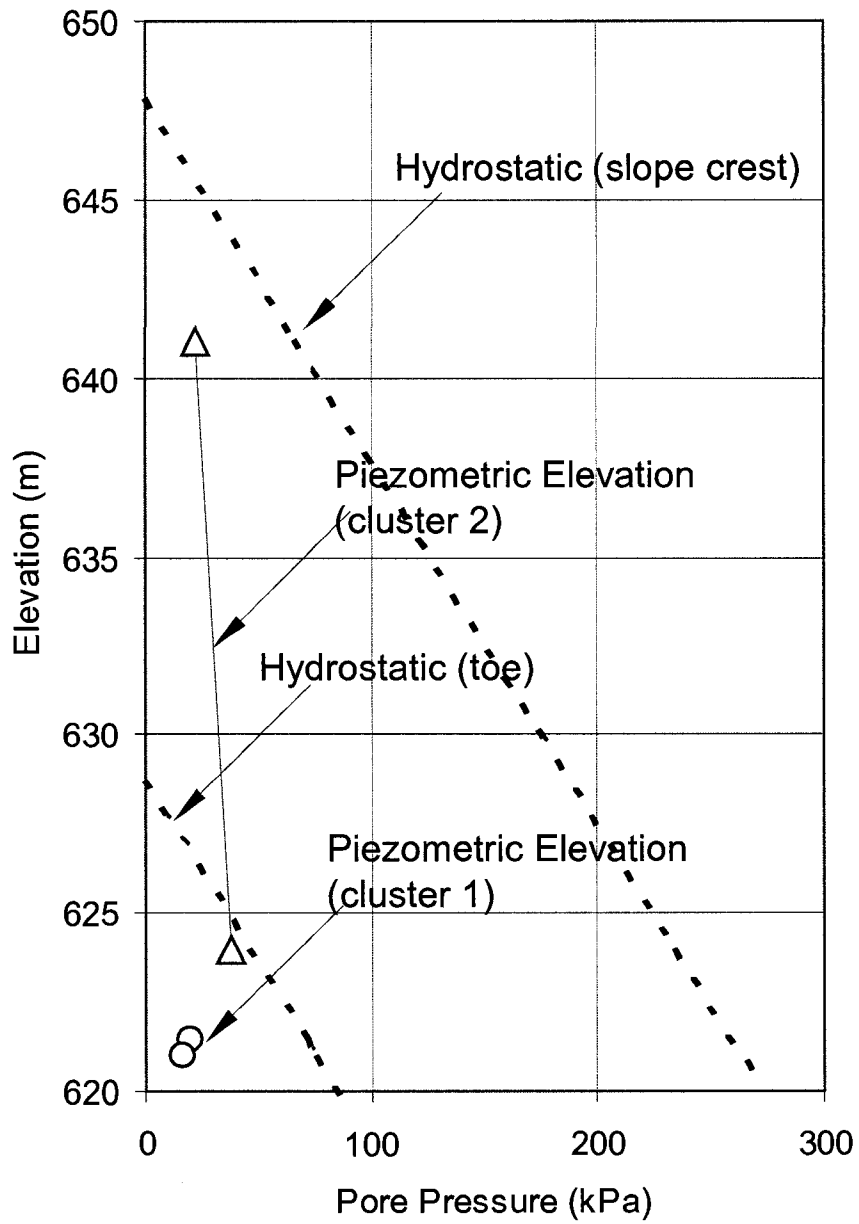


Figure 6-29 Pore pressure isochrone (07/04/2005)

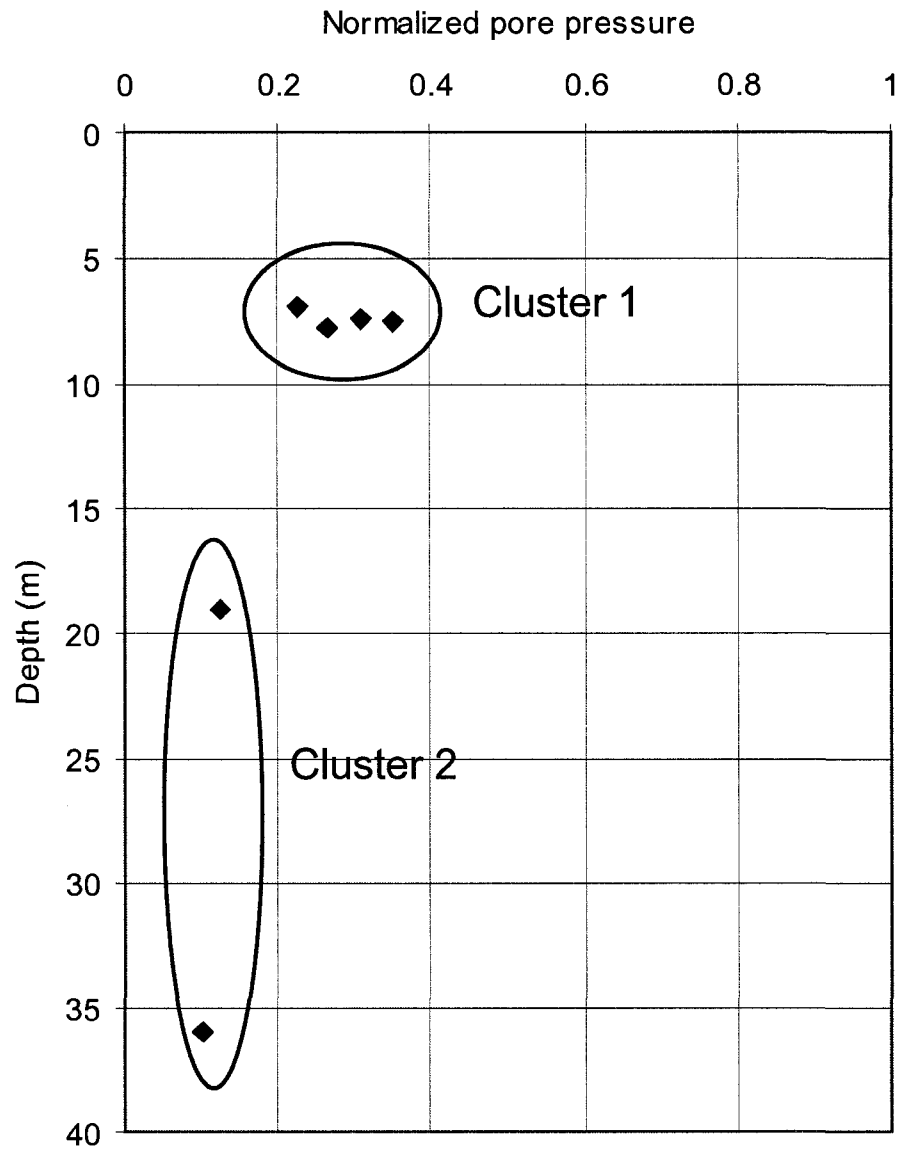


Figure 6-30 Normalized pore pressure plot

CHAPTER 7 Keillor road landslide

7.1 Introduction

Keillor Road Landslide is located on the outside bend of the North Saskatchewan River, where Keillor Road traverses down from a flat upland area to a low level terrace (Figure 7-1), about 1.5 km southwest of the University of Alberta, Edmonton. The Keillor Road Landslide started as a minor toe failure in 1989, causing some damage to a recreation trail. Then the movement progressed upslope in 1994, causing some damage to Keillor Road, located about 40 m above the toe level. The 1994 movements in Keillor Road resulted in the construction of an 8 to 15 m deep cast-in-place pile wall in 1997. The construction of the pile wall could not fortify the weakened bedrock, some cracks appeared on Keillor Road in August 2001 and a major failure occurred in the fall of 2002. Due to the failure, a 5 m deep graben appeared at the head of the displaced material and broken bedrock slid into the river. The toe of the slope moved 22 m into the river. In total, the volume of soil and rock involved in the landslide was in the order of 100,000 m³.

After the 2002 failure, continued slope movements caused further downward movement of the graben resulting in a further 3 m retrogression of the main scarp within 2 years. Movement of displaced materials continues to be observed up to the present day. To determine the cause of this landslide, field and laboratory investigations were conducted in the summer of 2003 and 2004 (Ruban and Sabourin 2003; SoeMoe et al. 2005). The field investigation included boring and sampling of the intact and disturbed bedrock. Inclined meters and piezometers were installed to monitor slope movements and the pore pressure regime of the slide area. Total station surveys were conducted on the damaged piles and the valley wall to monitor the post-failure slope movements. Index tests and direct shear tests were conducted on intact and disturbed bedrock samples to determine the engineering

properties of the bedrock. In this study, major considerations were given to the evolution of the river valley landslide, the engineering properties of the clay shale bedrock and the landslide mechanism.

7.2 Landslide history

7.2.1 1989 Toe failure

In 1989, a minor slide displaced the lower 16 m of the valley wall, where a recreational trail is located (Figure 7-2). From time to time, fill had been previously placed on this level to remediate a drop at the edge of the trail. The resulting slope failure was shallow, with the depth to the slip surface was likely only a few meters (Barlow 1989). A concrete pile wall was constructed at the downslope edge of the trail to prevent further instability.

7.2.2 1994 Keillor Road failure

After the 1989 toe slide, slope instability gradually moved up the valley wall where Keillor Road is located. Minor movement along Keillor Road was first identified in 1994 and additional movements were recorded in 1995 and 1996 (Ruban and Pulles 1996). The area, located on the outside of the Keillor Road curve on the valley wall, had been repaired periodically by the City of Edmonton due to settlements and cracks on the asphalt. In 1997, a cast-in-place concrete reinforced cantilever wall was constructed to stabilize the roadway (Figure 7-2). The depth of the installed piles ranged from 8 to 15 m (Lewycky 1997).

7.2.3 Major failure 2002

The pile wall performed satisfactorily until August 2001, when cracks started to appear across the roadway and the concrete pile wall. With time, the cracks developed to a vertical scarp and a major failure occurred in the fall of 2002 (Figure 7-3). The scarp was 50 m wide at the crown but widened to nearly 200 m at the river level. Due to the failure, the head of the displaced material moved downward and

formed a graben with a vertical drop of 5 m (Figure 7-4). The main body of the landslide slid into the river, and the toe moved 22 m into the river.

The main scarp was located 45 m above river level and the horizontal sliding plane was located 10 m above the river level. A counter scarp was located about 26 m from the main scarp. The steeply dipping main scarp and the counter scarp encompassed a graben which had the shape of an ellipse in plan. Cracks and ridges appeared on the valley wall as a result of slope movements and differential settlement.

Both the main scarp and the counter scarp sloped at about 80° to 85°. Mature trees inside the graben were sub-vertical to vertical. Concrete piles installed at the lower trail level were overturned by the slope movement (Figure 7-5). After a heavy rainfall, seepage holes appeared on the scarp and the rate of the slope movement increased. As the toe materials moved toward the river, the graben underwent additional settlement. Landslide relics were observed at the exposed scarp at toe, confirming that part of the landslide was the reactivation of an old landslide.

7.2.4 Air photo review

In order to identify the development of the landslide in Keillor Road, historical airphotos from 1978 to 2002 were reviewed and compared with the available information of the area. The following are some of the events deduced from this study.

- May 1978 airphoto shows landslide deposits in the upstream and downstream portion of the present slide area.
- No significant movements are observed on the valley wall during the period of 1980 to 1990.
- May 1995 airphoto shows several cracks along Keillor Road and disturbed trees at the valley wall.
- May 1997 airphoto shows the newly constructed cast-in-place concrete pile wall along the Keillor Road.

- In the June 1999 airphoto, disturbed trees are found on the valley wall immediately down slope of the Keillor Road to the lower trail level.
- In the May 2002 airphoto, tension cracks appeared on Keillor Road around the main scarp and a more disturbed tree line could be seen on the valley wall. Significant slope movement might have occurred on the valley wall by this time.

7.3 Site investigation and instrumentation

7.3.1 Pre-2002 investigation

No detailed investigation was conducted in response to the 1989 toe failure (Barlow 1989). In 1994, after subsidence was observed in Keillor Road, two inclinometers (B94-1 and B94-2) were installed within the subsidence zone in June 1994. Eleven boreholes (B95-1 to B95-11) were advanced in 1995 from the Keillor road surface with depths ranging from 3 to 15 m (Bergman and Ruban 1995). Three additional inclinometers (B01-1 to B01-3) were installed in November 2001 after cracks appeared in the roadway (Ruban and Sabourin 2003) (Figure 7-6).

7.3.2 Post-failure investigation

After the major failure in 2002, an extensive site investigation and instrumentation program was carried out in the spring of 2003 by the City of Edmonton (Eglauer and Ruban 2005). Drilling was conducted using a rotary drilling rig with a triple tube core barrel. Bedrock core samples were collected and detailed logging was conducted to determine the weak planes and bentonite seams. Four boreholes (B03-3, B03-6, B03-7 and B03-8), with depths ranging from 45 to 50 m were advanced behind the slope crest. Another four boreholes (B03-1, B03-2, B03-4, and B03-5), about 20 m deep, were advanced at the lower trail to the toe of the slope. Inclinometers were installed down to the river level, about 60 m deep behind the slope crest and about 20 m deep from the lower trail. Figure 7-6 shows the different stages of the site investigation program carried out in the slide area.

7.3.3 Stratigraphy

A stratigraphic profile of behind the valley wall, deduced from boreholes during 2003 investigation is presented in Figure 7-7. The stratigraphic profile behind the valley wall can be described as follows

- The bedrock, the Horseshoe Canyon Formation of the Edmonton Group, comprises interbedded layers of clay shale, bentonitic sandstone, sandstone, coals, and bentonite seams. Bedrock samples revealed that the clay shale was often brecciated with slickensides. Due to the depositional nature, the bedrock layers are not continuous.
- The bedrock is overlain by a 2 to 6 m thick till deposit. The till is stiff to very stiff, high plasticity, with numerous local bedrock fragments and a few carbonate fragments.
- The till is overlain by a layer of lacustrine clay. The lacustrine clay is 4 to 7 m thick, silty, soft to medium stiff, and has low to intermediate plasticity.

A stratigraphic profile of the valley wall, deduced from boreholes drilled through the displaced material is presented in Figure 7-8. This area, located 10 m below the slope crest, has drilling records dating back to 1995. Several inclinometers, water standpipes, and piezometers were installed in this area to monitor the slope condition. Drilling records revealed 2 to 3 m thick colluvium and fill materials overlying on the weathered bedrock. Drilling records of boreholes B94-1 and B94-2 noted a loss of drilling fluid during drilling, possibly through cracks in the displaced material. Inclinometer displacement in 1996 revealed that a failure plane was located 2 to 4 m below Keillor Road. By 2002, a deeper failure plane, located 5 to 10 m below Keillor Road was observed from these inclinometers. The progression of the failure plane indicates that the main scarp is progressing downward through the weak bedrock with time. The stratigraphic profile is presented in Figure 7-8, together with boreholes and inclinometer displacements in 1996 and 2002.

7.3.4 Pore pressure regime of the slide area

Water standpipes installed behind the valley wall revealed that a groundwater level is located in the overlying till deposit, about 10 m below the slope crest. In 1995, six

water standpipes were installed around the unstable area on the valley wall. The installation depths ranged from 3 to 15 m. Four standpipes where water was encountered were located inside the slide zone and the remaining standpipes were dry after installation (Figure 7-9). It is possible that the water level observed in these standpipes was from surface water seeping through cracks in the weathered bedrock.

Pneumatic piezometers were installed in the bedrock at several locations. In 2001, three piezometers were installed inside the displaced material. In 2003, four piezometers were installed below the surface of rupture, and seven piezometers were installed behind the slope crest. The piezometric elevations of two piezometers installed behind the valley wall are presented in Figure 7-10. Piezometer PZ-1, installed 20 m below the slope crest, showed only 0.5 m piezometric head. Piezometer PZ-2, installed 40 m below the slope crest, showed 8 m piezometric head after installation in 2003. As shown in the figure, Piezometer PZ-2 decreased steadily after installation and by September 2004, piezometer registered only 5 m piezometric head.

Figure 7-11 shows the displacement of Inclinator IN-02-2, and the piezometric pressure of Piezometer PZ02-1. Both inclinometer and piezometer were located at the toe of the slope, where most of the movements occurred. Piezometer PZ02-1 was located below the surface of rupture. As shown in the figure, as the displaced material moves along the surface of rupture, piezometric pressure of the bedrock decreases, possibly due to dilation of the bedrock. This reduction in pore pressure may improve the slope stability temporarily. Over time, swelling will occur, and the time-dependent reduction in strength will ensue.

To understand the pore pressure regime of the slide area, the measured piezometric pressures of the bedrock, together with the hydrostatic pressure calculated from the groundwater level, are plotted in Figure 7-12. As shown, the measured piezometric pressures from the bedrock are well below the hydrostatic pressure and in some cases, the readings are zero. These results indicate that significant deficient pore pressures still exist in the bedrock.

7.4 Laboratory Investigation

The laboratory investigation program included index testing and direct shear testing of core samples collected during the 2003 site investigation program. Several block samples were also collected from the shear zone at the toe. These samples were sealed and stored in a moisture and temperature controlled room until tested.

7.4.1 Index tests

Moisture content determination and index tests were performed on the core samples and the block samples collected from the rupture surface. Moisture content was determined following procedures of the ASTM Standard D2216 (2004) (laboratory determination of water content of soil, rock, and soil-aggregate mixtures). Liquid and plastic limits of the clay shale were determined following the ASTM Standard D4318 (2004) (standard test methods for liquid limit, plastic limit, and plasticity index of soils). A summary of moisture content and index tests are shown in Table 7-1.

Figure 7-13 shows the natural moisture content profile of the displaced materials below Keillor Road, where the main scarp is located. The moisture content of the fill and colluvium material ranged from 4 % to 9 %. The moisture content of the weathered bedrock, 4 to 8 m below Keillor Road, ranged from 25 % to 38 % depending on the weathering grade. At a deeper location, 10 m below Keillor Road, the moisture of the bedrock ranged from 15 % to 20 %, showing less weathering.

7.4.2 Direct shear tests

Consolidated drain direct shear tests were conducted in accordance with ASTM Standard D3080 (2004) (standard test method for direct shear test of soils under consolidated drained conditions) (Figure 7-14). Intact core samples, obtained from the bedrock behind the valley wall, were selected from the same elevation as the surface of rupture (Figure 7-6). Direct shear tests on core samples were conducted using five normal stresses (50, 100, 200, 400, and 800 kPa). For the shear plane samples, obtained from the sliding plane at the toe of the slope, direct shear tests

were conducted using 4 normal stresses (50, 100, 200, and 400 kPa). A summary of direct shear tests is presented in Table 7-2.

7.4.2.1 Sample Preparation

The core samples, obtained using a PQ triple tube core barrel, were 75 mm in diameter. To fit samples in the direct shear box of 63.5 mm diameter, samples were trimmed using a cutting ring and a sharp knife (Figure 7-15). The following procedure was utilized in sample preparation.

- Good quality core sample was obtained from the core box from the same depth as the surface of rupture.
- The core sample was cut to about 4 cm in length (Figure 7-15 a).
- Using a cutting ring as a template, the sample was trimmed to 1 or 2 mm larger than the final specimen size for a short distance ahead of the cutting edge (Figure 7-15 b).
- The cutting ring was pushed down slowly and steadily, keeping its axis vertical and ensuring that it was pushed squarely to avoid disturbance (Figure 7-15 c).
- Once the cutting ring covered the sample, the remaining surplus sample above and below the ring was cut off (Figure 7-15 d).
- A similar method was used to prepare the shear plane material.

7.4.2.2 Determination of rate of displacement

The rate of displacement at which specimens should be sheared in a drained direct shear test demands upon the drainage characteristics, the permeability, and the thickness of the sample. Since permeability is related to the coefficient of consolidation, the consolidation stage can provide data for estimating the likely time to failure (Head 1992). From the consolidation of a specimen under the applied normal pressure, a curve of settlement against the square-root-time (minute) can be obtained. A tangent is then drawn to the early straight line portion of the curve. This line is extended to intersect the horizontal line representing 100 % consolidation. The point of intersection gives the value of $\sqrt{t_{100}}$, which when multiplied by itself gives

the time intercept, t_{100} (min), as defined by Bishop and Henkel (1962). The time required to failure, t_f , is related to t_{100} by the following empirical equation:

$$t_f = 12.7xt_{100} \text{ min} \quad [7-1]$$

For the clay shale samples, significant swelling occurs at a low normal stress level. Swelling of 0.6 and 1.1 mm are observed at 50 and 100 kPa normal stresses. Only 0.1 mm swelling is observed when the normal stress is 200 and 400 kPa. Some consolidation is observed in with 800 kPa normal stress of the clay shale samples. Volume changes of the clay shale samples during the consolidation/swelling stage are presented in Figure 7-16. Calculated displacement rates ranged from 7.0×10^{-4} mm/min to 4.0×10^{-4} mm/min.

7.4.2.3 Testing Procedure

A summary of the testing procedure was as follows:

- Before shearing, the sample was allowed to consolidate/swell for 24 hours under an assigned normal stress.
- The rate of shearing was determined for each sample after the consolidation/swelling stage.
- The shear displacement was applied to the sample until it passes the peak strength. Usually, samples were sheared up to 6 mm for peak strength determination.
- To obtain the residual shear strength, the shear box was reversed to its original position and the sample was sheared again until a steady (residual) value of the shear strength was observed. This process was repeated until the sample achieved residual strength.

7.4.2.4 Results and discussion

The results of the direct shear tests on the intact clay shale samples are presented in Figure 7-17. Clay shale samples with low normal stress (100 kPa) show a ductile behavior, with a less distinct peak. This may be due to softening caused by swelling

during the consolidation stage. As the normal stress increases, the softening by swelling is less marked. At a higher normal stress, clay shale samples show brittle behavior with a distinct peak and less dilation. Sample dilation is seen in samples with normal stress up to 400 kPa. Only the sample with 800 kPa normal stress shows some contraction during shearing.

Stress-displacement curves for the residual strength of the clay shale samples are presented in Figure 7-18. As shown, the stress-displacement curves of the residual tests have no distinct peaks and show ductile behavior. Sample dilation during shearing is less marked compared to that of the peak shear test.

Direct shear tests conducted on the sliding plane materials are shown in Figure 7-19. The stress-displacement curves of the sliding plane material have no distinct peaks and show ductile behavior, similar to residual test of the clay shale samples. The main difference of the sliding plane material is that all the samples contracted during shearing, indicating disturbance caused by the landslide.

Direct shear tests on intact clay shale and sliding plane material revealed interesting strength and swelling characteristics. During the consolidation stage at low normal stress, clay shale samples swelled significantly. But during the shearing stage, these samples still showed significant swelling, indicating a stress path similar to the undisturbed samples, and unlike the behavior of remolded samples like sliding plane material. This finding is similar to the results obtained by Graham and Au (1985), conducted on overconsolidated Lake Agassiz clay.

Failure envelopes obtained from the direct shear tests are presented in Figure 7-20. As shown, the peak failure envelope of the intact samples is nonlinear with a distinct break in the slope at 200 kPa. Up to 200 kPa normal stress, clay shale samples behave as frictional material, showing a friction angle of 56° with zero cohesion. It is possible that swelling under low normal stress removed the cohesion part, and the clay shale sample behaves as a frictional material. At higher normal stress, the peak failure envelope of the clay shale sample has a friction angle of 30° with 190 kPa cohesion intercept. The failure envelope for residual strength of the intact sample is linear with a friction angle of 14.3° . A similar failure envelope is obtained from the

direct shear test of the shear plane material. A summary of the test results is presented in Table 7-3.

7.5 Post-failure landslide observations

After the major failure in 2002, a field observation program was planned to monitor the post-failure slope movement of the displaced material. This program includes landslide mapping, total station survey, and crack monitoring of the slide area. To monitor the slope movements with time, landslide features such as graben, tension cracks, scarps, and ridges were mapped monthly in the spring and the summer of 2003 and 2004 using a handheld GPS. The total station survey, conducted in the spring of 2003 and 2004, involved monitoring of the upper pile wall movement and the cross section survey of the landslide. Eighteen crack meters were installed at several cracks in the spring of 2003. The crack displacements were monitored weekly during the spring and summer of 2003 and 2004. Locations of the surveyed pile wall, the cross section used in the survey, and the crack meters are presented in Figure 7-21.

7.5.1 Pile settlement

Part of the main scarp cut the upper pile wall in half and the southern portion of the pile wall settled together with the graben (Figure 7-22). The survey result of the pile wall settlement, surveyed in the spring of 2003 and 2004 is presented in Figure 7-23. The maximum horizontal and vertical movements of the pile wall were 2.3 m and 5 m, respectively, in 2003 and an additional 1.7 m and 2.3 m, respectively, in 2004.

To determine the rate of pile wall movements, the maximum pile wall movements are plotted as shown in Figure 7-24. Pre-failure movements of 0.3 m horizontal and 0.5 m vertical are assumed to account for the movements prior to the 2002 failure. The rate of vertical movements decreased from 37.5 cm/month in 2003 to 19.2 cm/month in 2004. The rate of horizontal movements decreased from 16.8 cm/month in 2003 to 14.1mm/month in 2004.

7.5.2 Long-term monitoring of slope movements

Mapping of the landslide body was conducted monthly in the spring and summer of 2003 and 2004. Figure 7-21 shows the landslide map conducted in May 2003. In 2003, steep scarps are exposed at the center and right flank of the slide. The left flank is less distinct and is defined by a series of cracks about 1 to 2 m wide. The crown cracks are seen developing behind the main scarp. The graben, bounded by the main scarp and the counter scarp, is 28 m wide, 123 m long, and has an ellipse shape in the plan view. Several transverse ridges and tension cracks are located inside the graben. At the fringe of the slope, the graben disappeared as tension cracks. During the spring and summer of 2003, the lower main body is continuous with some longitudinal and transverse cracks. Steep scarps and cracks are also found at the toe of the slide. Displaced material at the toe extended 26 m into the river.

Slope movement significantly increased in the spring of 2004 due to snow melt and rainfall. A large part of the toe material broke up and slid into the river. The main scarp retrogressed 2 m upslope and the counter scarp moved a further 3 m toward the river from May 2003 to June 2004 (Figure 7-25). As the displaced material moves toward the river, more cracks appear on the valley wall.

7.5.3 Kinematics of the slide

In a landslide investigation, it is important to understand the mechanism and kinematics of the slide. On Keillor Road, inclinometers installed prior to the major failure revealed the development of the main scarp. Pre-failure cross-section, cross-section survey conducted in 2003 and 2004, together with the pile settlement are shown in Figure 7-26. As shown in the figure, the steeply dipping main scarp was determined from the two inclinometers installed at the main scarp. The surface of rupture was determined from the inclinometer displacement at the toe. The figure shows that the 1997 pile wall was not deep enough to prevent slope failure. Downward movement of the material inside the graben and the translational movement of the main body can be seen in the Figure 7-26 b and c. As the landslide progressed, more cracks appeared in the main body as a result of slope deformation.

The upper pile wall at Keillor Road moved downward, and piles at the trail near the toe tilted forward as the displaced material pushed the piles toward the river.

After the major failure in the fall of 2002, 18 crack meters were installed in the displaced material to monitor slope movement. Crack meter comprise of a quadrilateral array of four stakes initially in a nearly square configuration (Baum et al. 1988). Quadrilaterals can be placed at the lateral flank of a landslide or within the body of the slide deform with the landslide movements. Subsequent measurements of quadrilaterals are compared with previous measurements and used to compute displacements across landslide boundaries and strains and tilts within the body of the landslide. In the Keillor Road Landslide, wooden rods were used for quadrilaterals. The top of the rods were marked with nails for repeated positioning of tape measures as shown in Figure 7-27. Elevation difference was monitored with a manometer.

Crack Meters (CM) 1 to 11 were installed in the crown cracks located behind the main scarp. CM 14 to 16 were installed at the toe along the lower trail, and CM 12, 13, 17, and 18 were installed on the main body of the slide (Figure 7-25). Vertical and horizontal movements of the cracks were monitored regularly during the spring and summer of 2003 and 2004. The horizontal movements of six crack meters are presented in Figure 7-28, together with the daily rainfall data measured at the University of Alberta Weather Station, 2 km from the slide. CM-13, located in the toe of the slide, slid down to the river after a period of heavy rain in July 2004. CM-16 was damaged in early June of 2004 during heavy rainfall. As shown in the figure, the maximum movements are observed at the toe of the slide and significant increase in movement is observed during heavy rainfall. The average movements of the main scarp, the graben, and the toe in 2003 were 125, 250, and 350 mm/month, respectively. The average movements of the main scarp, the graben, and the toe in 2004 are 250, 500, and 850 mm/month, respectively.

A summary of average crack movements is presented in Table 7-4 . The movement increased in 2004 due to above average rainfall during that year. According to Cruden and Varnes' (1996) landslide velocity scale, post-failure slope movements fall in the range of slow to very slow.

In order to determine slope instability related to rainfall, the yearly rainfall data in the Edmonton area from 1987 to 2004 is presented in Figure 7-29, together with the recorded slope movements in the Keillor Road Landslide. As shown in the figure, three episodes of failure were observed during a year of lower rainfall following a year of above average rainfall. Therefore, other factors in addition to the pore pressure may have initiated slope failure.

7.6 Slope stability analysis

To obtain a reasonable estimate of the factor of safety, one must understand the pore pressure condition of the slide area. As presented in Section 7.3.4, the piezometers installed in the bedrock registered a very low or zero piezometric pressure. A perched water level was located in the overlying glacial deposits, but no consistent water table was located on the valley wall, even though seepage flow can be observed after rainfall. The groundwater table and the measured piezometric elevations of the bedrock in Keillor Road are presented in Figure 7-30.

Slope stability analyses are carried out using the SARMA (1979) method of limit equilibrium analysis which can be used to determine the stability of slopes of a variety of shapes. Strength parameters of the bedrock and the sliding plane are determined from the laboratory tests as shown in Table 7-3. The major unknown is the pore water pressure acting on the slope during the initial failure. Using the residual shear strength along the horizontal sliding plane without the water table produces a factor of safety of 1.8. When the full water table is used behind the main scarp, the factor of safety is reduced to 0.45. These results suggest that the strength parameters being mobilized at the initial failure may be greater than the residual strength, and that actual piezometric pressure during failure may be located some depths below the main scarp.

Parametric analyses were carried out to model a range of field conditions. It is assumed that a vertical crack formed at the scarp and was filled with water. A friction angle of 18° with varied cohesion values are used for the main scarp and the

horizontal sliding plane. For the analysis, full hydrostatic pressure acting on the main scarp was assumed. Since the measured piezometric pressure of the bedrock is low, the piezometric pressure on the sliding plane was assumed to be zero. Figure 7-31 shows the slide boundary and the groundwater levels assumed in the analyses.

Figure 7-32 shows the changes in the factor of safety with different cohesion intercepts for a series of main scarp distances from the toe. As shown, the factor of safety increases with a decrease in main scarp distance from the toe and an increase in the cohesion. The slope of factor of safety versus cohesion is linear for each main scarp distance.

Figure 7-33 shows the reduction in the factor of safety with the main scarp distances from the toe for the different cohesion values. As expected, the factor of safety decreased with an increase in the distance of the main scarp from the toe. For the Keillor Road Landslide geometry, mobilized shear strength parameters of $\phi' = 18^\circ$ and $c' = 10$ kPa are suggested.

7.7 Summary

A study of the Keillor Road slide provides an understanding of the landslide mechanism in Upper Cretaceous Bedrock slope. The slide evolved from a minor movement at the toe to a major landslide, taking out part of Keillor Road. The boring records showed that slickensides existed in the underlying bedrock. The development of the steeply dipping main scarp is observed from inclinometer readings. The main scarp might have followed the stress relief joints created by the valley formation. The weathering and softening caused a time dependent reduction in shear strength, especially in the cohesion of the material. The major failure might have been caused by the combined results of time dependent reduction of shear strength, the toe erosion by the river, and the surface and groundwater pressures.

Field instrumentation data revealed that a perched water level is located in the overlying till deposit. Piezometers installed in the bedrock showed that significant deficient pore pressures exist in the bedrock.

The stability analyses suggest that initial slope movement may have been caused by hydrostatic pressure acting on the main scarp. The measured piezometric pressures do not represent the initial failure conditions.

Crack monitoring data revealed that the movement of displaced material is related to the amount of rainfall available. The rate of slope movement ranged from 125 to 850 mm/month based on surface crack meter measurements. The rate of movement decreased during the winter months but increased in the spring and the summer due to snow melt and rainfall.

Table 7-1 Summary of index tests

	Bentonitic clay shale	Sliding Plane
Natural moisture content (%)	21-24	31-34
Liquid limit (%)	115-122	55-60
Plastic limit (%)	27-30	18-22

Table 7-2 Summary of direct shear tests performed on Keillor Road samples

Material Type	Sample Type	Sampling Elevation (m)	Normal Stress (kPa)
Clay shale	Core sample	626.0 (Coring)	50, 100, 200, 400, 800
Sliding plane materials	Block sample	625.0 (Toe)	50, 100, 200, 400

Table 7-3 Summary of the laboratory test results for Keillor Road samples

	Bentonitic clay shale	Sliding Plane Material
Natural water content (%)	21-24	31-34
Liquid limit (%)	115-122	55-60
Plastic limit (%)	27-30	18-22
Peak strength	$c' = 0, \phi' = 56^\circ$ ($\sigma_n < 200$ kPa) $c' = 185$ kPa, $\phi' = 30.2^\circ$ ($\sigma_n > 200$ kPa)	-
Residual strength	$c' = 13$ kPa, $\phi' = 14.4^\circ$	$c' = 3$ kPa, $\phi' = 14.8^\circ$

Table 7-4 Average movement of the slide body

Location	Movement 2003 (mm/month)	Movement 2004 (mm/month)
Main scarp	125	250
Graben	250	500
Toe	350	850

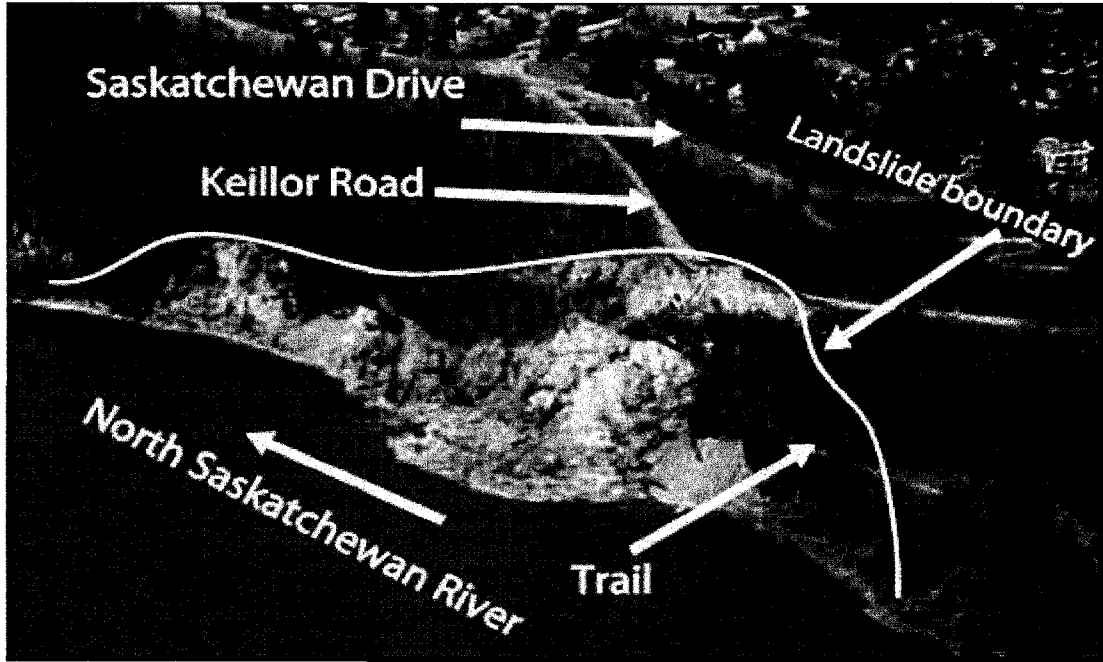


Figure 7-1 Keillor Road landslide (May 2005, the City of Edmonton)

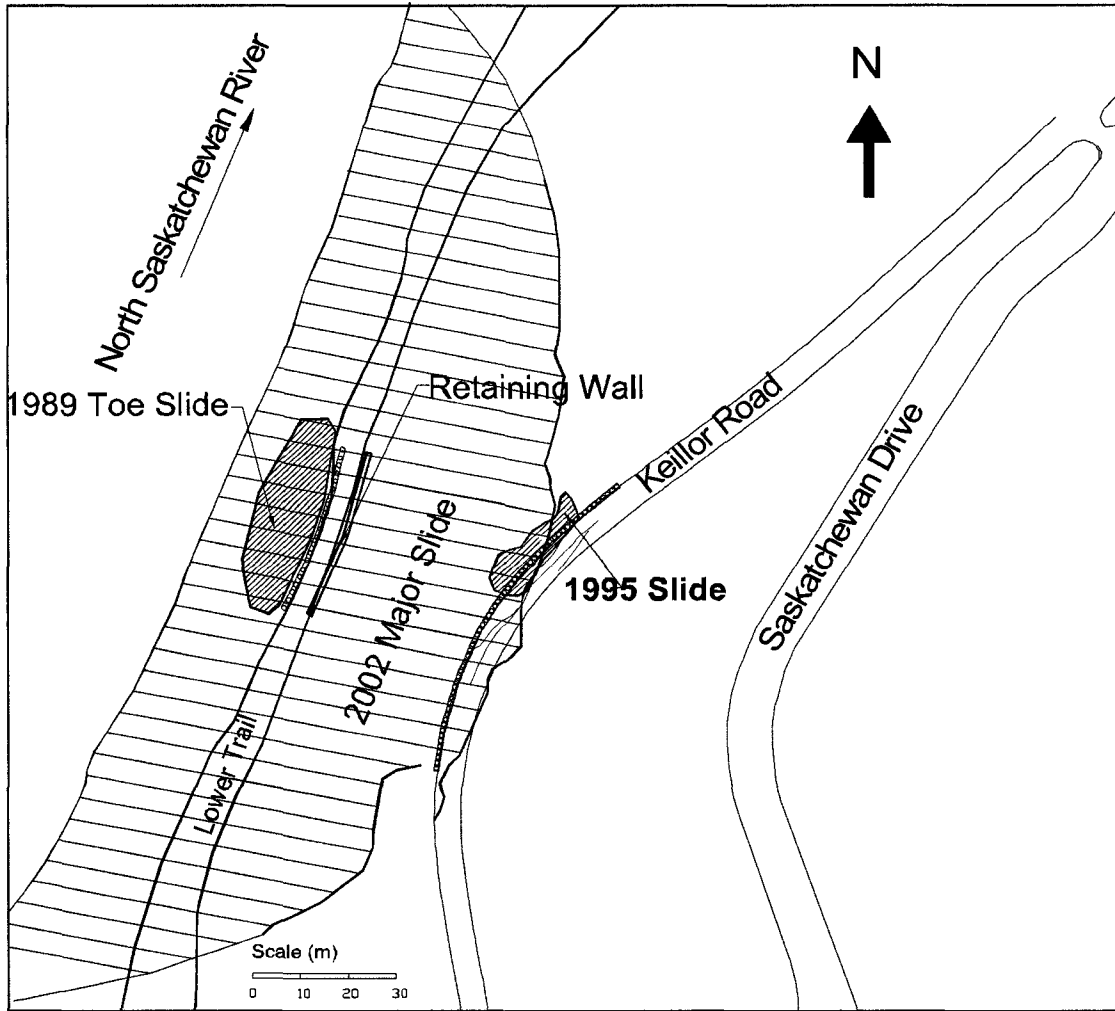


Figure 7-2 Map of slide area and site investigation plan

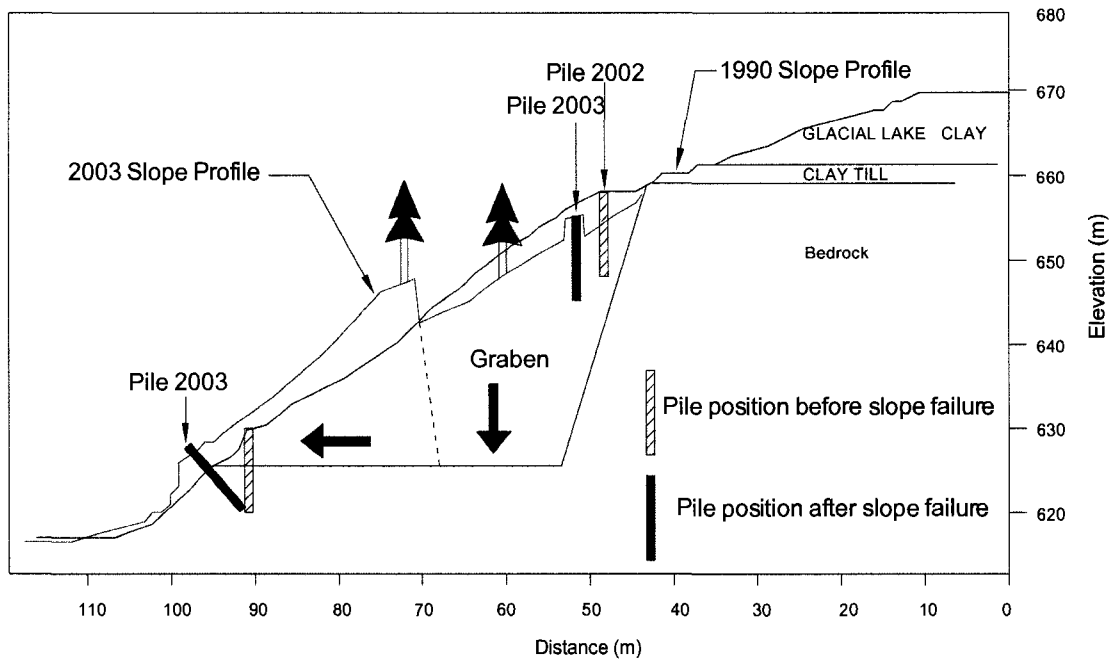


Figure 7-3 Pre-failure and post-failure profile of Keillor Road Landslide (2003)



Figure 7-4 Downward movement of the upper pile wall (picture from May 2003)



Figure 7-5 Forward tilting of the lower pile wall (picture from May 2003)

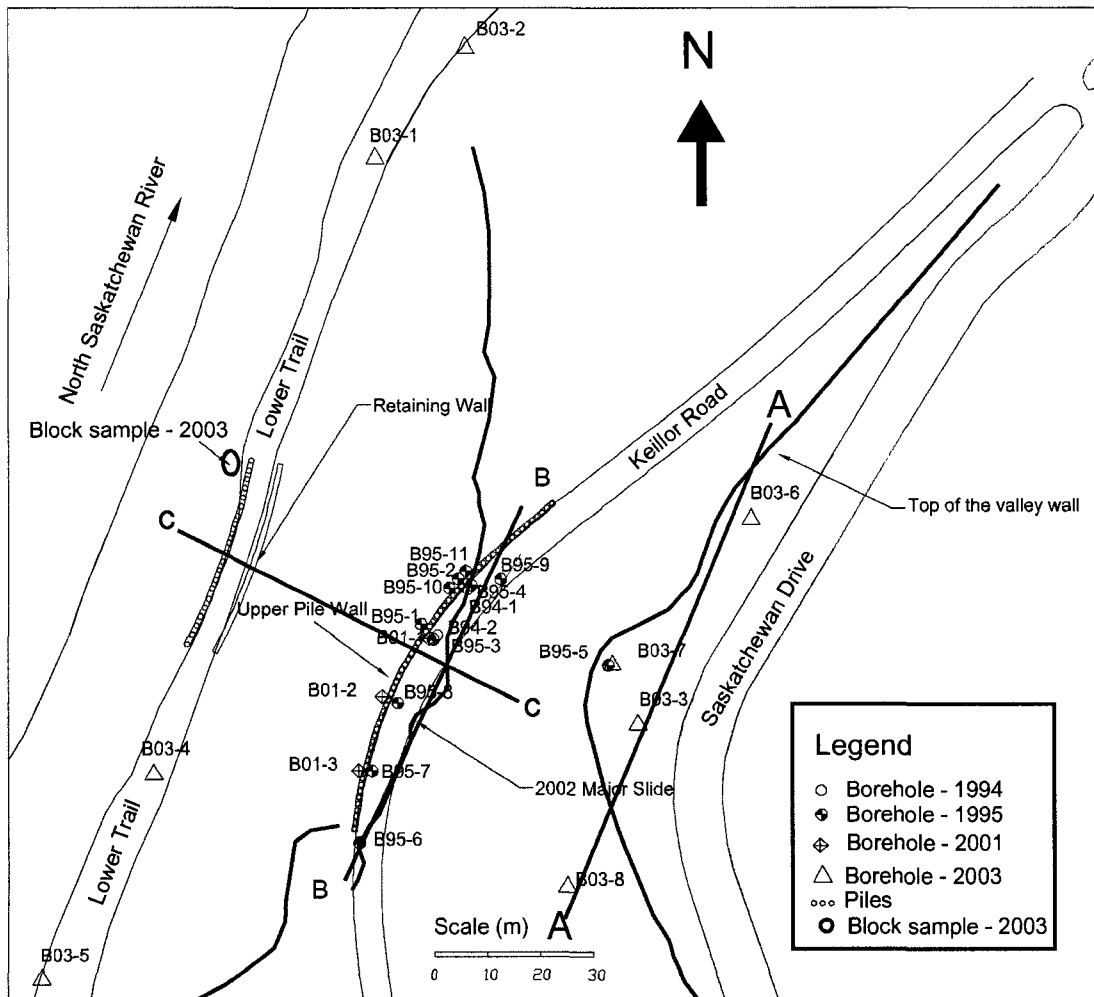


Figure 7-6 Site Investigation Plan

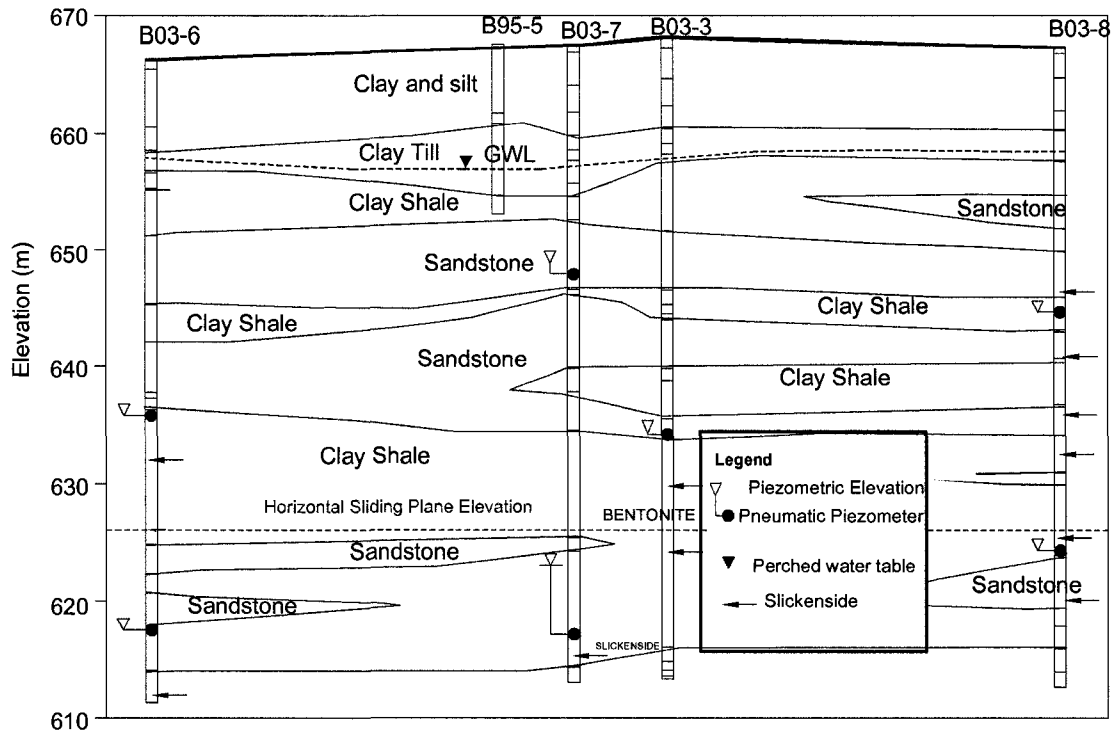


Figure 7-7 Stratigraphic profile behind the valley wall (Figure 7-5 Section A-A)

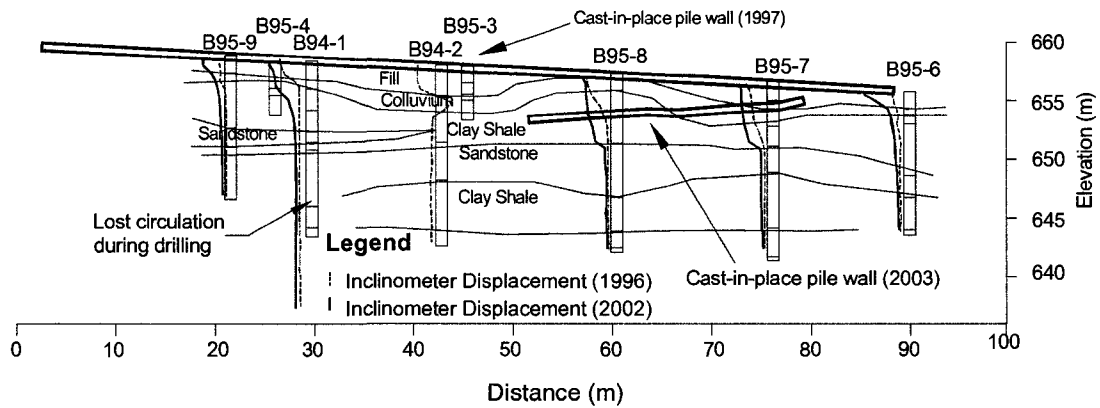


Figure 7-8 Stratigraphic profile along Keillor Road (boreholes located at the landslide area, Figure 7-5 Section B-B)

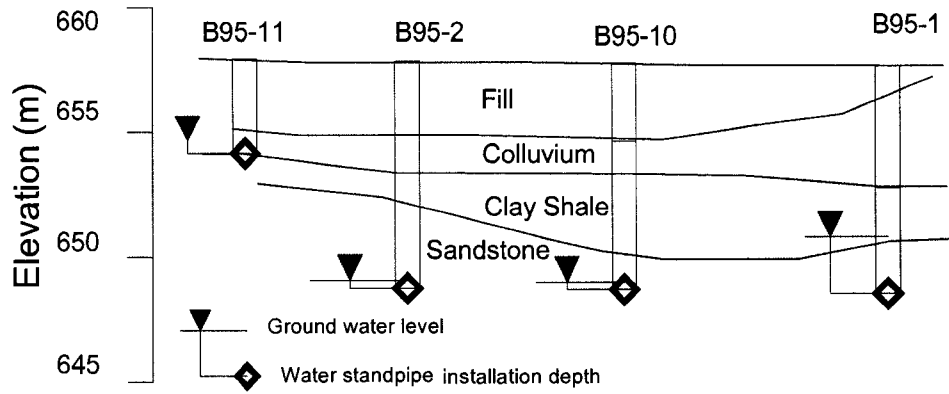


Figure 7-9 Water level observed in the slide zone

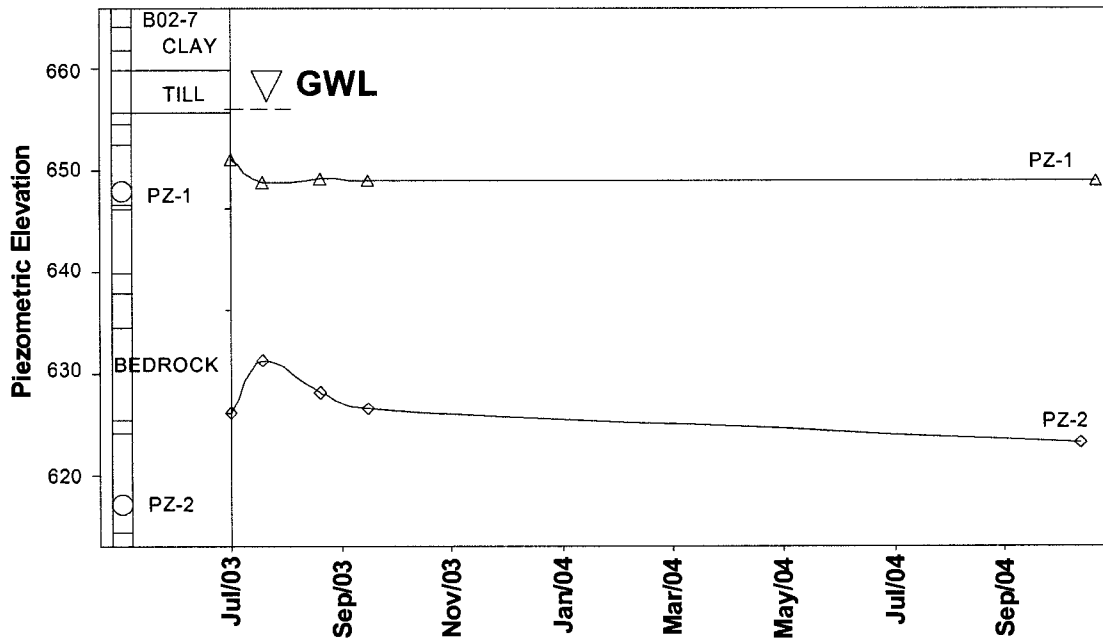


Figure 7-10 Long-term monitoring of piezometers

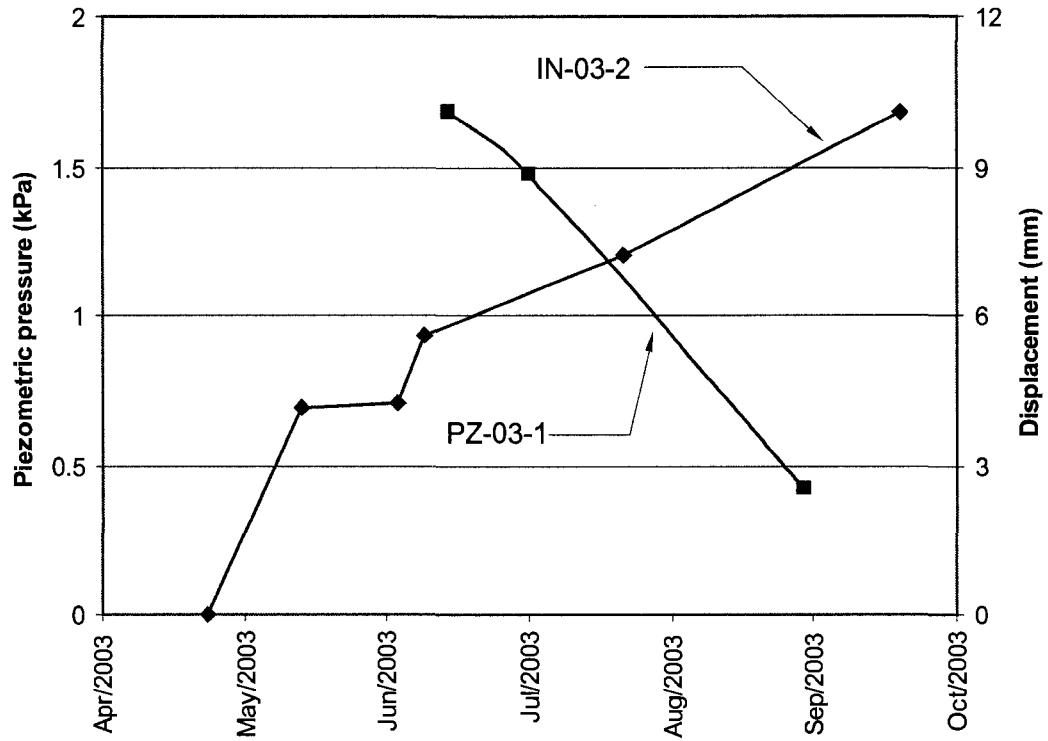


Figure 7-11 Changes in piezometric pressure due to slope movement

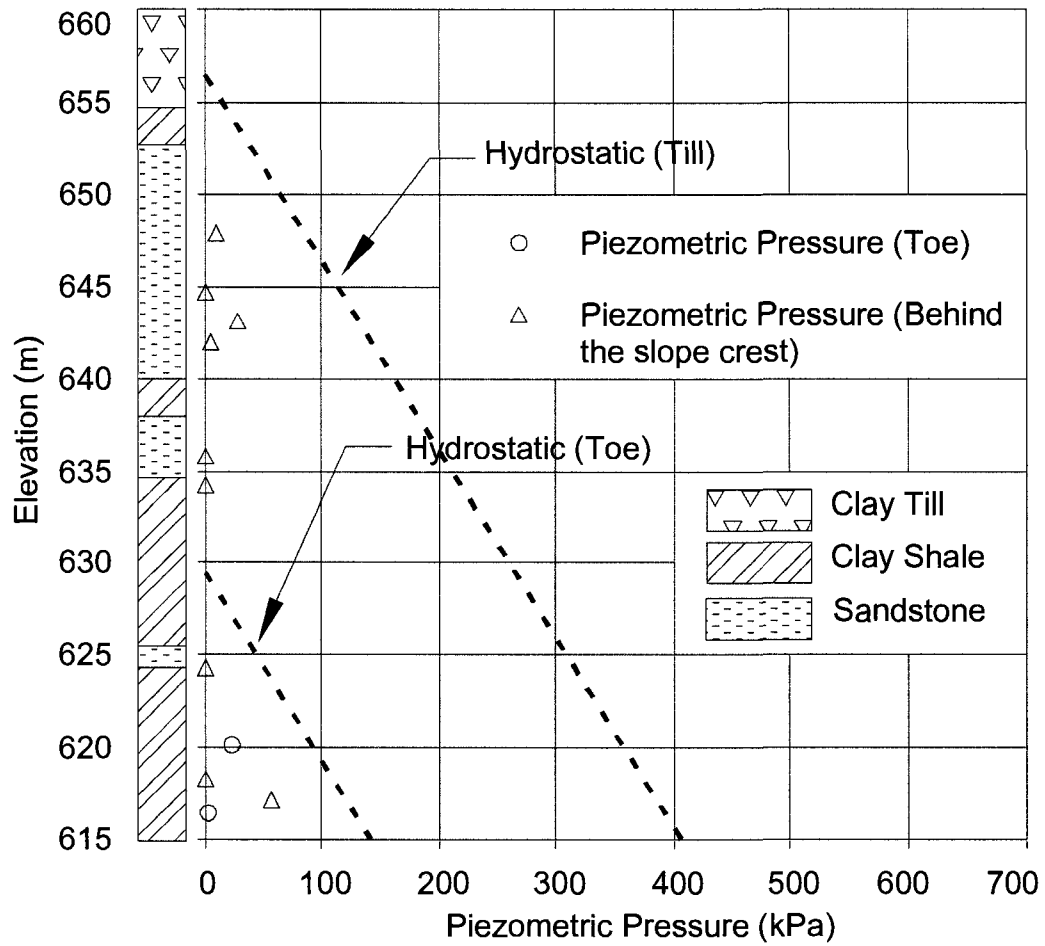


Figure 7-12 Pore pressure distribution in the slide area

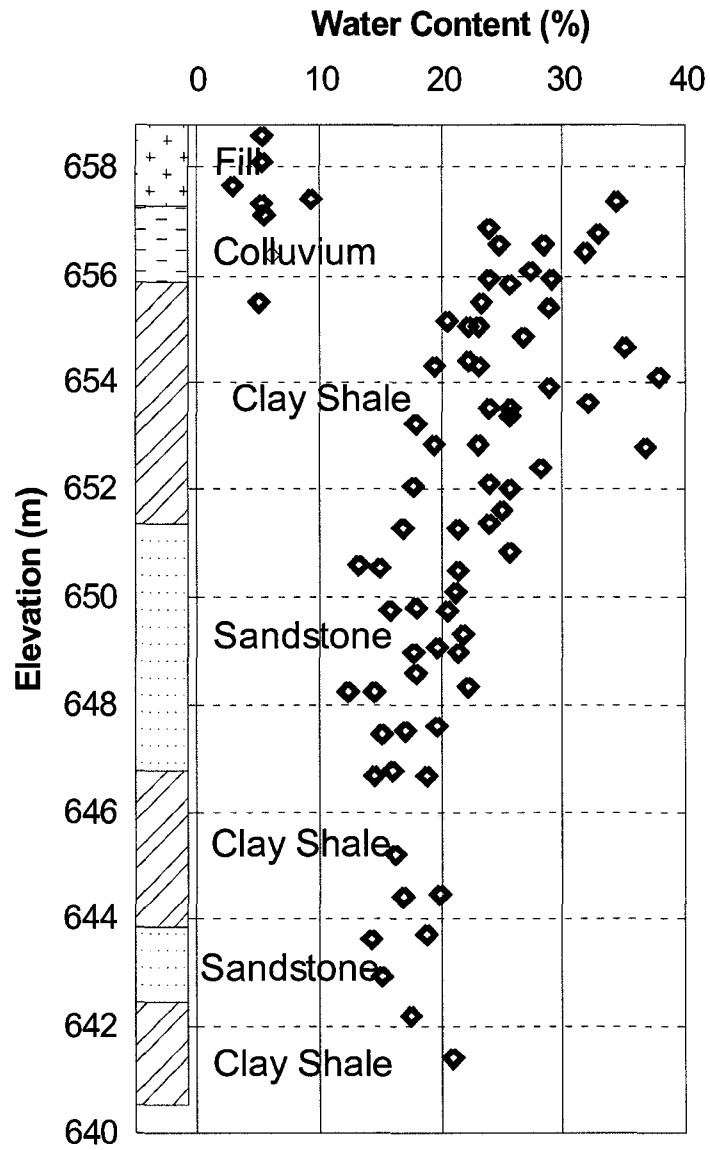


Figure 7-13 Natural water content profile below the main scarp

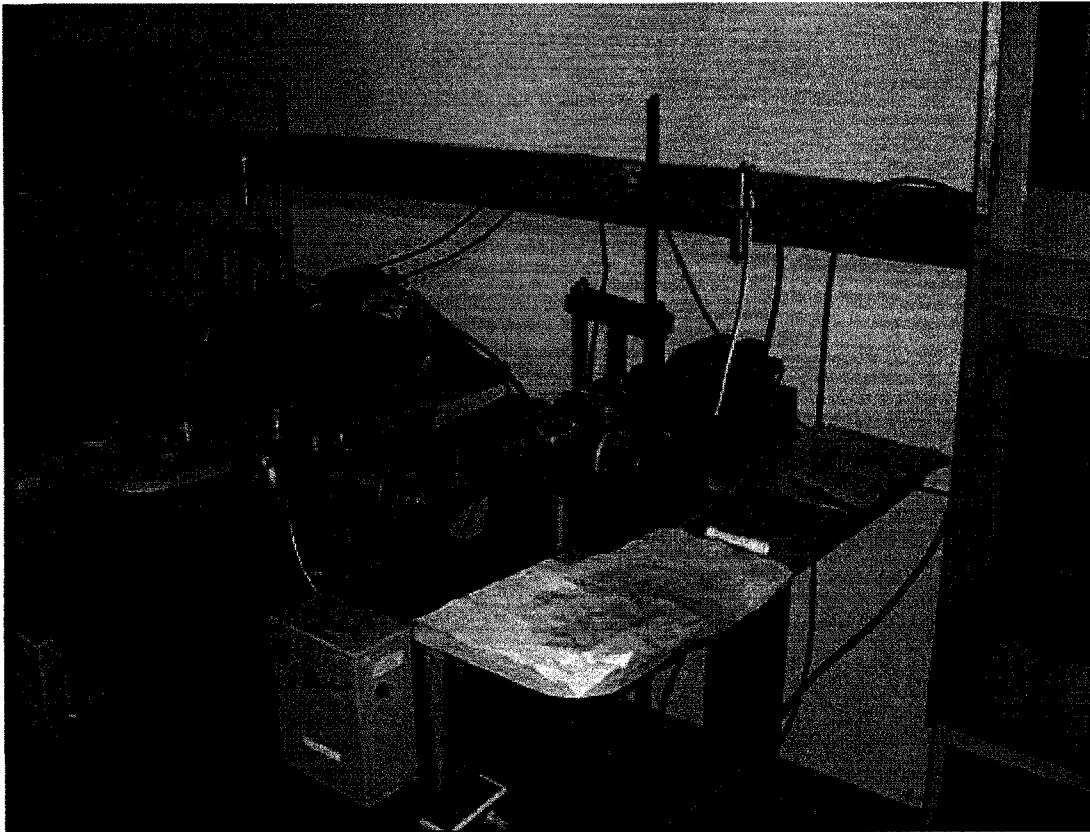


Figure 7-14 Direct shear testing apparatus

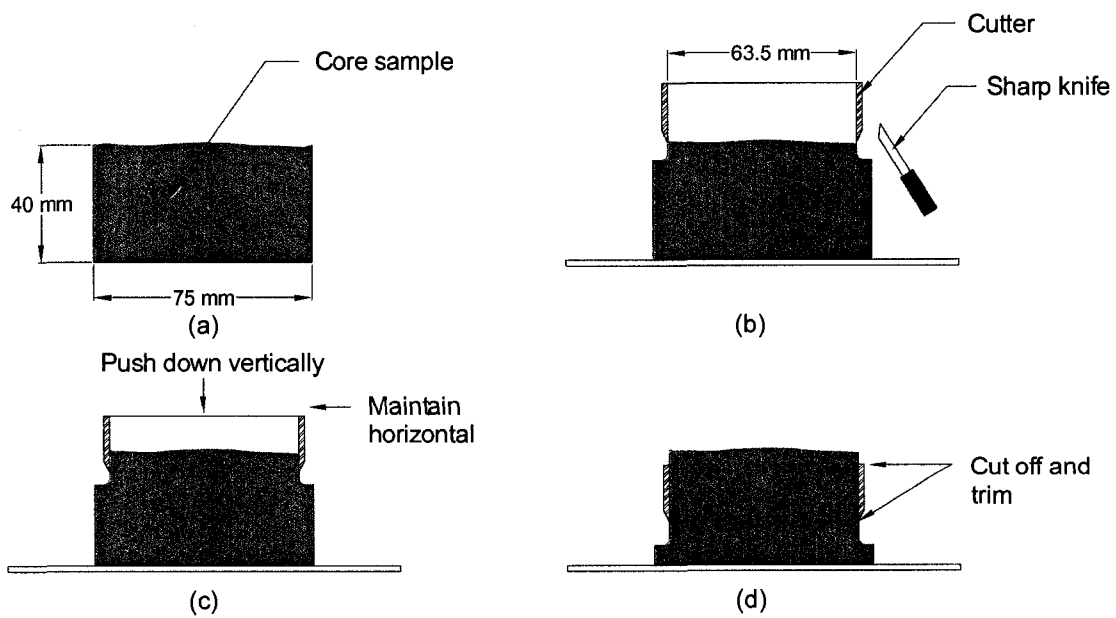


Figure 7-15 Sample preparation for direct shear test

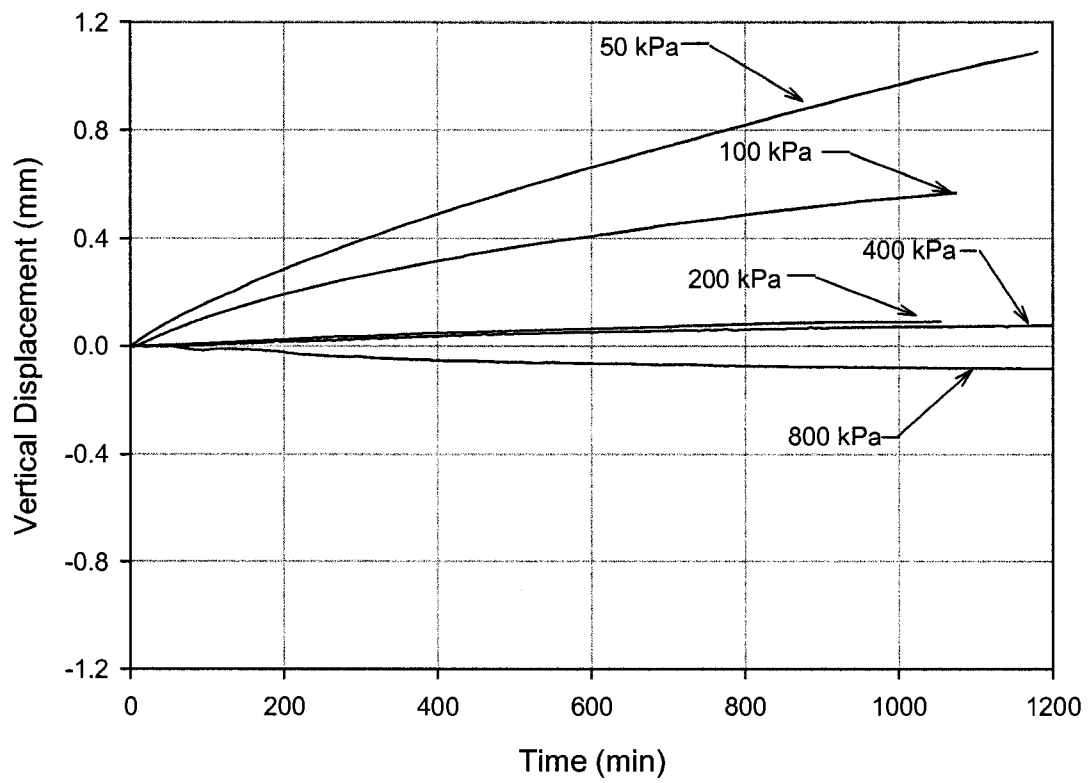


Figure 7-16 Volume change of intact samples during a 24-hour consolidation/swelling period

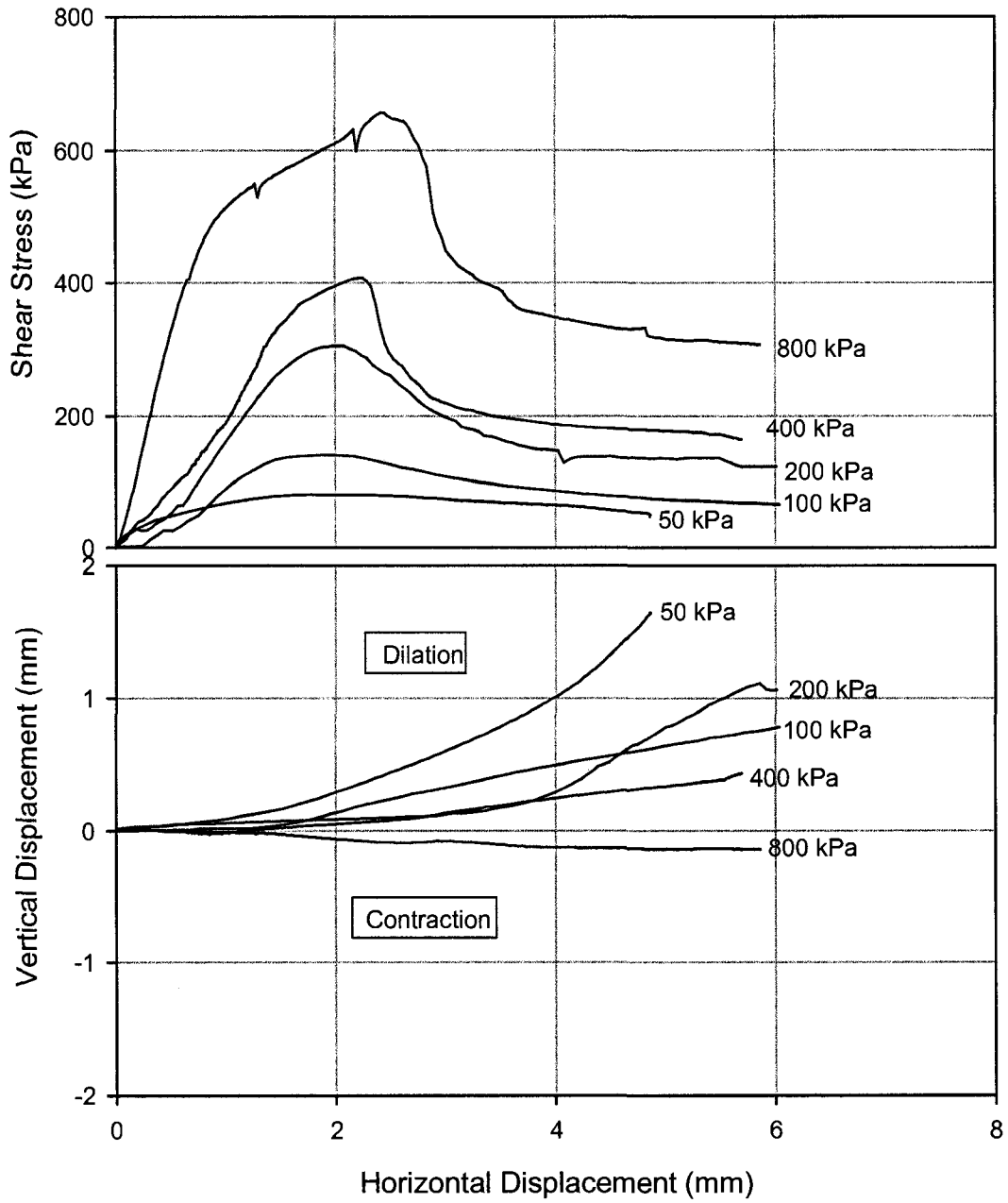


Figure 7-17 Direct shear test results of the bedrock (peak)

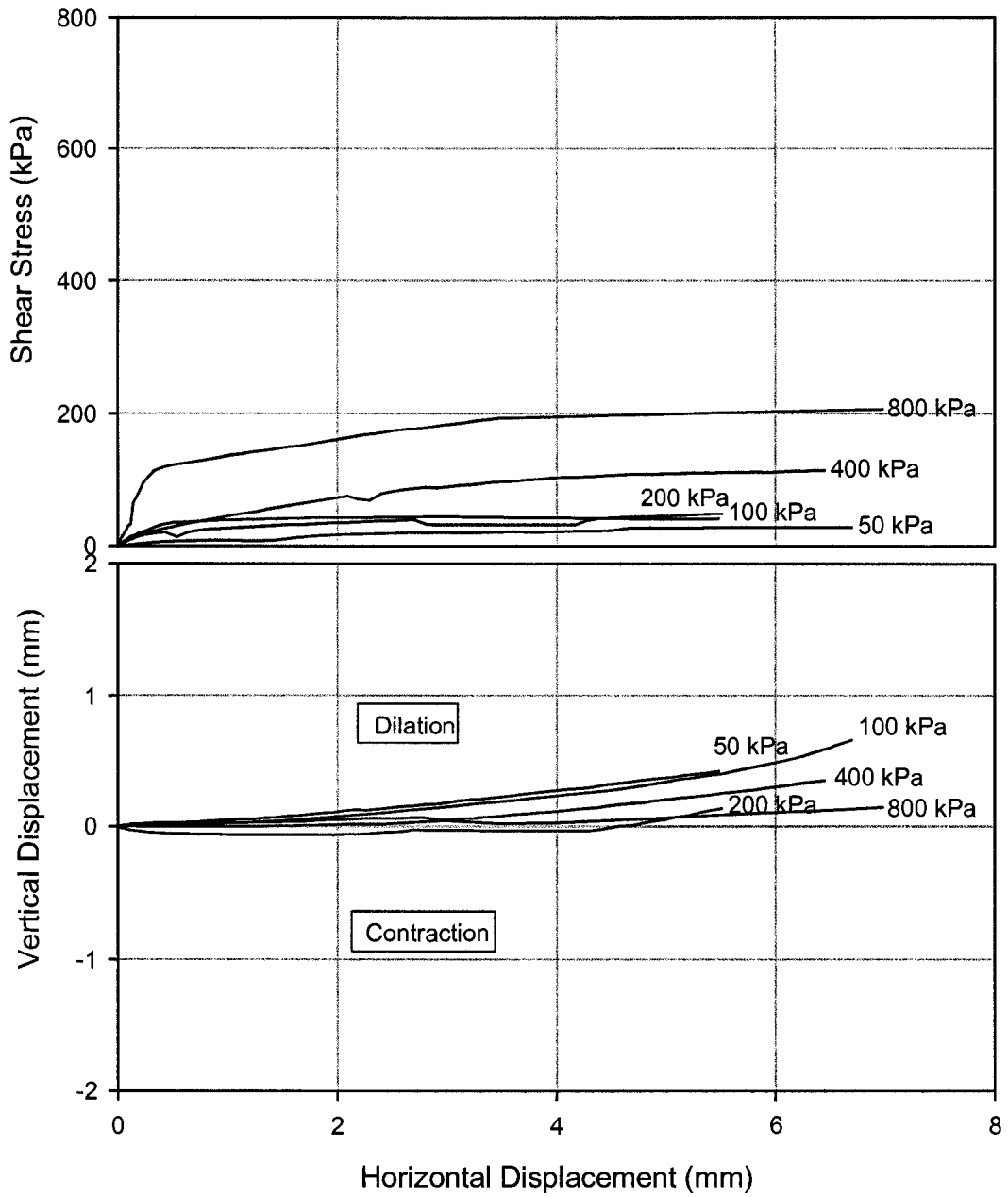


Figure 7-18 Direct shear test of the bedrock (residual)

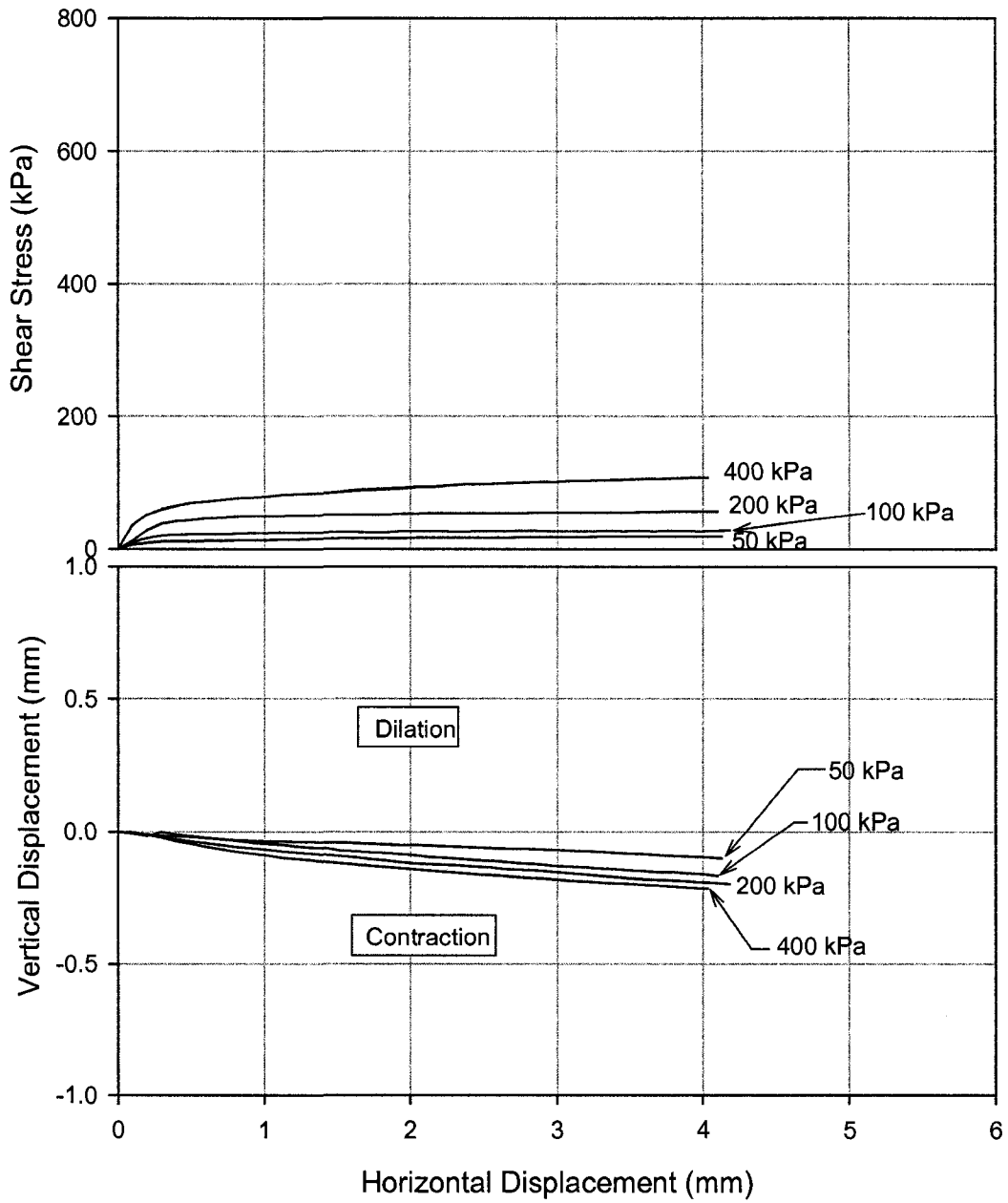


Figure 7-19 Direct shear test results of sliding plane material

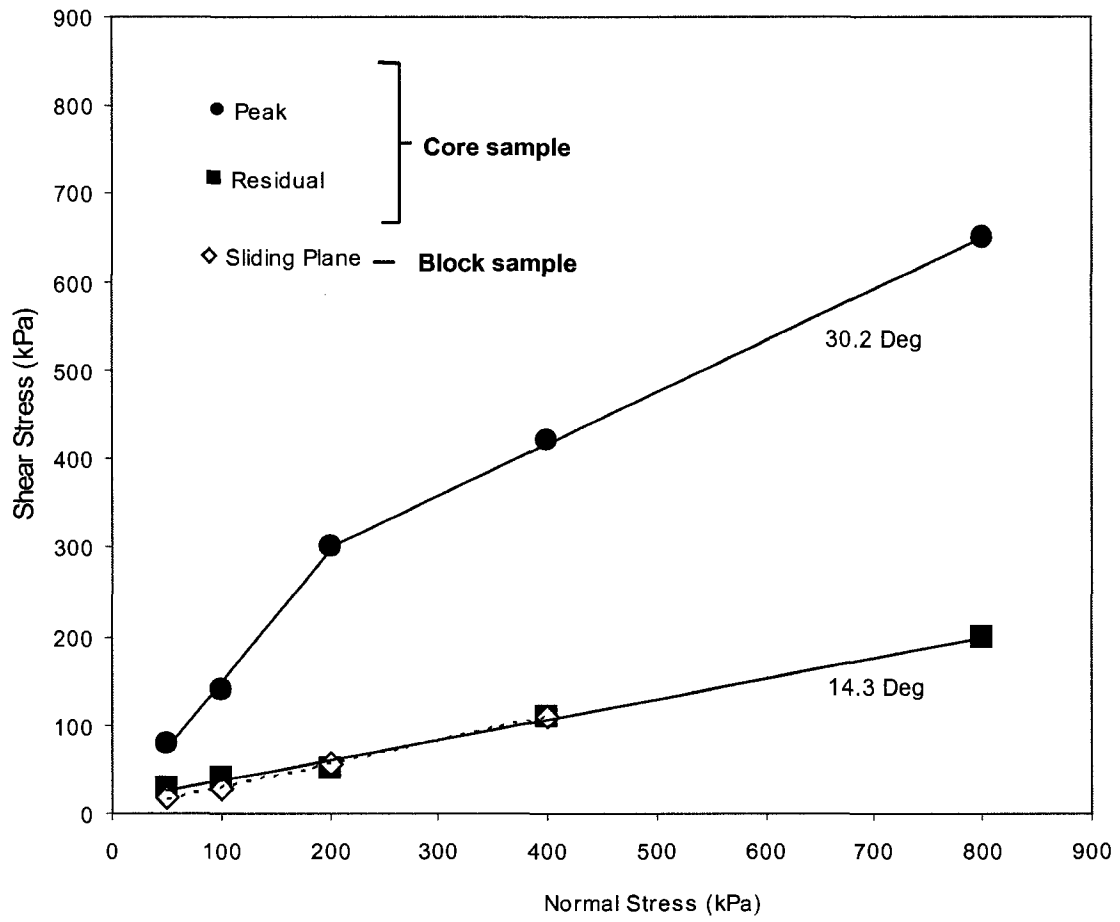


Figure 7-20 Failure envelope obtained from direct shear tests

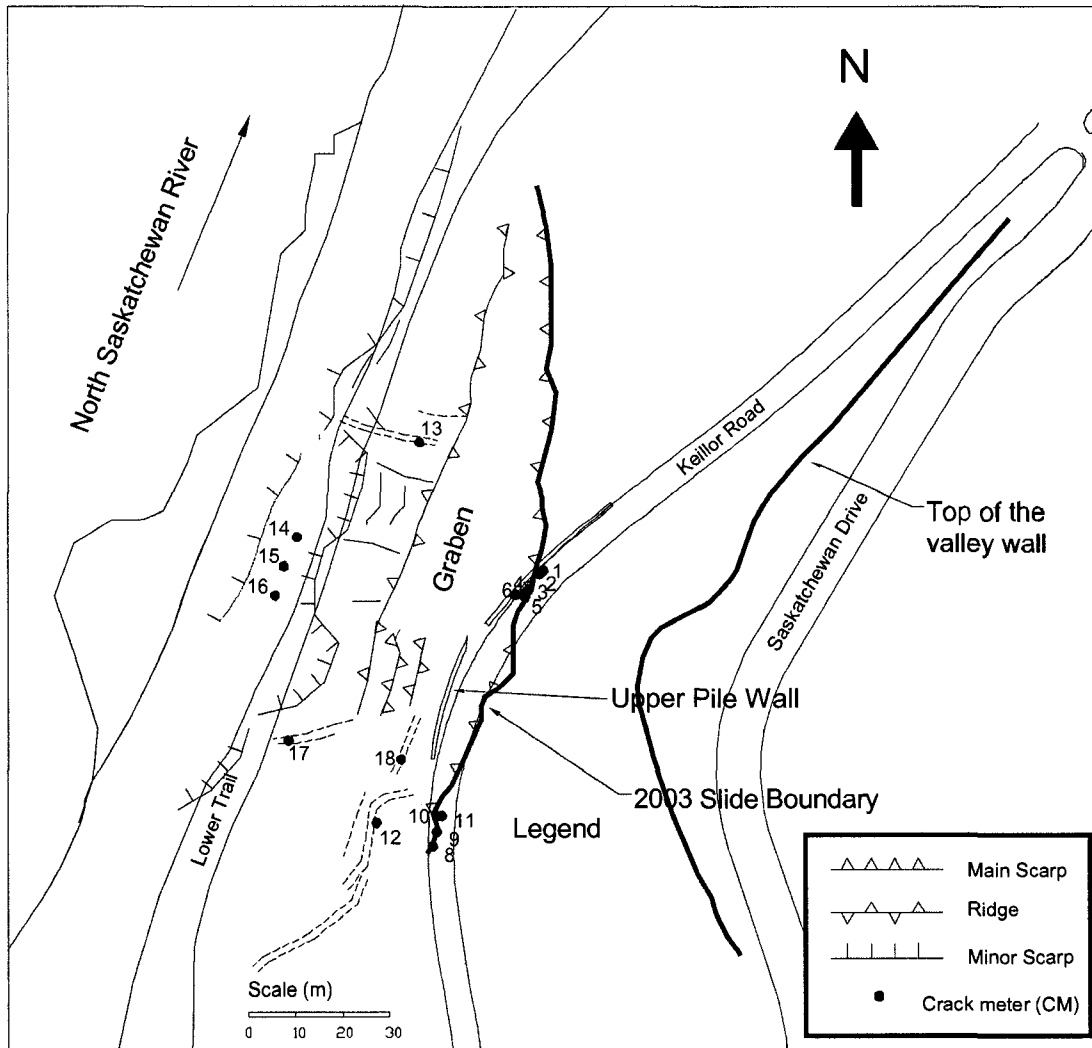
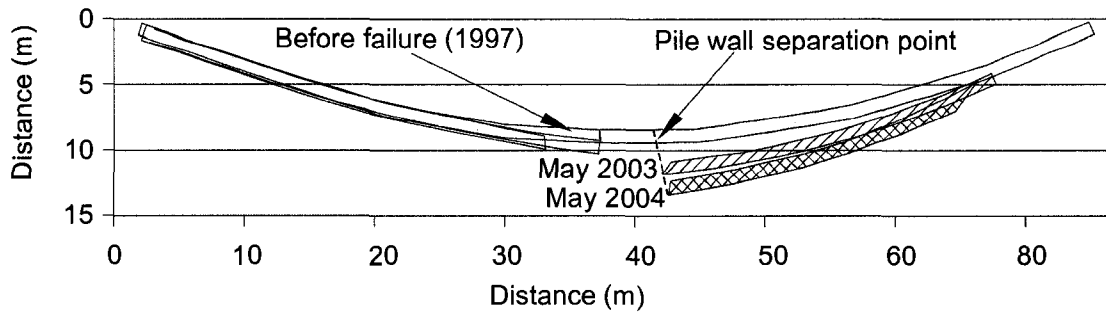


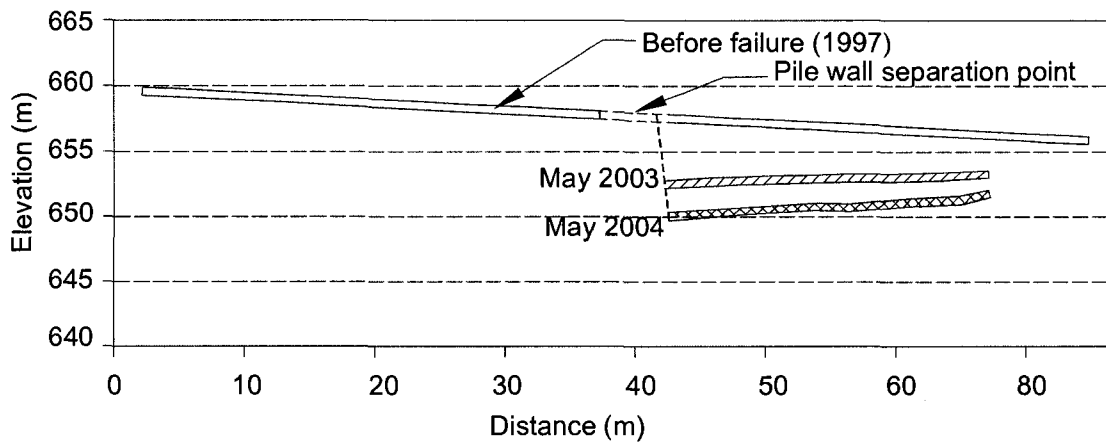
Figure 7-21 Landslide map of Keillor Road (Spring 2003)



Figure 7-22 A photograph of the damaged pile wall at the Keillor Road Landslide (May 2004)

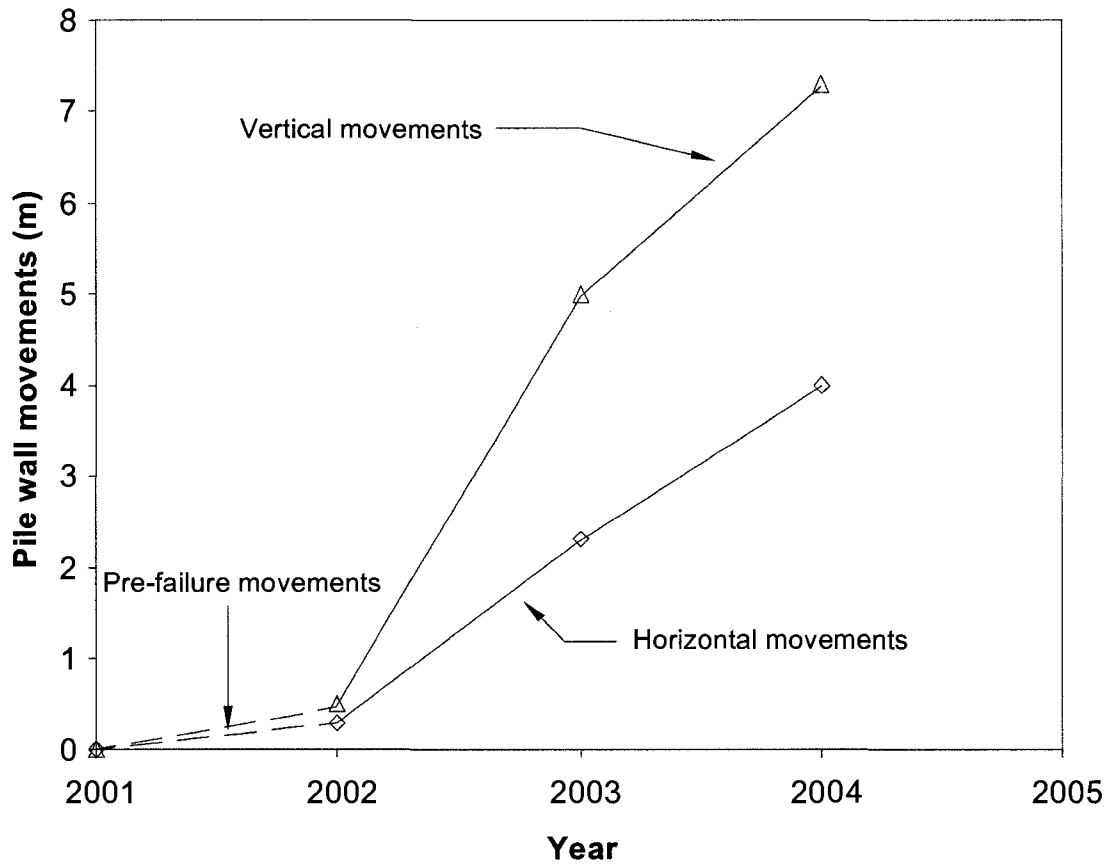


(a) Horizontal movements of piles



(b) Vertical movements of piles

Figure 7-23 Movements of the cast-in-place piles



Year	Movements (m)		Rate (cm/month)	
	Horizontal	Vertical	Horizontal	Vertical
2001-2002	0.3	0.5	2.5	4.2
2002-2003	2.0	4.5	16.8	37.5
2003-2004	1.7	2.3	14.1	19.2

Figure 7-24 Horizontal and vertical displacement of the pile wall in the Keillor Road Landslide

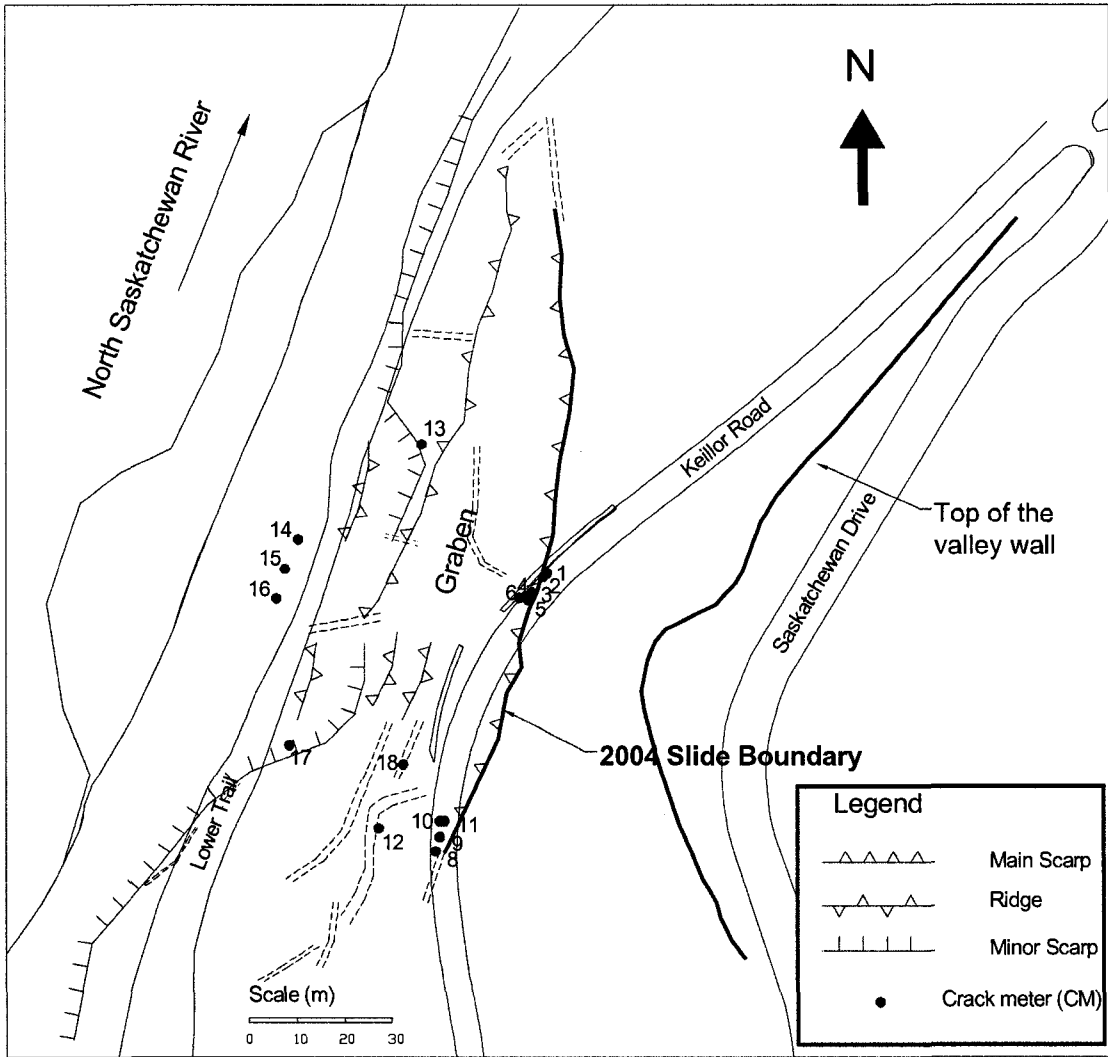


Figure 7-25 Map of Keillor Road Landslide, 2004

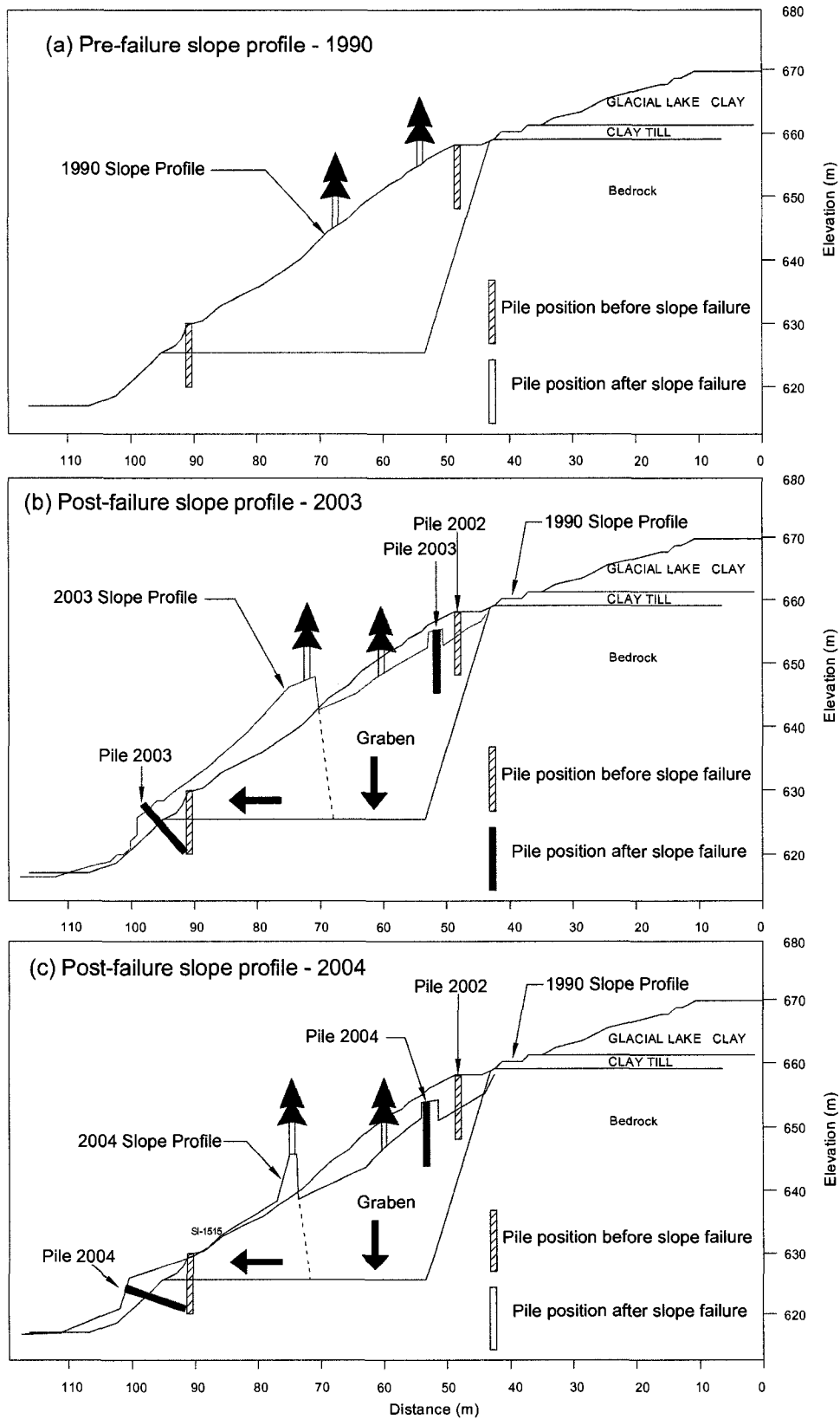


Figure 7-26 Slope profile survey (Pre-failure, 2003 and 2004, Figure 7-5 Section C-C)



Figure 7-27 Crack monitoring at the Keillor Road Landslide

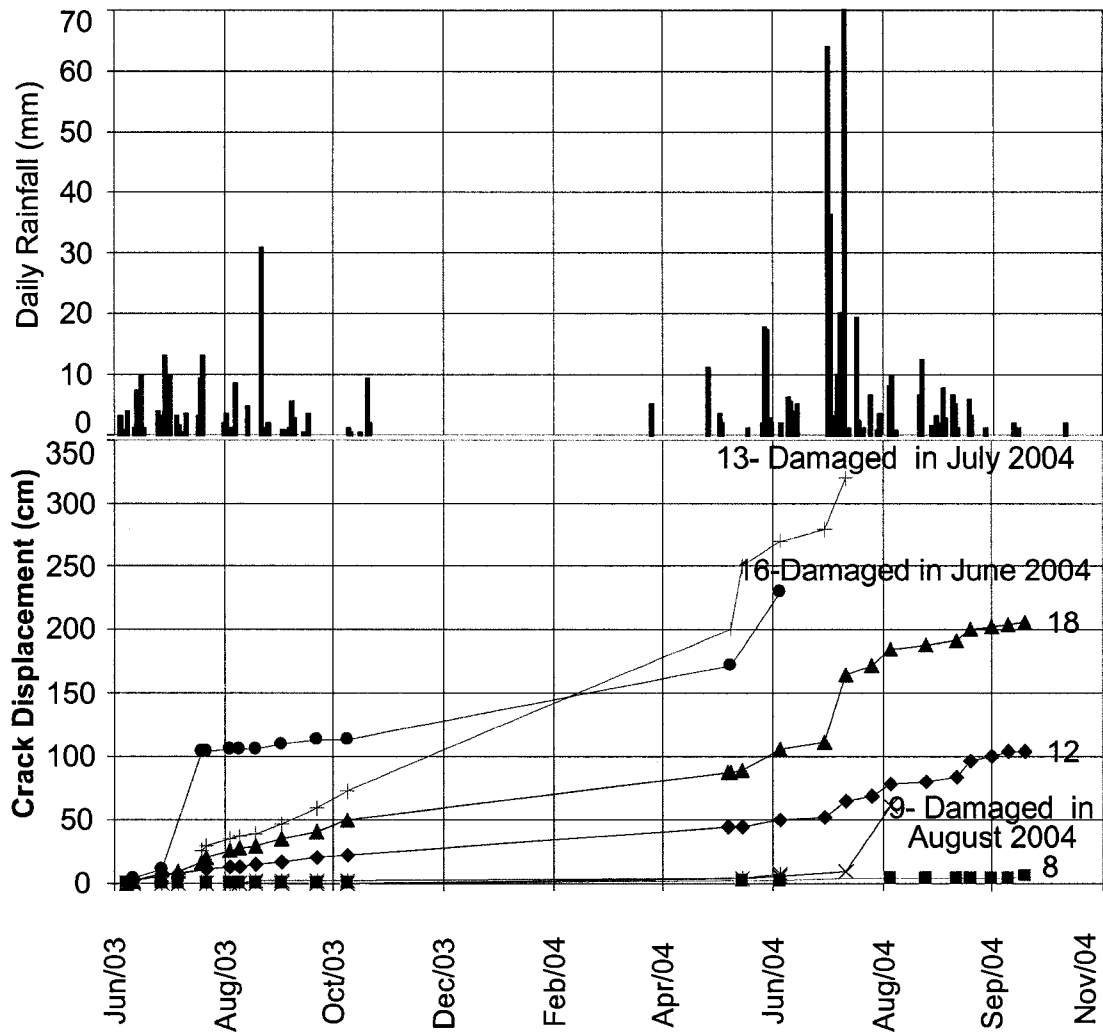


Figure 7-28 Cumulative horizontal displacement of crack meters at the Keillor Road Landslide

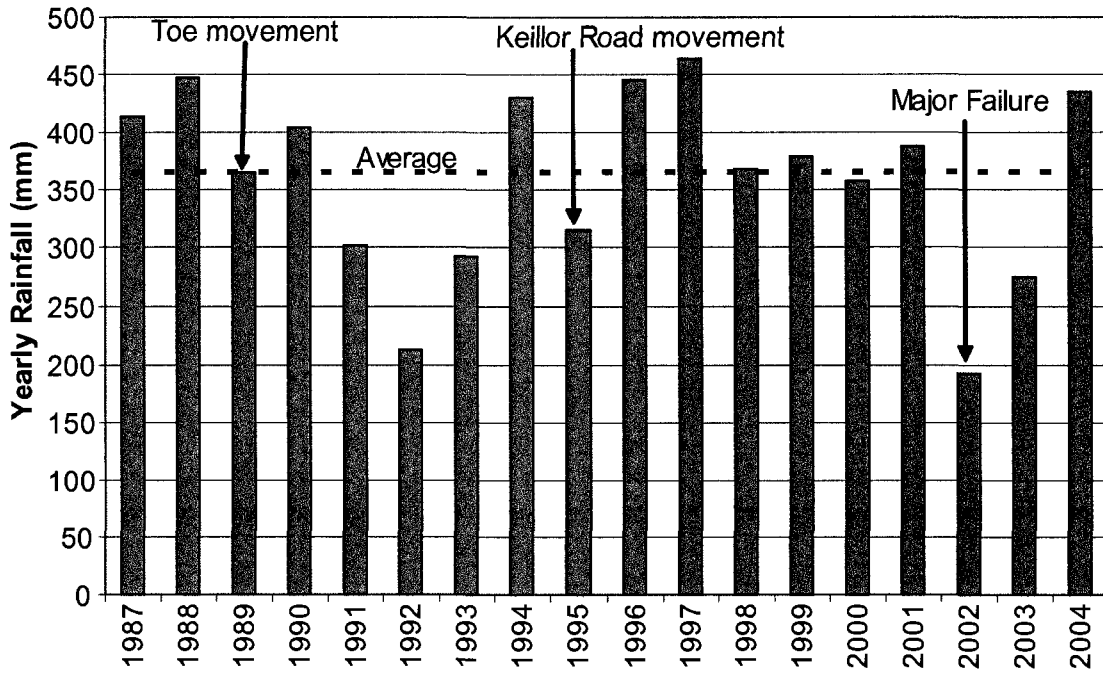


Figure 7-29 Yearly rainfall (University of Alberta Weather Station)

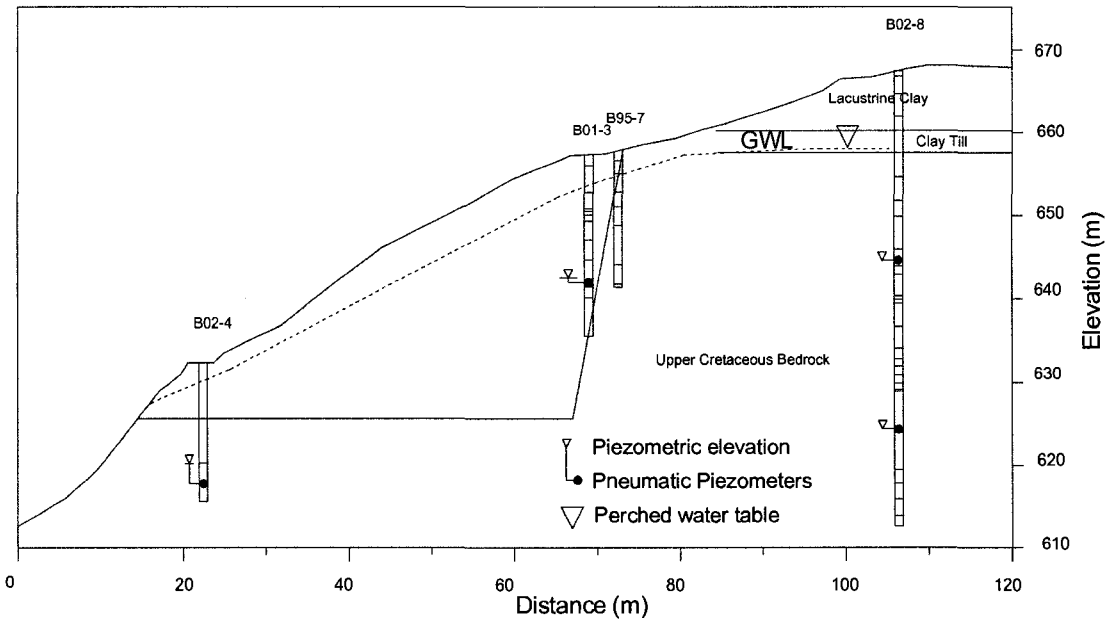


Figure 7-30 Pore pressure distribution in Keillor Road

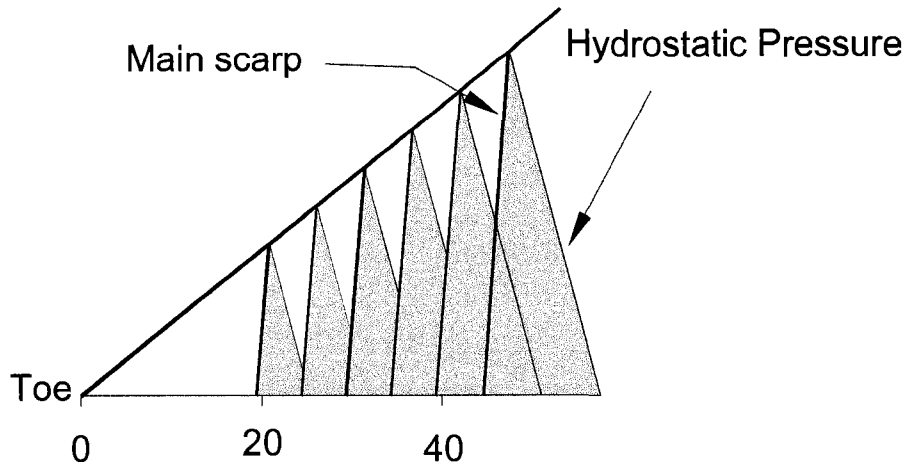


Figure 7-31 Slide geometry and groundwater levels used in the analysis of pore pressure distribution in Keillor Road

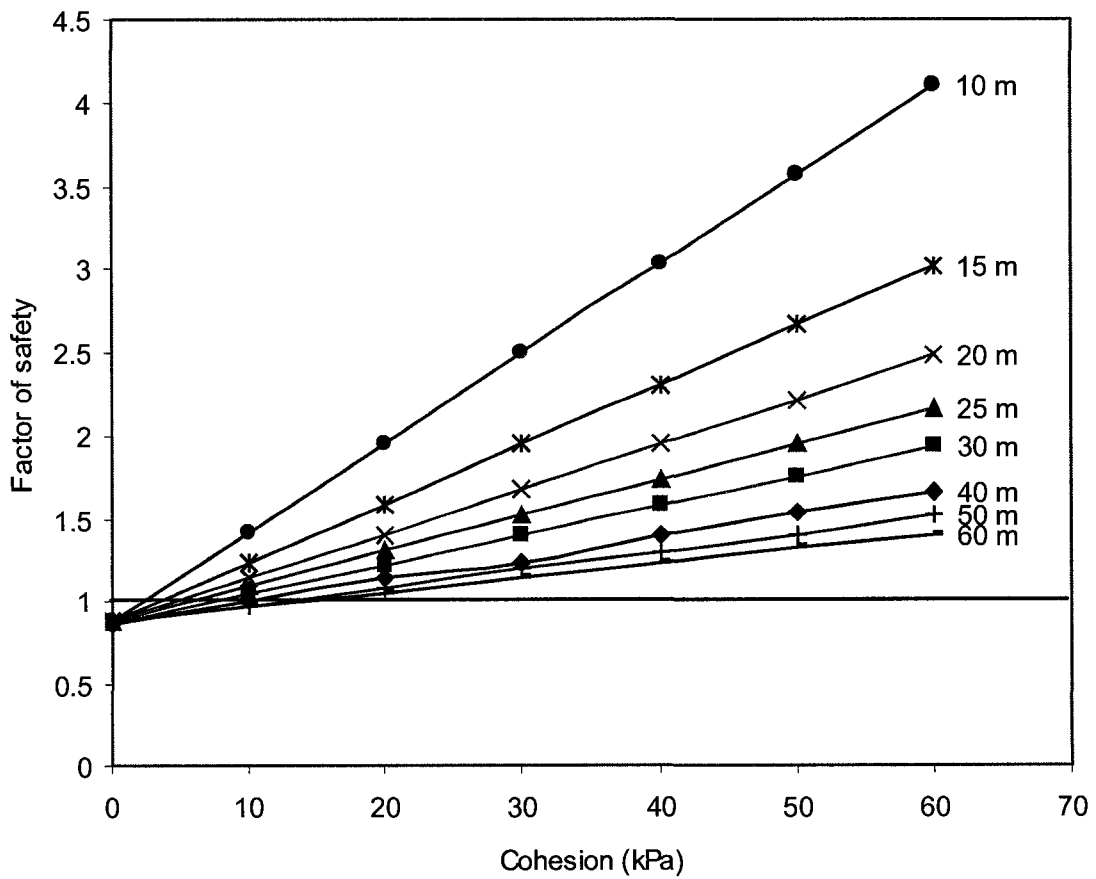


Figure 7-32 Parametric study of factor of safety with cohesion and main scarp distance (Keillor Road Landslide)

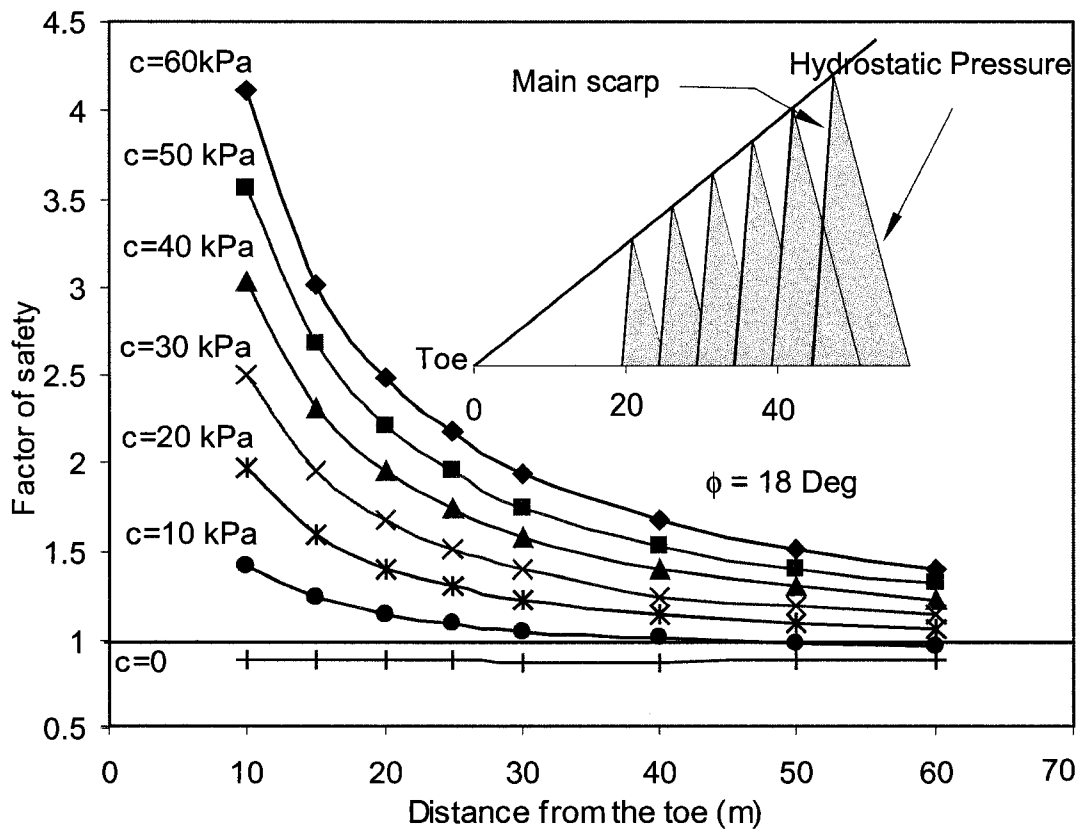


Figure 7-33 Parametric study of factor of safety with cohesion and main scarp distance (Keillor Road Landslide)

CHAPTER 8 Whitemud road landslide

8.1 Introduction

On the morning of October 23, 1999, a large landslide occurred along a 270 m section of the North Saskatchewan River Valley in Edmonton. The failure affected seven residential lots on the west side of Whitemud Road between the intersection of Ramsay Road and 43rd Avenue (Figure 8-1). Due to the failure, the upper two-thirds of the valley slope slid along a surface of rupture located in the bedrock. As the failure progressed, the soil and rock above the failure plane cascaded over the bedrock and slid into the river. The total volume of soil and bedrock involved in the landslide was in the order of 250,000 m³. After the initial failure, 50,000 m³ went into the river channel, and 200,000 m³ stayed on the slope. As the main body translated along the surface of rupture, subsidence occurred at the head of the displaced material, resulting in a vertical drop of up to 18 m.

8.2 Landslide history

8.2.1 1999 failure

The major movements of the Whitemud Road Landslide took place in a single day on October 23, 1999. The surface of rupture was 7 m below the bedrock contact with the overlying till layer. According to field observation, the landslide development can be divided into three zones (Barlow 2000): central, northern, and southern zones (Figure 8-1). The central zone was the largest zone and encompassed the backyard of Lots 6, 7, and 8 and a portion of Lots 5 and 9. In the morning of October 23, 1999, the area at the top of the slope had subsided about one meter. The subsidence then continued gradually, and the back portion of the house on Lot 7 broke away and dropped 15 to 18 m in about 45 minutes. Afterwards, the failure advanced to Lots 6

and 8 where continuing downward movements occurred. The average width of the ground lost in the backyards of the properties was about 15 m. Figure 8-2 shows the exposed piles below the house on Lot 5.

Later that morning, the slide shifted to the northern zone. A thin layer of soil and vegetation slid along the upper slope immediately below Lots 9, 10 and 11, then detached and slid into the failure zone. The northern zone also exhibited a translational failure mechanism along a surface of rupture located in weak bedrock.

Then the activity of the slide shifted to the south, below a recreational trail. This area was about 40 m wide and showed the most rapid ground movements with the detachment that formed the present scarp, and most of the subsidence occurred within 20 minutes. The displaced material had more mobility due to the high quantity of groundwater seepage in this zone. Immediately after the failure, most of the displaced material slid into the river channel, and the surface of rupture in the mudstone was clearly visible.

Continued movements of displaced materials have been observed up to the present time. Some of the movements were associated with groundwater seepage and the construction of an access road used for horizontal drain installation.

8.2.2 Airphoto review

Prior to the 1999 slide, several movements had occurred downstream of the North Saskatchewan River Valley. In 1967, a failure occurred 300 m downstream of the 1999 slide area. In 1976, a second failure occurred north of the 1967 failure (Figure 8-3). The second failure involved the overlying glacial deposits and the bedrock. Displaced materials are located well out into the river. From the period of 1997 to 1999, displaced trees at the river level as well as significant debris and tree accumulation are visible in airphotos. Significant observations before the landslide are listed below.

- No significant slope movements were observed prior to 1997.

- The movements of the lower portion of the slide commenced at some point in 1997 or 1998. The evidence was a block of soil and trees tumbling down over the river edge. Ground cracking was observed in a trail located in the middle of the slope.
- Minor cracking in the cement work in Lots 6 and 7 was noticed by the summer of 1998.
- By the summer of 1999, the translational movements in the lower slope had progressed and formed a scarp above the level of an animal trail located at mid slope.

The lots along the valley crest on Whitemud Road (Lots 5 to 14) were developed over a 20-year period, as the air photos between 1967 and 1988 indicate. Prior to the development of the road and lots, the slope crest along the river valley showed knob and kettle terrain with hills and hollows. Significant lot grading was required to reduce the grade on Lots 9 through 13 and to bring up the grade between Lots 6 and 8. The largest portion of fill was used to fill in a kettle hole located on Lot 7. The locations of the kettle holes and the raised area before the developments are shown in Figure 8-4.

8.3 Site investigation and instrumentation

8.3.1 Pre-failure investigation

Prior to the 1999 failure, two site investigations were conducted in the Whitemud Road area. McCormick (1977) conducted a site investigation in October and November 1976 for a top-of-bank study. The study area was located at Whitemud Road and a recreational trail at the south. Three boreholes (76-01, 76-02 and 76-03) were advanced using a truck-mounted, continuous flight hollow stem auger. Disturbed and undisturbed samples were collected for laboratory tests, and standpipe piezometers were installed to monitor the groundwater table. All boreholes were advanced up to the base of the till layer, about 30 m deep. Index tests and unconsolidated, undrained triaxial tests were conducted on the clay and till samples.

Constant (1979) conducted an investigation for a proposed subdivision development on Whitemud Road. Two boreholes were drilled to establish the geotechnical conditions of the slope. Borehole 79-1 was advanced from Lot 9, and borehole 79-2 was advanced from Lot 7. In addition to the continuous coring undertaken in 79-2, undisturbed soil samples were collected with Shelby tubes at regular intervals. Index tests and unconfined compressive strength tests were carried out on samples collected from the site. Pre-failure borehole locations are presented in Figure 8-5.

8.3.2 Post-failure investigation

After the major failure in 1999, the City of Edmonton conducted field investigations and instrumentations in different stages (Figure 8-6). The first stage was conducted immediately after the major failure in 1999 (Barlow 2000). The investigation program involved drilling eight holes and installing instruments along Whitemud Road and the recreational trail to the south. Samples of the till and bedrock units were collected for detailed examination and laboratory testing.

Six boreholes were drilled using a wet rotary coring rig. Continuous coring was conducted within the till deposit and proceeded to the termination depth of the holes, which extended to the river level. A hollow-stem auger rig was used for the remaining two boreholes to obtain better samples in the till and at the contact between the till and bedrock. In situ testing and sampling were conducted in boreholes 99-1 and 99-3 to characterize the sand. Standard penetration tests were conducted to get a measure of the relative density of the sand and to retrieve samples for more detailed logging and classification.

The second stage of the field program involved boreholes advanced directly within the displaced material. This stage was conducted in May 2000 after two houses had been removed and an access ramp had been graded onto the slide mass. Boreholes were advanced at a total of 13 locations through the displaced material and down into undisturbed strata below the surface of rupture. The first eight locations involved continuous dry coring with a hollow stem auger rig. The final four boreholes were advanced using a solid stem auger to probe the extent of the sand deposits.

The third stage of the field program was related to the installation of horizontal drains. A total of 18 boreholes were drilled in 2001 and 2002 to determine the sand's thickness. Water standpipes were installed in these boreholes to monitor the improvement of the drain installation.

Instrumentation included inclinometers, pneumatic piezometers, and water standpipes. The grout-in installation method was utilized for piezometer installation. The water standpipes, 5 cm diameter PVC pipes with 6 m slotted sections, were installed in the overlying glacial deposits and inside the displaced material.

8.3.3 Stratigraphy

The stratigraphic profile behind the valley wall can be described as follows;

- The Upper Cretaceous bedrock of the Horseshoe Canyon Formation comprises of sandstone, mudstone and clay shale with bentonite lenses. The sandstone varies from a low plastic sandy clay to a weakly cemented soft rock. The mudstone and clay shale are generally hard, massive, high plastic and without any distinct fissility. Three distinct bentonite layers of thickness varying from 50 to 400 mm were identified from the deep drill holes (Figure 8-7).
- The bedrock is overlain by a 8 to 10 m thick till deposit. The till has a clay matrix with numerous local bedrock fragments and a few carbonate fragments, mostly in the sand fraction.
- The overlying till is a 30 to 35 m thick kame deposit of sand. The kame deposit was typically formed by meltwater channels under the retreating ice sheet (Shaw 1993). The sand is generally in a dense to very dense state with the moisture content less than 10 %.
- The kame is overlain by a layer of lacustrine clay formed under the glacial Lake Edmonton (Bayrock and Hughes 1962). The lacustrine clay is 1 to 6 m thick, silty, soft to medium stiff with a low to intermediate plasticity.

8.4 Pore pressure regime of the Whitemud Road area

8.4.1 Pore pressure behind the valley wall

Water standpipes and piezometers installed prior to the 1999 failure (Constant 1979; McCormick 1977) and post-failure drill holes (Barlow 2000) revealed the presence of a perched water level in the overlying sand deposit (Figure 8-8). The groundwater level is located 20 to 25 m below the slope crest where the contact of the sand and till is located. The measured groundwater levels in 1979 and 1999 indicated that the groundwater level had increased 2 to 5 m during this period.

Pneumatic piezometers installed in the bedrock revealed significant deficient pore pressure in the bedrock. Piezometric pressures measured in the bedrock were well below the hydrostatic pressure of the groundwater level and in some cases, readings were zero. Figure 8-9 presents the pore pressure response of the bedrock behind the valley wall together with the measured groundwater level in the sand deposit.

8.4.2 Pore pressure inside the displaced material

The pore pressure response of the displaced material can be divided into two parts, as groundwater level and piezometric pressure of the bedrock play different roles. Water standpipes installed inside the displaced material revealed that the groundwater level is located 3 to 5 m below the ground surface. This groundwater level is responsive to seasonal rainfall and snowmelt.

Pneumatic piezometers installed inside the displaced bedrock told a different story. The piezometric pressure of the displaced bedrock ranged from 12 to 50 kPa and these piezometers did not respond to groundwater level changes. But the piezometers registered pore pressure response to the slope movement and swelling of the displaced bedrock.

The response of the piezometers installed in the displaced material is presented in Figure 8-10. The groundwater level of the displaced material varies due to seasonal rainfall and snow melts. Readings of piezometers installed inside the bedrock close

to the horizontal sliding plane increased during the period of December 1999 to August 2002, possibly due to swelling of the bedrock. In the summer of 2002, significant slope movements occurred in the displaced material and the piezometric pressure of the bedrock decreased, possibly due to dilation of the bedrock.

In order to determine the variation in the piezometric pressure of the bedrock at depth, the measured piezometric pressures are plotted against elevations, as shown in Figure 8-11. The hydrostatic pressure calculated from the groundwater level is also presented in the figure. As shown, the piezometric pressures of the intact bedrock ranged from 0 to 10 kPa, piezometric pressure of the bedrock inside the displaced material ranged from 12 to 50 kPa, indicating the higher rate of softening in the valley wall. This reading also confirmed that significant deficient pore pressure still exists in the bedrock due to valley formation. This increased pore pressure of the bedrock inside the displaced material indicates the effect of softening processes occurring at the slope face.

8.5 Laboratory investigation

The engineering properties of the glacial deposit and the bedrock conducted before and after the Whitemud Road slide are presented in this section (Barlow 2000; Constant 1979; McCormick 1977).

8.5.1 Index Tests

The moisture content of clay and fill material ranged from 5 to 35 %, depending on the amount of sand content. The moisture content of the sand deposit generally ranged from 3 to 15%. Comparison of moisture content measured during 1979 and 1999 revealed that there was a 5 to 15% increase in moisture content in the bedrock samples during this period. This increase in moisture content indicates the swelling process occurring in the bedrock with time. The moisture content profile of the intact soil and rock samples collected during the years 1979 and 1999 are presented in Figure 8-12.

The index test results of the till, bedrock, and bentonite samples are presented in Figure 8-13. The till is low in plasticity with a liquid limit range of 10 to 50 %. The mudstone and sandstone samples fall in a range of medium to high plasticity, depending on the bentonite content, with a liquid limit range of 50 to 150 %. Extremely high plasticity was observed in the bentonite samples with a liquid limit range of 270 to 380 %.

The results of the grain size analyses on different materials are presented in Figure 8-14. The bentonite sample has the highest clay content, about 90 %. The bentonitic mudstone has a clay content of 50 %, and the carbonaceous mudstone has a clay content of 35 %. Higher sand and silt contents were found in the till sample. The sand sample is poorly graded and most of the particles range between 0.2 to 0.08 mm.

8.5.2 Strength tests

Unconfined compression tests and unconsolidated, undrained triaxial tests were carried out on the clay and till samples during the 1977 and 1979 development investigations. The undrained shear strength of the glacial lake clay ranged from 30 to 150 kPa and the undrained shear strength of the till samples ranged from 190 to 340 kPa.

In the 1999 investigation, consolidated drained direct shear tests were conducted on till, bedrock, and bentonite samples. In the bedrock samples, significant swelling occurred during the consolidation/swelling stage for a normal stress up to 300 kPa. After the consolidation/swelling stage, the samples were sheared at a very slow rate (0.00049 mm/min) to allow time for pore pressure dissipation. To obtain the residual shear strength of the intact samples, reverse shear tests were conducted until the steady (residual) value of shear strength was achieved.

Mudstone samples with a low normal stress (up to 100 kPa) show a ductile behavior, with a less distinct peak. This may be due to softening caused by swelling during the consolidation stage. As the normal stress increases, the softening by swelling is less marked. At a higher normal stress, mudstone samples show brittle behavior with a

distinct peak, and less dilation. The stress-displacement curves of the residual tests have no distinct peak and show ductile behaviour.

The failure envelopes obtained from the direct shear tests are presented in Figure 8-15. The peak failure envelopes of the intact mudstone samples are nonlinear with a distinct break in the slope at 300 kPa. Linear failure envelopes are obtained for the till and the residual strength test of the mudstone samples.

The failure envelopes of the intact and failure plane bentonite samples are presented in Figure 8-16. The failure envelopes of the intact bentonite are slightly nonlinear, with a break at 300 kPa. For the intact samples, a peak friction angle of 17° and a cohesion intercept of 40 kPa were obtained from the test. The failure envelopes of the failure plane samples are linear for the peak and residual tests. A peak friction angle of 12° and a cohesion intercept of 86 kPa were obtained for the failure plane samples. Residual friction angles of 10° and 7.4° were obtained for intact and failure plane samples, respectively.

A summary of the index tests and direct shear tests is presented in Table 8-1. Due to a break in the failure envelopes, two peak-strength parameters were determined using the effective normal stress of 300 kPa. In the intact and failure plane bentonite samples, failure plane samples show a higher moisture content and lower shear strength.

8.6 Post-failure landslide observations (Whitemud Road Landslide)

8.6.1 Failure plane geometry

As discussed in section 8.2, major movements in the Whitemud Road landslide occurred within one day. A distinct a graben feature formed at the head of the displaced material as the main body translated along a weak plane in the bedrock. To improve the understanding of the landslide mechanism, an attempt is made to determine the failure plane geometry and post-failure slope movements. The following procedures are used to determine the failure plane geometry.

- Compare pre-failure and post-failure contours of the slide area

- Construct a cross-section of the landslide, together with the available borehole data.
- The failure plane is defined by inclinometer displacement and the exposed main scarp.

Figure 8-17 presents pre-failure and post-failure cross-sections of the slide area and identifies soil and rock layers deduced from drill holes (SoeMoe et al. 2006). As shown in the figure, the failure geometry of the Whitemud Road slide comprises a steeply dipping main scarp and a surface of rupture seated in the bedrock. Drill holes inside the displaced material revealed two different profiles. Drill holes inside the graben are mostly sand, indicating most of the materials inside the graben are from the overlying sand deposit. Drill holes outside the graben boundary revealed an almost undisturbed stratigraphic profile—sand and till overlying bedrock—indicating that these materials just translated along a weak plane.

8.6.2 Long-term monitoring of slope movements

Continued movement of displaced materials occurred a long time after the major failure in 1999. These movements are typically related to seasonal variation of the groundwater level and construction activity of the valley wall. Although the inclinometers installed behind the valley wall show movements of less than 10 mm from 1999 to 2004, significant slope movements are observed from the inclinometers installed inside the displaced material.

The horizontal displacements deduced from the inclinometers installed in the displaced material, together with daily rainfall data from March 2000 to September 2002 are presented in Figure 8-18. The rate of movement of displaced material increased from 1.5 mm/m in 2000 to 3.6 mm/month in 2001 and 7.0 mm/month in 2002. The significant slope movement in 2002 was partly due to construction activities during the installation of horizontal drains. The maximum movement was located at the center of the displaced material.

To obtain the relationship between rainfall and slope movements, annual rainfall data from 1990 to 2004 are plotted together with the events of slope movements in Figure

8-19. As shown in the figure, above average rainfall occurred in 1997 when minor slope movements were observed in the slide area. But the major failure occurred in a year of average rainfall. Also, the rate of movements increased in the displaced material in 2002, a year of lower than average rainfall.

The response of slope movements is also observed from piezometer readings. An example of a decrease in pore pressure in bedrock due to slope movement is shown in Figure 8-20. The figure represents the response of piezometer PZ-00-3 and displacement observed from inclinometer IN-00-3, located in the displaced material. Initially, the piezometric pressure of PZ-00-03 increased possibly due to swelling and pore pressure equalization. When slope movements increased in the summer of 2002, the piezometric pressure decreased sharply, possibly due to dilation of the bedrock. Similar decreases in the piezometric pressure during slope movements are found in other piezometers. This decrease in pore pressure might have helped to stabilize the slope as the strength of the bedrock increased due to the reduction in pore pressure. Over time, the pore pressure will equalize to steady state seepage condition, and the increase will eventually decrease the strength of the displaced materials.

8.7 Remedial measures

Slope failures along the North Saskatchewan River Valley are part of natural processes as the slope angle changes to the long-term position. If stabilizing measures are not taken in the Whitemud Road slide, further retrogression may damage Whitemud Road and the properties located behind the road. In the summer of 2002, eleven horizontal drains were installed through the bedrock and overlying glacial deposits to reduce the groundwater level behind the valley wall and the displaced material. A 2 to 3 m deep pit was excavated in the bedrock at 42 m below the slope crest and horizontal drains were installed in radial directions. The drain installation angle ranged from 4 to 10° from the horizontal. During the installation, some drains were not able to penetrate to the target length due to a loss of drilling fluid in the thick sand deposit. In total, 1457 m of horizontal drains were installed the slide area. The detailed installation plan is presented in Figure 8-21. As shown in the

figure, only drains in the southern part were able to penetrate behind the valley wall. Most of the drains in the northern part of the slide are located inside the displaced material.

To verify the amount of discharge from each drain, flow rate monitoring of the drains was conducted in 2002, 2003 and 2004. In 2002, the maximum flow rate of 145 l/min was observed from drain no. 12 which was installed in the sand deposit with a length of 125.6 m. Drain no. 1 had the maximum flow rate of 60 l/min. The remaining drains had the flow rates ranged from 1 to 10 l/min as shown in Figure 8-22. Significant reduction of flow rates was observed in the monitoring data in 2003 and 2004 (Figure 8-23). Drain no. 3, 5, 6, 8, 9 and 10 achieved flow rates from 1 to 13 l/min.

Water standpipe readings before and after the drain installation revealed that the drains are effective in lowering groundwater level behind the valley wall and the displaced material. But this reduction is limited to areas penetrated by the drains. A 2 to 4 m reduction in groundwater level was observed in water standpipes located behind the slope crest (Figure 8-24). Furthermore, a 2 to 3 m reduction in groundwater level was observed in water standpipes located inside the displaced material (Figure 8-10).

8.8 Stability analyses

Stability analyses were conducted using the Morgenstern and Price (1965) limit equilibrium method with SLOPE/W software. Since the response of the pore pressure during the time of failure is unknown, pore pressures measured after the slope failure are utilized in the analyses. The main objective is to determine whether the failure is a first-time or reactivated slide. If the failure is a first-time slide, it is expected that the mobilized shear strength would be higher than the residual strength. If the mobilized shear strength is close to the residual strength, the slide might have been a reactivated side.

The peak and residual strength of the clay, till, mudstone, and bentonite seam are determined from unconfined compression tests and direct shear tests. Fully softened

strengths are assumed between the peak and residual strengths. The strength parameters used in the analyses are presented in Table 8-2.

The analyses were conducted using a section located at the center of the slide. The slope geometry was obtained from the pre-failure slope profile. The rupture surface was determined from the inclinometer displacements and the boring logs. The analyses were conducted using peak, fully softened and residual strength parameters.

Two groundwater conditions were considered in the analyses. The first condition utilizes the groundwater level for the overlying glacial deposit and the measured piezometric pressure in the bedrock. The second condition assumes that the groundwater level is affecting both glacial deposit and bedrock. This is to simulate the condition when the hydrostatic pressure is acting on the main scarp. Figure 8-25 shows the cross-section used in the analyses together with the stratigraphic profile, the groundwater table, the piezometric pressure of the bedrock, and the failure planes.

For the peak strength, both pore pressure conditions achieved a factor of safety above unity. A lower factor of safety was achieved when using the assumption that the groundwater level was acting on both the glacial deposit and the bedrock. For the fully softened strength parameters, a factor of safety of 1.24 is achieved when different pore pressure conditions are used for the glacial deposit and the bedrock. Under fully softened conditions, a factor of safety of 1.04 is achieved when the groundwater level is acting on the glacial deposit and the bedrock. For the residual strength parameters, a factor of safety of 1.05 is achieved when different pore pressure conditions are used for the glacial deposit and the bedrock. Under the residual condition, a factor of safety of 0.89 is achieved when the groundwater level is acting on the glacial deposit and the bedrock. The results obtained from the stability analyses are presented in Table 8-3.

To determine the effect of groundwater level increase due to urban development, stability analyses were conducted using the 1979 groundwater level and the results were compared with those using the present groundwater level. The results indicate

a reduction of 1 to 5 % in the factor of safety due to a 4 m to 5 m increase in the groundwater level in the sand deposit.

8.9 Summary

A detailed study of the Whitemud Road Landslide is presented as a case study. The landslide occurred along the North Saskatchewan River Valley, involving weak bedrock and overlying Pleistocene deposits. Field monitoring and laboratory investigations are studied and interpreted to understand the landslide mechanism of the North Saskatchewan River Valley slides.

Slope failure was caused by a combination of factors, namely toe erosion by the river, residential developments behind the slope crest, the rise of the groundwater table, and softening of the bedrock material. Determining the triggering factors of the slide is complicated since no instrumentation data were available before the slide. Even though groundwater may be one of the factors, the major failure occurred in the fall, a period of less rainfall. A summary of this case study follows.

- In the slide area, a perched water level is located in sand a deposit, about 25 m below the flat upland area. Piezometers installed in the underlying bedrock confirmed that deficient pore pressures exist in the bedrock.
- Post-failure slope movements are related to periods of high precipitation which significantly contributed to the development of high pore water pressure in the displaced material.
- Horizontal drains are found to be effective in reducing the groundwater level in the overlying sand deposit and the displaced material.
- Stability analyses reveal the mobilized shear strength along the horizontal sliding plane is lower than the peak strength.
- Detailed field monitoring, especially of the pore pressure condition during the time of failure, is required to obtain a reliable assessment.
- Horizontal drains were installed through the bedrock to the overlying glacial deposits and displaced materials. The effectiveness of the drain installation was determined from reductions in the groundwater table and the piezometric pressure of the bedrock. The horizontal drains penetrated the kame deposit

in the southern part of the slide area. In this area, a 1 to 2 m decrease in the groundwater table was observed. No water was observed from the drains installed inside the displaced materials after 1 year.

Table 8-1 Summary of index tests and direct shear tests

Material	w_n (%)	LL	PL	Peak strength	Residual strength
Carbonaceous Mudstone (44.4-44.5 m depth)	18- 22	50-80	22-32	$\phi = 47.59^\circ, c = 31.5 \text{ kPa}$ ($\sigma_n' < 300 \text{ kPa}$) $\phi = 18.8^\circ, c = 258 \text{ kPa}$ ($\sigma_n' > 300 \text{ kPa}$)	$\phi = 13^\circ$ $c = 0$
Bentonitic Mudstone (40.2-40.4m depth)	28- 35	60- 140	28-40	$\phi = 29.9^\circ, c = 91.5 \text{ kPa}$ ($\sigma_n' < 300 \text{ kPa}$) $\phi = 15.1^\circ, c = 183 \text{ kPa}$ ($\sigma_n' > 300 \text{ kPa}$)	$\phi = 12.5^\circ$ $c = 0$
Till (19.1-19.7 m depth)	10- 14	40-65	13-18	$\phi = 15.6^\circ, c = 49 \text{ kPa}$	$\phi = 14^\circ$ $c = 0$
Bentonite (30.8-39 m depth)	44- 45	150- 280	38-35	$\phi = 17^\circ, c = 40 \text{ kPa}$	$\phi = 10^\circ$ $c = 0$
Bentonite (Failure plane)	48- 53	277- 340	41-45	$\phi = 12^\circ, c = 85.9 \text{ kPa}$	$\phi = 7.4^\circ$ $c = 0$

Table 8-2 Strength parameters used in analyses of the Whitemud Road Landslide

	Peak		Fully softened		Residual	
	ϕ	c (kPa)	ϕ	c (kPa)	ϕ	c (kPa)
Clay	25 °	0	25 °	0	-	-
Sand	35 °	0	35 °	0	-	-
Clay Till	15.6 °	49	15.6 °	0	14 °	0
Mudstone	29 °	60	18 °	0	13 °	0
Bentonite	17 °	40	12 °	0	10 °	0
Failure plane	12 °	85	12 °	0	7.5 °	0

Table 8-3 Factor of safety obtained from analyses of the Whitemud Road slide area

Pore pressure Consideration		Strength		
Glacial Deposit	Bedrock	Peak	Fully softened	Residual
GWL	Piezometric Pressure	2.155	1.240	1.046
GWL	GWL	1.874	1.038	0.887

GWL – groundwater level

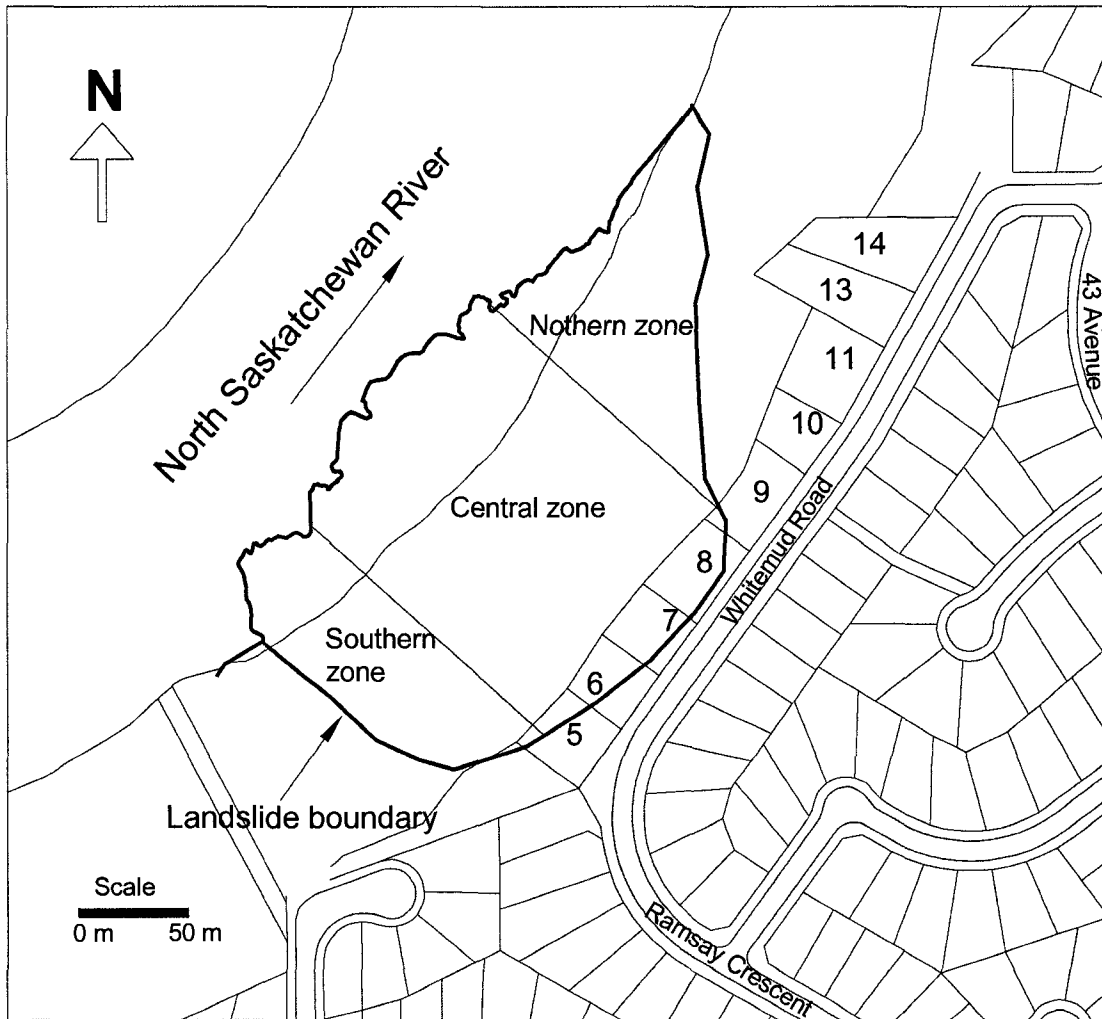


Figure 8-1 Location of Whitemud Road slide



Figure 8-2 Photograph of exposed piles on lot 5 (November 1999)



Figure 8-3 Landslides along Whitemud Road (May 2002, the City of Edmonton, Line 17E, Scale 1: 5000)

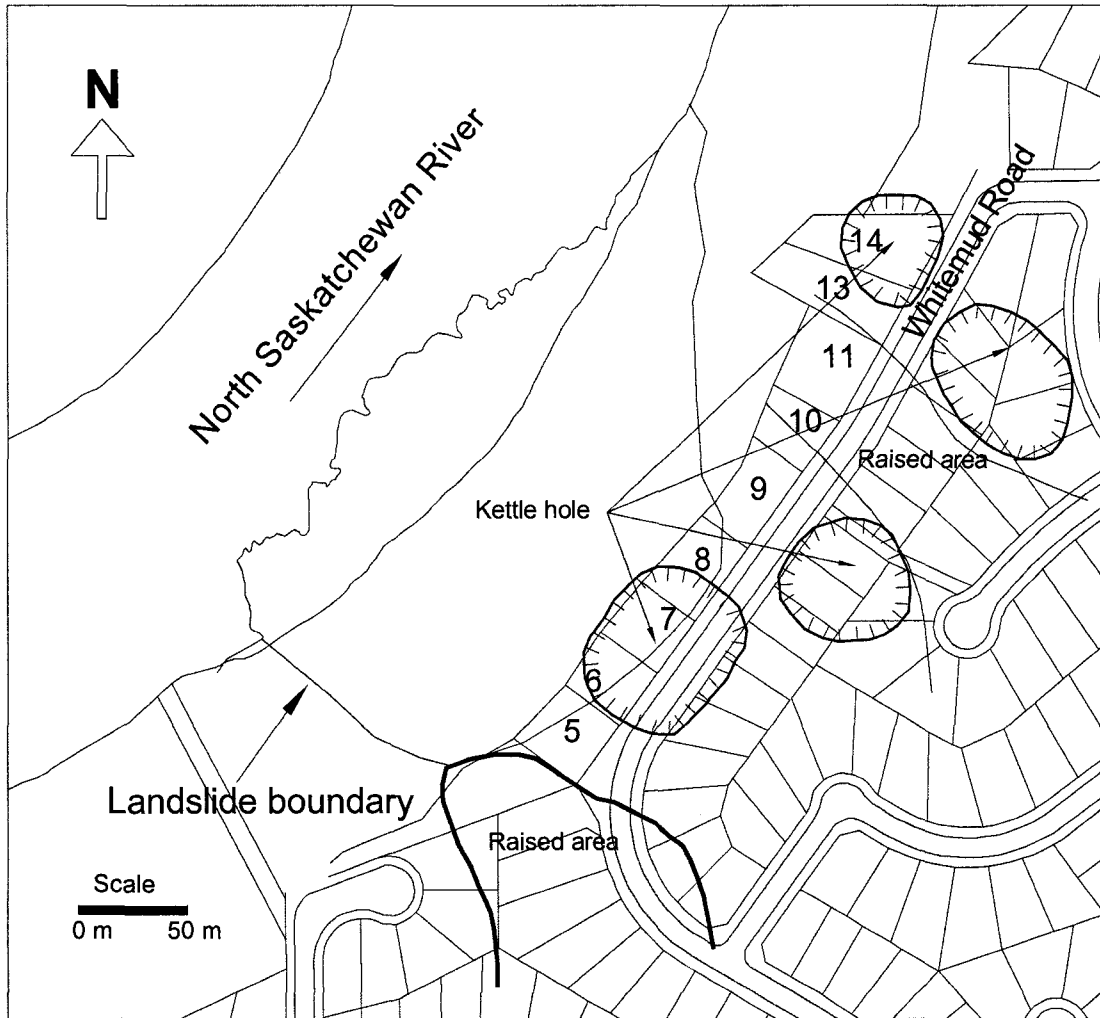


Figure 8-4 Locations of kettle holes and raised area before developments (based on airphotos from 1962, 1967 & 1976)

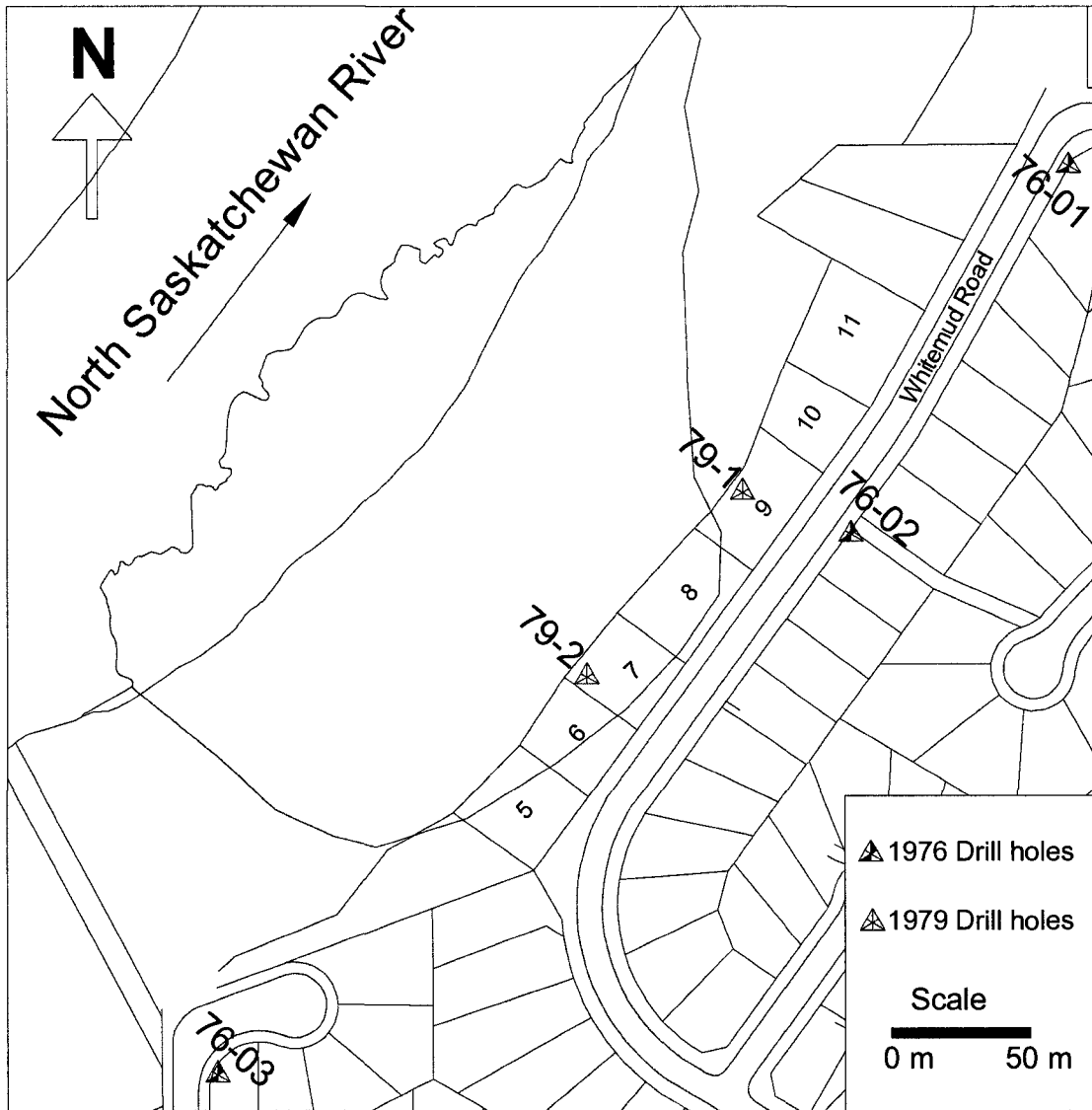


Figure 8-5 Test hole location of pre-failure investigation

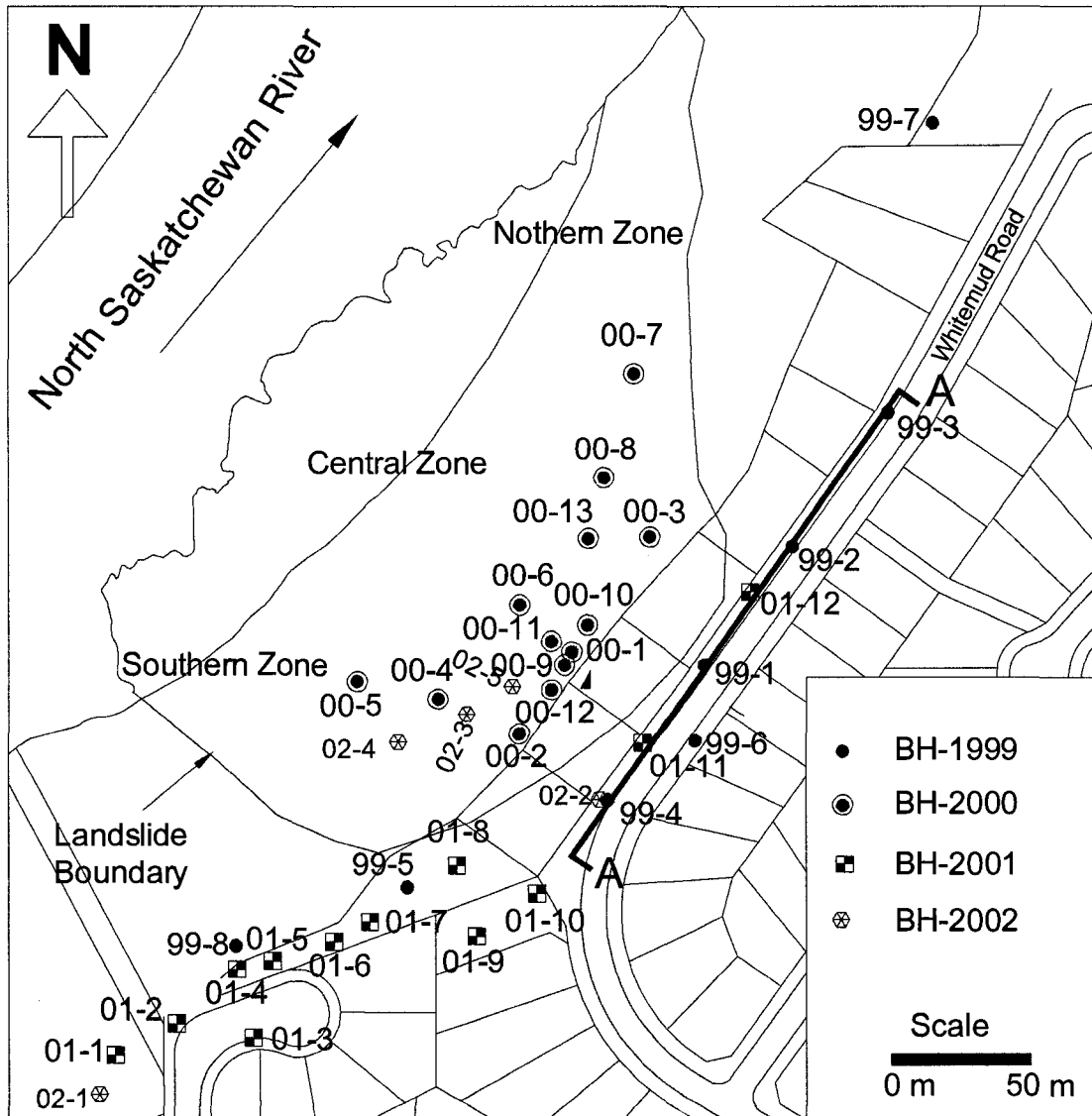


Figure 8-6 Test hole location of post-failure investigation

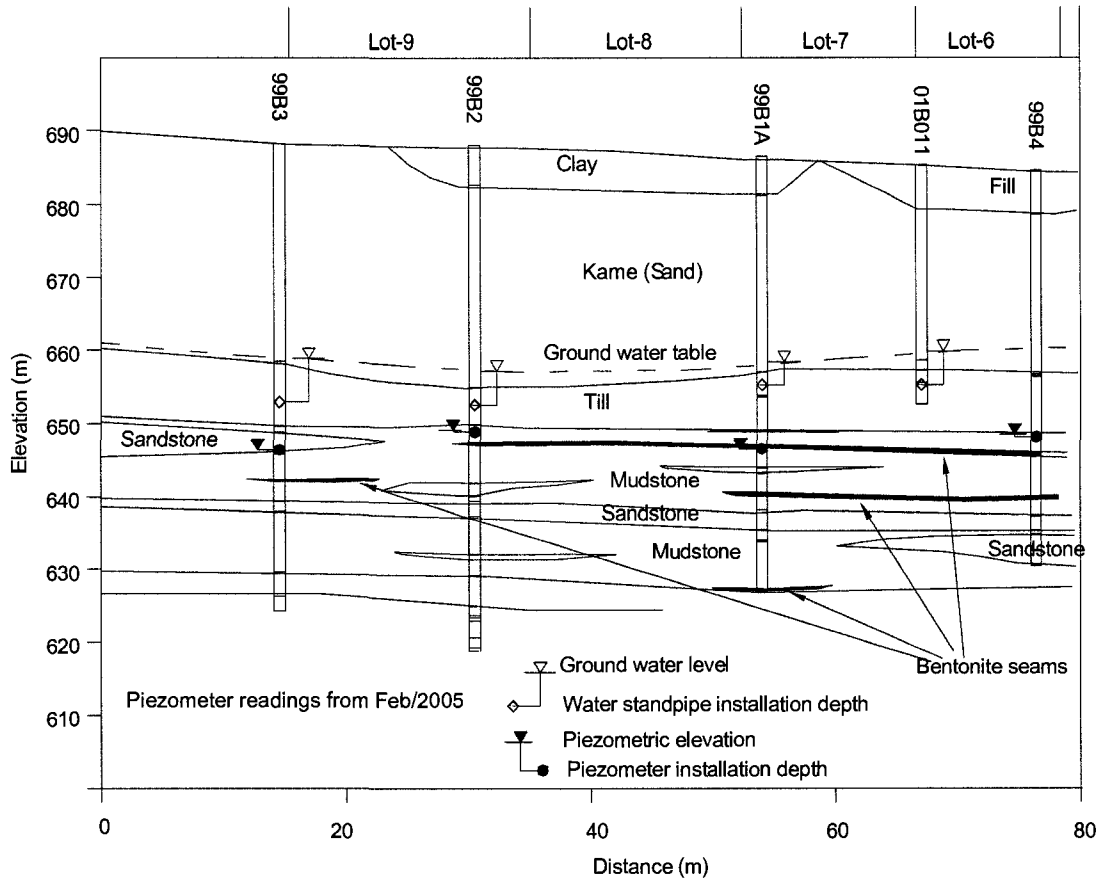


Figure 8-7 Cross-section behind the river valley along Whitemud Road (Figure 8-6, Section A-A, piezometer data from February 2005)

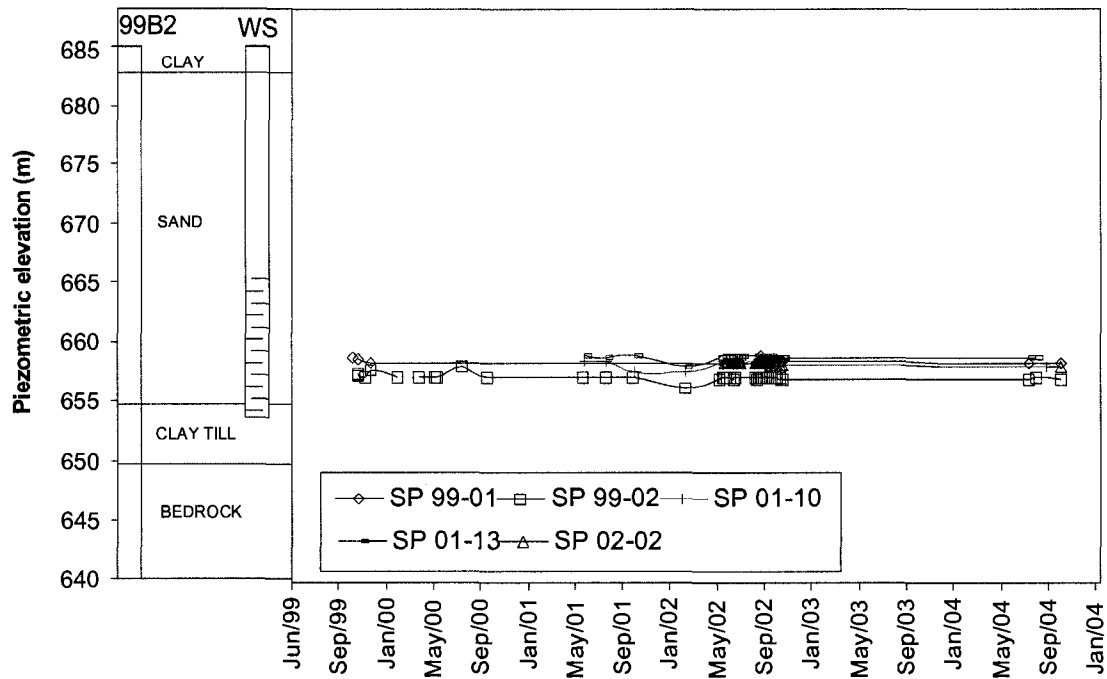


Figure 8-8 Groundwater level behind the valley wall

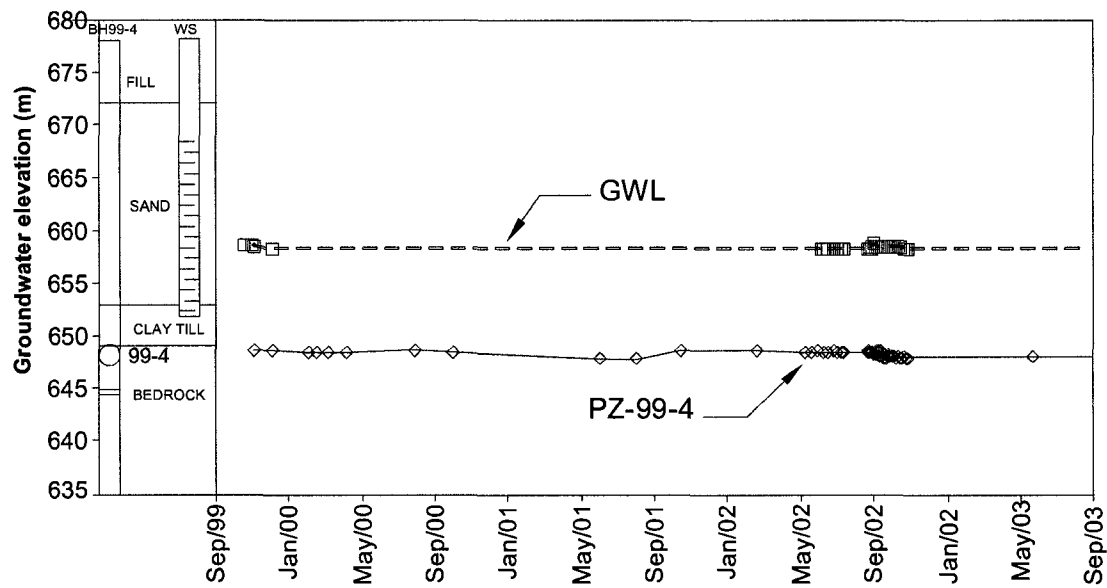


Figure 8-9 Piezometric elevation of the bedrock behind the valley wall

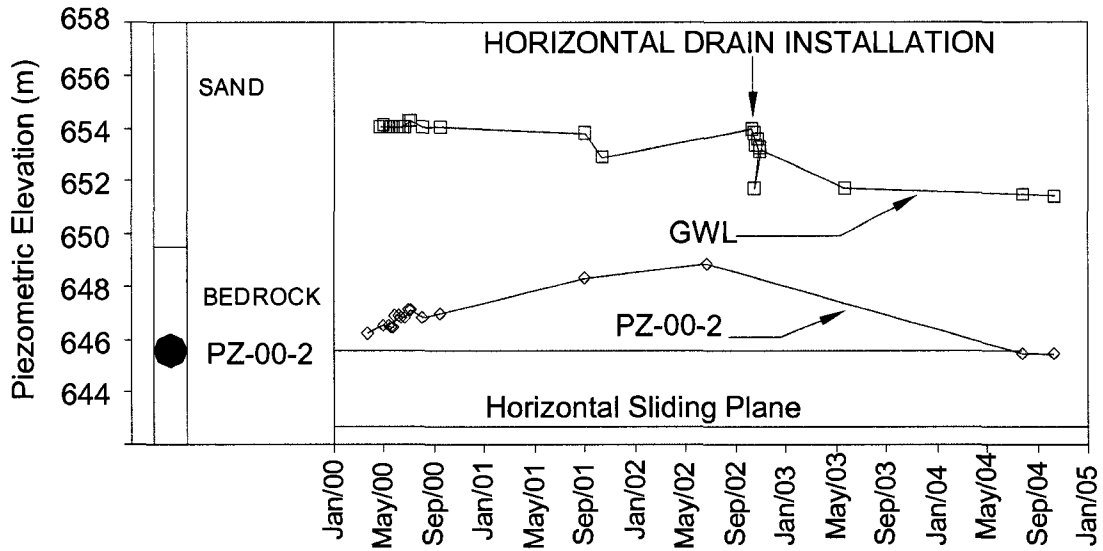


Figure 8-10 Pore pressure response of displaced materials

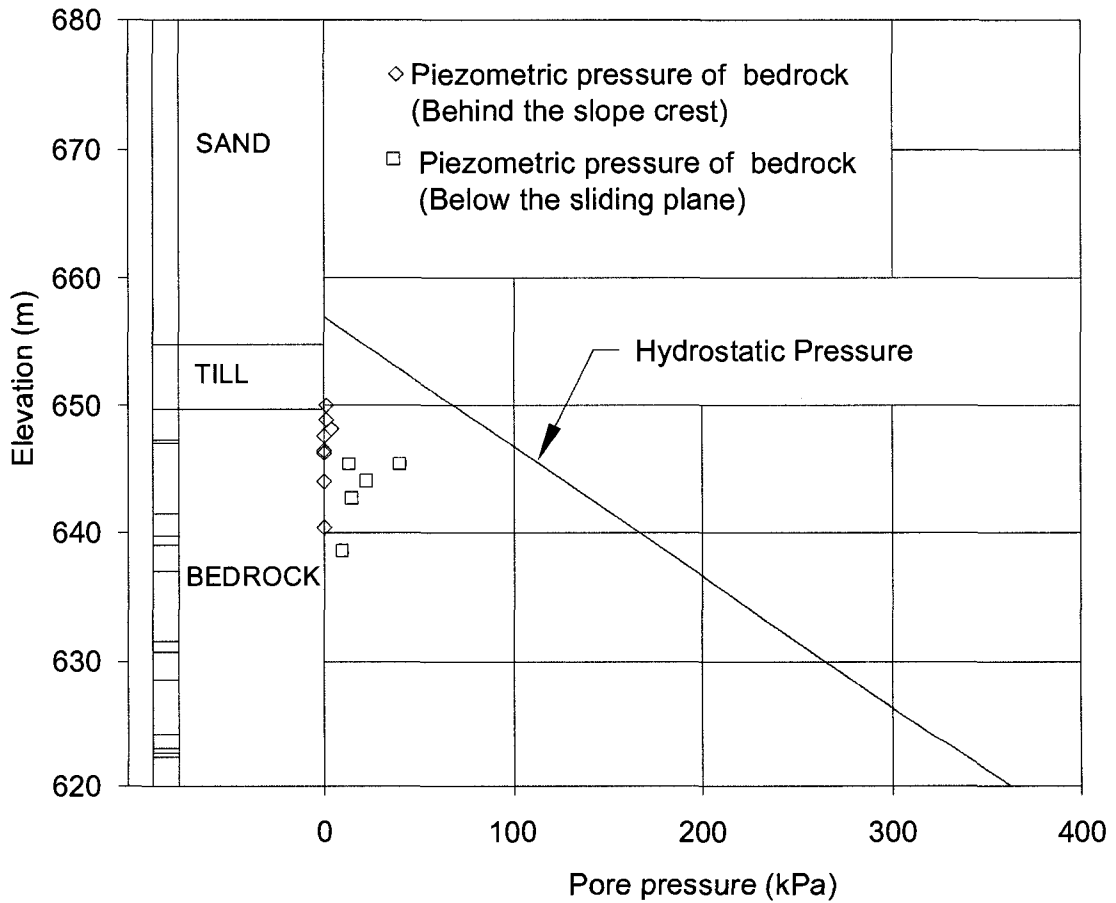


Figure 8-11 Piezometric pressure profile of the bedrock

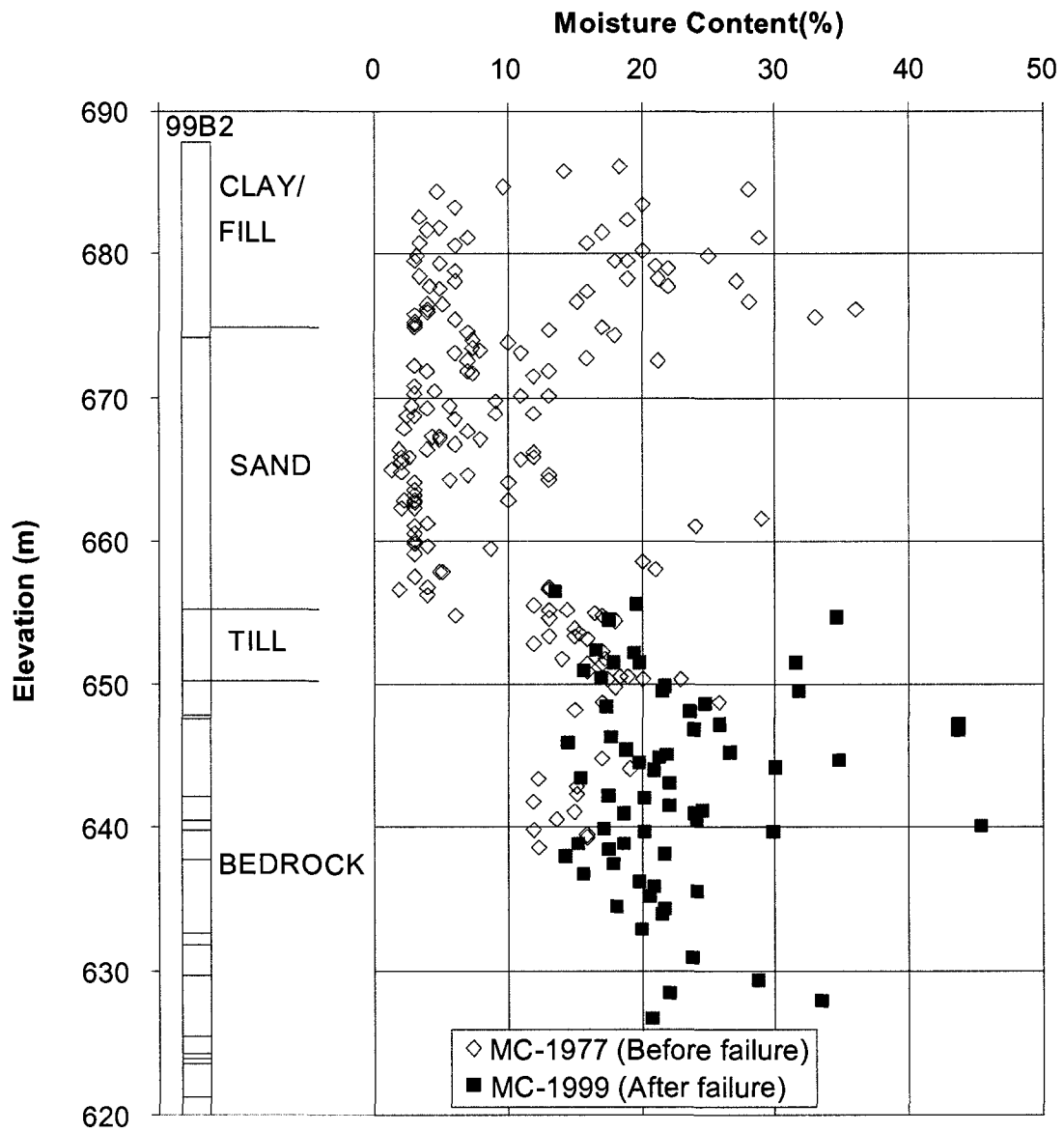


Figure 8-12 Moisture content profile at Whitemud Road Landslide

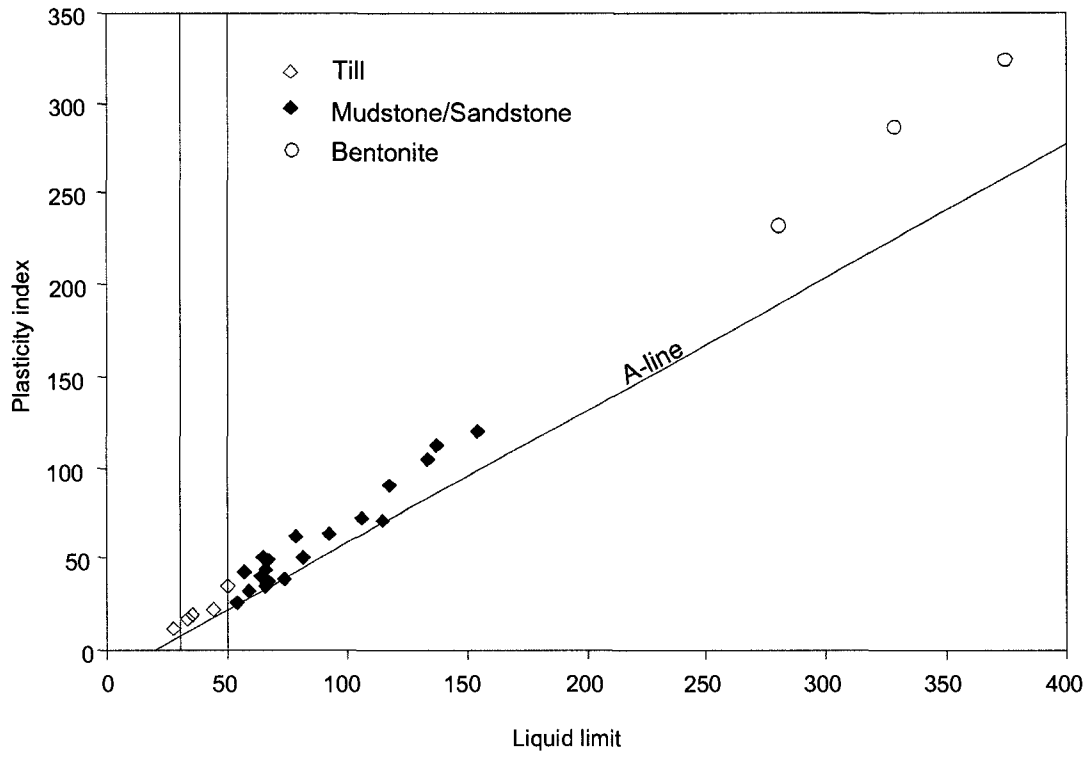


Figure 8-13 Plasticity chart of till and bedrock

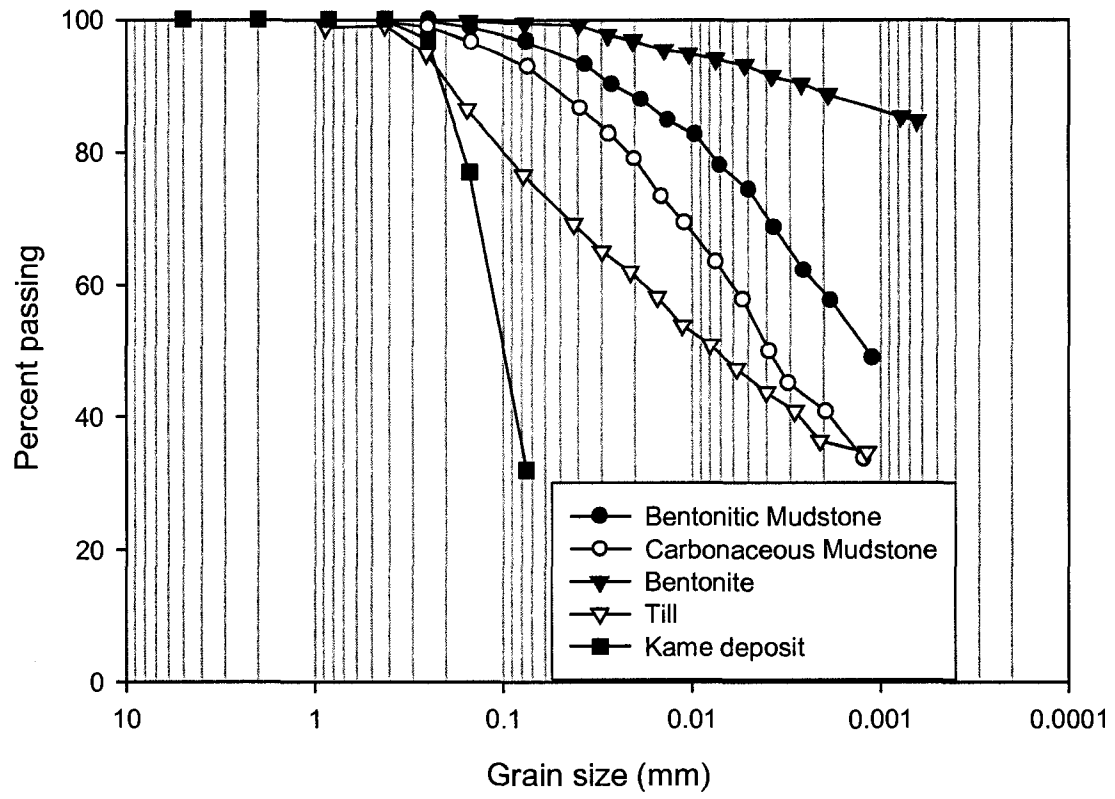


Figure 8-14 Sieve analysis of different materials in the Whitemud Road slide area

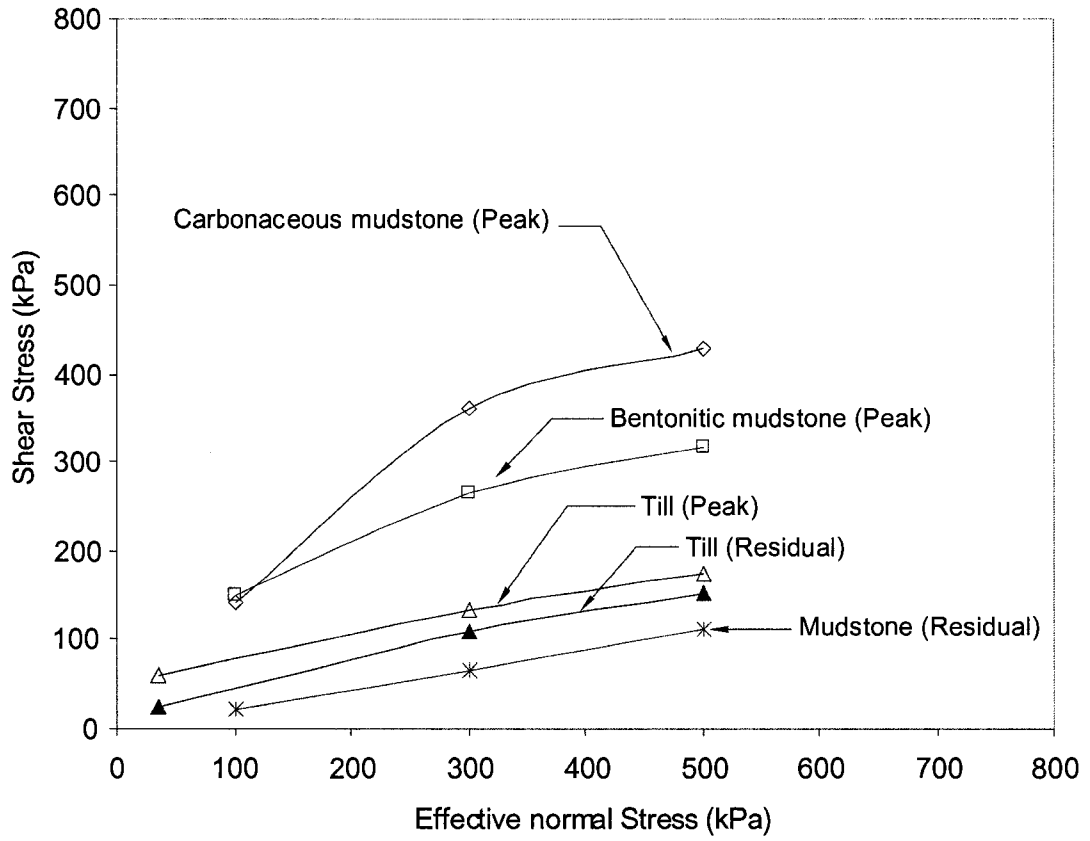


Figure 8-15 Direct shear test results of Whitemud Road slide materials

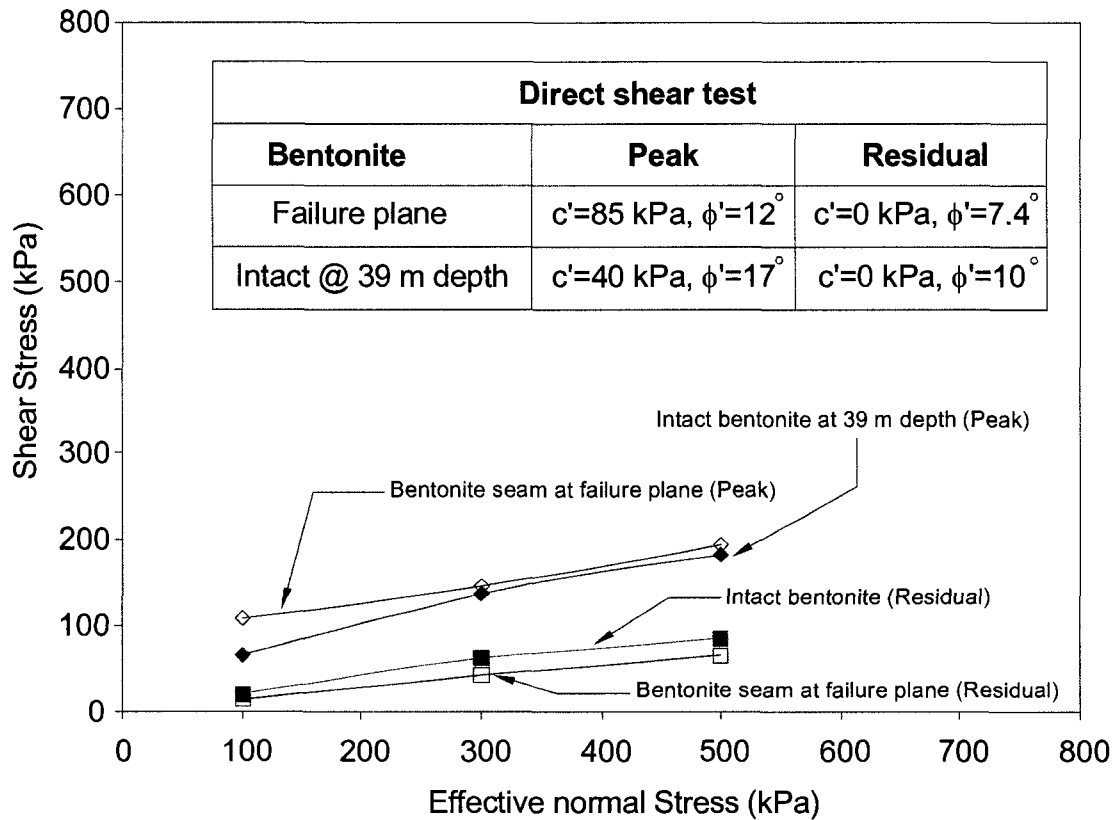


Figure 8-16 Direct shear test of Bentonite in the Whitemud Road slide area

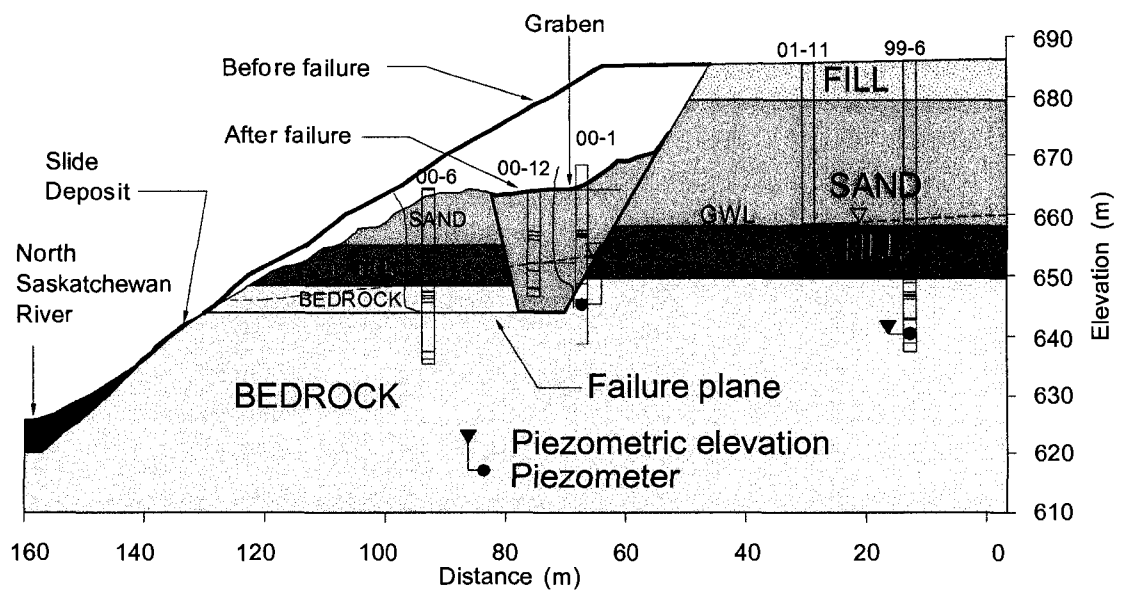


Figure 8-17 Pre-failure and post-failure cross-section of the Whitemud Road Landslide

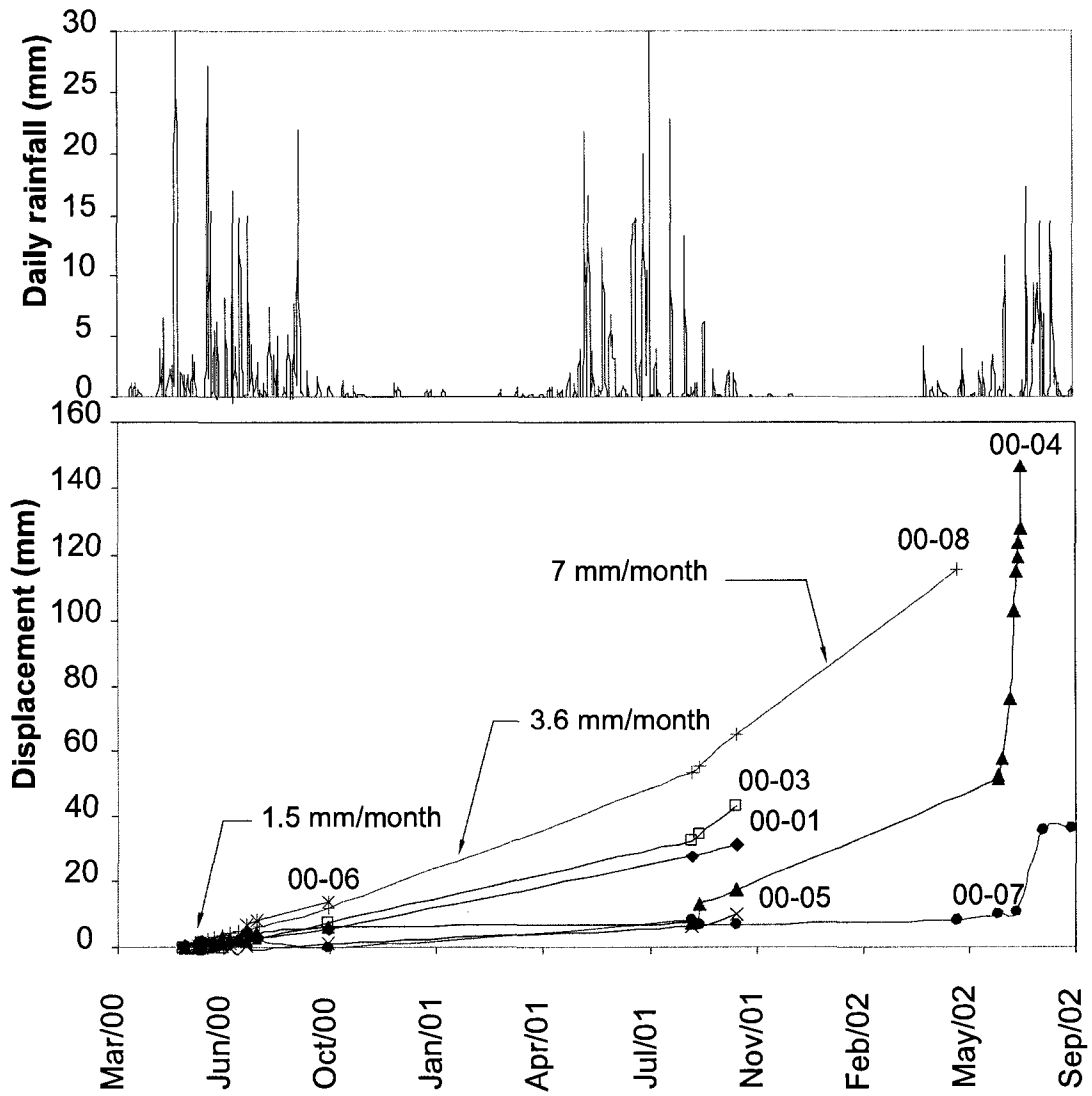


Figure 8-18 Horizontal displacement of displaced material in the Whitemud Road Landslide

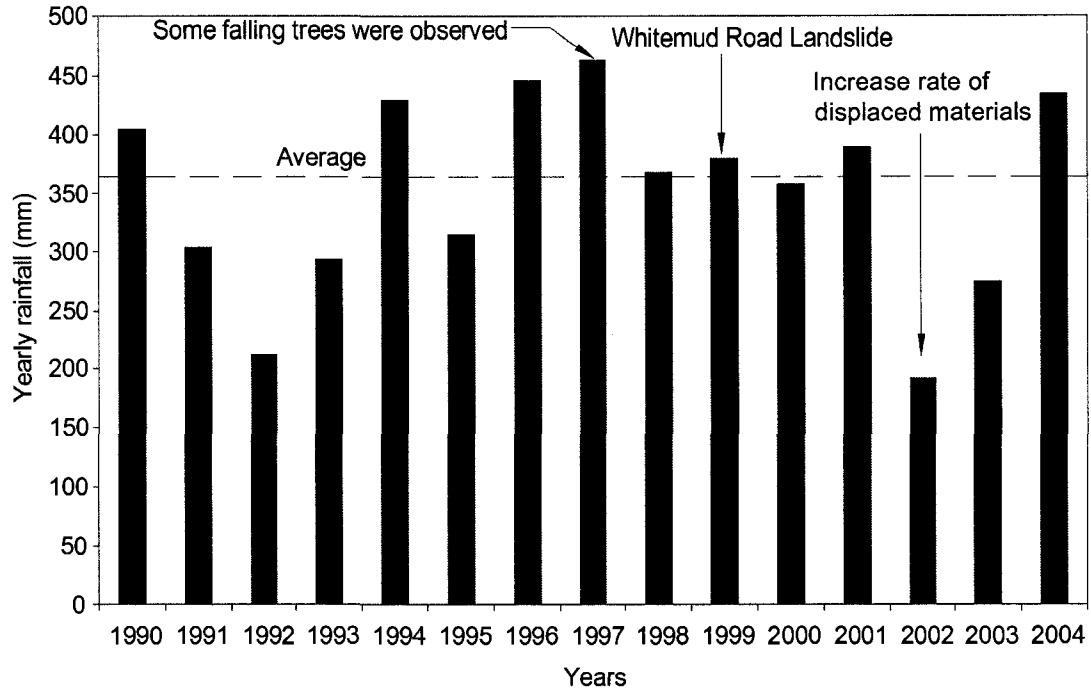


Figure 8-19 Total annual rainfall data together with landslide incidents on Whitemud Road

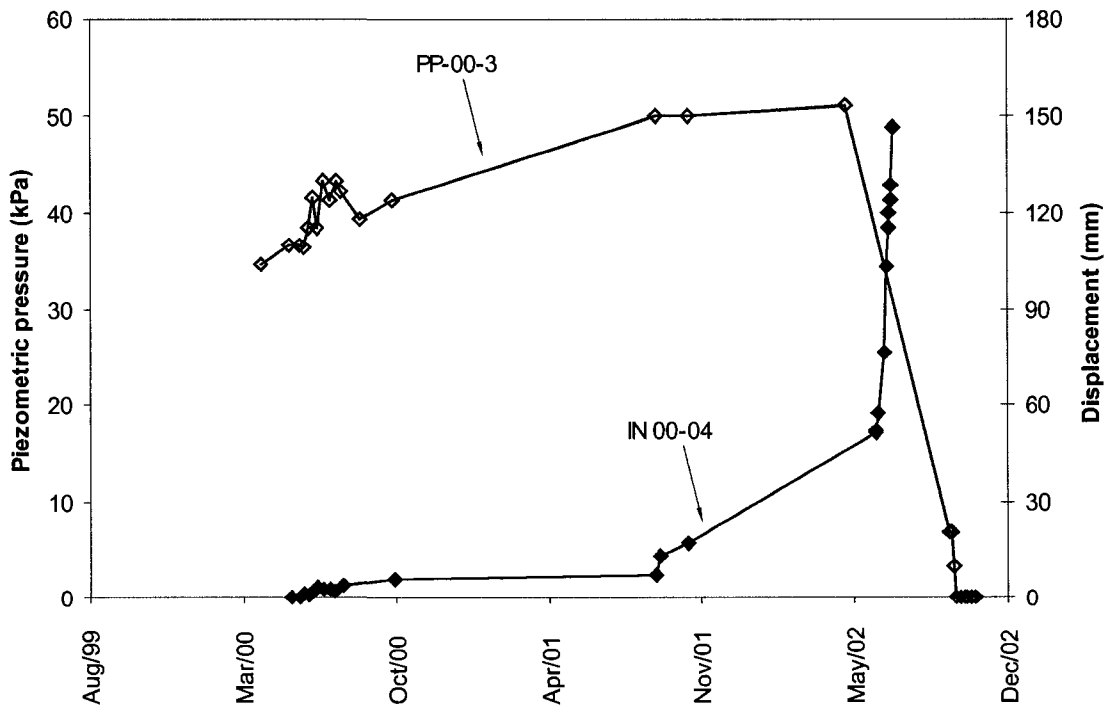


Figure 8-20 Comparison of slope movement and piezometric pressure in the Whitemud Road slide area

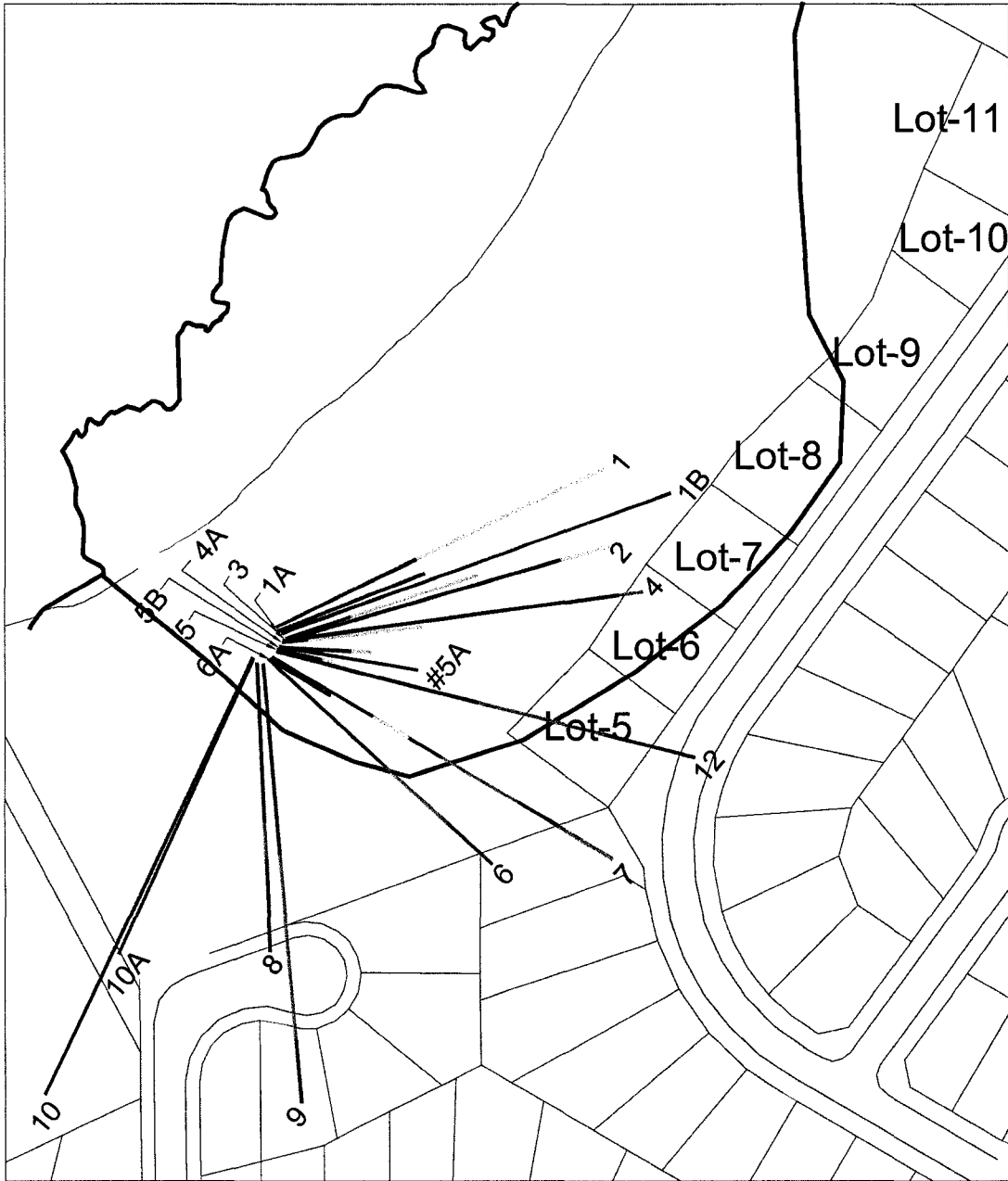


Figure 8-21 Plan view of drain installation in the Whitemud Road slide area

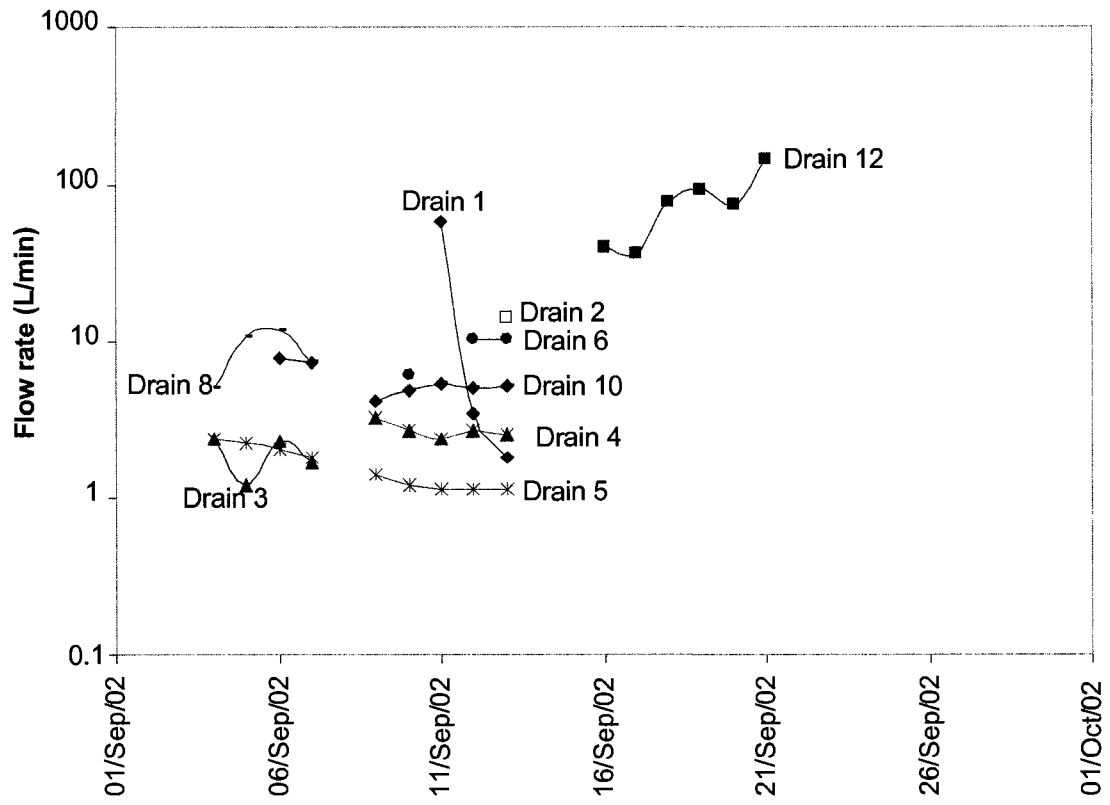


Figure 8-22 Drain monitoring data (September 2002)

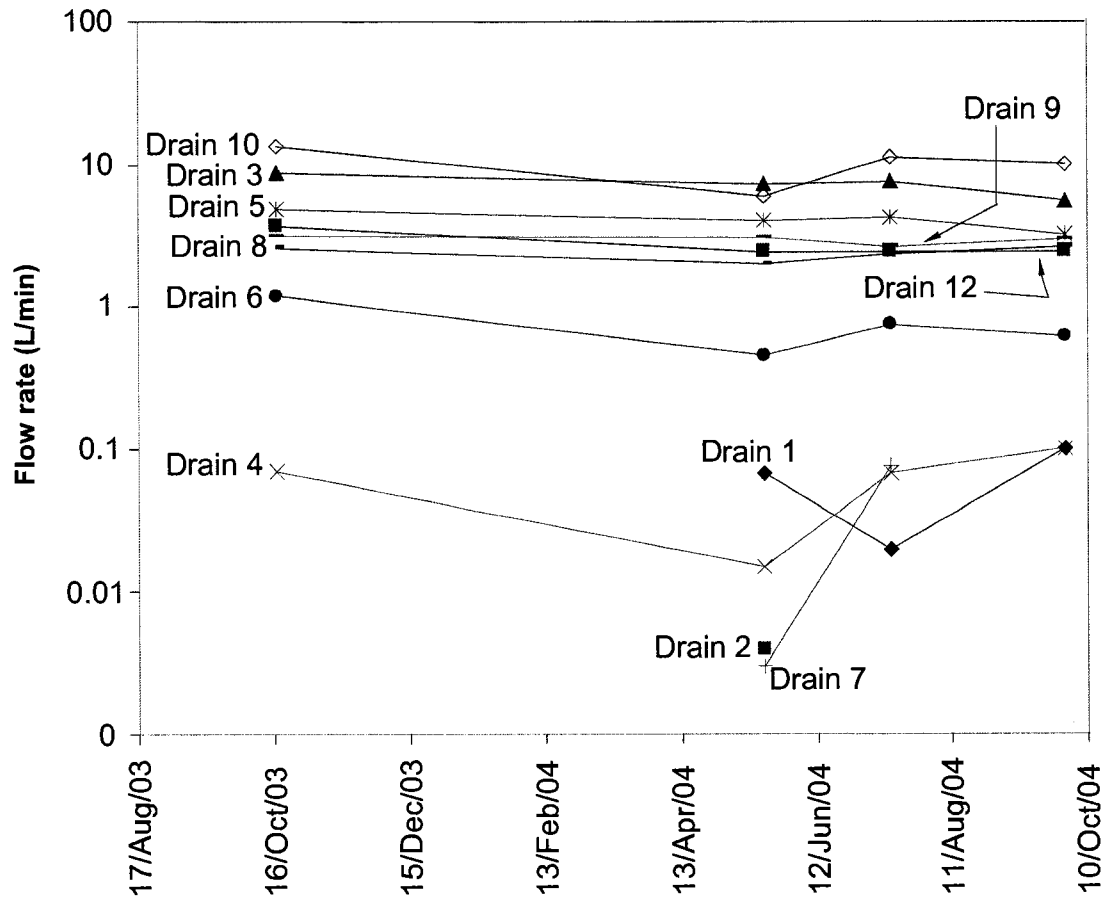


Figure 8-23 Drain monitoring data (2003 & 2004)

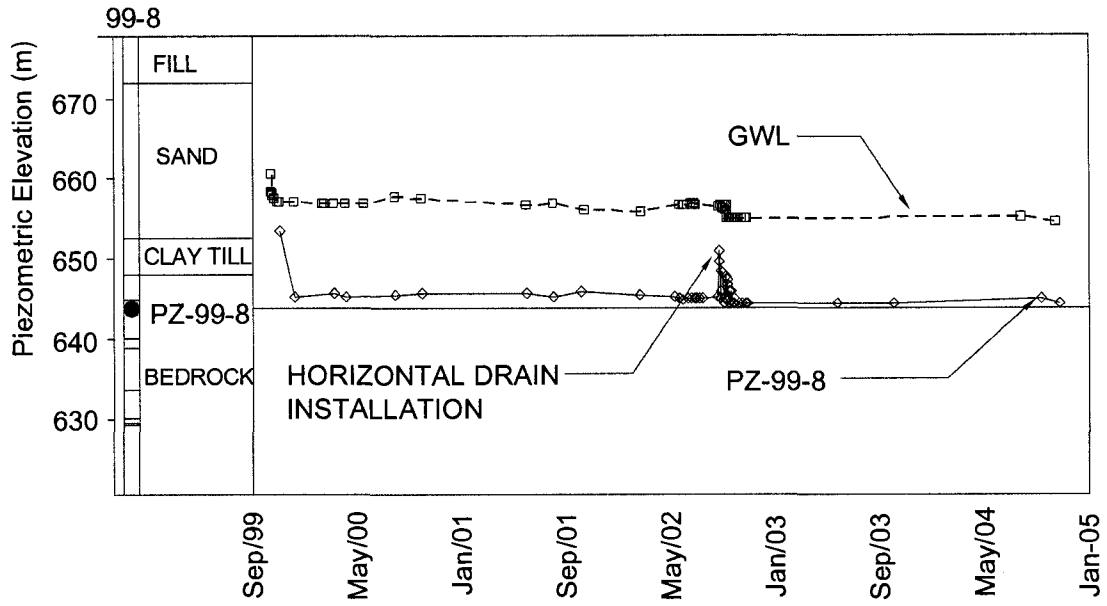


Figure 8-24 Pore pressure response due to drain installation

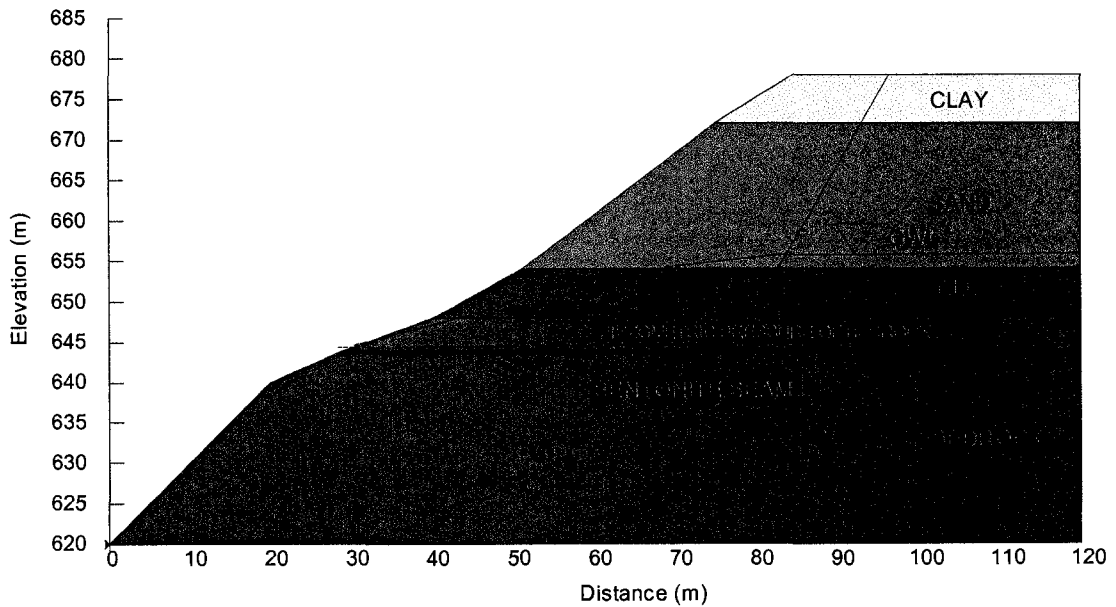


Figure 8-25 Cross-section used in stability analyses of the Whitemud Road slide area

CHAPTER 9 Forest heights park landslide

9.1 Introduction

Forest Heights Park is located on the eastern bank of the North Saskatchewan River, immediately south of the Dawson Bridge in the eastern part of the City of Edmonton. The valley wall around this area is known for active slope movements since the early 1900s, when coal mining was being conducted in the area. As the City of Edmonton expanded, this area was designated as a recreational park with public access roads and recreational trails (Figure 9-1).

Around the park area, the flat upland area is occupied by McNally High School, sport fields, and public buildings. The average elevation of the slope crest is about 660 m. The valley wall is about 45 m in height and occupied by steep scarps, grabens, longitudinal ridges, and localized level terraces, indicating old landslide features. The overall slope from the crest to the river is about 2.7 H:1V. The elevation of the river level is about 617 m. In the early 1980's, a toe berm was constructed as a part of bank stabilization and protection works. Even after the toe berm construction, the slope movements continued to affect the valley wall up to the present day. Due to the retrogression, recreational trails behind the valley wall have had to be relocated several times in the past 30 years.

The near surface bedrock around Forest Heights Park is Upper Cretaceous in age and known as the Horseshoe Canyon Formation (Irish 1970). The bedrock comprises fine grained bentonitic sandstone and siltstone interbedded with bentonitic claystone. Coal seams and bentonite beds of variable thickness are common throughout the formation together with beds of claystone and sandstone. Within the study area, local variations in bedrock occur frequently and are attributed to

subsidence from old underground coal workings. The bedrock is overlain by 10 to 15 m of thick till and lacustrine deposits. The valley wall is covered by colluvial material.

Even though there is no detailed record of initial slope failure, this site is an ideal location to study long-term slope movements. The present study includes field mapping of the valley wall, site investigation, and instrumentation. With support from the City of Edmonton, site investigation and instrumentation were conducted on an active landslide area, located in the southern part of the park. The site investigation includes sampling and coring of the overlying glacial deposits and the bedrock. The main focuses of the current investigation are as follows:

- The effect of coal mining on stability of the valley wall,
- Long-term slope movements of the active landslides, and
- Post-failure landslide mechanisms.

A river valley view of Forest Heights Park is presented in Figure 9-2.

9.2 Coal mine workings below Forest Heights Park

Several small coal mines operated within Forest Heights Park in the early 1900s. According to Taylor (1971), the present park boundary is located within the previously mined area and these mines had cave-in and subsidence problems. The exact locations of these underground mines are not known and are currently obscured by soil and vegetation. Coal was extracted from 2 seams, the Weaver seam and the Clover Bar seam, located 30 m and 70 m below the slope crest (Godfrey 1993). Among the several mines in the park area, only the Dawson mine worked in the deeper Cloverbar seam while the other mines worked in the shallow Weaver seam (Taylor 1971). Figure 9-3 presents the mine boundaries and mine adits along with the present slope condition.

9.3 Slope instability at Forest Heights Park

Immediately below the flat upland area, steep main scarps and grabens occupy the valley wall. From time to time, retrogression at the slope crest requires realigning

part of the recreational trail behind the slope crest. Old landslide features, such as steep scarps, grabens and tension cracks, encompass the valley wall. Transverse ridges and transverse cracks are also found throughout the mid-slope area. A terrace level is located at a 25 to 30 m below the crown, where a lower recreational trail is located. The slope below the terrace is also irregular with transverse cracks and scarps. The North Saskatchewan River is located 10 m below the terrace level. Till is exposed at the toe of the slope in the northern area of the park, while the remaining area of the toe is occupied by displaced bedrock. The bedrock at the toe suffers varying degrees of slope deterioration. Retrogressive slides are found in several locations as shown in Figure 9-4.

9.4 Geotechnical investigation

Earlier studies of slope instability in Forest Heights Park (Scott and Townsend 1976; Townsend 1975; Townsend 1980) concentrated on several active slope movement areas and resulted in the construction of a toe berm in 1985. Even after the construction of the toe berm, slope movements continued to affect the valley wall.

In the fall of 2004, an extensive site investigation and instrumentation program was conducted in the southern area of Forest Heights Park, where continued slope movements affect the valley wall (Figure 9-5). The field investigation program included sampling and coring of the glacial and bedrock deposits behind the valley wall and through the displaced material at the toe of the slope. Three boreholes (B04-01 to B04-03) were advanced behind the slope crest to a depth of 50 m, and three boreholes (B04-04 to B04-06) were advanced from the lower trail to a depth of 20 m. To monitor the slope movements and the groundwater regime at the site, water standpipes, vibrating wire piezometers, pneumatic piezometers, and inclinometers were installed in these boreholes. The borehole locations, together with previous boreholes around the study area, are presented in Figure 9-5.

9.4.1 Stratigraphy

The stratigraphy was established from available borehole logs in the study area. The stratigraphic profile behind the valley wall is presented in Figure 9-6 and can be described as follows:

- Below the flat upland area is a 5 to 6 m thick lacustrine clay deposit interbedded with silt layers. The lacustrine clay is medium to high in plasticity and with a moisture content range of 30 to 42 %. A 2 to 3 m thick layer of fill is found in the northern part of the slope.
- Lacustrine clay is underlain by a 9 to 10 m thick sand and till deposit. The sand deposit is generally in a dense to very dense state with a moisture content of less than 10 %. The till is low in plasticity and has a moisture content range of 15 to 25 %.
- The till deposit is underlain by Upper Cretaceous bedrock, comprising clay shale and sandstone interbedded with coal and bentonite seams. The clay shale is low to medium in plasticity with a moisture content range of 18 to 22 %. Bentonite seams vary in thickness from 20 to 250 mm, but these layers are not continuous throughout the valley wall. Bentonite is very high to extremely high in plasticity with a moisture content range of 40 to 45 %.

Stratigraphic profile at the toe of the slide was deduced from three boreholes (B04-04 to B04-06) drilled the lower trail is presented in Figure 9-7 and can be described as follows:

- Just below the trail level, 1 to 2 m thick colluvium material overlies the displaced bedrock. The colluvium material comprises of high plastic clay mixed with sand and coal pieces.
- The displaced bedrock below the colluvium mainly comprises of clay shale, coal and bentonite seams.

The moisture content profile of three boreholes (B04-01, B04-02, and B04-04) is presented in Figure 9-8. The moisture contents of boreholes B04-01 and B04-02 were from the intact bedrock (boreholes behind the valley wall) and the moisture contents of borehole B04-04 were from the displaced materials (boreholes drilled from the lower trail through the displaced material). As shown in the figure, higher

moisture contents of 25 to 40 % were found in samples located between elevations 610 to 624 m, where major slope movements had occurred in the past. The results also show similar moisture content between intact and displaced samples at these elevations.

9.4.2 Groundwater Conditions

Water standpipes installed behind the valley wall revealed that the groundwater level in the overlying sand and till deposit is about 12 m below the slope crest. The groundwater level is also observed in the displaced material, about 1 m below the lower trail. Seepage holes and wet zones are found throughout the valley wall, especially during snow melts and heavy rainfalls.

Piezometers installed in the bedrock indicate a different pore pressure regime. Piezometric heads of 3 and 6 m were observed from the piezometers installed at 19.2 and 36.2 m in the bedrock. Long-term monitoring data also revealed that the piezometric pressure of the bedrock is not related to the groundwater level in the overlying glacial deposit. Piezometers installed in the bedrock did not respond to changes in the groundwater level due to snow melt and rainfall. The results of measured groundwater level and piezometric pressure in the bedrock are shown together with the present cross section A-A (see plan view in Figure 9-5) of the bedrock in Figure 9-9.

Figure 9-10 presents the pore pressure response of the bedrock together with the hydrostatic pressure calculated from the groundwater level. As shown, piezometric pressure in the bedrock is significantly lower than the hydrostatic pressure calculated from the overlying glacial deposit and displaced material. This lower piezometric pressure is in agreement with the Koppula and Morgenstern (1984) suggestion that the valley bottoms of some American and Canadian rivers could still be subject to vertical swelling deformation due to previous geological erosion. The swelling of the bedrock may also be one of the factors contributing to delayed failure of the river valley slopes.

9.5 Stability analyses of the river valley

Slope stability analyses were conducted to assess the present condition of the slope. Since the study area is located in an old landslide area, it is assumed that the shear strength along the failure planes had already reached a residual value. Since the laboratory strength parameters are not available for this site, the strength parameters obtained from the Whitemud Road Landslide are used for the stability calculations. The parameters used in the analyses are presented in Table 9-1.

The stability analyses are carried out on Cross-section A-A as shown in Figure 9-11. In this section, the horizontal sliding plane was determined from the inclinometer displacement and a steeply dipping main scarp was assumed to intercept the surface of rupture at depths. Analyses were conducted using the Morgenstern and Price method (Morgenstern and Price 1965) with SLOPE/W software (Krahn 2004a). Several scenarios are analyzed to determine mobilized shear strength along the rupture surface and the effects of different pore pressure regimes on the stability of the valley wall.

To determine the influence of the groundwater level on the stability of the slope, analyses were carried out assuming two groundwater conditions. In the first case it is assumed that the groundwater level was affecting both displaced material and the sliding plane. In the second case it is assumed that the groundwater level was affecting the upper displaced material. For analysis of the surface of rupture, measured piezometric pressure was utilized. Stability analyses were conducted for both fully softened strength and residual strength. When a friction angle of 14° was used for the surface of rupture, the factors of safety were 1.0 and 1.35 for the two groundwater conditions, respectively. A lower factor of safety is achieved when a friction angle of 10° is used in the analyses. A summary of the analyses is presented in Table 9-2.

Evidence indicates that the slope movements are related to the groundwater level. During heavy rainfall, surface water may seep through the interconnected cracks inside the displaced material and can exert hydrostatic pressure on the cracks. This condition was also found in the Keillor Road Landslide. To determine the stability of

the slope with different scarps, stability analyses were carried out using different distances between the main scarp and the toe. The locations of the main scarps are presented in Figure 9-12. This analysis utilized a friction angle of 10° on the surface of rupture. For the pore pressure condition, the groundwater level and the piezometric pressure of the bedrock are used in the analyses. Although the global factor of safety is 1 (slide no. 5), the factor of safety of the other scarp could fall below unity depending on the groundwater level.

Analysis of the data revealed that the stability of the valley wall is sensitive to the position of the groundwater level in the overlying glacial deposit and the displaced material. The results also confirm that piezometric pressure of the bedrock is not critical in the stability of the slope and it would require a higher groundwater level in the displaced material to reduce the factor of safety to lower than unity. When the measured groundwater level and piezometric pressure of the bedrock were used in the analysis, a mobilized shear strength of 10° was obtained for the surface of rupture to achieve a safety factor of one. It is possible that during snow melt and heavy rainfall, the groundwater level in the displaced material increases and reactivates the old landslide.

9.6 Causes of slope instability

Several factors affect the movement of the Forest Heights Park landslide. Major factors involved are discussed in the following sections.

9.6.1 Toe erosion by the river

Toe erosion by the river is one of the factors controlling the stability of the valley wall. Most of the landslides in the North Saskatchewan River Valley occur on an outside bend of the river. In the Forest Heights Park landslide, slope movements continued after toe berm construction and field studies revealed that the surface of rupture is located above the toe berm. It is possible that present slope movements are the results of groundwater level changes in the displaced material. In June 2005, heavy rainfall caused the North Saskatchewan River level to rise above the toe berm and

caused significant toe erosion. Immediately after that, tension cracks appeared along the lower trail, as shown in Figure 9-13.

9.6.2 Coal mining

The effects of coal mining on the stability of the valley wall can be described as follows;

- Coal mining below the valley wall would have caused the weakening of bedrock above and accelerated the propagation of cracks deeper into the bedrock.
- Subsidence above the old mine workings would have caused significant weakening of the bedrock and facilitated subsequent softening.
- Increased groundwater flow through the cracks would have accelerated the softening process of the bedrock.
- Hydrostatic pressure could build up inside the cracks during heavy rainfall, and this could significantly reduce the safety factor of the valley wall.

Since most of the old mine workings extracted coal from the Weaver seam located in the middle of the valley wall, it is possible that coal extraction from the Weber seam affected the stability of the valley wall. The effect of coal mining from the Clover Bar coal seams would be minimal since it is located 25 m below the surface of rupture. The location of the coal seams together with the displaced material is presented in Figure 9-14.

9.6.3 Deficient pore pressure in the bedrock

Swelling is one of the controlling factors in the delayed failure of valley slopes in Edmonton. The piezometric pressure in the bedrock confirms that significant deficient pore pressure exists in the bedrock. During slope movements, readings of piezometers installed in the displaced material decreased as the bedrock dilated due to movement (Figure 9-15). This pore pressure reduction in the bedrock is the result of stress changes occurring in the valley wall due to slope movement. With time,

pore pressure in the bedrock will equalize with the surrounding seepage condition and will cause swelling of the bedrock.

The long term pore pressure measurement in the bedrock behind the valley wall is shown in Figure 9-16. This figure shows the pore pressure response of two vibrating wire piezometers, PZ-1 and PZ-2, installed 19.2 and 36.2 m below the slope crest. The long term groundwater level (GWL) of the glacial deposit is also shown in the figure. As shown in the figure, the GWL undergoes seasonal variation, but the piezometers installed in the bedrock do not respond to groundwater level changes in the overlying glacial deposit. Initially, PZ-1 registered a piezometric head of 2.4 m, but it decreased to 1.2 m after 10 months. PZ-2 registered a piezometric head of 2.8 m after installation and no significant changes were observed during the monitoring period. This pore pressure reduction in the bedrock behind the valley wall might be related to the movement of displaced material on the valley wall. With time, pore pressure in the bedrock will equalize and cause swelling of the bedrock.

9.6.4 Post-failure slope movements and pore pressure response of the bedrock in Forest Heights Park

Inclinometers installed behind the slope crest showed no significant movements during the period of November 2004 to September 2005. But inclinometers installed in the lower trail showed movement immediately after installation in November 2004 and movement increased in March 2005 due to snow melt. In late April 2005, slope movement damaged both inclinometers and piezometers installed in the lower trail. The movement zone is located 45 m below the slope crest, about 1 m above the river level. Present toe movement ranged from 25 to 40 mm/year, very slow according to a landslide movement scale introduced by Cruden and Varnes (1996).

To determine the effect of slope movements and pore pressure response of the bedrock, water standpipe data, pore pressure response of the bedrock below the sliding plane, and horizontal displacements of the inclinometer at the toe are plotted as shown in Figure 9-15. As shown, the groundwater level is located at elevation 622 m, but the piezometer installed below the movement zone registered only 2.5 m pressure head. Since its installation in November 2004, inclinometers registered

movements at the toe, but toe movements stopped during the winter months in 2005. But snow melt in March 2005 reinitiated the toe movement. During that period, piezometric pressure of the bedrock decreased with time, responding to dilation of the bedrock. Before the toe movement damaged the instruments in late April 2006, the piezometric head of the bedrock below the surface of rupture was reduced to 1.5 m, indicating significant dilation in the bedrock during that period.

9.7 Post-failure Landslide Mechanism

Slope movement in Forest Heights Park is a continuation of old landslides in the area. Along the valley wall, slope movements are occurring at different rates and movement will continue until the slope becomes inactive. There is also a chance that the slope might reactivate and cause retrogression of the valley wall.

At present, slope movement in Forest Heights Park is controlled by groundwater levels in the cracks. Downward movement of displaced material inside the graben may contribute to retrogression of the slope crest. A review of historical air photos revealed that the slope crest retrogressed about 3 to 4 m from 1980 to 2002. The post-failure landslide mechanism observed in Forest Heights Park is presented in Figure 9-17. As shown, translational movement of toe material may contribute to the downward movement of displaced material inside the graben, which may cause retrogression of the slope crest.

With time, erosion by the river will remove the displaced material at the toe and the landslide cycle can be repeated. An example of such a landslide cycle is found in cross-section B-B (see plan view in Figure 9-5), where a thick till deposit is found at the toe of the slope (Figure 9-18). As shown in the figure, two graben features are found at the head of the displaced material and the till deposit is found at the toe, located 35 m below its original elevation. It is possible that the present toe is located in the former graben, where the downward movement resulted in the upper till layer resting above the surface of rupture. Since the till deposit at the toe has suffered several stages of landsliding, the strength of these materials is lower than the intact materials in their original position.

9.8 Summary

A study of the Forest Heights Park Landslide revealed the pertinent features associated with a long-term movement of the river valley wall. The valley wall is occupied by old landslide features such as steep scarps, tension cracks, and grabens. Continued slope movements affect the present valley wall, causing damage to recreational trails along the valley wall. The toe of the slope is moving at a very slow rate, about 25 to 40 mm/year.

The presence of old mines below the park has a detrimental effect on the stability of the valley wall. Coal mining below the valley wall would have caused weakening of bedrock above and accelerated the propagation of cracks deeper into the bedrock. Coal extraction from the Weaver seam might have accelerated the weathering and softening of the bedrock. Extraction of coal from a lower coal seam, Clover Bar, has not significantly affected the slope stability of the valley wall.

The groundwater table is located in the overlying glacial deposit 12 m below the slope's crest and 1 m below the lower trail in the displaced material. The piezometers installed in the bedrock confirmed that deficient pore pressures exist in the bedrock. The measured piezometric head of the bedrock ranged from 1.2 to 2.8 m up to a depth of 36 m. Long term pore pressure equalization of the bedrock might be one of the factors causing delayed movement of the river valley slope. Stability analyses of the present slope confirmed that the groundwater level in the glacial deposit and the displaced material control slope movements.

Table 9-1 Parameters used in analyses of the Forest Heights Park river valley

Material	Softened		Residual	
	c (kPa)	ϕ (Deg)	c (kPa)	ϕ (Deg)
Clay	-	25 °	-	-
Sand	-	35 °	-	-
Till	25	25 °	-	-
Bedrock	-	18 °	-	14 °
Sliding plane	-	14 °	-	10 °

Table 9-2 Factor of safety from the analyses of slope stability in Forest Heights Park

Case No.	Groundwater condition	Sliding plane strength	Factor of safety
1	Perched water table	$\phi = 14^\circ$	1.0
2	Groundwater table and piezometric pressure	$\phi = 14^\circ$	1.35
3	Perched water table	$\phi = 10^\circ$	0.75
4	Groundwater table and piezometric pressure	$\phi = 10^\circ$	1.06

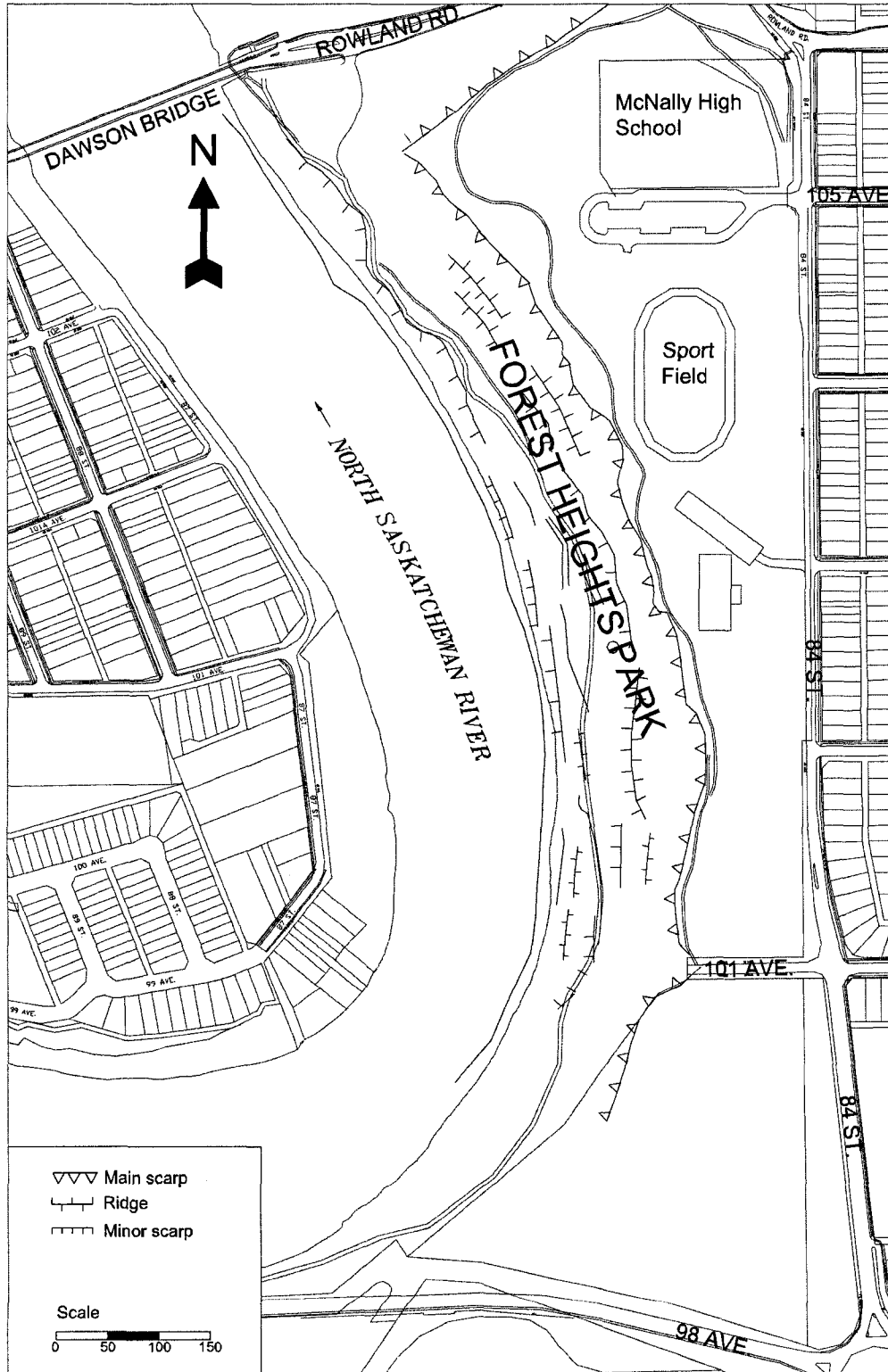


Figure 9-1 Location of Forest Heights Park

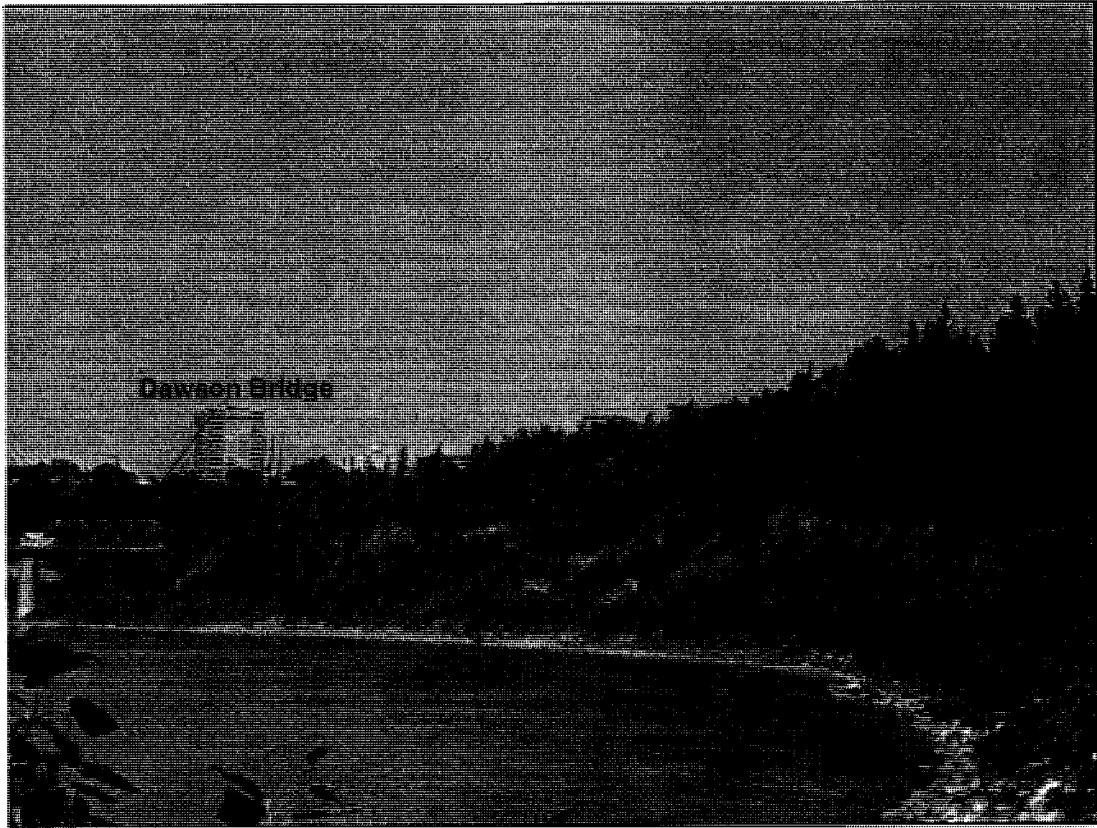


Figure 9-2 River valley view of Forest Heights Park (looking North, taken on 15th July 2004)

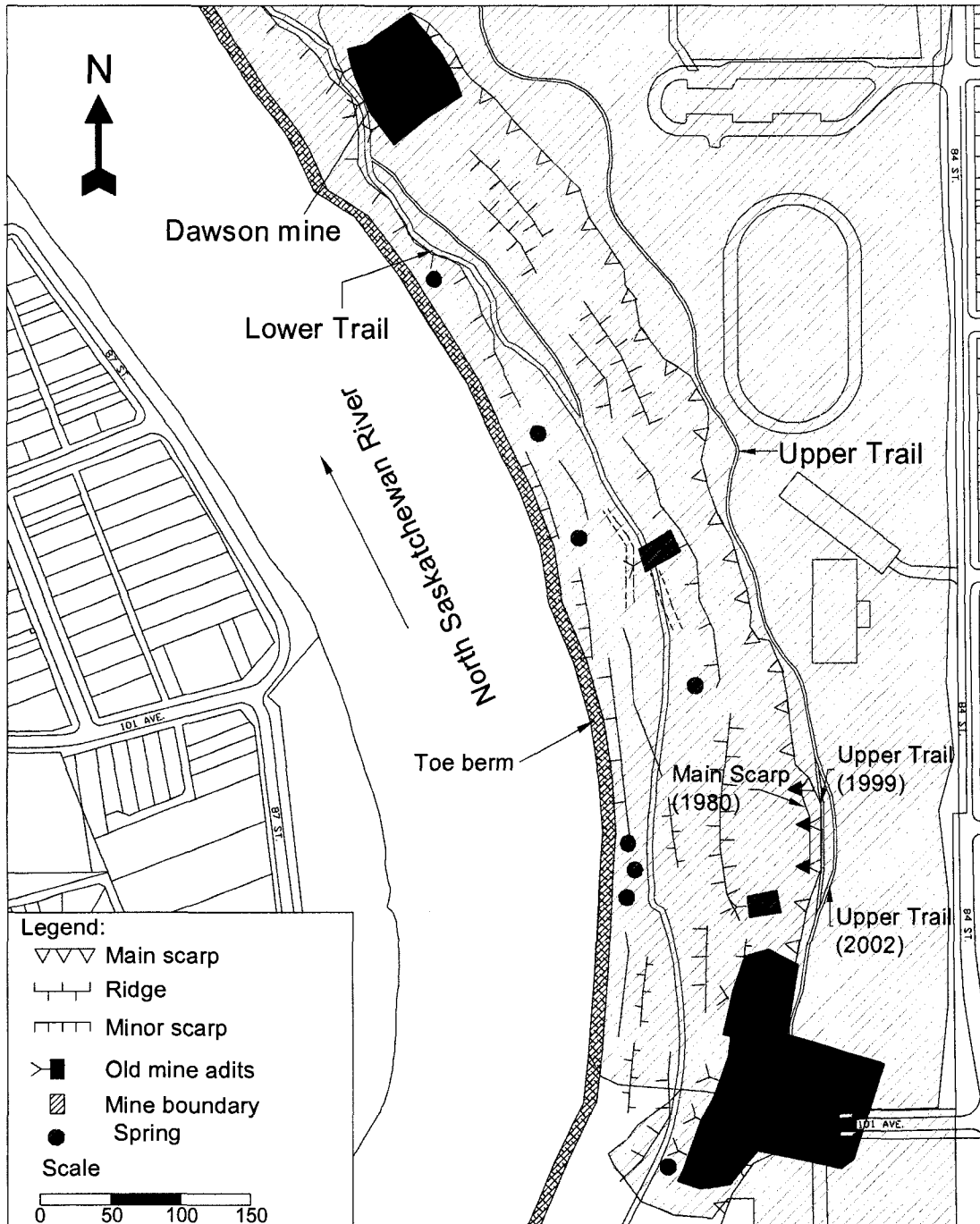


Figure 9-3 Locations of old mine adits in Forest Heights Park (mine locations from Taylor 1971)



Figure 9-4 Toe slump in displaced bedrock (taken on 15th July 2004)

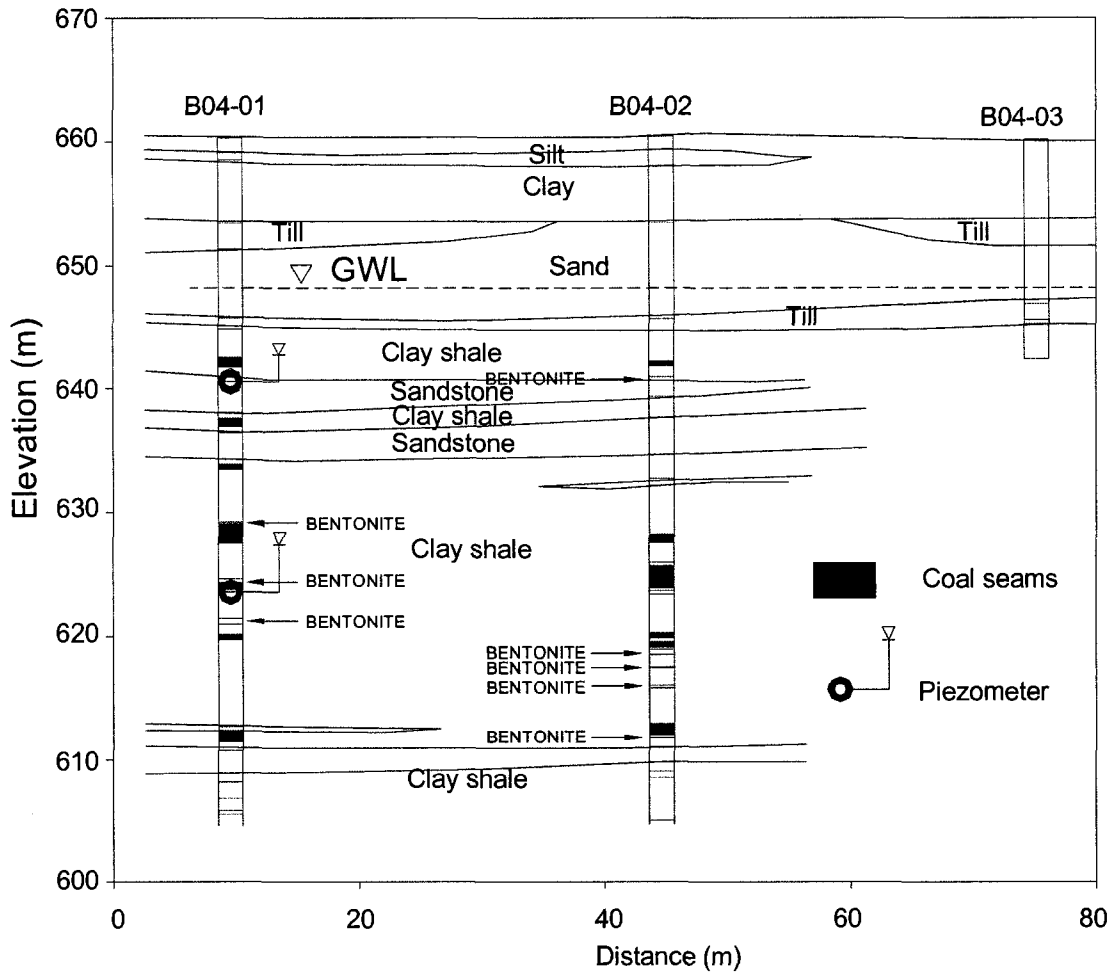


Figure 9-6 Stratigraphic profile behind the river valley wall

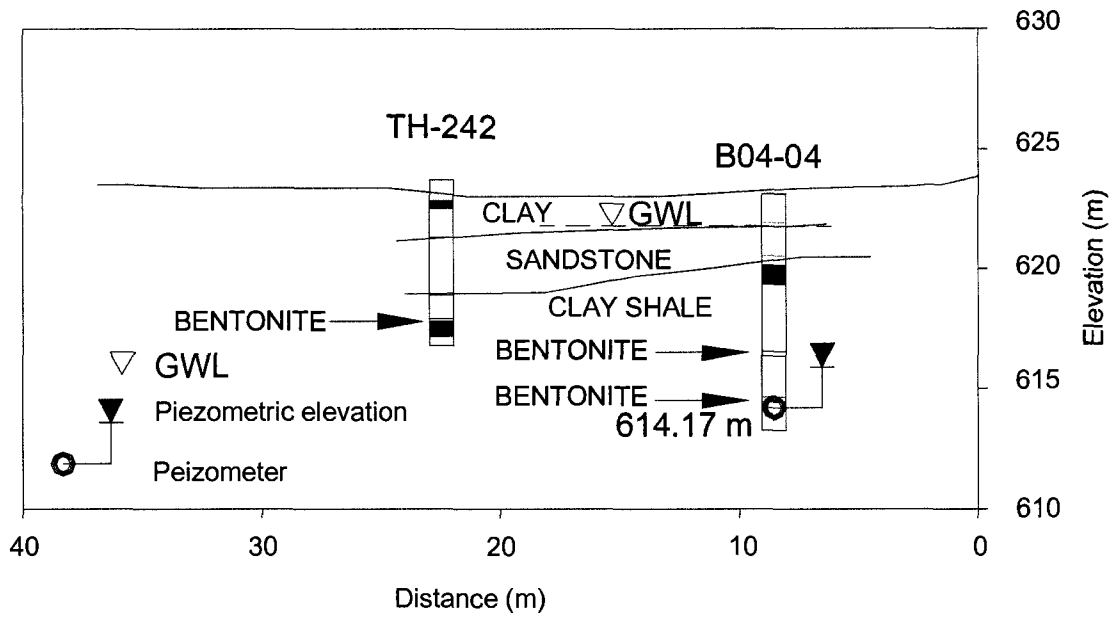


Figure 9-7 Stratigraphic profile at the toe of Forest Heights Park

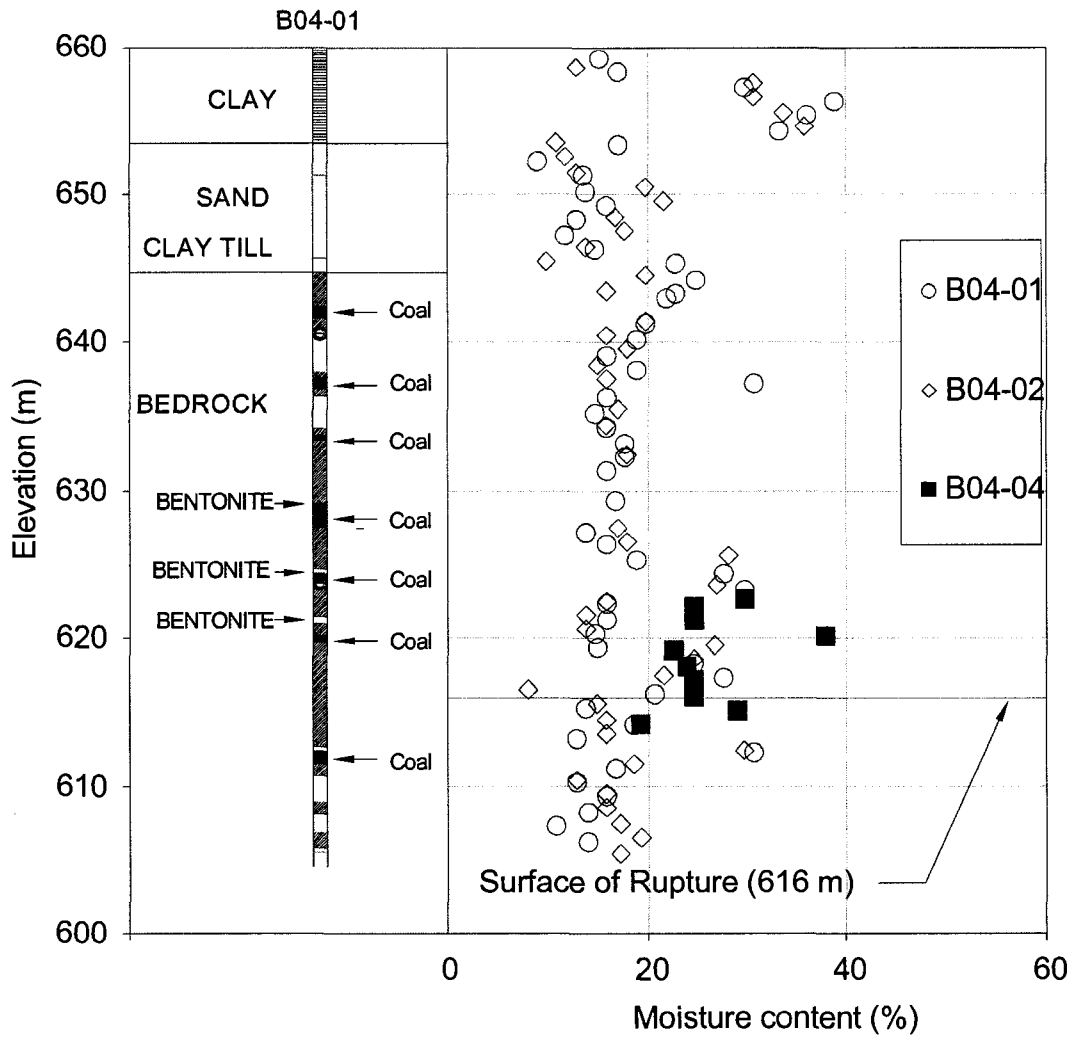


Figure 9-8 Moisture content profile obtained from boreholes behind the valley wall and at the toe of the slope

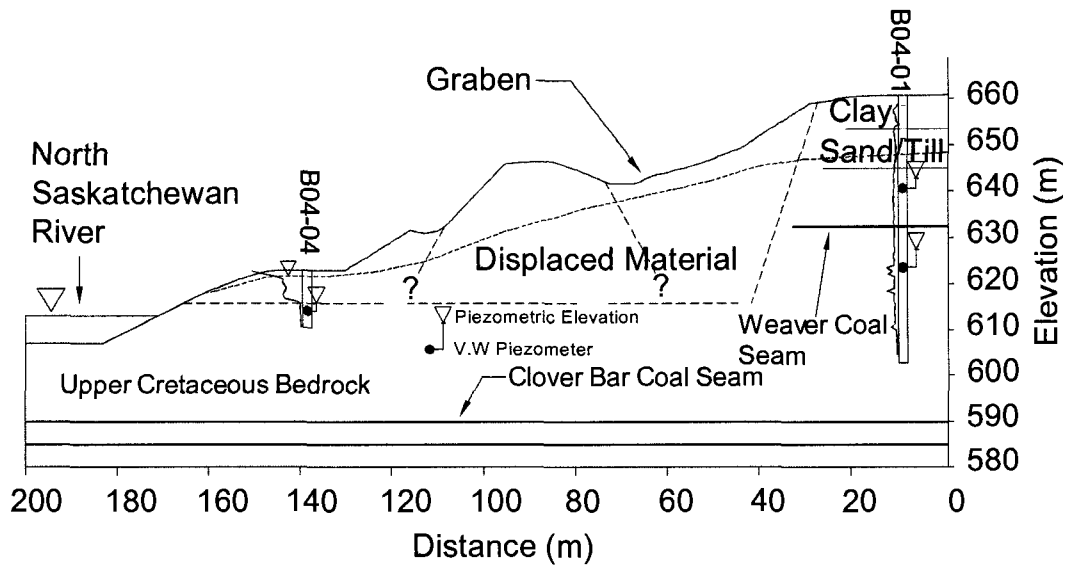


Figure 9-9 Cross-section A-A and piezometric elevations of the bedrock and groundwater level in Forest Heights Park

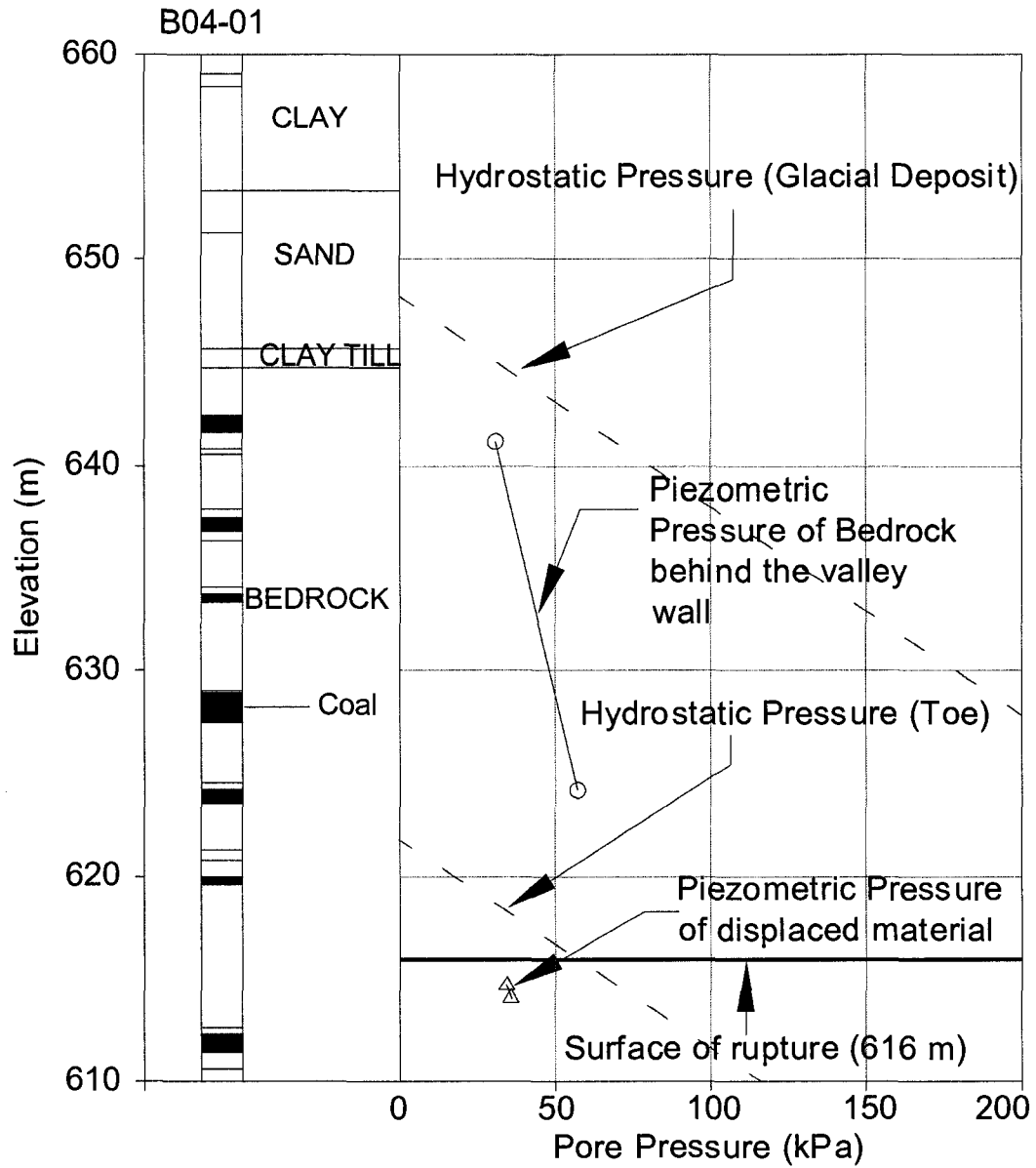


Figure 9-10 Piezometric pressure of bedrock behind the valley wall and displaced material in Forest Heights Park

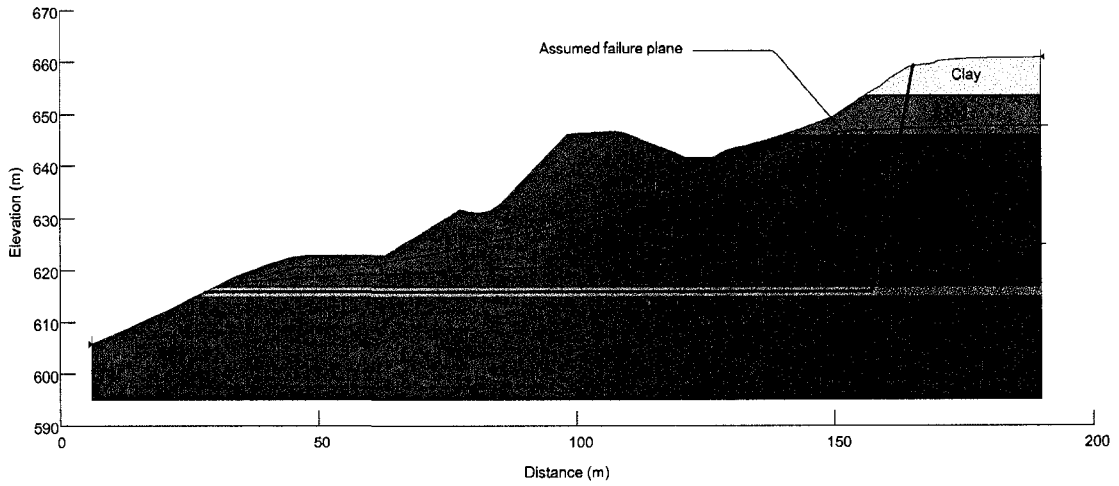


Figure 9-11 Cross-section used in the stability analyses of the Forest Heights Park river valley wall

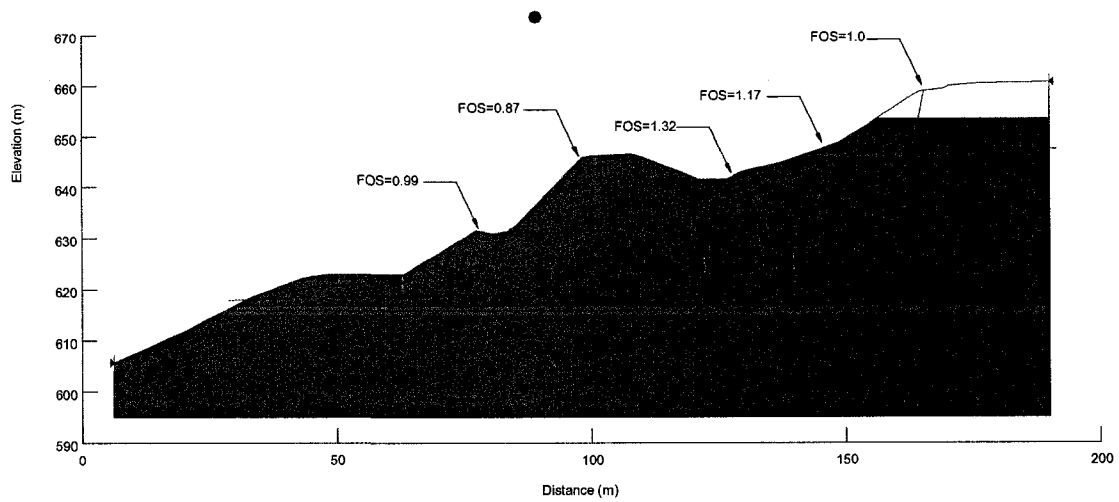


Figure 9-12 Stability analysis of different main scarps in Forest Heights Park



Figure 9-13 Tension cracks in the lower trail of Forest Heights Park

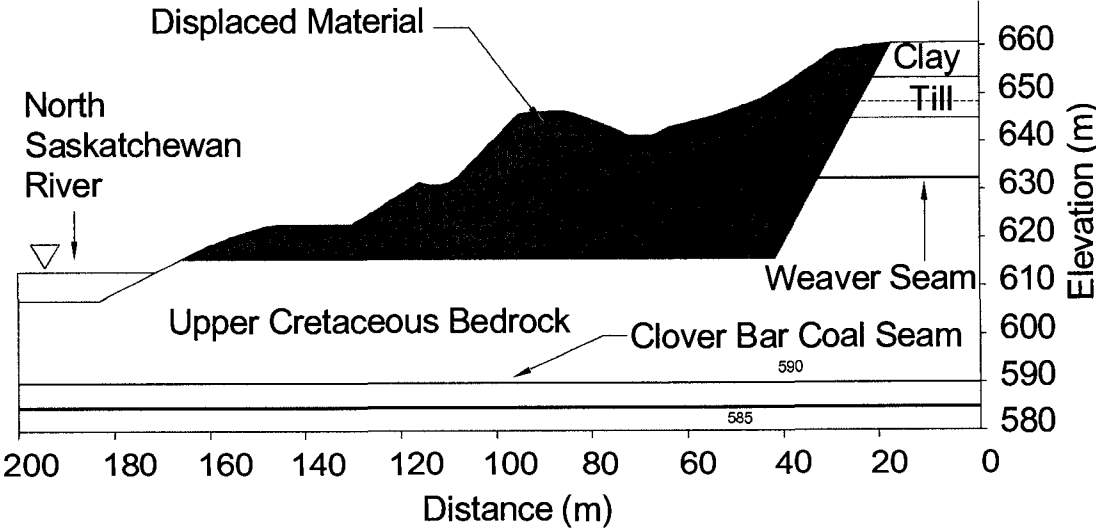


Figure 9-14 Cross section of the valley wall and coal seam elevations in Forest Heights Park

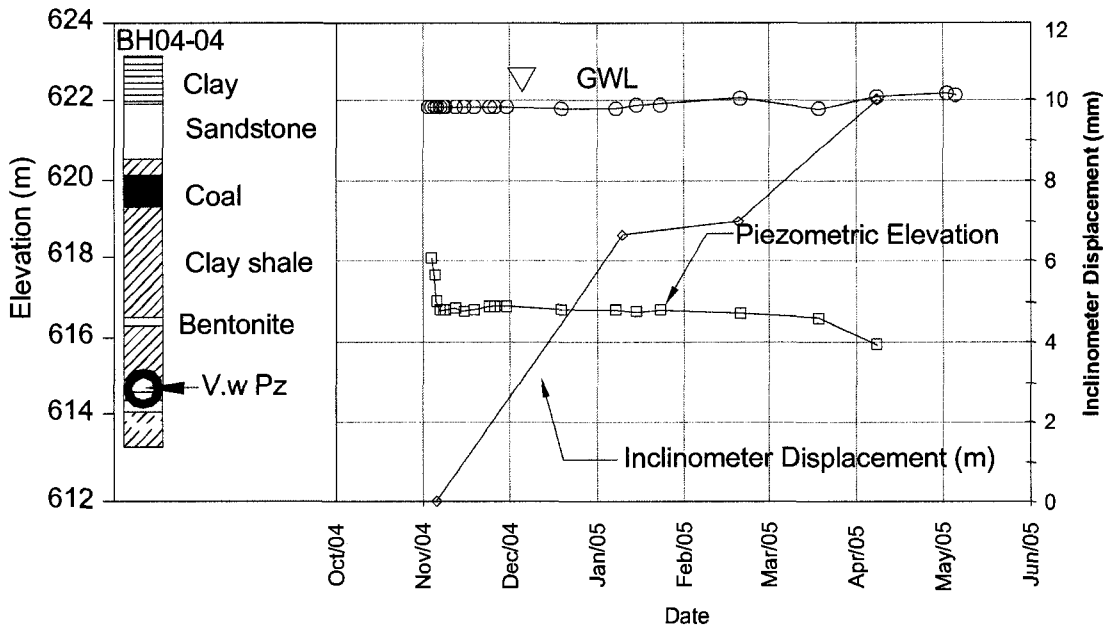


Figure 9-15 Piezometric elevation and inclinometer displacement in the Forest Heights Park slide area

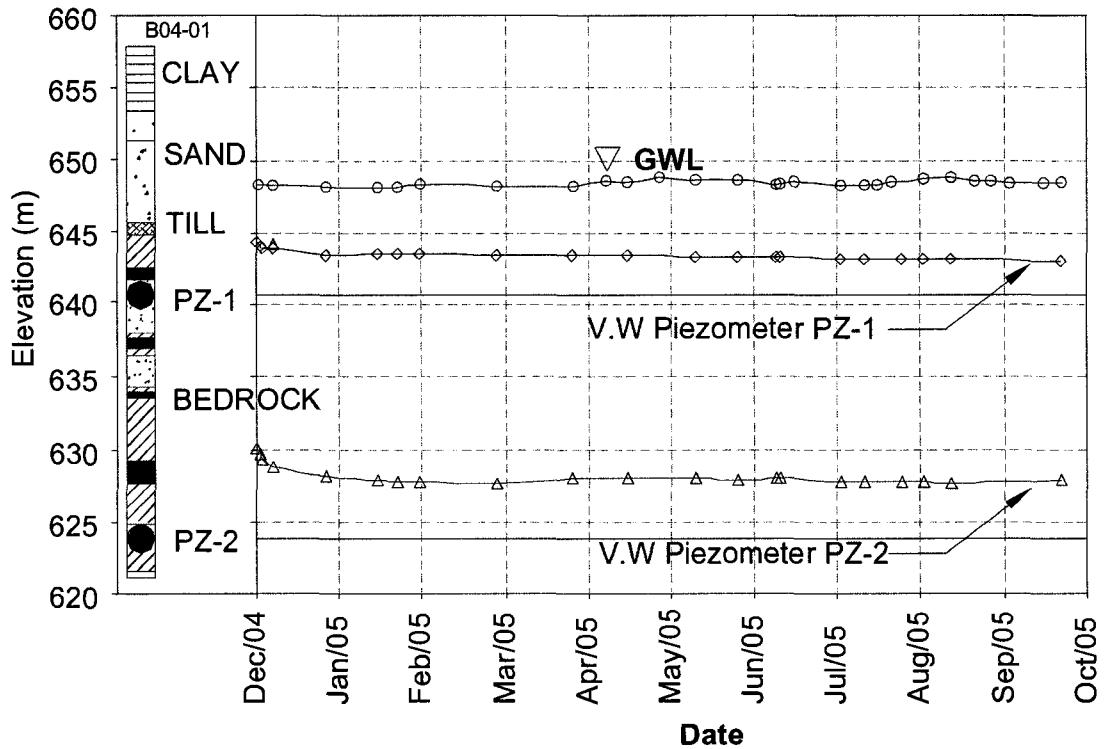


Figure 9-16 Long-term pore pressure response of bedrock in Forest Heights Park

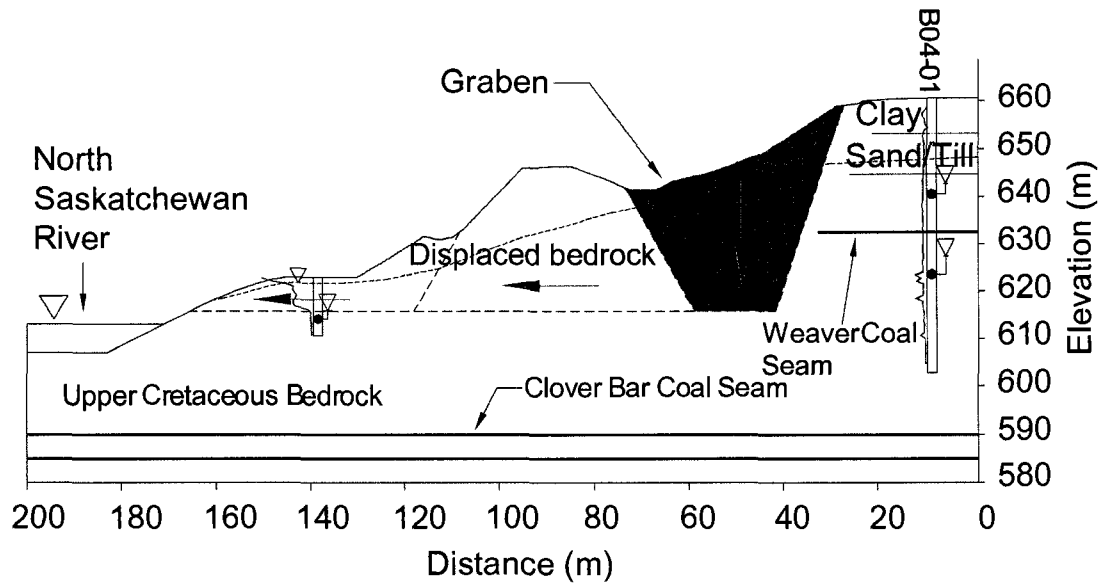


Figure 9-17 Post-failure slope movement in Forest Heights Park

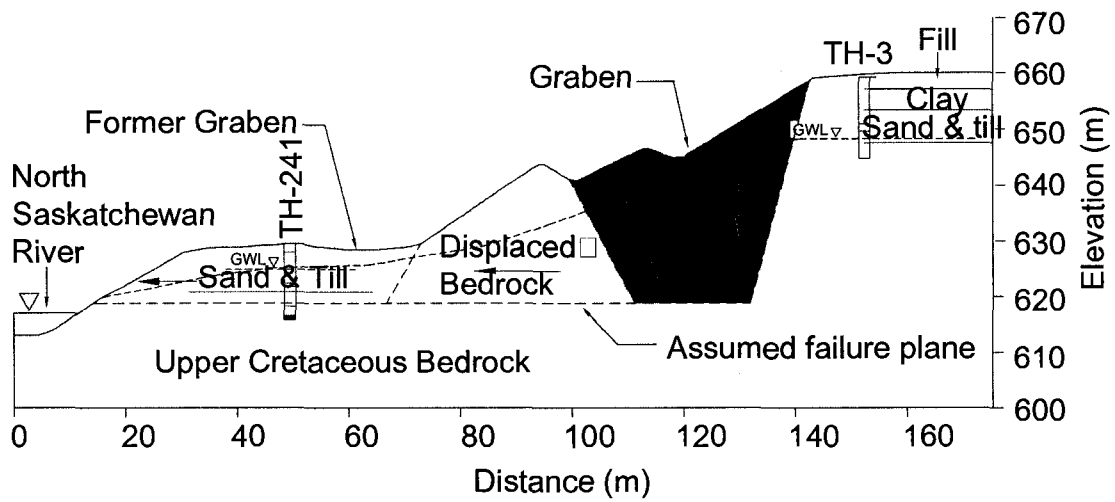


Figure 9-18 Cross Section B-B showing exposed till at the toe of the slope in Forest Heights Park

CHAPTER 10 Stages in the translational sliding of 2 inclined blocks

10.1 Introduction

As presented in three case studies, landslide mechanisms in weak rock slopes are complex and involve several landside stages. These failures have a common failure mechanism: a steeply dipping main scarp, a graben at the head of displaced material, and translational movements of the main body along a weak plane located in the bedrock. Pre-failure and post-failure cross-sections observed from the Whitemud Road Landslide are presented in Figure 10-1. In this case, due to complex failure geometry, typical soil mechanics and rock mechanics stability analysis may not represent the actual failure mechanisms.

This chapter presents a simple model of two inclined blocks, which can be used for stability analysis of the river valley slides (SoeMoe et al. 2003). The advantage of this model is that the reduction in the safety factor due to the formation of a graben can be accounted for in the stability analysis. Stability analyses of the Keillor Road Landslide are presented using the two inclined block model and the results are compared with field observations.

10.2 Five landslide stages

Movements observed in landslides along the North Saskatchewan River Valley revealed the development of landslide stages with time. These landslides have a common mode, a translational movement along a bentonite layer. These slope movements can be characterized in five stages, from initial toe movement to major failure. Five landslide stages are presented with field observations from the Keillor Road Landslide.

Stage 1 involves the development of cracks in the horizontally-bedded Cretaceous bedrock. The excavation of a valley by a river reduces the originally high horizontal stresses in the surrounding strata that may cause the natural fissures in the bedrock to open up. Toe erosion by the river may cause minor failures such as the 1989 toe failure and the 1995 Keillor Road failure (Figure 10-2).

In Stage 2, cracks may extend deep into the bedrock, intersecting weak planes located within the bedrock (Figure 10-3). Surface water may infiltrate through interconnected cracks. During heavy rainfall, significant hydrostatic pressure may be exerted on these cracks and push the displaced material along a weak horizontal plane. In this stage, the displaced material moves as a single block along a horizontal sliding plane. Movement dilates the main scarp, pore water pressure, and the rate of movement drops, sometimes to zero.

In Stage 3, the head of the displaced materials is unsupported and over several months or more, an uphill-facing counter-scarp is formed which separates a downward-tapering wedge, the active block (Figure 10-4). When the combined force of the water pressure and the active block is greater than the resisting force of the passive block, a major failure occurs (2002 failure).

In Stage 4, a graben may form due to the downward movement of the active block. The downward movement of the active block is halted when its tip comes to rest on the weak plane that has allowed displacement of the passive block (Figure 10-5).

In Stage 5, continued movement may depend on the erosion of the toe by the river and the water pressure acting on the scarps (Figure 10-6). Field monitoring in 2003 and 2004 involved Stage 4 and Stage 5 of the landslide movements.

10.3 A simple model of the Landslide Mode

10.3.1 Assumptions of the analysis

This five-stage landslide mode is modeled in two dimensions assuming both active and passive blocks are infinitely wide. Displaced material is uniform with a weak plane DO which forms a lower surface of rupture (Figure 10-7). The main scarp CD develops following valley rebound and stress relief joints. The main scarp has a dip θ and is filled with water to height Z_w . The weak plane DO can be horizontal or with a dip α and the water level at the weak plane is defined by Z_s . The active block is defined by a portion of the main scarp CF and a portion of the counter scarp EF (Figure 10-8). Water levels on the active block are defined by Z_a and Z_c . The weight of the sliding block W , the uplift force due to water pressure on the sliding surface U_s , and the water pressure in the main scarp U_b , all act through the centroid of the sliding mass. A slice of unit thickness is considered and it is assumed that release surfaces are present so that there is no resistance to sliding at the lateral boundaries of the failure.

Properties of the displaced material OBCD are defined by average values of unit weight and friction angle. Only friction angle is required for the weak plane DO. Slope geometry is defined by slope height H , active block height H_a , slope angle β , main scarp dip θ , counter scarp dip δ , distance from the valley crest to the main scarp R , and the weak seam or surface of rupture which is assumed to be horizontal or with a dip α . Water pressures acting on the main scarp, the counter scarp, and the sliding plane are defined by Z_w , Z_c , and Z_s . Figure 10-8 shows the slope geometry used in the analysis.

10.3.2 Single block mechanism (Stages 1 and 2)

It is assumed that the main scarp is open but the displaced material is in intact condition. The average unit weight and the strength properties of the displaced material and the weak seam are required for the analyses. At this stage, the movement is a single block and the sliding occurs along the weak plane as shown in Figure 10-7. The limit equilibrium solution was introduced by Hoek & Bray (1977) and

assumes translational sliding of a rigid body along a plane. The driving force is generated by the water pressure on the main scarp and the weight of the sliding block if the sliding plane has a dip. The resisting force is obtained from the shear resistance of the weak layer.

10.3.3 Two inclined blocks model (Stages 3 and 4)

After initial sliding along the weak layer at stage 2, the head of the displaced material is unsupported and, over a few months, a counter scarp develops which forms an active block at Stage 3 as shown in Figure 10-8. The active block is defined by the counter scarp dip δ and the height of active block H_a . At this stage, the stability calculation can be divided into two parts. The first part is the determination of the resultant force R_2 , which applies pressure on the passive block. The second part is to determine the stability analysis of the passive block.

10.3.4 Calculation of the resultant force R_2

The resultant force R_2 of the active block is determined by the method of force polygons. Forces required for equilibrium of the active block are the weight of the active block W_a , the water forces at the main scarp and the counter scarp U_1 and U_2 , and the resultant forces acting on the main scarp and the counter scarp R_1 and R_2 . The water forces apply pressure normal to the main scarp and the counter scarp. Water force U_1 acts in the direction of $(90-\theta)$ and U_2 acts in the direction of $(90-\delta)$. The water forces acting on the active block are calculated from the groundwater level Z_a and Z_c as shown in Figure 10-8. It is assumed that full frictional forces are mobilized along the main scarp and the counter scarp. The resultant force R_1 acts in the direction of $(90+\phi-\theta)$ on the main scarp and the resultant force R_2 acts in the direction of $(90+\phi-\delta)$ on the counter scarp. In some cases, the resultant force R_1 can be negative due to high water pressure. In that case, the groundwater level at the main scarp and the counter scarp needs to be adjusted.

The resultant water force U_f is obtained from the horizontal component of water force U_h and the vertical component of water force U_v . The effective weight of the active

block W_e can be obtained by reducing the vertical component U_v from the total weight of the active block W_a . By using W_e and U_h , the resultant force R_f can be obtained. After obtaining R_f , the resultant forces R_1 and R_2 can be calculated using the sine rule. Figure 10-9 shows the force polygon used in the calculation of resultant force R_2 .

10.3.5 Calculation of the safety factor of the passive block

The safety factor of the passive block is obtained by dividing the resisting forces by the driving forces. Driving forces on the passive block include the resultant force of the active block R_2 , water pressure along the main scarp U_b , and the weight of the passive block W_p , if the weak plane has a dip α . The resisting force is obtained from the shear resistance of the weak layer. Figure 10-10 shows the resultant forces acting on the passive block. Detailed calculations of the two inclined block model are presented in Appendix A.

10.4 Stability analysis of the Keillor Road Landslide

Stability analyses are carried out for the Keillor Road Landslide using the two inclined block model. The results obtained from the analyses are compared with the results using the SARMA method (Sarma 1979). Parametric analyses are performed by changing groundwater level, and the material properties of the main block and the weak layer. In order to model the landslide stages, stability analyses are conducted for the single block model and the two inclined block model. The slope geometry used in the analysis is presented in Table 10-1.

The first parametric study is conducted to determine the initial failure at Stage 2. In this stage, the main body is still intact and moving as a single block. The failure is caused by high hydrostatic pressure behind the main scarp. Analyses are conducted by varying the main scarp distance and groundwater levels behind the main scarp. Variation in the factor of safety with the main scarp distance and three groundwater levels, 10, 15, and 30 m above the surface of rupture are presented in Figure 10-11. For the Keillor Road Landslide geometry, where the main scarp is located 40 m away

from the toe, the groundwater level has to be 30 m above the surface of rupture to achieve a safety factor of one.

After the initial failure at Stage 2, the groundwater level behind the main scarp will decrease due to dilation of the bedrock and the factor of safety will increase above unity. As shown in Figure 10-12, when the water level is reduced to 20 m above the surface of rupture, the factor of safety of the single block is 1.3. With time, an uphill-facing counter scarp forms separating the main body into an active block and a passive block. The variation in factor of safety due to the formation of the active block is presented in Figure 10-12. When the main scarp is 40 m behind the toe and the water level is 20 m above the surface of rupture, the factor of safety will be less than unity when the active block height is about 18 m.

Parametric studies are also conducted to determine variation in the factor of safety with the main scarp and counter scarp dips. Figure 10-13 shows the variation in the factor of safety with variation in the main scarp dip, while keeping the counter scarp dip constant. As shown in the figure, the factor of safety decreases as the main scarp dip increases for both single block and two block analyses.

Figure 10-14 presents the variation in factor of safety with the counter scarp angle, while keeping the main scarp dip constant. As shown, the minimum factor of safety is achieved in when the counter scarp dip is about 65° .

The two inclined block model revealed that a decrease in factor of safety of 25 to 30 % occurs when the counter scarp and the active block are completely formed. This decrease is due to the increase in the driving forces on the passive block from the active block. When the results are compared with SARMA analysis, this simple model gives a 10 % lower factor of safety. The critical ranges in Table 10-2 suggest the ranges for these parameters within which the lowest factor of safety may lie.

10.5 Summary

Landslides in the North Saskatchewan River Valley show a common mode, a translational movement along a bentonite layer. These landslides also evolved different stages, starting from a toe failure at the earlier stage to a major failure, retrogressing upslope with time. The two inclined block model can be used to analyze five kinematic stages, starting from a single-block and leading to a two-block movement. The formation of a counter scarp, separating active and passive blocks, triggers an acceleration of slope movement as driving forces are increased by 30 %. At low water level, a reduction in the factor of safety due to the formation of an active block is more pronounced.

Table 10-1 Slope geometry and strength parameters at the Keillor Road Landslide

Slope height (H)	40 m
Main scarp Distance (R)	25m
Slope angle (β)	37 °
Main scarp dip (θ)	85 °
Sliding plane dip (α)	0 °
Counter scarp dip (δ)	80 °
Friction angle of main block (ϕ_b)	14 °
Friction angle of weak plane (ϕ_s)	10 °
GWL at the main scarp (Z_w)	20 m
GWL at the weak plane (Z_s)	0 m

Table 10-2 Critical ranges obtained from the analyses

Distance of the main scarp, R	15 to 40 m or 0.4H to 1H
Counter scarp dip, δ	60° to 65°
Main scarp dip, β	62° to 70°
Depth of the active block, H_a	18 m or 0.45H

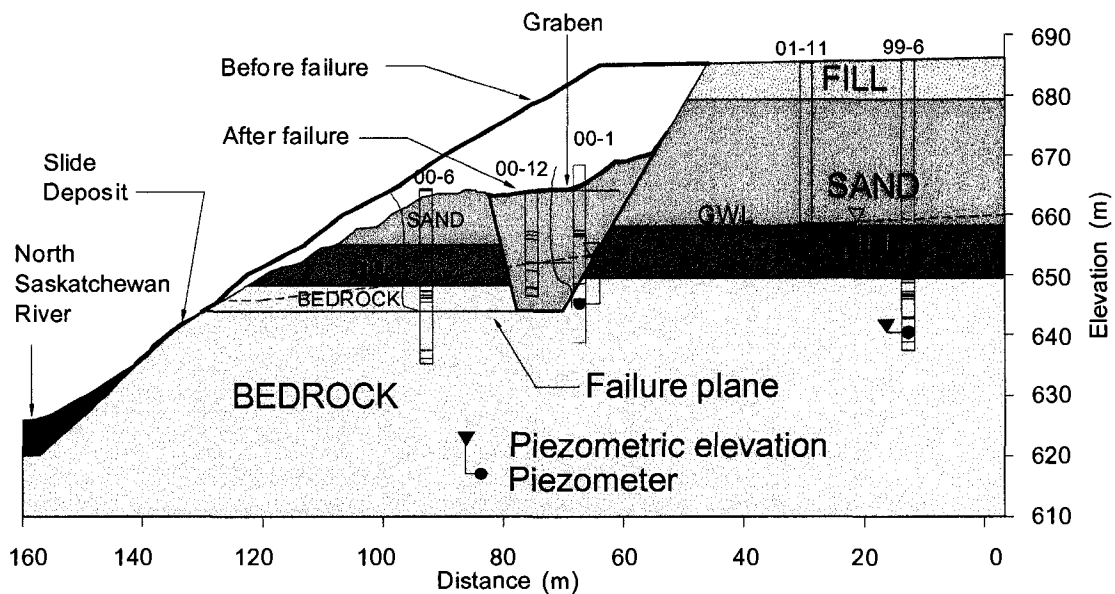


Figure 10-1 Pre-failure and post-failure cross-section (Whitemud Road Landslide)

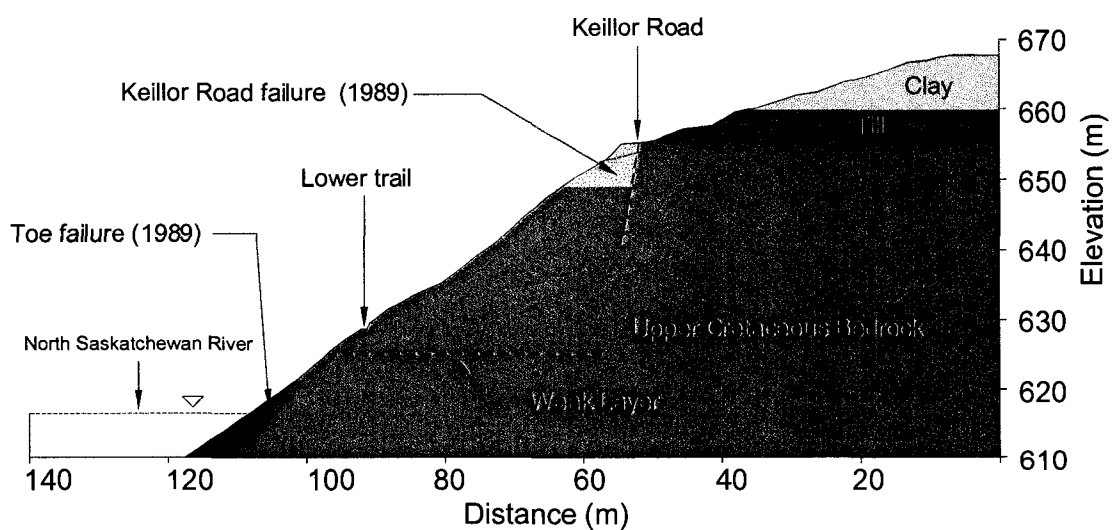


Figure 10-2 Development of minor scarps (Stage-1)

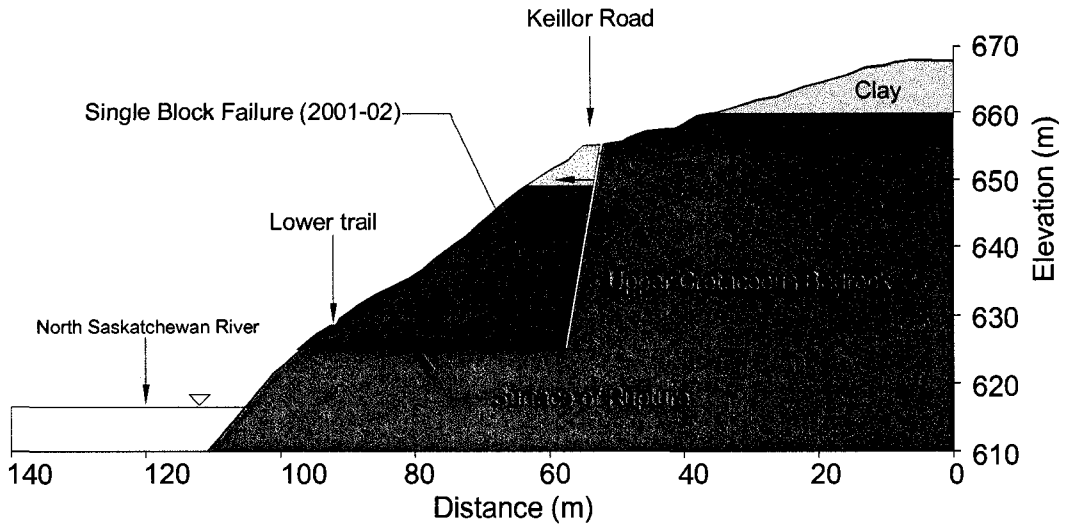


Figure 10-3 Development of the main scarp (Stage-2)

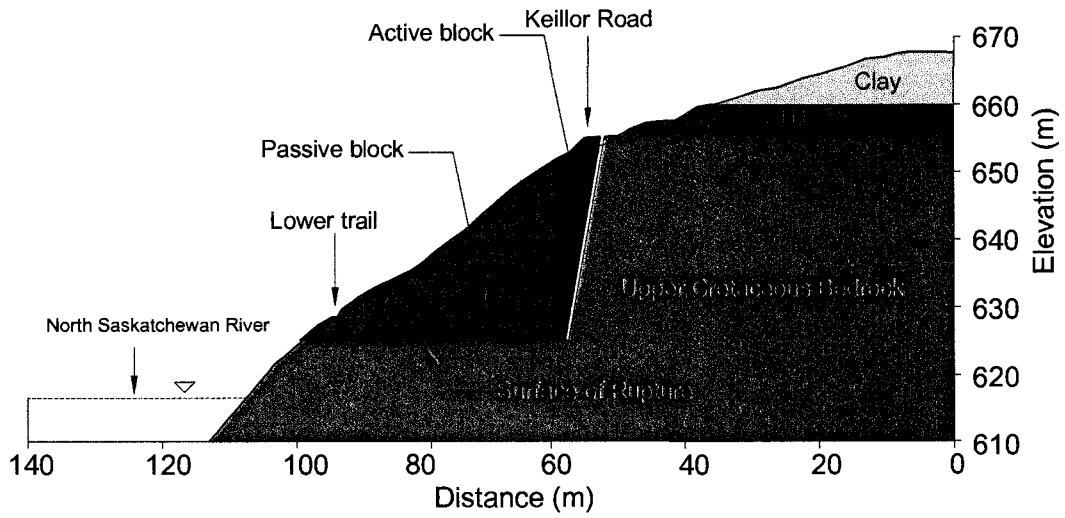


Figure 10-4 Development of a counter scarp (Stage 3)

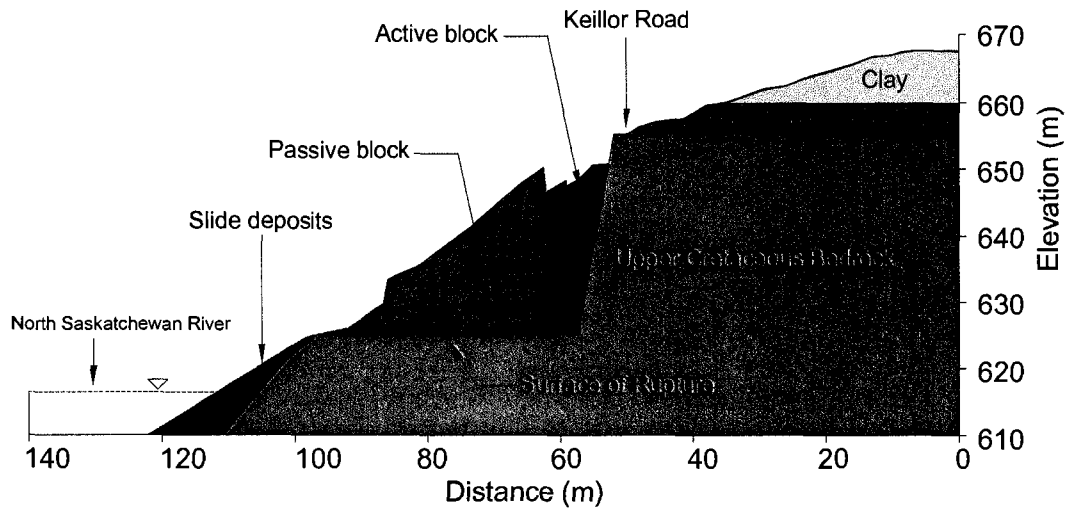


Figure 10-5 Major failure due to downward movement of an active block (Stage-4)

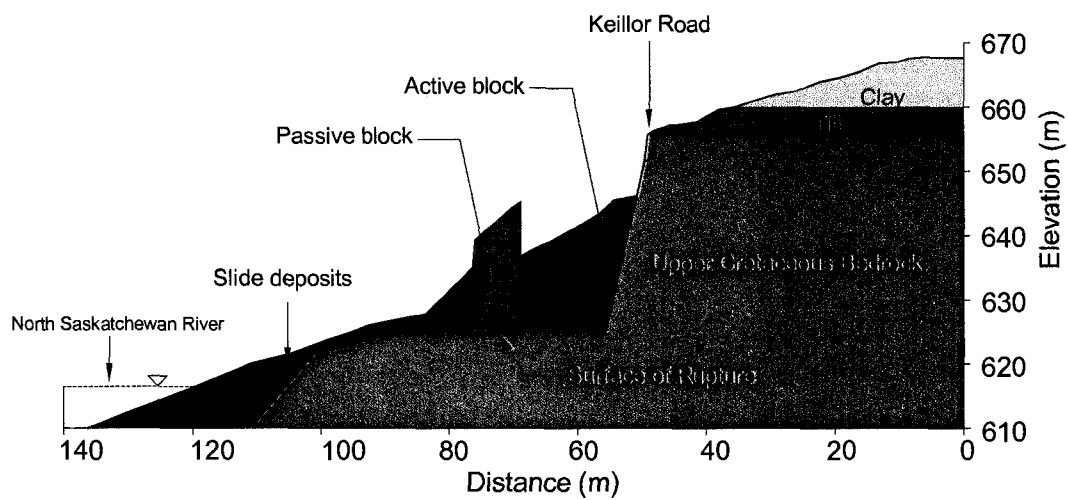


Figure 10-6 Post-failure slope movements (Stage-5)

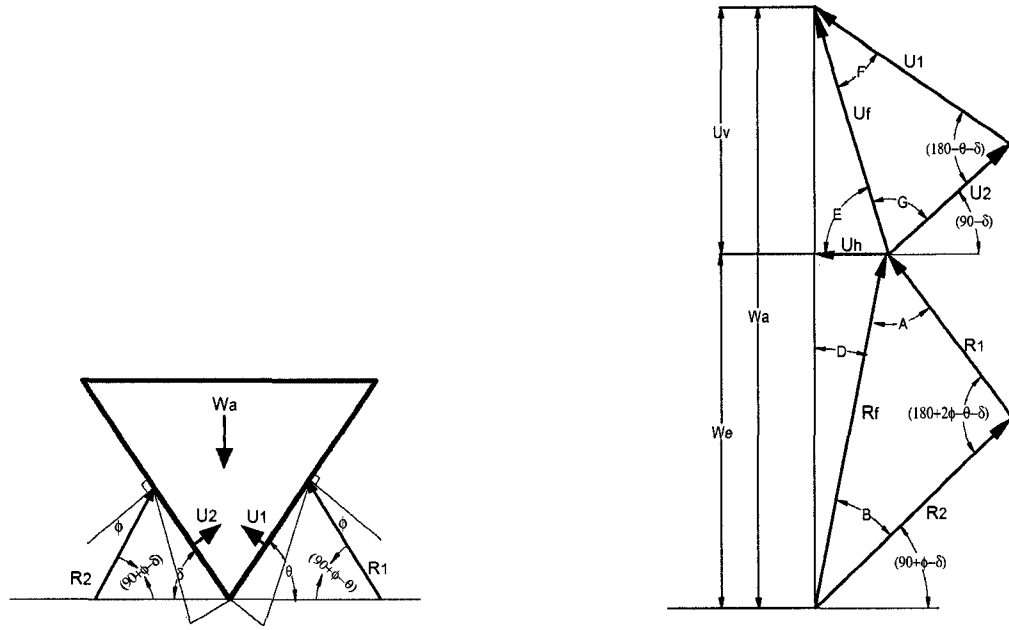


Figure 10-9 Calculation of resultant force, R_2 of the active block

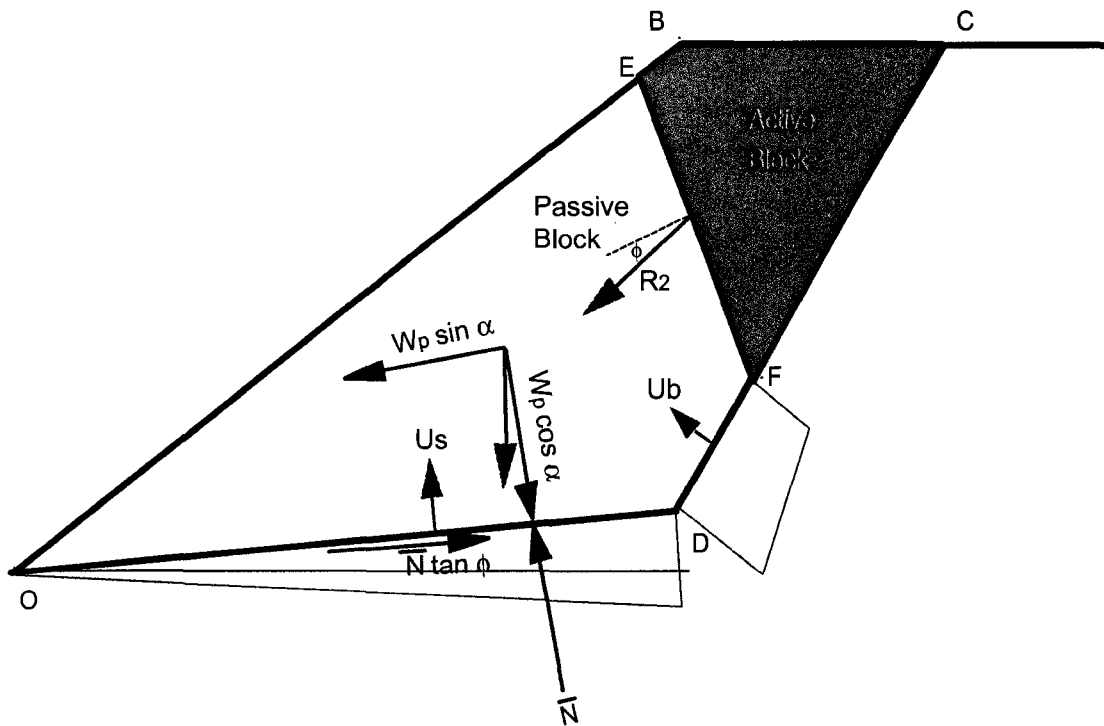


Figure 10-10 Calculation of the factor of safety of the passive block

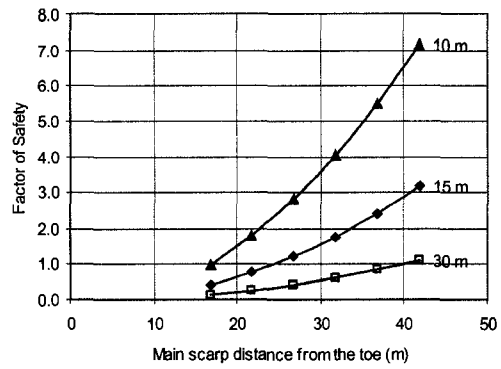
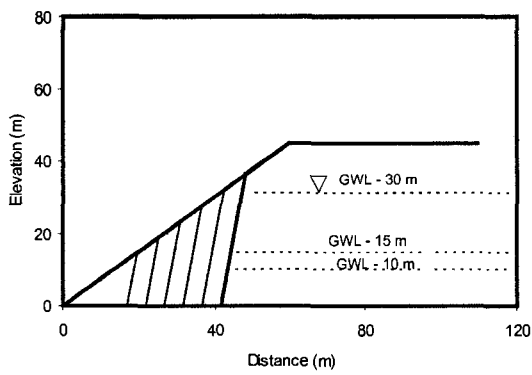


Figure 10-11 Variation of the factor of safety with main scarp distance R

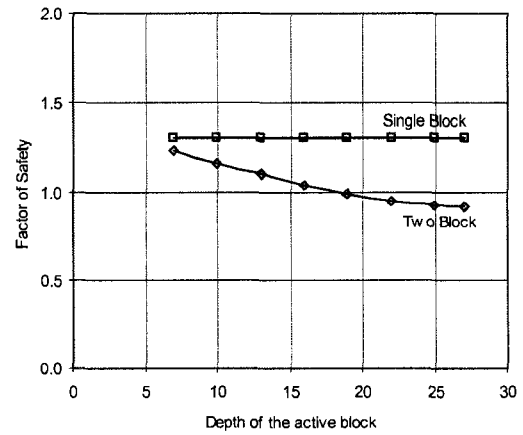
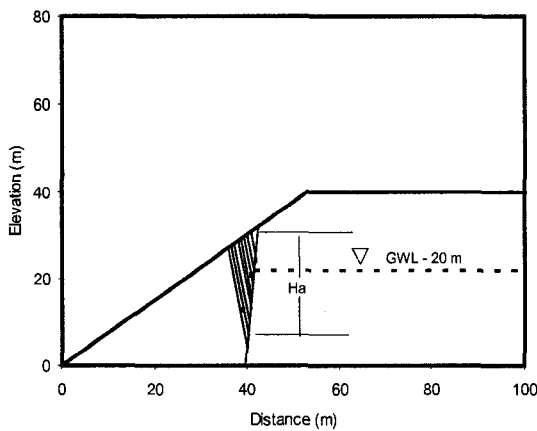


Figure 10-12 Variation of the factor of safety with active block depth H_a

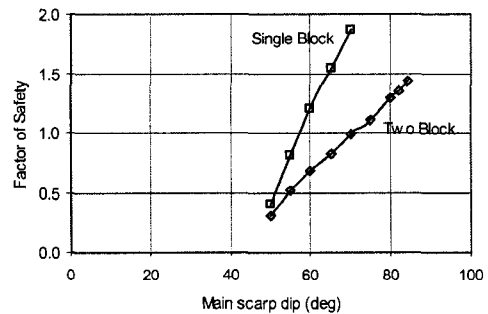
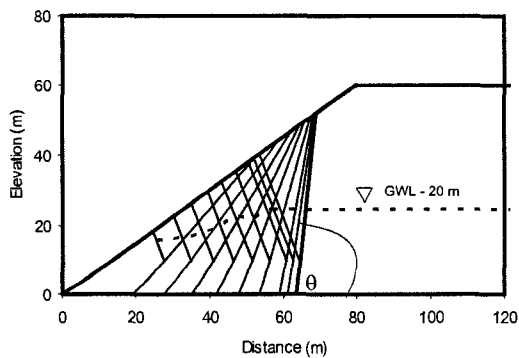


Figure 10-13 Variation of the factor of safety with main scarp dip θ

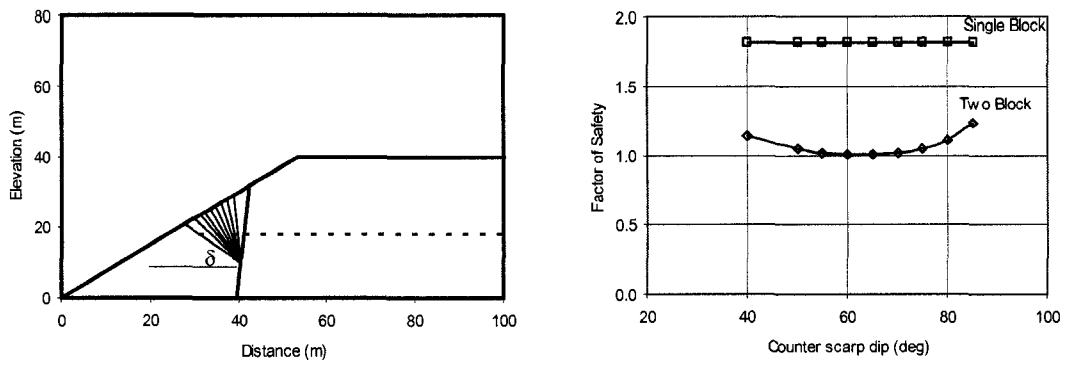


Figure 10-14 Variation of the factor of safety with counter scarp dip δ

CHAPTER 11 Long term stability of weak rock slopes

11.1 Introduction

As presented in Chapters 7 to 9, river valley landslides in weak rocks are complex involving several landslide stages. According to Cruden and Varnes (1996) classification, river valley landslides in Edmonton can be classified as retrogressive, complex, rapid to slow, rock slide - earth slide. Present case studies also confirmed that the rate of pre and post-failure movement depends on the relative thickness of overburden materials and bedrock above the surface of rupture. Among the various factors affecting the river valley landslides, the seepage and the groundwater level changes are major triggering factors in the river valley landslides. Due to the limited number of instruments available from the current study, the effect of seepage and groundwater level changes on river valley slopes is not well established. Thus, a further study is necessary to correlate various factors affecting the river valley landslides. For that, an instrumentation program is proposed and presented with an example of the Keillor Road landslide.

11.2 Delayed failure of river valley slopes

Case studies revealed that landslides in the North Saskatchewan River Valley comprised of both first time slides and reactivated slides. In a first time slide, failures occur on slopes that have not been previously sheared by landslides. Old landslides can also be reactivated by small changes slope geometry or groundwater condition. In any cases, river valley landslides in weak rocks occur by a combination of various factors, including toe erosion by the river, residential developments behind the slope crests, the rise of groundwater levels due to urban development, and softening of the bedrock at the valley wall. Landslide can also be initiated by man-induced factors such as urban development, slope excavation, and surcharge load at the slope crest.

The flowchart of slope instability mechanisms in weak rocks slopes, together with both natural and man-induced processes is presented in Figure 11-1.

11.2.1 Pre-failure movements

There are no detailed records of pre-failure slope movements since investigations are usually conducted after the slope failure. Current study revealed that pre-failure movements can be characterized by minor failures at the toe and the mid-slope area. The review of historical airphotos could expose some of the pre-failure movements. Based on field observations in Whitemud Road and Keillor Road landslides, pre-failure slope movements can be ranged from 2 to 12 years.

11.2.2 Major failure movements

Current studies revealed that the duration of major slope failure can range from several days to several years. As described by Terzaghi (1950), rate of movements accelerate during the landslide. Field monitoring data of various landslides in weak rocks revealed that the rate of movements depends on type and thickness of overburden materials and thickness of bedrock above the surface of rupture. In Whitemud Road Landslide, most of the major movements had completed within one day. However, Keillor Road Landslide took more than two years to complete the major movements.

11.2.3 Post-failure movements

After a major failure, displaced material rests on the rupture surface and the factor of safety improve with the new slope configuration. During this period, some changes in the external condition such as increase in groundwater level may reduce the factor of safety to below unity. Current study revealed that post-failure slope movements are related to increase in groundwater level behind the slope crest and cracks. Continue slope movements are observed long time after the major failure.

11.3 Characteristic of river valley landslides in Edmonton

In order to determine the pre-failure and post-failure characteristics of various landslides along the North Saskatchewan River Valley in Edmonton, available information from five landslides, Whitemud Road Landslide (SoeMoe et al. 2006), Keillor Road Landslide (SoeMoe et al. 2005), Forest Heights Park Landslide (SoeMoe et al. 2007), Lesueur Landslide (Cruden et al. 2002; Thomson 1971b) and Grierson Hill Landslide (Martin et al. 1998; Martin et al. 1984), are compiled together as shown in Table 11-1. This table contains 7 columns indicating type and thickness of overburden materials, bedrock thickness above the surface of rupture, observed movements during pre-failure, major failure and post-failure and pre-failure and post-failure slope angle.

Depending on the type and thickness of overburden material, landslide in weak rocks along the North Saskatchewan River can be divided into 3 types.

- Thick overburden above the surface of rupture (30 to 41 m thick)
- Thin overburden above the surface of rupture (15 to 21 m thick)
- No overburden

Case studies revealed that thick overburden materials above the surface of rupture effect the rate of movements during the major failure. Both Whitemud Road Landslide and Lesueur Landslide have thick overburden materials, completed most of the major failure in one day. Even though no detailed record for the duration of major failure in Grierson Hill Landslide, it is estimated that major failure may take several days to several months. Bedrock slopes may take longer time to complete major failure and in Keillor Road Landslide case, it took more than two years to complete the major failure.

Different post-failure rate of movements are also observed in river valley landslides. Depending on external condition, these movements can be increased or decreased with time. Major factors affecting the post-failure movements are toe erosion by the river, groundwater level rises, increase in seepage due to rainfall and snow melt and changes in slope geometry. Martin et al. (1998) presents long term monitoring of Grierson Hill Landslide and found that rate of movements significantly reduced after

the stabilization measures. The summary of post-failure movements of three landslides is presented in Table 11-2.

The idealized post-failure movements of river valley slopes are present in Figure 11-2. In this figure, the post-failure slope movements are correlated with groundwater level and piezometric pressure of the bedrock. During a heavy rainfall, the increase hydrostatic pressures in the crack may cause the reduction in the factor of safety and increase the slope movement. Due to the movements, the piezometric pressure of the bedrocks decrease which in turn increase stability of the slope. After the rainfall, the water pressure in the cracks reduces and the factor of safety increase above the unity. Over time, the pore pressure in the bedrock increase and the factor of safety reduces as shown in the figure.

11.4 Landslide investigation

Field studies revealed that the groundwater regime near the valley wall is complex, partly due to permeability contrast between low permeable layers such as overlying clay, till and bedrock and the high permeable layers such as coal seams and sands. Seepage can occur through joints and fractures located in the bedrock. The groundwater flow through the poorly permeable till and Upper Cretaceous bedrock is predominantly downward, but the decrease in head is a function of the permeability and the position within the flow system. Groundwater flow in the poorly permeable material becomes horizontal near the river valley or vicinity of a drainage channel. The rapid seepage of water from such source may initiate unfavorable conditions on slopes since joint and fissures are common in these bedrocks. In order to define the role of groundwater on slope instability, it is important to understand following factors for river valley slopes:

- Seepage and groundwater level,
- Groundwater flow near the valley wall,
- The swelling and pore pressure equalization; and
- Deformation monitoring.

11.4.1 Seepage water and groundwater level

Field study revealed that the snow melt and heavy rainfall can significantly increase the seepage and groundwater level near the river valley wall. Usually, in order to monitor groundwater level, water standpipes are installed around the slide area and monitor with a dip meter. But this type of monitoring depends on monitoring schedule and is difficult to obtain real time changes in groundwater level during the heavy rain fall. In order to monitor changes in real time, water standpipes should be fitted with vibrating wire piezometers connected to a data logger. In this way, groundwater level changes in real time could be monitored.

11.4.2 Groundwater flow near the valley wall

Due to permeability contrast between low permeability bedrock, fractures and coal seams, it is important to establish flow pattern near the valley. In order to establish groundwater regime near the valley wall, several piezometers should be installed along the valley wall at certain locations.

11.4.3 Swelling and pore pressure equalization

As discussed by various researchers (Koppula and Morgenstern 1984; Morgenstern 1977; Skempton 1964; Skempton 1970), swelling the pore pressure equalization is one of the factors causing strength reduction with time. Thus it is important to establish long term pore pressure changes in bedrocks near the active landslide area. Since pore pressure can be negative due to stress relief and unloading (Bishop 1954; Koppula and Morgenstern 1984), piezometers installed for this purpose should be equipped with High Air Entry Filters and flushing mechanism. Flushable piezometer developed in the current research (Chapter 6) could be used for this purpose.

11.4.4 Deformation monitoring

In order to correlate slope movements with pore pressure changes, deformation monitoring instruments such as inclinometers, survey targets and crack meters should be installed. Deformation monitoring should be taken at regular frequency.

11.5 Proposed field instrumentation program

In order to incorporate the instrumentation program, proposed field instrumentation program for Keillor Road is presented in Figure 11-3. This figure presents a cross section of Keillor Road Landslide (cross-section C-C, Figure 7-5) together with proposed instrumentation plan. In order to establish the groundwater level, water standpipes should be placed along the slope, starting from the slope crest to the toe. Vibrating wire piezometers with low air entry filters should to be placed at different elevations along the slope to establish the groundwater regime of the area. Flushable piezometers with high air entry filters should be placed below the surface of rupture and inside the displaced material to monitor the pore pressure equalization and swelling of the bedrock. Finally, inclinometers should be placed along the slope to monitor the slope movements.

11.6 Summary

This chapter presents the summary case studies conducted in the current study. Field monitoring data revealed that the rate of major movements depends on the type and thickness of overburden material and thickness of bedrock above the surface of rupture. Continue slope movements are observed long time after the major failure. Pre-failure slope angles of river valley landslides ranged from 23 to 45 ° and post-failure slope angle ranged from 11 to 27 °.

In order to understand the role of seepage and groundwater regimes of the river valley slopes, a new instrumentation program is proposed for future investigation. The example of instrumentation program is presented with the Keillor Road Landslide profile.

Table 11-1 Summary of slope movements for major river landslides in Edmonton

Landslide Name	Overburden Type and Thickness	Bedrock above Failure Plane	Pre-failure failure	Major failure	Post-failure movements	Pre-failure Slope Angle	Post-failure Slope Angle
Whitemud Road Landslide (1999)	Fill – 4 to 7 m Kames – 20 to 25 m Till – 6 to 9 m	5 to 8 m	1997 to 1999	24 hours	1999 to present	31 to 38 °	22 to 24 °
Keillor Road Landslide (2002)	No overburden	33 to 36 m	1989 to 2001	2002 to 2004	2004 to present	40 to 45 °	23 to 27 °
Forest Heights Park Landslide (1900s)	Clay – 7.0 to 10 m Till – 8.0 to 11 m	28 to 32 m	N/A	N/A	1900s to present	N/A	15 to 18 °
Lesueur Landslide (1963)	Clay – 5 to 8 m Till – 6 to 7 m Saskatchewan Sand & Gravel – 6 to 8 m	12 m	April 1963 to Sept 1963	24 hours	1963 to present	23 to 30 °	16 to 18 °
Grierson Hill Landslide (1901)	Clay – 8 to 10 m Till – 6 to 8 m	26.9 m	N/A	Several days	1901 to present	29 to 35 °	11 to 12 °

Table 11-2 Summary of post-failure rate of movements

Landslide	Post-failure movements (Toe)	Post-failure movements (Crest)
Whitemud Road Landslide	1.5 to 7 mm/month	25 to 30 mm/month
Keillor Road Landslide	125 to 250 mm/month	350-850 mm/month
Grierson Hill Landslide	1 to 5 mm/month	0.75 to 2.2 mm/month

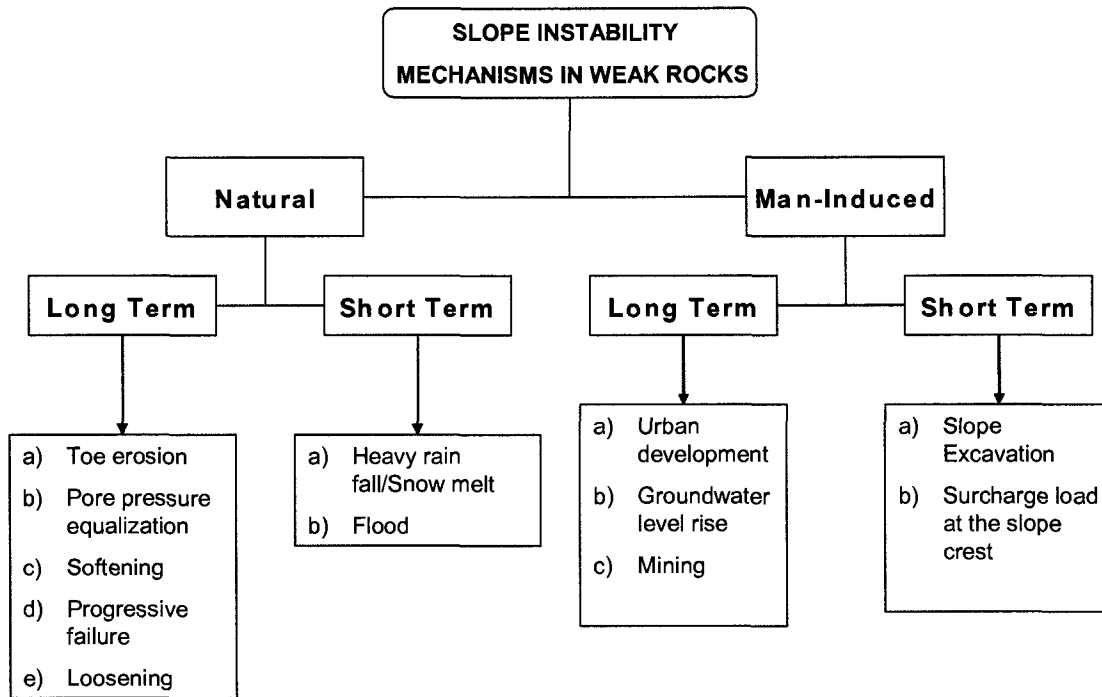


Figure 11-1 Slope instability mechanisms in weak rocks (modified from Thomson and Tiedemann 1982)

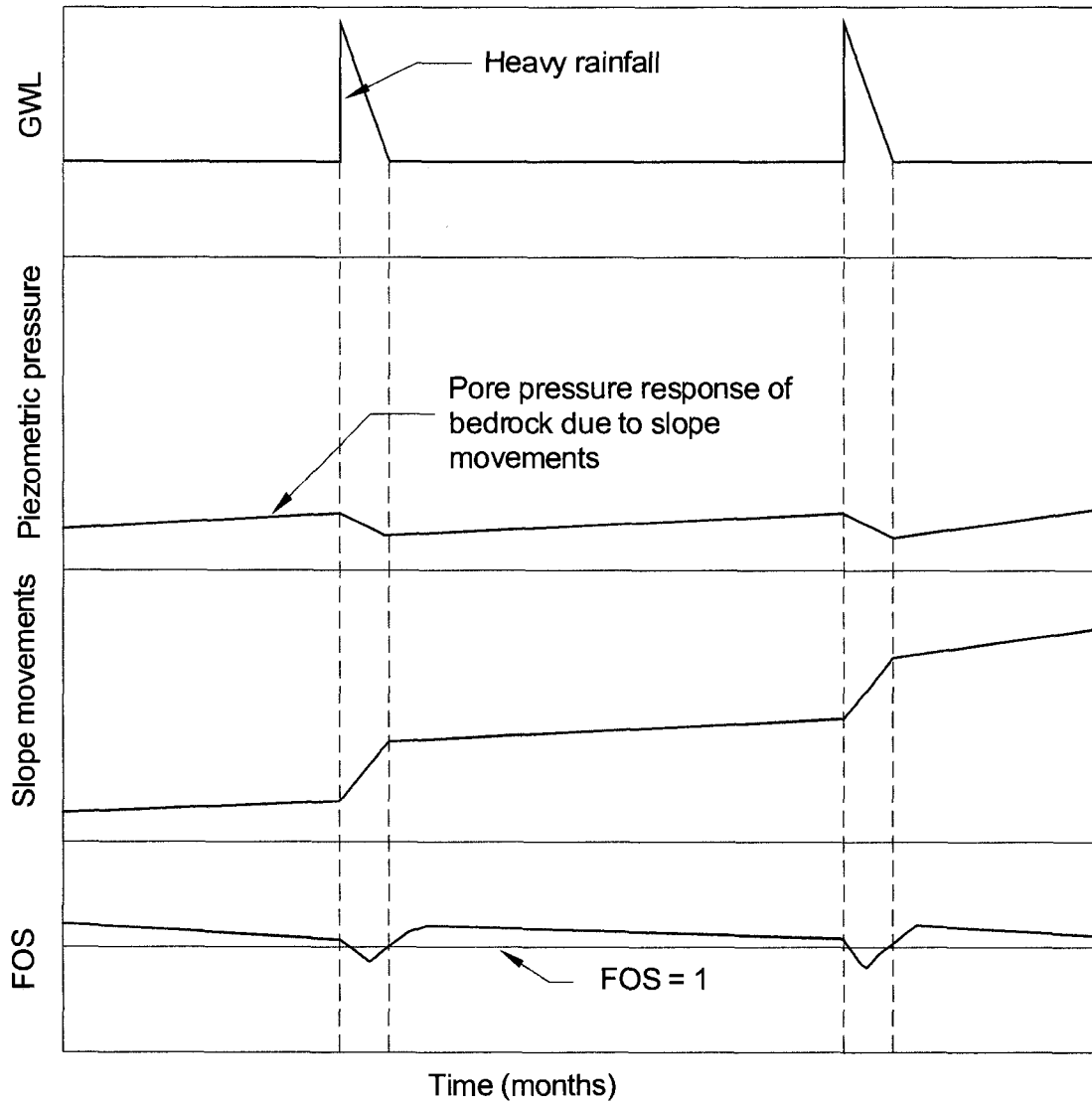


Figure 11-2 Post-failure slop movements related to groundwater table, piezometric pressure and factor of safety

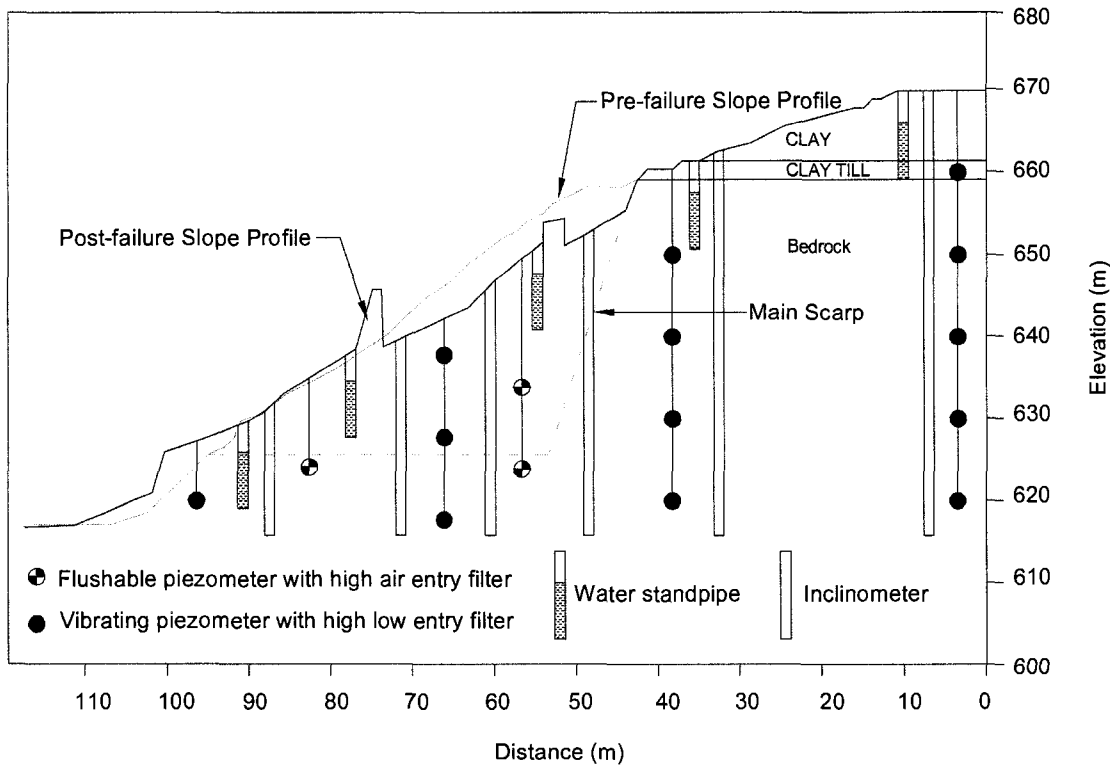


Figure 11-3 Proposed instrumentation for Keillor Road Landslide

CHAPTER 12 Conclusions

12.1 Conclusions

This thesis focuses on the study of landslides along the North Saskatchewan River Valley. The major focus is on pore pressure measurements in weak rock and the mechanisms of translational landslides.

A series of laboratory and field tests were conducted to improve pore pressure measurements in weak rock. Laboratory tests were carried out to determine the optimum water:cement:bentonite ratio to use for grouting field piezometer installations. Before testing, grout mixes were stored in temperature and moisture controlled room. The unconfined compressive strength of grout mix C, a water:cement:bentonite ratio of 2:1:0.3, achieved the highest strength and lowest permeability of all grout mixes tested. An unconfined compressive strength of 1170 kPa and a permeability range of 4.3 to 6.1×10^{-7} cm/sec were achieved with 28 day-old grout mix C.

The pore pressure responses of grout mix C and clay shale samples were monitored using a modified triaxial cell and a small pressure transducer. A good pore pressure response was obtained from these tests and it was decided that the grout-in installation method could be successfully used in the field piezometer installation.

A flushable adaptor was developed and tested in the field. The advantage of using a flushable adaptor is its ability to circulate water from the ground. The flushable adaptor can be used with a normal vibrating wire piezometer. The field investigation involved the installation of different types of piezometer in the Upper Cretaceous bedrock of the Horseshoe Canyon Formation.

The monitoring results showed that significantly low pore pressures existed in the bedrock. Only slight differences in pore pressure measurements were observed with the use of high air entry or low air entry filters. Long-term monitoring of the ground water level and the piezometric pressures revealed there was no connection between a perched water level and the piezometric pressure of the bedrock. Piezometers installed below the sliding plane responded to slope movements by showing a decrease in piezometric pressure. The field monitoring results confirmed that the grout-in installation works well with both pneumatic piezometers and vibrating wire piezometers.

Landslide mechanisms and kinematics were studied from three case histories along the North Saskatchewan River Valley. The case studies found that the slope failures were caused by a combination of different factors: toe erosion by the river, residential developments behind the slope crest, rise of the groundwater level, and softening of the bedrock.

The Keillor Road Landslide evolved from a minor slide at the toe to a major slide taking out part of Keillor Road. Development of the steeply dipping main scarp was observed with inclinometer readings. At Keillor Road, the entire landslide occurred in the bedrock formation. The monitoring data revealed that the movement of displaced material was directly related to the amount of rainfall. The rate of slope movement ranged from 12.5 to 85 cm/month, depending on the amount of rainfall occurring. The rate of movements decreased during winter months but increased again in spring and summer.

The Whitemud Road Landslide was a first-time slide which mobilized the fully softened strength along the rupture surface. A major influencing factor was the thick kame deposit which overlays the Upper Cretaceous bedrock. At the center of the slide, the kame deposit was directly in contact with the bedrock, and this contact could have accelerated the softening processes. The initial movements took place with downward movements of the head and translational movements of the main body of the slide. Horizontal drains were installed in the bedrock, the glacial deposits, and the displaced material. These drains penetrated the kame deposit only in the

southern part of the slide area. In this area, the groundwater level was lowered by 1 to 2 m by the drains. No water was observed from the drains installed inside the displaced materials after 1 year.

Forest Heights Park is located in an old landslide area with steep scarps and grabens. Analyses of the slope stability was complicated by the presence of old mine workings. Instrumentation data revealed that the groundwater level was located in an overlying glacial deposit 12 m below the slope crest. Piezometers installed in the bedrock showed deficient pore pressures. Measured piezometric heads ranged from 3 to 7 m, depending on the depth of the installation. Stability analyses were conducted using the residual shear strength of the bedrock. The analyses showed that the factor of safety was close to unity and the mobilized shear strength of the horizontal rupture surface ranged from 10° to 14° , depending on the location of the groundwater table.

Landslides in the North Saskatchewan River Valley show a common mode—a translational movement along a bentonite layer. These landslides evolved in different stages, starting from a toe failure at the earlier stage to a major failure, retrogressing upslope with time. A two inclined block model was used to analyze five kinematic stages, starting from a single-block and leading to a two-block movement. The formation of a counter scarp, separating active and passive blocks, triggers an acceleration of slope movement as driving forces are increased by 30 %. At low water level, a reduction in the factor of safety due to the formation of an active block is more pronounced.

12.2 Recommendations

- In this study a limited number of field data were available for the analyses. It is recommended that more investigations be carried out and instrumentation works be performed to improve our understanding of the mechanisms of landslides.
- More study is required to determine the relationship between slope movements and piezometric pressure changes in the bedrock.

- The case studies revealed that a few boreholes are not enough to investigate slope stability problems. The field investigation and instrumentation need to cover the entire extent of a slide zone to determine the slope conditions.
- The present investigation did not register a negative pore pressure in the bedrock. However, a negative pore pressure might exist in the bedrock due to dilation of bedrock.
- Piezometer readings are good indicators of slope activity. It would be useful to compare piezometric pressure changes over time between stable slopes and unstable slopes.

References

- Andriashek, L.D. 1988. Quaternary stratigraphy of Edmonton map area, NTS83H., Natural Resources Division, Alberta Research Council.
- ASTM(D2166) 2004. Standard test method for unconfined compression test. ASTM, Philadelphia, Pennsylvania, USA.
- ASTM(D3080) 2004. Standard Test Method for Direct Shear Test of Soils Under Consolidated Drained Conditions. ASTM, Philadelphia, Pennsylvania, USA.
- ASTM(D4318) 2004. Standard test methods for liquid limit, plastic limit and plasticity index of soils. ASTM, Philadelphia, Pennsylvania, USA.
- ASTM(D5084) 2004. Standard test methods for measurement of hydraulic conductivity of saturated porous materials using a flexible wall permeameter. ASTM, Philadelphia, Pennsylvania, USA.
- Atkinson, J.H., and Bransby, P.L. 1978. The mechanics of soils; An introduction to critical state soil mechanics. McGraw-Hill, London.
- Barlow, J.P. 1989. Whitemud Park equestrian trail slope failure investigation, Hardy BBT Ltd., Report submitted to the City of Edmonton, Parks and Recreation Department, Reference number: 928-32-23-08.
- Barlow, J.P. 2000. Whitemud road landslide geotechnical assessment, AMEC Earth and Environmental Ltd, Report to the City of Edmonton, Reference number: 925-28-21-13.
- Baum, R.L., Johnson, A.M., and Fleming, R.W. 1988. Measurement of Slope Deformation Using Quadrilaterals, U. S. Geological Survey Bulletin 1842.
- Bayrock, L.A., and Hughes, G.M. 1962. Surficial geology of the Edmonton district, Alberta, Research Council of Alberta, Report 62-6.
- Bergman, M.H., and Ruban, A.F. 1995. Slide investigation, Keillor Road, EBA Engineering Consultants Ltd, Report to the City of Edmonton, Public Works Department, Reference number: 931-32-02-02.
- Bishop, A.W. 1954. The use of pore-pressure coefficients in practice. *Geotechnique*, **4**: 148-152.

- Bishop, A.W. 1955. The use of the slip circle in the stability analysis of slopes. *Geotechnique*, **5**: 7-17.
- Bishop, A.W., and Bjerrum, L. 1960. The relevance of the triaxial test to the solution of stability problems. *In Proceedings, Research Conference on Shear Strength of Cohesive Soils*. Boulder, Colorado.
- Bishop, A.W., and Henkel, D.J. 1962. The measurement of soil properties in the triaxial test. Edward Arnold Ltd.
- Bishop, A.W., Kennard, M.F., and Penman, A.D.M. 1960. Pore-pressure observations at Selsset Dam. *In Pore Pressure and Suction in Soils*. Butterworths. 30th and 31st March, 1960, Vol.1, pp. 91-102.
- Bishop, A.W., Webb, D.L., and Lewin, P.I. 1965. Undisturbed samples of London Clay from the Ashford Commonshaft: strength-effective stress relationships. *Geotechnique*, **15**: 1-31.
- Bjerrum, L. 1967. Progressive failure in slopes of overconsolidated plastic clay and clay shales. *Journal of Soil Mechanics and Foundation Division, ASCE*, **93**(5): 3-49.
- Botts, M.E. 1986. The effects of slaking on the engineering behaviour of clay shales. Ph.D Thesis, University of Colorado.
- Brooker, E.W. 1967. Strain energy and behavior of overconsolidated soils. *Canadian Geotechnical Journal*, **4**(3): 326-333.
- Brooker, E.W., and Lindberg, D.A. 1965. Field measurement of pore pressure in high plastic soils. *In International Research and Engineering Conference on Expansive Clay Soils*. Texas A & M University, College Station, Texas, pp. 57-68.
- Brooker, E.W., Scott, J.S., and Ali, P. 1968. A transducer piezometer for clay shales. *Canadian Geotechnical Journal*, **5**: 256-264.
- Carlson, V.A. 1967. Bedrock topography and surficial aquifers of the Edmonton district, Alberta, Report 66-3, Alberta Research Council.
- Chandler, R.J. 1984. Recent European experience of Landslides in over-consolidated clays and soft rocks. *In Proceedings, 4th International Symposium on Landslides*. Toronto, Vol.1, pp. 61-80.
- Constant, B.D. 1979. Evaluation of slope stability, proposed subdivision on Ramsey Heights, Riverbend, BBT Geotechnical Consultants Ltd., Report submitted to the City of Edmonton, Reference Number: 925-27-02-08.

- Contreras, I.A., Grosser, A.T., and Strate, R.H.V. 2007. The use of the fully-grouted method for piezometer installation. *In* 7th International Symposium of Field Measurements in Geomechanics. Boston, Massachusetts. ASCE, pp. 1-20.
- Cruden, D.M. 1997. General co-report session 4: Slope stability and protection. *In* Geotechnical Engineering of Hard Soils - Soft Rocks, Balkema, Rotterdam. pp. 1957-1983.
- Cruden, D.M., and Varnes, D.J. 1996. Landslide types and process, Special Report 247, Transportation Research Board, National Research Council, Washington. pp. 36-75.
- Cruden, D.M., Thomson, S., and Tsui, P.C. 1989. The geotechnical characteristics of an ice-thrust mudstone, Wabamun Lake area, Alberta. *Canadian Geotechnical Journal*, **26**: 227-234.
- Cruden, D.M., Thomson, S., and Hoffmann, B.A. 1991. Observation of Graben geometry in landslides. *In* Slope stability engineering, developments and applications. Isle of Wight. 15-18 April 1991. Thomas Telford, pp. 33-35.
- Cruden, D.M., Martin, C.D., and SoeMoe, K.W. 2003. Stages in the translational sliding of 2 inclined blocks: observations from Edmonton. *In* Proceedings, 56th Canadian Geotechnical Conference. Winnipeg, Manitoba, Vol.1, pp. 823-830.
- Cruden, D.M., Peterson, A.E., Thomson, S., and Zabeti, P. 1998. The Lesueur Landslide: 35 years old and still active. *In* 51st Canadian Geotechnical Conference, pp. 17-22.
- Cruden, D.M., Peterson, A.E., Thomson, S., and Zabeti, P. 2002. Thirty-five years of activity at the Lesueur landslide, Edmonton, Alberta. *Canadian Geotechnical Journal*, **39**: 266-278.
- Das, B.M. 1993. Principles of Geotechnical Engineering.
- DJM_Research_Group 1984. The manual for the dry jet mixing method. pp. 20-31.
- Dunncliff, J. 1988. Geotechnical instrumentation for monitoring field performance. John Wiley & Sons, Inc, New York.
- Dunncliff, J. 1993. Geotechnical instrumentation for monitoring field performance. John Wiley & Sons, Inc, New York.
- Eglauer, A., and Ruban, A.F. 2005. Instrumentation Installation, Keillor Road, Edmonton, EBA Engineering Consultants Ltd., Report to the City of Edmonton, Engineering Services: Reference number: .

- Eigenbrod, K.D., and Morgenstern, N.R. 1971. A slide in Cretaceous bedrock at Devon, Alberta. *In Proceedings, Geotechnical Practice for Stability in Open Pit Mining*. Vancouver, pp. 223-238.
- Elliot, R.H.J. 1958. Sub-surface correlation of the Edmonton Formation. *Edmonton Geological Society Quarterly*, June 1958: 1-6.
- Esu, F. 1966. Short-term stability of slopes in unweathered jointed clays. *Geotechnique*, **16**: 321-328.
- Esu, F., Distefano, D., Grisolia, M., and Tancredi, G. 1984. Stability of a high cut in overconsolidated Lacustrine deposit. *In Proceedings, 4th International Symposium on Landslides*. Toronto, Vol.2, pp. 63-68.
- Fenelli, G.B., and Picarelli, L. 1990. The pore pressure field built up in a rapidly eroded soil mass. *Canadian Geotechnical Journal*, **27**: 387-392.
- Filho, P.R. 1976. Laboratory tests on a new borehole seal for piezometers. *Ground Engineering*, **9**(16-18): 16-18.
- Godfrey, J.D. 1993. Edmonton beneath our feet. *Edmonton Geological Society*.
- Gould, J.P. 1960. A study of shear failure in certain Tertiary marine sediments. *In Research conference on Shear Strength of Cohesive Soils*, ASCE. Boulder, Colorado.
- Graham, J., and Au, V.C.S. 1985. Effects of freeze-thaw and softening on a natural clay at low stresses. *Canadian Geotechnical Journal*, **22**: 69-78.
- Gregory, C.H. 1844. On railway cuttings and embankments; with an account of some slips in the London clay, on the line of the London and Croydon Railway. *Min. Proc. Inst. C. E.*, **3**: 135-145.
- Hayley, D.W. 1968. Progressive failure of a clay shale slope in Northern Alberta. M.Sc. Thesis, Department of Civil Engineering, University of Alberta, Edmonton, Alberta.
- Head, K.H. 1992. *Manual of soil laboratory testing, Volume 2*. Pentech Press Ltd, London.
- Hoek, E., and Bray, J.W. 1977. *Rock slope engineering*. Institute of Mining and Metallurgy, London.
- Hutchinson, J.N. 1988. Morphological and geotechnical parameters of landslides in relation to geology and hydrogeology. *In Proceedings of the fifth international symposium on landslides. Edited by C. Bonnard*. Lausanne, Switzerland.

- 10th to 15th July, 1988. A.A.Balkema/Rotterdam/Brookfield/1988, Vol.1, pp. 3-35.
- Hvorslev, M.J. 1951. Time lag and soil permeability in groundwater observations. Bulletin 36, Waterways Experiment Station, Vicksburg, Miss.
- Irish, E.J.W. 1970. The Edmonton Group of south-central Alberta. Bulletin of Canadian Petroleum Geology, **18**(2): 125-155.
- Kathol, C.P., and McPherson, R.A. 1975. Urban geology of Edmonton. Alberta Research Council, p. 61.
- Koppula, S.D., and Morgenstern, N.R. 1984. Deficient pore pressures in an eroding soil mass. Canadian Geotechnical Journal, **21**: 277-288.
- Krahn, J. 2004a. Stability modelling with SLOPE/W. GEO-SLOPE International Ltd., Calgary, Alberta.
- Krahn, J. 2004b. Seepage modeling with SEEP/W. GEO-SLOPE International Ltd., Calgary, Alberta.
- Lea, F.M. 1956. The chemistry of cement and concrete. Edward Arnold Ltd, London.
- Lewycky, D. 1997. Initial project review for the construction of a concrete pile retaining wall at Keillor Road & approximately 75 Avenue, The City of Edmonton, Public Work, Report 928-32-23-11.
- Locker, J.G. 1969. The petrographic and engineering properties of fine-grained sedimentary rocks of central Alberta, Ph.D thesis; University of Alberta, Edmonton.
- Long, M., Menkiti, C., and Follett, B. 2004. Some experience in measuring pore water suction in Dublin glacial till. Geotechnical News, **22**(3): 21-27.
- Martin, R.L., Lewycky, D.M., and Ruban, A.F. 1998. Long term movement rates in a large translational landslide. *In* Proceedings, 51st Canadian Geotechnical Conference, pp. 23-30.
- Martin, R.L., Williams, D.R., Blanko, L.A., and Morgenstern, N.R. 1984. The Grierson hill slide, Edmonton, Alberta. *In* Proceedings. 37th Canadian Geotechnical Conference. Toronto, pp. 125-134.
- Matheson, D.S., and Thomson, S. 1973. Geological Implications of Valley Rebound. Canadian Journal of Earth Sciences, **10**: 961-978.
- McCormick, G. 1977. Top-of-Bank study, Whitemud Road Extension, 45 Avenue and 156 Street, R. M. Hardy & Associates Ltd., Report submitted to the City of Edmonton, Reference number: 925-27-01-04, Edmonton.

- McKenna, G.T. 1995. Grouted-in installation of piezometers in boreholes. *Canadian Geotechnical Journal*, **32**: 355-363.
- Mesri, G., and Shahein, M. 2003. Residual strength mobilized in first-time slope failures. *Journal of Geotechnical and Geoenvironmental Engineering*, **129**(1): 12-31.
- Mikkelsen, P.E. 2002. Cement-bentonite grout backfill for borehole Instruments. *In Geotechnical News*, pp. 38-42.
- Mikkelsen, P.E., and Green, G.E. 2003. Piezometers in fully grouted boreholes. *In Symposium on Field Measurements in Geomechanics, FMGM 2003*. Oslo, Norway. September 2003.
- Mollard, J.D. 1977. Regional landslide types in Canada. *In Landslides*. pp. 29-56.
- Morgenstern, N.R. 1977. Slopes and excavations in heavily over-consolidated clays: State-of-the-Art report. *In Proceedings, 9th international conference on soil mechanics and foundation engineering*. Tokyo, Vol.2, pp. 547-581.
- Morgenstern, N.R. 1979. Geotechnical behaviour of clay shales - an overview. *In International Symposium on Soil Mechanics*, Vol.1, pp. 29-42.
- Morgenstern, N.R. 1990. Instability mechanisms in stiff soils and weak rocks. *In Tenth Southeast Asian Geotechnical Conference*. Taipei, Taiwan. 16-20 April.
- Morgenstern, N.R., and Price, V.E. 1965. The analysis of the stability of general slip surfaces. *Geotechnique*, **15**: 79-93.
- Morgenstern, N.R., and Eigenbrod, K.D. 1974. Classification of argillaceous soils and rocks. *Journal of the Geotechnical Engineering Division*, **100**: 1137-1156.
- Okamoto, R., Kojima, K., and Yoshinaka, R. 1981. Distribution and engineering properties of weak rocks in Japan. *In Proceedings, The International Symposium on Weak Rock*. Tokyo, Vol.2, pp. 1269-1283.
- Ower, J.R. 1958. The Edmonton Formation. *Edmonton Geological Society Quarterly*, **2**(1): 3-11.
- Painter, W.T. 1965. An investigation of the Lesueur landslide, Edmonton, Alberta. M.Sc thesis, University of Alberta.
- Patton, F.D. 1966. Multiple modes of shear failure in rock. *In 1st Congress of International Society of Rock Mechanics*. Lisbon, Vol.1, pp. 509-514.
- Penman, A.D.M. 2002. Measurement of pore water pressure in embankment dams. *Geotechnical News*: 43-49.

- Penman, A.D.M. 2003. Discussions of "Measurement of pore water pressure in embankment dams". *Geotechnical News*: 42-51.
- Pennell, D.G. 1969. Residual strength analysis of five landslides. Ph.D. thesis, Department of Civil and Environmental Engineering, University of Alberta, Edmonton, Alberta.
- Peterson, R. 1954. Studies of Bearpaw Shale at a damsite in Saskatchewan. *In* Proceeding, American Society of Civil Engineering, Vol. 80 Separate No. 476, pp. 1-28.
- Peterson, R. 1958. Rebound in the Bearpaw shale in Western Canada. *Geological Society of America, Bulletin*, **69**: 1113-1123.
- Pettijohn, F.J. 1957. *Sedimentary rocks*. 2nd Ed.,. Harper & Brothers, N. York.
- Ridley, A.M., and Burland, J.B. 1996. A pore water pressure probe for the in situ measurement of a wide range of soil suctions. *In* *Advances in site investigation practice*. Edited by C. Craig. London. Thomas Telford, pp. 510-520.
- Ridley, A.M., Dinneen, K., Burland, J.B., and Vaughan, P.R. 2003. Soil matrix suction: Some examples of its measurement and application in geotechnical engineering. *Geotechnique*, **53**(2): 241-253.
- Roscoe, K.H., Schofield, A.N., and Worth, C.P. 1958. On the yielding of soils. *Geotechnique*, **8**(1): 22-53.
- Ruban, A.F., and Pulles, B.C.M. 1996. Keillor Road Slide, EBA Engineering Consultants Ltd., Report to the City of Edmonton, Public Works, Materials Engineering, Reference number: 928-32-23-07.
- Ruban, A.F., and Sabourin, M. 2003. Keillor Road instability, Edmonton, Alberta, EBA Engineering Consultants Ltd., Report submitted to the City of Edmonton, Engineering Services, Reference number: 928-32-23-12.
- Sarma, S.K. 1979. Stability analysis of embankments and slopes. *Journal of Geotechnical Engineering Division, American Society of Civil Engineers*, **105**: 1511-1524.
- Scott, C.C., and Townsend, D.L. 1976. Geotechnical evaluation of existing slopes, Forest Heights Park, Capital City Recreation Park, Edmonton, Alberta, R. M. Hardy & Associates Ltd., Report submitted to the Alberta Environment, Reference number: 934-36-01-02.

- Scott, J.S., and Brooker, E.W. 1968. Geological and engineering aspects of Upper Cretaceous shales in Western Canada, Report paper 66-37, Geological Survey of Canada, Department of Energy, Mines and Resources.
- Shaw, J. 1993. Edmonton beneath our feet. Edmonton Geological Society. p. 150.
- Sherard, J.L. 1981. Piezometers in earth dam impervious sections. *In* Recent Developments in Geotechnical Engineering for Hydro Projects. *Edited by* F. Kulhay. ASCE, New York, pp. 125-165.
- Sinclair, S.R., and Brooker, E.W. 1967. The shear strength of Edmonton Shale. *In* Proceedings, The Geotechnical Conference Oslo. Oslo, Vol.1, pp. 295-299.
- Skempton, A.W. 1948. The rate of softening in stiff fissured clays, with special reference to London. *In* Proceedings of 2nd International Conference on Soil Mechanics. Rotterdam, Vol.2, pp. 50-53.
- Skempton, A.W. 1954. The pore-pressure coefficients A and B. *Geotechnique*, **4**: 143-147.
- Skempton, A.W. 1964. Long-term stability of clay slopes. *Geotechnique*, **14**(2): 77-102.
- Skempton, A.W. 1970. First time slides in over-consolidated clays. *Geotechnique*, **20**: 320-324.
- Skempton, A.W. 1978. Slope stability of cuttings in brown London clay. *In* 9th International Conference on Soil Mechanics and Foundation Engineering, Vol.3, pp. 261-270.
- Skempton, A.W., and Delory, F.A. 1957. Stability of natural slopes in London clay. *In* Proceedings, 4th International Conference on Soil Mechanics and Foundation Engineering. London, Vol.2, pp. 378-381.
- Skempton, A.W., and Petley, D.J. 1967. The shear strength along structural discontinuities of stiff clays. *In* Proceedings of the Geotechnical Conference. Oslo, Vol.2, pp. 29-46.
- Small, C.A. 1989. Failure in Mine Highwall in soft sedimentary rock. M.Sc Thesis, University of Alberta, Edmonton.
- SoeMoe, K.W., Cruden, D.M., and Martin, C.D. 2003. A simple model of a hazardous landside mode on the interior plains: the sliding of two inclined blocks. *In* 3rd Canadian Conference on Geotechnique and Natural Hazards. Edmonton, Alberta, Vol.1, p. 379.

- SoeMoe, K.W., Cruden, D.M., Martin, C.D., Lewycky, D., and Lach, P.R. 2005. 15 Years of Movements at Kellor Road, Edmonton. *In* Proceedings, 58th Canadian Geotechnical Conference. Saskatoon, Saskatchewan, Vol.1.
- SoeMoe, K.W., Cruden, D.M., Martin, C.D., Lewycky, D., and Lach, P.R. 2006. Delayed failure of a river valley slope: Whitemud Road Landslide. *In* Proceedings, 59th Canadian Geotechnical Conference. Vancouver. October 1-4, 2006, Vol.1, pp. 1476-1483.
- SoeMoe, K.W., Cruden, D.M., Martin, C.D., Lewycky, D., and Lach, P.R. 2007. Study of a century old landslide in Edmonton: The Forest Height Park Landslide. *In* Proceedings, 60th Canadian Geotechnical Conference. Ottawa. October 21-24, 2007, Vol.1, pp. 770-777.
- Stein, R. 1982. Hydrogeology of the Edmonton area (southeast segment), Alberta, Report Earth Science Report 79-6, Alberta Research Council.
- Suzuki, Y. 1982. Deep chemical mixing method using cement hardening agent. *In* Symposium on soil and rock improvement technique using geotextile, reinforced earth and modern piling method. Bangkok, pp. 1-24.
- Taylor, R.S. 1971. Atlas: Coal-mine workings of the Edmonton area.
- Tedder, K.H. 1986. Slope stability in the North Saskatchewan River valley, University of Alberta, Edmonton.
- Terzaghi, K. 1936. Stability of slopes of natural clay. *In* First international conference on soil mechanics and foundation engineering. Harvard University, Cambridge, Mass, Vol.1, pp. 161-165.
- Terzaghi, K. 1950. Mechanism of landslides. Application of geology to engineering practice, Geology Society of America: 83-123.
- Terzaghi, K., and Peck, R.B. 1967. Soil Mechanics in Engineering Practices, 2nd ed. Wiley, New York.
- Terzaghi, K., Peck, R.B., and Mesri, G. 1996. Soil Mechanics in Engineering Practices, 3rd ed. Wiley, New York.
- Thomson, S. 1970. Riverbank stability study at the University of Alberta, Edmonton. Canadian Geotechnical Journal, 7: 157-168.
- Thomson, S. 1971a. Analysis of a Failed Slope. Canadian Geotechnical Journal, 8: 596-599.

- Thomson, S. 1971b. The Lesueur landslide, a failure in Upper Cretaceous clay shale. *In* 9th Annual Symposium on Engineering Geology and Soil Engineering. Boise, Idaho, pp. 257-288.
- Thomson, S., and Hayley, D.W. 1975. The Little Smokey Landslide. *Canadian Geotechnical Journal*, **12**: 379-392.
- Thomson, S., and Tiedemann, C.E. 1982. A review of factors affecting landslides in urban areas. *Bulletin of the Association of Engineering Geologists*, **19**: 55-65.
- Townsend, D.L. 1975. Pre-design construction cost estimate, low level berm and bank stabilization, Capital City Recreation Park, R. M. Hardy & Associates Ltd, Report submitted to the Alberta Environment, Reference number: 934-40-19-01, Edmonton.
- Townsend, D.L. 1980. Geotechnical analysis of four slides, Forest Heights Park, Hardy Associates (1978) Ltd., Report submitted to the City of Edmonton, Parks and Recreation Department, Reference number:934-36-01-03.
- Underwood, L.B. 1967. Classification and identification of shales. *Journal of the Soil Mechanics and Foundations Division, ASCE*, **93**(SM6): 97-116.
- Underwood, L.B., Thorfinnson, S.T., and Black, W.T. 1964. Rebound in redesign of Oahe Dam hydraulic structures. *Journal of Soil Mechanics and Foundation Division, ASCE*, **90**(SM2): 65-86.
- Varnes, D.J. 1958. Landslide types and processes. *Landslides and engineering practice*. Highway Research Board, Report 29, pp. 20-47.
- Varnes, D.J. 1978. Slope movement types and processes, Report Special Report 176, pg 11-33, Washington.
- Vaughan, P.R. 1969. A note on sealing piezometers in boreholes. *Geotechnique*, **19**(3): 405-413.
- Vaughan, P.R. 1973. The measurement of pore pressures with piezometers. *In* *Field Instrumentation in Geotechnical Engineering*. London, Butterworths. 30th May - 1st June 1973.
- Vaughan, P.R., and Walbancke, H.J. 1973. Pore pressure changes and delayed failure of cutting slopes in overconsolidated clays. *Geotechnique*, **23**(4): 531-539.
- Yang, J.-F.J. 1987. Role of lateral stress in slope stability of stiff overconsolidated clays and clayshales. Ph.D. thesis, Iowa State University, Iowa.

Yoshida, N., Morgenstern, N.R., and Chan, D.H. 1990. A failure criterion for stiff soils and rocks exhibiting softening. *Canadian Geotechnical Journal*, **27**(195-202).

APPENDIX A The Sliding of Two Inclined Blocks

Assumptions of the analysis

- This four-stage landslide mode is modeled in two dimensions assuming both active and passive blocks are infinitely wide.
- Displaced material is uniform with a weak plane, DO which forms a lower surface of rupture.
- The main scarp, CD develops following valley rebound and stress relief joints. The main scarp has a dip, θ and is filled with water to height Z_w .
- The weak plane, DO can be horizontal or with a dip, α , and the water level at the weak plane is defined by Z_s .
- The active block is defined by the portion of the main scarp, CF and the counter scarp, EF.
- Water levels on the active block are defined by Z_a and Z_c . The forces, the weight of the sliding block, W , the uplift force due to water pressure on the sliding surface, U_s , and the water pressure in the main scarp, U_b , all act through the centroid of the sliding mass.
- A slice of unit thickness is considered and it is assumed that release surfaces are present so that there is no resistance to sliding at the lateral boundaries of the failure.
- Properties of the displaced material, OBCD, are defined by average values of unit weight and friction angle. Only friction angle is required for the weak plane, DO.
- Slope geometry is defined by slope height, H , active block height, H_a , slope angle, β , main scarp dip, θ , counter scarp dip, δ , distance from the valley crest to the main scarp, R , and the weak seam or surface of rupture which is assumed to be horizontal or with a dip, α .

Single block mechanism (Stage 1 and 2)

- It is assumed that the main scarp is open but displaced material is in intact condition.
- Average unit weight, the strength properties of the displaced material and the weak seam are required for the analyses.
- Movement is a single block mechanism and the sliding occurs along the weak plane.
- The driving force is generated by the water pressure on the main scarp and the weight of the sliding block if the sliding plane has a dip.
- The resisting force is obtained from the shear resistance of the weak layer.

Two inclined blocks model (Stage 3 and 4)

- After initial sliding along the weak layer at stage 2, the head of the displaced material is unsupported and over a few months, a counter scarp develops which forms an active block at Stage 3.
- The active block is defined by the counter scarp dip, δ , and the height of active block, H_a .
- At this stage, the stability calculation can be divided into two parts. The first one is the determination of the resultant force, R_2 , which applies pressure on the passive block.
- The second one is to determine the stability analysis of the passive block.

Calculation of Resultant force, R_2

- The resultant force, R_2 , of the active block is determined by the method of force polygons.
- Forces required for equilibrium of the active block are the weight of the active block, W_a , the water forces at the main scarp and the counter scarp, U_1 & U_2 , and the resultant forces acting on the main scarp and the counter scarp, R_1 & R_2 .

- The water forces apply pressure normal to the main scarp and the counter scarp. Water force, U_1 acts in the direction of $(90-\theta)$ and U_2 , acts in the direction of $(90-\delta)$. The water forces acting on the active block are calculated from the ground water level, Z_a and Z_c .
- It is assumed that full frictional forces are mobilized along the main scarp and the counter scarp.
- The resultant force, R_1 , acts in the direction of $(90+\phi-\theta)$ on the main scarp and the resultant force, R_2 , acts in the direction of $(90+\phi-\delta)$ on the counter scarp. In some cases, the resultant force, R_1 can be negative due to high water pressure. In that case, ground water level at the main scarp and the counter scarp need to be adjusted.
- The resultant water force, U_f , is obtained from the horizontal component of water force, U_h and the vertical component of water force, U_v .
- The effective weight of the active block, W_e , can be obtained by reducing the vertical component, U_v , from the total weight of the active block, W_a . By using W_e and U_h , the resultant force, R_f can be obtained.
- After obtaining R_f , the resultant forces R_1 and R_2 can be calculated using the sine rule.

Geometry – One block mechanism

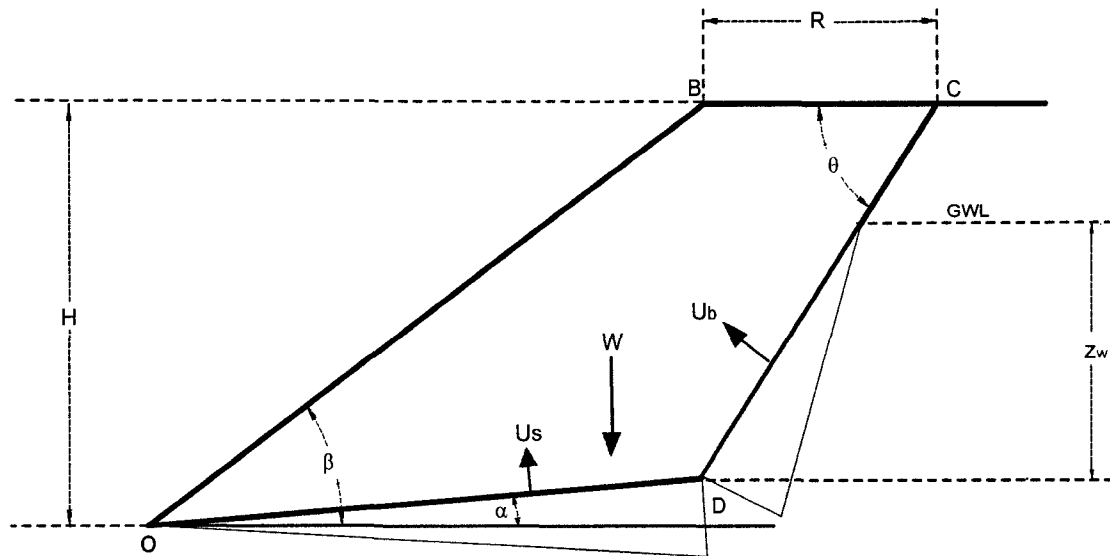


Figure A 1 Single block

Known Parameters		Unknown Parameters	
ϕ_b	- Friction angle (main Block)	B	- Slope crest
ϕ_s	- Friction angle (weak plane)	C	- Main scarp/Bench intersection
H	- Slope height	D	- Weak plane/Main scarp intersection
β	- Slope angle	N	- Slope length (O to B)
α	- Weak plane or failure plane dip	Q	- Main scarp length (D to C)
θ	- Main scarp dip	L	- Failure plane length (O to D)
R	- Distance from the slope crest to the main scarp	A	- Sliding block area
O	- Origin	W	- Sliding block weight
Z_w	- Height of water table from toe of the slope		

$$N = \frac{H}{\sin \beta} \quad [1]$$

$$B = \{H \cot \beta, H\} \quad [2]$$

$$C = \{H \cot \beta + R, H\} \quad [3]$$

$$D = C - \{Q \cos \theta, Q \sin \theta\} \quad [4]$$

$$D = \{L \cos \alpha, L \sin \alpha\} \quad [5]$$

Equating [4] & [5]

$$L = \frac{C_x - Q \cos \theta}{\cos \alpha} \quad [6]$$

$$L = \frac{C_y - Q \sin \theta}{\sin \alpha} \quad [7]$$

Equating [6] & [7] and solve for Q

$$Q = \frac{C_y \cot \alpha - C_x}{\sin \theta \cot \alpha - \cos \theta} \quad [8]$$

Area Calculation

$$A = \frac{1}{2} \|B_x D_y - B_y D_x\| + \frac{1}{2} \|(D_x - B_x)(C_y - B_y) - (D_y - B_y)(C_x - B_x)\| \quad [9]$$

$$W = A \gamma \quad [10]$$

Water Forces – Mono Block

Assume maximum pressure at the base of main scarp

P_b = Water pressure at the base of main scarp

U_b = Water force at the main scarp

U_s = Water force at the sliding plane

$$Z_f = L \sin \alpha \quad [11]$$

$$Z_t = Z_w - Z_f \quad [12]$$

$$P_b = \gamma_w \cdot Z_t \quad [13]$$

$$U_b = \frac{1}{2} \frac{Z_t^2 \gamma_w}{\sin \theta} \quad [14]$$

$$U_s = \frac{1}{2} Z_t \gamma_w L \quad [15]$$

Geometry – Two blocks mechanism

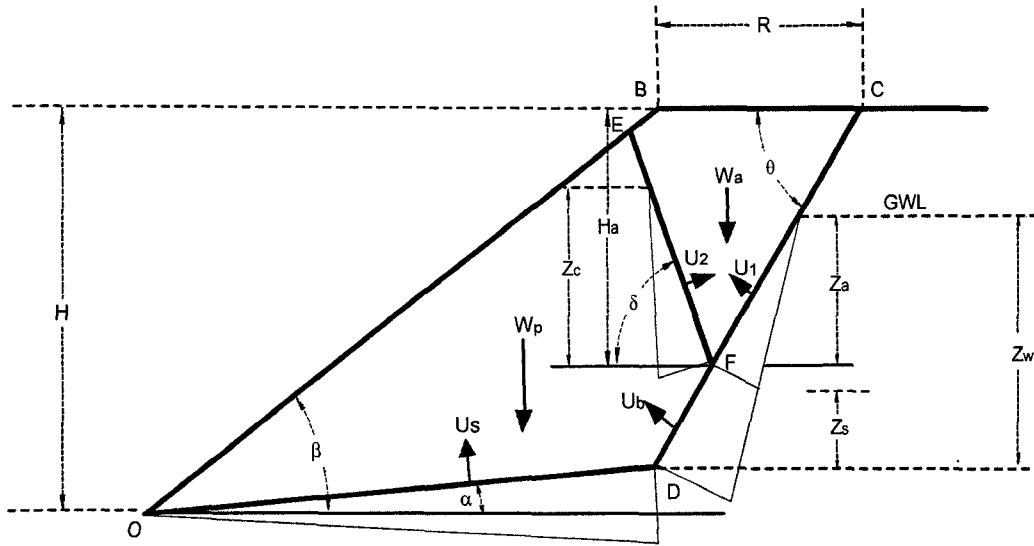


Figure A 2 Two block analysis

Known Parameters	Unknown Parameters
ϕ_b - Friction angle (main Block)	B - Slope crest
ϕ_s - Friction angle (weak plane)	C - Main scarp/Bench intersection
H - Slope height	D - Failure plane/Main scarp intersection
β - Slope angle	E - Counter scarp/Slope face intersection
α - Weak plane or failure plane dip	F - Counter scarp/Main scarp intersection
θ - Main scarp dip	N - Slope length (O to B)
R - Distance of main scarp from the slope crest	Q - Main scarp length (D to C)
O - Origin	L - Failure plane length (O to D)
Z_w - Height of water table	S - Length of active block in the main scarp side
δ - Counter scarp dip	U - Length of active block at the slope crest
H_a - Height of active block	T - Length of active block outside the slope
	H_d - Height of block to be deducted
	A - Sliding block area
	A_a - Area of active block
	A_p - Area of passive block
	W - Weight of sliding block

$$N = \frac{H}{\sin \beta} \quad [16]$$

$$B = \{H \cot \beta, H\} \quad [17]$$

$$C = \{H \cot \beta + R, H\} \quad [18]$$

$$D = C - \{Q \cos \theta, Q \sin \theta\} \quad [19]$$

$$D = \{L \cos \alpha, L \sin \alpha\} \quad [20]$$

Equating [19] & [20]

$$\{C_x, C_y\} - \{Q \cos \theta, Q \sin \theta\} = \{L \cos \alpha, L \sin \alpha\}$$

$$L = \frac{C_x - Q \cos \theta}{\cos \alpha} \quad [21]$$

And,

$$L = \frac{C_y - Q \sin \theta}{\sin \alpha} \quad [22]$$

Equate equations [21] & [22] and solve for Q

$$Q = \frac{C_y \cot \alpha - C_x}{\sin \theta \cot \alpha - \cos \theta} \quad [23]$$

Calculation of Active Block Geometry

$$S = \frac{H_a}{\sin \theta} \quad [24]$$

$$F = C - \{S \cos \theta, S \sin \theta\} \quad [25]$$

$$F_x = C_x - S \cos \theta$$

$$F_y = C_y - S \sin \theta$$

$$U = \frac{H_a}{\tan \delta} + \frac{H_a}{\tan \theta} \quad [26]$$

If $U > R$

$$T = \left[\frac{H_a}{\tan \delta} + \frac{H_a}{\tan \theta} \right] - R \quad [27]$$

$$V = \frac{T \sin \delta}{\sin(180 - \beta - \delta)} \quad [28]$$

$$H_d = V \sin \beta \quad [29]$$

$$E = B - \{V \cos \beta, V \sin \beta\} \quad [30]$$

$$E_x = B_x - V \cos \beta$$

$$E_y = B_y - V \sin \beta$$

If $U < R$

$$E_x = C_x - U$$

$$E_y = H$$

Area of Active Block

If $U < R$

$$A_a = \frac{1}{2} H_a U \quad [31]$$

If $U > R$

$$A_a = \frac{1}{2} H_a U - \frac{1}{2} H_d T \quad [32]$$

Area of Passive Block

$$A_p = A - A_a \quad [33]$$

Calculation of Pore pressure acting on the Active Block

$$Z = H - Z_w$$

$$Z_a = H_a - Z$$

Z_b = Height of water pressure at counter scarp

Water force acting on the active block

$$U_1 = \frac{1}{2} \frac{Z_a^2 \gamma_w}{\sin \theta} \quad [34]$$

$$U_2 = \frac{1}{2} \frac{Z_b^2 \gamma_w}{\sin \delta} \quad [35]$$

Calculation of Resultant forces for active block (Dry Case)

- It is assumed that after forming active block, full friction angle is mobilized along the back scarp and counter scarp.
- Resultant forces R act in the direction inclined at friction angle from normal to the scarp.

W_a - Weight of active block

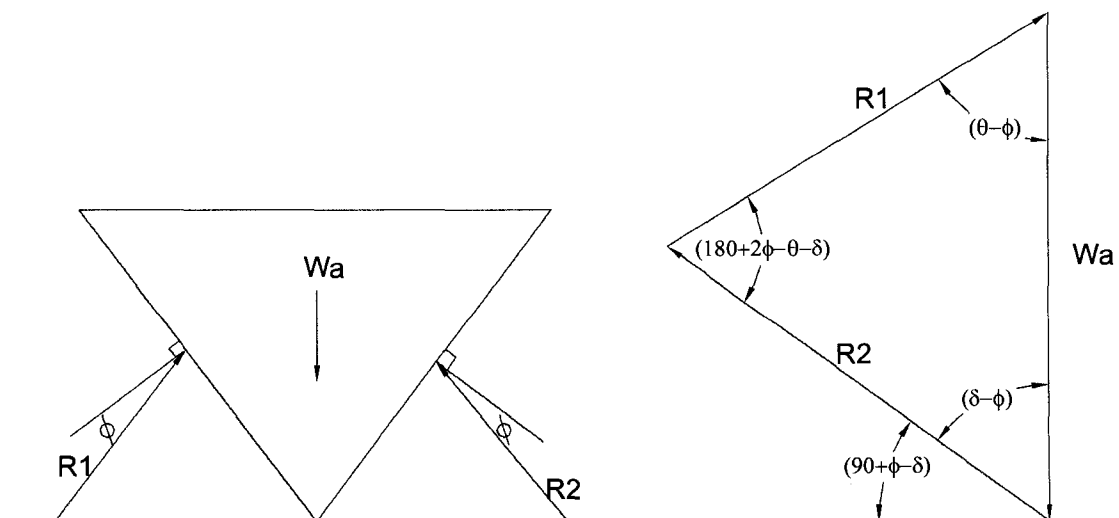


Figure A 3 Calculation of resultant force R2, Dry case

According to sine rule

$$\frac{W_a}{\sin(180 + 2\phi_b - \theta - \delta)} = \frac{R_1}{\sin(\delta - \phi_b)}, \quad \frac{W_a}{\sin(180 + 2\phi_b - \theta - \delta)} = \frac{R_2}{\sin(\theta - \phi_b)}$$

$$R_1 = \frac{W_a \sin(\delta - \phi_b)}{\sin(180 + 2\phi_b - \theta - \delta)} \quad [36]$$

From the active block, resultant force R_2 act on the passive block increasing the driving force.

Component of R_2 parallel to sliding plane

$$R_{2h} = R_2 \cos(90 + \phi_b - \delta - \alpha)$$

Component of R_2 normal to sliding plane

$$R_{2v} = R_2 \sin(90 + \phi_b - \delta - \alpha)$$

Weight of passive block

Weight of passive block can be obtained by reducing active block weight from total weight of sliding block.

$$W_p = W_t - W_a$$

Calculation of Factor of Safety (Dry Case)

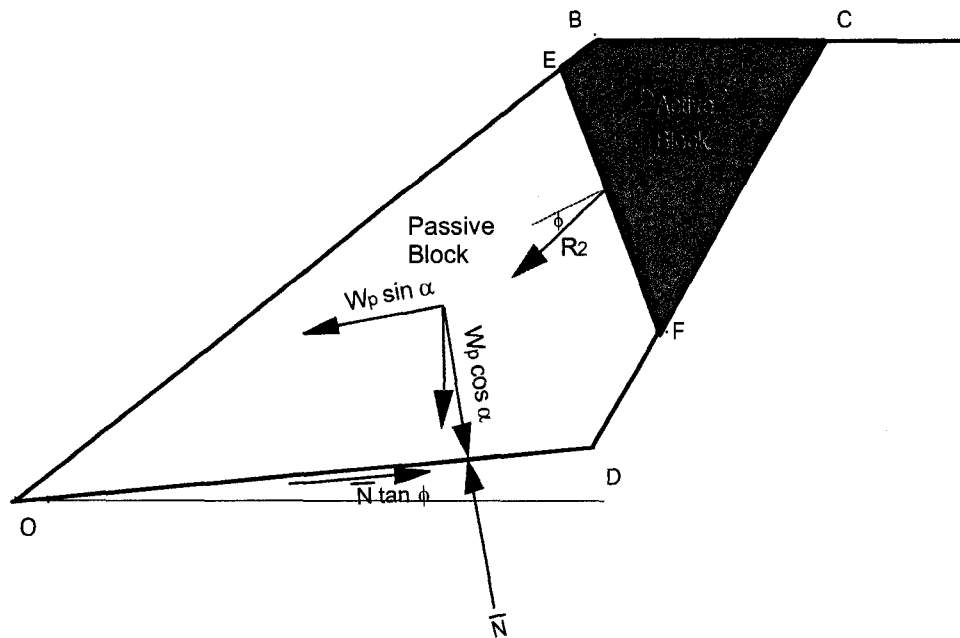


Figure A 4 Calculation of the factor of safety (Dry case)

$$\text{Driving Force} = R_{2h} + W \sin \alpha$$

Normal force at the failure plane

$$N = W \cos \alpha + R_2 \sin(90 + \phi_b - \delta - \alpha)$$

$$\text{Resisting Force} = N \tan \phi_s$$

$$F.S = \frac{[W \cos \alpha + R_2 \sin(90 + \phi_b - \delta - \alpha)] \tan \phi_s}{R_2 \cos(90 + \phi_b - \delta - \alpha) + W \sin \alpha} \quad [37]$$

Calculation of Resultant forces for active block (with ground water pressure)

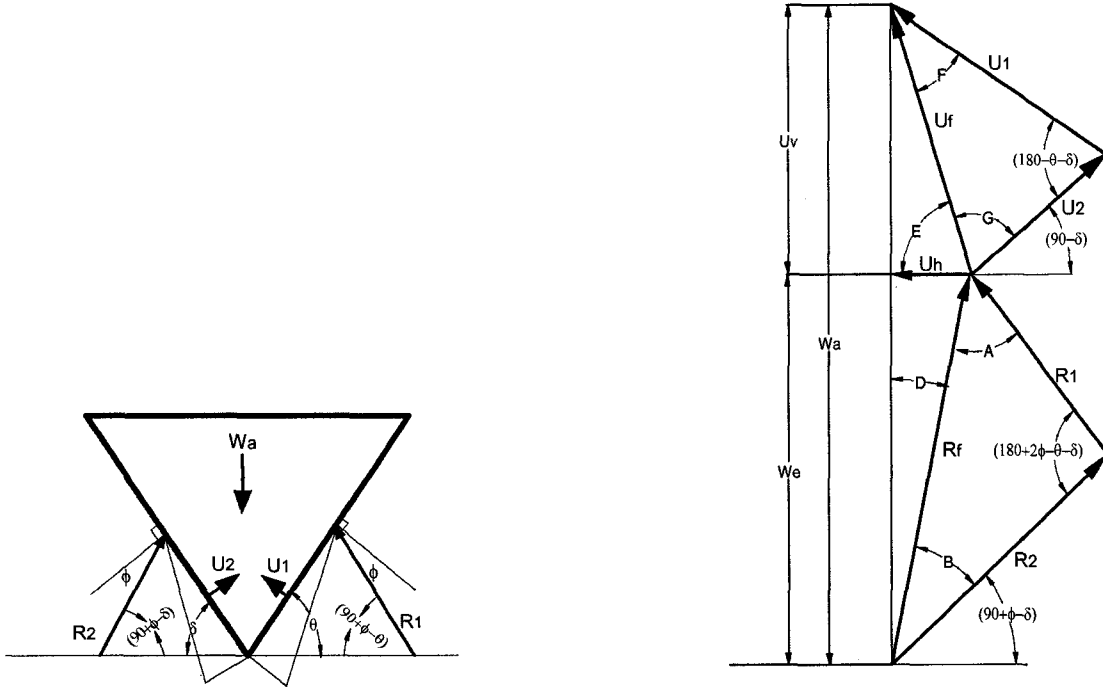


Figure A 5 Calculation of resultant force R2,

$$U_v = U_1 \sin(90 - \theta) + U_2 \sin(90 - \delta) \quad [38]$$

$$U_h = U_1 \cos(90 - \theta) - U_2 \cos(90 - \delta) \quad [39]$$

$$U_f = \sqrt{U_v^2 + U_h^2} \quad [40]$$

$$G = \sin^{-1} \frac{U_1 \sin(180 - \theta - \delta)}{U_f} \quad [41]$$

$$E = 180 - G - (90 - \delta) \quad [42]$$

$$W_e = W_a - U_v \quad [43]$$

$$R_f = \sqrt{U_h^2 + W_e^2} \quad [44]$$

$$D = \sin^{-1} \frac{U_h}{R_f} \quad [45]$$

$$R_1 = \frac{R_f \sin B}{\sin(180 + 2\phi_b - \theta - \delta)} \quad [46]$$

$$R_2 = \frac{R_f \sin A}{\sin(180 + 2\phi_b - \theta - \delta)} \quad [47]$$

Water pressure acting on passive block

$$U_{bp} = U_b - U_1 \quad [48]$$

Water pressure along sliding plane

$$U_{bh} = U_{bp} \cos(90 - (\theta - \alpha))$$

$$U_{bv} = U_{bp} \sin(90 - (\theta - \alpha)) \quad [49]$$

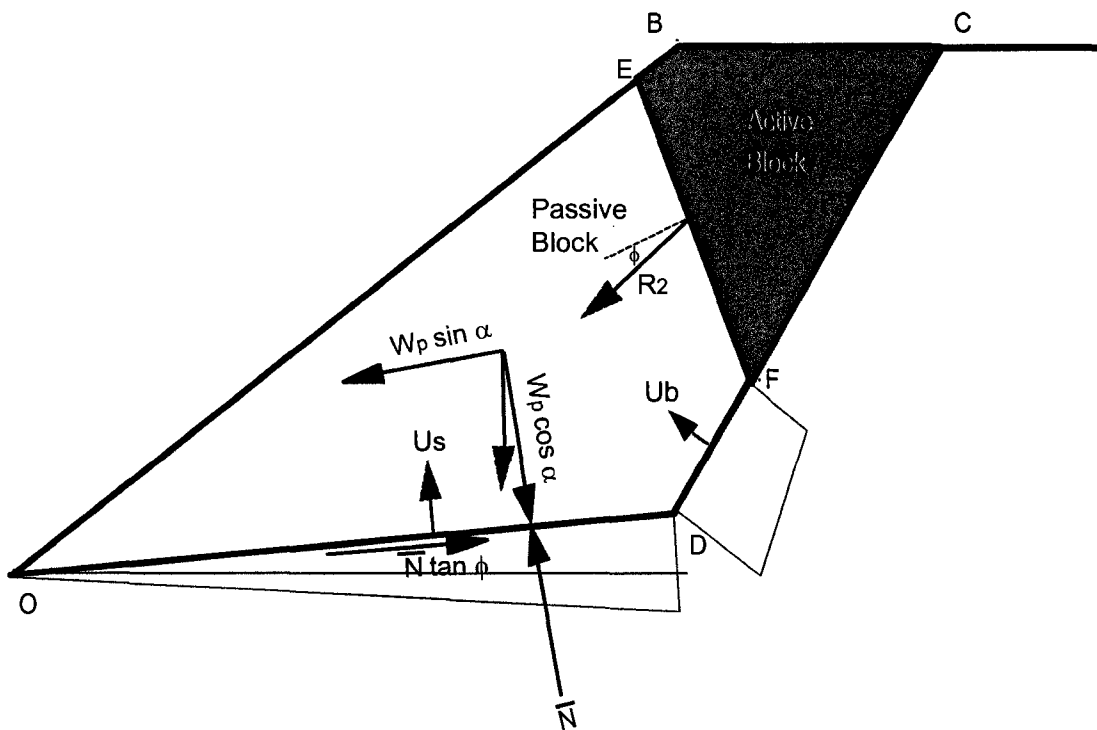


Figure A 6 Calculation of factor of safety for passive block

Net Normal Force on the sliding plane

$$N = W \cos \alpha + R_2 \sin(90 + \phi_b - \delta - \alpha) - U_{bp} \sin(90 - (\theta - \alpha)) - U_s \quad [50]$$

Total Driving Force

$$F_d = W \sin \alpha + R_2 \cos(90 + \phi_b - \delta - \alpha) + U_{bp} \cos(90 - (\theta - \alpha)) \quad [51]$$

Total Resisting Force

$$F_r = N \tan \phi_s \quad [52]$$

$$F.S = \frac{[W \cos \alpha + R_2 \sin(90 + \phi_b - \delta - \alpha) - U_{bp} \sin(90 - (\theta - \alpha)) - U_s] \tan \phi_s}{W \sin \alpha + R_2 \cos(90 + \phi_b - \delta - \alpha) + U_{bp} \cos(90 - (\theta - \alpha))} \quad [53]$$